Understanding the Molecular Mechanisms of Cardiovascular Calcification

Ophélie Gourgas, M.Sc.

Doctor of Philosophy

Department of Mining and Materials Engineering

McGill University, Montreal, Canada

A thesis submitted to the Faculty of Graduate and Postdoctoral Studies of McGill University in partial fulfillment of the degree of Doctor of Philosophy.

Abstract

Deposition of calcium phosphate (Ca-P) minerals in cardiovascular tissues, also known as cardiovascular calcification, is a major health disorder with increasing prevalence and high morbidity and mortality facing the elderly and patients with life-threatening diseases. Currently, there are no approved therapeutic options available for this pathologic condition, except invasive surgeries and costly transcatheter procedures to which not all the patients are suited. The main reason behind this lack of effective therapies is that the molecular mechanisms underlying both vascular and valvular calcifications are unknown. Specifically, the physicochemical details of mineral formation and transformation in this process are still elusive.

In our first study, we analyzed mineral formation and evolution in an animal model that faithfully recapitulates medial calcification in humans, to understand how this type of calcification is initiated on the vascular extracellular matrix. Using a combination of material science techniques, we studied how minerals form and transform over time and space in this *in vivo* system. Calcium was adsorbed first on the elastin (ELN)-rich elastic laminae, and then precursor phases formed which then transformed into more crystalline apatite phases. These events were repeated after each nucleation event, providing a snapshot of the overall mineral evolution at each time point analyzed. This work suggested the importance of analyzing mineral phases rather than just overall calcification extent, to diagnose and possibly prevent disease progression.

In our next study, we developed an *in vitro* model involving ELN to study medial arterial calcification. We used crosslinked ELN-like polypeptide (ELP) membranes immersed in simulated body fluid (SBF) as models to study medial calcification. We showed that Ca-

P minerals first deposited on fibers and filaments and then spread out to globular structures present in the membranes. Mineral phase evolution matched that previously observed in our mouse model of medial calcification, showing that this simple system captured some of the key *in vivo* findings. Overall, this work clarified the mechanism of mineral formation on ELN and provided an *in vitro* model that can be tuned to further understand the molecular mechanism involved and/or to design effective strategies to face this pathologic condition.

Next, we studied the effect of increasing SBF ionic concentration on mineral formation and transformation on crosslinked ELP membranes *in vitro*. Our results showed that increasing SBF ionic concentration significantly enhanced the kinetics of mineral deposition, and strongly affected the chemistry and morphology of the minerals deposited on the ELP membranes and the overall mineralization process. While the use of low concentration SBF seems to be more appropriate to study medial calcification associated with the loss of calcification inhibitors, higher SBF ion concentration may be more relevant to study medial calcification in patients with life-threatening diseases, such as chronic kidney disease.

Finally, we studied the physicochemical properties of mineral deposits found in human aortic valve calcification (AVC). We showed that minerals in AVC have different composition and morphology in men than in women. Calcifications in women were overall less crystalline and contained larger amounts of precursor phases. These phase differences were mirrored by differences in morphology. We identified compact material, calcified fibers, and spherical particles in women, while compact material was the only mineral morphology found in men. Overall, this work suggested that mineralization is

slower in women than in men and follows a different pathway. These results paved the way for new, sex-specific methods to diagnose, prevent and treat this disease.

As a whole, our studies to investigate the physicochemical properties of the mineral deposits and the mineral phase transformations in cardiovascular calcification have provided critical insights that will be useful to further understand the underlying pathophysiological processes. This knowledge may also serve as a basis for novel therapeutic approaches to prevent cardiovascular calcification initiation and/or progression.

Résumé

Le dépôt de minéraux à base de phosphate de calcium (Ca-P) dans les tissus cardiovasculaires, également appelé calcification cardiovasculaire, est un trouble majeur de la santé caractérisé par une prévalence accrue ainsi que par une morbidité et une mortalité élevées chez les patients âgés et ceux atteints de maladies mettant leur vie en danger. Actuellement, il n'existe aucun traitement thérapeutique connu pour cette pathologie, à l'exception des chirurgies invasives et des interventions de réparation par cathétérisme coûteuses et ne convenant pas à tous les patients. L'absence de traitement efficace est principalement dû à la méconnaissance des mécanismes moléculaires des calcifications vasculaires et valvulaires. En effet, les détails physico-chimiques de la formation et de la transformation des minéraux dans ce processus demeurent difficiles à cerner.

Dans notre première étude, nous avons analysé la formation et l'évolution des minéraux dans un modèle animal qui récapitule la calcification médiale chez l'homme, afin de comprendre comment celle-ci est initiée sur la matrice extracellulaire vasculaire. En utilisant une combinaison de techniques de la science des matériaux, nous avons étudié la façon dont les minéraux se forment et se transforment dans le temps et l'espace au sein de ce système *in vivo.* Le calcium a d'abord été adsorbé sur les couches de lames élastiques riches en élastine (ELN), puis des minéraux précurseurs se sont formés pour ensuite se transformer en apatites plus cristallines. Ces événements se sont répétés après chaque nucléation, fournissant ainsi une capture instantanée de l'évolution globale des minéraux à chaque instant analysé. Ce travail a suggéré l'importance d'analyser les

phases minérales plutôt que de seulement estimer l'étendue globale de la calcification, afin de diagnostiquer et d'éventuellement prévenir la progression de la maladie.

Dans l'étude suivante, nous avons développé un modèle *in vitro* à base d'ELN afin d'étudier la calcification artérielle médiale. Nous avons utilisé des membranes réticulées formées à partir d'un polypeptide dérivé de l'ELN (ELP) et immergées dans un fluide corporel simulé (SBF) en tant que modèles pour étudier la calcification médiale. Nous avons montré que les minéraux se déposaient d'abord sur les fibres et les filaments, puis s'étendaient aux structures globulaires présentes dans les membranes. L'évolution des phases minérales correspondait à celle précédemment observée dans notre modèle murin de calcification médiale, montrant ainsi que ce simple système pouvait capturer la plupart des événements ayant lieu *in vivo*. Globalement, ces travaux ont clarifié le mécanisme de formation des minéraux sur l'ELN et ont fourni un modèle *in vitro* pouvant être ajusté pour mieux comprendre le mécanisme moléculaire impliqué et/ou pour concevoir des stratégies efficaces pour faire face à cette pathologie.

Nous avons ensuite étudié l'effet de l'augmentation de la concentration ionique du SBF sur la formation et la transformation des minéraux sur des membranes d'ELP réticulées *in vitro*. Nos résultats ont montré que l'augmentation de la concentration ionique dans le SBF améliorait de manière significative la cinétique de la déposition minérale, et affectait fortement la chimie et la morphologie des minéraux formés sur les membranes d'ELP ainsi que le processus de minéralisation global. Dans l'ensemble, cette étude a suggéré que bien que l'utilisation de SBF à faible concentration soit plus appropriée à l'étude de la calcification médiale associée à la perte d'inhibiteurs de la calcification, une concentration plus élevée en SBF pourrait être plus pertinente pour

l’étude de la calcification médiale chez des patients atteints de maladies mettant leur vie en danger, telle que la maladie rénale chronique.

Enfin, nous avons étudié les propriétés physico-chimiques des gisements de minéraux présents dans la calcification de la valve aortique (AVC) humaine. Nous avons montré que la composition et la morphologie des minéraux dans l'AVC étaient différentes chez l'homme et la femme. Les calcifications chez les femmes étaient globalement moins cristallines et contenaient de plus grandes quantités de phases précurseurs. Ces différences de phases étaient reflétées par des différences de morphologie. Nous avons montré que les minéraux étaient composés de matériaux compacts, fibres calcifiées, et particules sphériques chez les femmes, alors que les minéraux étaient seulement formés de matériaux compacts chez les hommes. Dans l’ensemble, ces travaux ont suggéré que la minéralisation était plus lente chez les femmes que chez les hommes et qu’elle suivait un chemin différent. Ces résultats ont ouvert la voie à de nouvelles méthodes sexo-spécifiques pour diagnostiquer, prévenir, et traiter cette maladie.

Dans l’ensemble, nos études sur les propriétés physico-chimiques des gisements minéraux et les transformations des phases minérales dans la calcification cardiovasculaire ont fourni des informations essentielles qui seront utiles pour mieux comprendre les processus physiopathologiques sous-jacents. Ces connaissances peuvent également servir de base à de nouvelles approches thérapeutiques pour prévenir l’initiation et / ou la progression de la calcification cardiovasculaire.

Acknowledgments

Firstly, I would like to express my most sincere gratitude to my supervisor Prof. Marta Cerruti and my co-supervisor Prof. Monzur Murshed for being great mentors in this research journey. Thank you for your unlimited technical guidance, immense knowledge, patience, and motivational support in carrying out research and writing research articles and thesis. I was inspired not only by your scientific skills, but also by your human qualities, which made this PhD journey a very enriching experience.

My sincere thanks go to all our collaborators and contributors who helped me complete my research. Especially, I would like to thank Dr. Adel Schwertani, Prof. Simon Sharpe, Prof. Antonio Nanci, Juliana Marulanda, Abhinav Parashar, Lisa Muiznieks, Kashif Khan, Bin Yu, and Dainelys Guadarrama Bello. Without their support it would not be possible to complete this highly interdisciplinary research project. I would also like to thank Dr. Yongfeng Hu, Dr. Qunfeng Xiao, and Dr. Aimee MacLeannan of the Canadian Light Source (CLS) for their unlimited help with data acquisition and analysis.

I also thank the current and past colleagues from the Biointerface Lab, for your support, advice, and help during my PhD. Special thanks to Danae Guerra, Emily Buck, Sophia Smith, and Yiwen Chen for your invaluable support, suggestions, encouragements, and all the good memories.

I would like to acknowledge support from the CLS, which is supported by the Canada Foundation for Innovation, the Natural Sciences and Engineering Research Council of Canada (NSERC), the University of Saskatchewan, the Government of Saskatchewan, the Western Economic Diversification Canada, the National Research Council Canada, and the Canadian Institutes of Health Research. I would also like to acknowledge the

other financial sources that made this project possible: The Canada Research Chair Foundation, the Heart and Stroke Foundation, The Jacques de Champlain Award, the Fonds Québécois de la Recherche sur la Nature et les Technologies (FQRNT), the Center for Self-Assembled Chemical Structures, the NSERC, and the McGill Engineering Doctoral Award (MEDA).

I thank my friends and family for their continued support and encouragement. I would specifically like to send my deepest gratitude to my parents, Annie and Guillaume, and my brother, William. Thanks for your unconditional love and support over the years, for supporting every decision I make, and for always believing in me.

Last but not least, I owe thanks to my very special person, my partner, Adam, for your unfailing love, continuous moral support, and patience. Thanks for always inspiring me to become better. It would be hard to imagine having made it to this point without you.

Table of Contents

List of figures

List of tables

Glossary of abbreviations and symbols

β-TCMP	Magnesium-substituted β-tricalcium phosphate
1.5 x SBF	Simulated body fluid with ionic concentration 1.5 times higher than serum
2 x SBF	Simulated body fluid with ionic concentration 2 times higher than serum
3 x SBF	Simulated body fluid with ionic concentration 3 times higher than serum
ACP	Amorphous calcium phosphate
ALPL	Alkaline phosphatase
AS	Aortic stenosis
ATP	Adenosine triphosphate
ATR	Attenuated total reflection
AVA	Aortic valve area
AVC	Aortic valve calcification
BMP	Bone morphogenetic protein
Ca	Calcium
Ca-P	Calcium phosphate
CHA	Carbonated hydroxyapatite
CKD	Chronic kidney disease
CLS	Canadian Light Source
DCPD	Dicalcium phosphate dehydrate
ECM	Extracellular matrix
EDS	Energy-dispersive x-ray spectroscopy

EDX	Energy-dispersive x-ray
ELN	Elastin
ELP	Elastin-like polypeptide
Enpp1	Ecto-nucleotide pyrophosphatase/phosphodiesterase 1
FGF23	Fibroblast growth factor 23
FIB	Focused ion beam
FTIR	Fourier transform infrared
FWHM	Full width at half maximum
Gla	Gamma carboxylated glutamic acid
Gly	Glycine
HA	Hydroxyapatite
LCF	Linear combination fitting
LVEF	Left ventricular ejection fraction
MDCT	Multi detector computed tomographic
MGP	Matrix gla protein
mRNA	Messenger ribonucleic acid
NEXAFS	Near-edge x-ray absorption fine structure
OCP	Octacalcium phosphate
OPG	Osteoprontegerin
P	Phosphate
PBS	Phosphate-buffered saline

PCA	Principle component analysis
PiT-1	Type III sodium-phosphate co-transporter
Pmax	Maximum pressure gradient across the valve
Pmean	Mean pressure gradient across the valve
PPi	Inorganic pyrophosphate
Pro	Proline
PXE	Pseudoxanthoma elasticum
RANK	Receptor activator of nuclear kappa B
RANKL	Receptor activator of nuclear factor kappa B ligand
SAED	Selected area electron diffraction
SBF	Simulated body fluid
SEM	Scanning electron microscopy
SMCs	Smooth muscle cells
SXRMB	Soft X-ray Microcharacterization Beamline
TEM	Transmission electron microscopy
Tris	Tris(hydroxymethyl)aminomethane
Val	Valine
VECs	Valvular endothelial cells
VICs	Valvular interstitial cells

VSMCs	Vascular smooth muscle cells
XPS	X-ray photoelectron spectroscopy
XRD	X-ray diffraction
XRF	X-ray fluorescence

Contribution of authors

This thesis is presented as a collection of manuscripts written by the candidate under the supervision of **Prof. Marta Cerruti** and **Prof. Monzur Murshed**. These papers are presented in **Chapters 4**, **5**, **6**, and **7** of this thesis.

Given the highly interdisciplinary nature of this research, extensive collaboration was required for the successful completion of this work. The role of each co-author is explained below.

Chapter 4

As **first author of this manuscript**, I envisioned and performed all the characterization experiments (Fourier transform infrared (FTIR), Raman, x-ray photoelectron spectroscopy (XPS), x-ray diffraction (XRD), energy-dispersive x-ray spectroscopy (EDS), scanning electron microscopy (SEM), and synchrotron-based spectroscopies) on the calcified mouse arteries. I collected, analyzed, and interpreted all the data. I also performed the statistical tests and wrote the manuscript.

Prof. Marta Cerruti supervised and directed me throughout my research, helped with data interpretation, and extensively revised the manuscript drafts.

Prof. Monzur Murshed supervised the research, revised the manuscript, and approved the final version of the paper. Generation of mice and preparation of aorta tissues were performed in his lab under his guidance.

Dr. Juliana Marulanda was working as a PhD student at McGill University (Faculty of Dentistry) under the supervision of Prof. Monzur Murshed. Her contribution involved generating the mice, preparing the tissues for analysis, and writing the respective

experimental sections of the manuscript. She also helped with acquisition of near-edge x-ray absorption fine structure (NEXAFS) and X-ray fluorescence (XRF) data at the CLS.

Dr. Peng Zhang was working as a Post-doctoral Fellow at McGill University under the supervision of Prof. Marta Cerruti. He helped with collecting synchrotron NEXAFS and XRF data at the CLS.

Chapter 5

As **first author of the manuscript**, I envisioned and performed most of the experiments. I prepared the scaffolds for *in vitro* experiments under the supervision of Dr. Lisa D. Muiznieks. I carried out the *in vitro* mineralization of ELP membranes in SBF. I performed FTIR, Raman, XPS, XRD, EDS, SEM, and NEXAFS on the calcified ELP membranes. I collected, analyzed, and interpreted all the data. I also run the statistical tests and wrote the manuscript.

Prof. Marta Cerruti supervised the research, helped with data interpretation, and extensively revised the manuscript drafts.

Dr. Lisa D. Muiznieks was working as a Post-doctoral Fellow at the Hospital for Sick Children (Molecular Medicine) under the supervision of Prof. Simon Sharpe. Her contribution involved expression and purification of ELPs, preparing the scaffolds for *in vitro* experiments, performing the mechanical tests, offering discussions and recommendations, and writing the respective experimental sections of the manuscript. She also revised the manuscript and approved its final version.

Prof. Simon Sharpe is a professor in the Department of Biochemistry at the University of Toronto and a scientist at the Hospital for Sick Children (Molecular

Medicine). He helped by providing the facilities for ELP expression and purification, scaffolds preparation, and mechanical testing, offering discussions and recommendations. He revised and approved the final version of the manuscript.

Dainelys Guadarrama Bello is a PhD candidate at Prof. Antonio Nanci's lab at the Faculty of Dental Medicine (Université de Montréal). Her contribution included help with preparing samples for transmission electron microscopy (TEM) and selected area electron diffraction (SAED) analysis. She interpreted the TEM and SAED data, revised and accepted the final version of the manuscript.

Prof. Antonio Nanci is a professor at the Faculty of Dental Medicine and Faculty of Medicine (Université de Montréal). His contribution included proposing some experiments, providing facilities for TEM and SAED experiments, revising and accepting the final version of the manuscript.

Chapter 6

As **first author of the manuscript**, I prepared the scaffolds for *in vitro* experiments under the supervision of Dr. Lisa D. Muiznieks. I carried out the *in vitro* mineralization of ELP membranes in the three different SBF solutions. I performed FTIR, XPS, XRD, EDS, SEM, and NEXAFS on the calcified ELP membranes. I collected, analyzed, and interpreted all the data. I also run the statistical tests and prepared the final version of the manuscript.

Prof. Marta Cerruti supervised the research, helped with data interpretation, and extensively revised the manuscript drafts.

Dr. Lisa D. Muiznieks expressed and purified the ELPs, help with preparing the scaffolds for *in vitro* experiments, offered discussions and recommendations, and wrote the respective experimental sections of the manuscript.

Prof. Simon Sharpe helped by providing the facilities for ELP expression and purification, scaffolds preparation, offering extensive discussions and recommendations.

Chapter 7

As **first author of the manuscript**, I performed Raman, EDS, SEM, and NEXAFS on the calcified human aortic valves. I collected, analyzed, and interpreted all the data. I also run the statistical tests and wrote the manuscript.

Prof. Marta Cerruti supervised the research, helped with data interpretation, and extensively revised the manuscript drafts.

Kashif Khan is a PhD candidate at the McGill University Health Center (Cardiology and Cardiac Surgery) under the supervision of Dr. Adel Schwertani. He prepared the histological sections, performed semi-quantitative analyses on the sections, and ran some of the statistical tests. He also wrote the respective experimental sections, revised the manuscript, and approved its final version.

Dr. Adel Schwertani is a cardiothoracic surgeon and supervises a research lab at the McGill University Health Center (Cardiology and Cardiac Surgery). He provided the human samples, offered discussions and recommendations, revised and approved the final version of the manuscript.

Thesis outline

This thesis is written in a manuscript-based format. The chapters are divided as follows: **Chapter 1** presents a brief description of the problems related to cardiovascular calcification and the rationale behind studying mineral phases and mineral phase transformation in cardiovascular calcification *in vivo* and *in vitro*. **Chapter 2** introduces the research hypotheses and objectives.

Chapter 3 reviews the literature relative to this investigation.

Chapters 4, **5**, **6**, and **7** present the four manuscripts showing the findings of the objectives established in this work. **Chapter 8** summarizes contributions of this research to advance knowledge in the field of cardiovascular calcification. **Chapter 9** discusses general conclusions of this work and future perspectives. Finally, **Appendix** includes the list of other papers published.

Chapter 1. General introduction

Mineralization of bone, cartilage, and tooth extracellular matrix (ECM) is a physiological process. These mineralized tissues provide critical biomechanical functions and serve as reservoir for essential mineral ions. In contrast, soft tissue mineralization, also known as ectopic calcification, is a pathological condition associated with a variety of genetic and metabolic disorders (1). Although most soft tissues can undergo pathological calcification, cardiovascular calcification appears as the most common one.

Cardiovascular calcification is a process in which calcium phosphate (Ca-P) mineral deposits form in vessel walls and heart valve leaflets. This can lead to tissue stiffening, plaque rupture, and heart failure (2-4). Cardiovascular calcification is a major health disorder with increasing prevalence and high morbidity and mortality facing the elderly and people with type II diabetes, chronic kidney diseases (CKDs), and atherosclerosis (5-7). Heart disease is the second leading cause of death in Canada and about 2.4 million Canadian adults over 20 live with diagnosed heart disease (8).

Cardiovascular calcification has been traditionally considered as a passive and degenerative process; however, it is now viewed as an active and regulated process that shares many common determinants with hard tissues mineralization (9, 10). Despite the rapid advances in our understanding of this pathologic condition and a few ongoing clinical trials, currently there are no effective therapies for cardiovascular calcification. The only available therapeutic options for calcific vascular and valvular heart disease are invasive transcatheter procedures or surgeries that do not fully address the wide spectrum of these conditions and to which not all patients are suited (3). Thus, an urgent

medical need exists for medical treatments that can halt or slow down disease progression.

Vascular calcification can occur in the intimal and medial layers of the vessel walls. Intimal calcification is commonly associated with atherosclerotic plaques and results from a sequence of events initiated by inflammation, which stimulated the osteochondrogenic transdifferentiation of vascular smooth muscle cells (VSMCs) (11, 12). In contrast, medial calcification occurs in the absence of inflammation and is strongly associated with aging, CKD, and type II diabetes (13, 14). While the molecular mechanism of intimal calcification is quite well understood, the process leading to medial calcification is still elusive.

Although the molecular mechanism of medial calcification is unresolved, several studies have shown the critical role of elastin (ELN) as the main mineral nucleator in this process (15-18). Still, the physicochemical details of mineral nucleation and growth on the medial layer of vessel walls are unknown. This hinders our understanding of how minerals interact with ECM and of the overall molecular mechanism of medial calcification.

Mineral deposition can also happen on the ECM of valve leaflets. Aortic valve calcification (AVC) is the most common valvular heart disease in the developed world and the second most common indicator for cardiac surgery (19, 20). Mineral deposits can severely narrow the opening of the aortic valve, thus leading to aortic stenosis (AS). While it is known that AVC is an active process involving biological pathways with many similarities to intimal arterial calcification (19, 21, 22), we still lack precise molecular insights into the process governing AVC.

Recently, the impact of sex as key modulator of AVC emerged. In fact, several studies have shown that for the same AS severity, women present significantly lower calcification loads than men, thus suggesting important pathophysiological differences between sexes in AVC (23-27). However, the causes of this sex-related difference are still unknown, and more work needs to be done to understand the mechanisms leading to AVC in men and women.

Chapter 2. Hypotheses and objectives

We hypothesize that an interdisciplinary approach combining *in vivo* and *in vitro* models with materials science can provide critical insights into pathophysiological processes underlying cardiovascular calcification.

To test this hypothesis, we establish four main objectives:

(i) Investigate the physicochemical details of mineral nucleation and growth using an *in vivo* model of medial arterial calcification

Medial calcification significantly increases morbidity in life-threatening diseases, and no therapies are available because of lack of understanding the underlying molecular mechanism. In this work, we studied mineral formation and evolution in an animal model that faithfully recapitulates medial calcification in humans, to understand how this type of calcification is initiated on the vascular ECM.

(ii) Develop an *in vitro* model involving ELN to study medial arterial calcification

The next objective is to develop an *in vitro* model to further understand the process of mineral deposition in medial calcification. In fact, the complexity of the artery's structure hampers a complete understanding of this process *in vivo*. Since ELN is the mineral nucleator ECM involved in medial calcification, *in vitro* models involving ELN could greatly improve our understanding of this process. We proposed crosslinked ELN-like polypeptides (ELP) membranes immersed in simulated body fluid (SBF) as models to study medial calcification.

(iii) Study the effect of ionic concentration in SBF on the minerals formed *in vitro* on crosslinked ELP membranes

Using the *in vitro* model developed in Objective (ii), we investigated the effect of increasing SBF ionic concentration on mineral nucleation and phase transformation. We analyzed changes in mineral composition and morphology using a variety of spectroscopic and microscopic techniques.

(iv) Investigate the impact of sex on mineral formation and evolution in AVC

Mineral deposition in AVC can severely narrow the opening of the aortic valve, and thus leads to AS. Currently, there are no therapies to halt or slow down disease progression and the mechanisms governing AVC are poorly understood. Recently, it has been shown that for the same AS severity, women present significantly lower calcification loads than men, thus suggesting pathophysiological differences between sexes in AVC. To further understand these differences, we analyzed mineral deposits from surgically excised calcified human aortic valves from men and women.

Chapter 3. Literature review

3.1. Vascular calcification

3.1.1. Types of vascular calcification

Two distinct forms of vascular calcification exist based on the affected vascular layer (Figure 3.1). Tunica intima, the first vascular layer which can be calcified, is the innermost layer of the arterial wall. It is composed of endothelial cells and a small amount of subendothelial connective tissues. Intimal calcification is the most common form of vascular calcification and is mainly found in association with atherosclerotic plaques (Figure 3.1) (28). In atherosclerotic lesions, calcification occurs in the form of dispersed punctate or patchy mineral crystals associated with VSMCs, macrophages, and the necrotic core of atheroma localized in the intima (11, 12). Calcifications in the fibrous cap overlying the necrotic core of atherosclerotic plaques could lead to microfractures and plaque rupture, leading to acute thrombosis and possibly fatal myocardial infarctions (29, 30).

Calcification can also occur in the arterial media, which is the middle layer of the arterial wall containing VSMCs surrounded by alternate concentric networks of collagen and elastic fibers within the vascular wall. Elastic fibers are mainly composed of two different distinguishable components: ELN and microfibrils consisting of numerous proteins such as microfibrillar-associated glycoproteins, fibrillin, and fibullin (31). During the process of medial calcification, Ca-P minerals are deposited within and around the elastic lamina (Figure 3.1) (15-18). In humans, medial calcification associated with generalized stiffening of the arterial medial is known as Mönckeberg sclerosis (31). In contrast with intimal calcification, it occurs independently of atherosclerotic lesions and is

more prevalent in aging, and in patient with CKDs and type II diabetes mellitus (13, 14). Medial calcification leads to increased vessel wall stiffness and decreased vascular compliance; this may lead to increased arterial pulse velocity and pulse pressure, with an increased risk of cardiovascular mortality (13, 14).

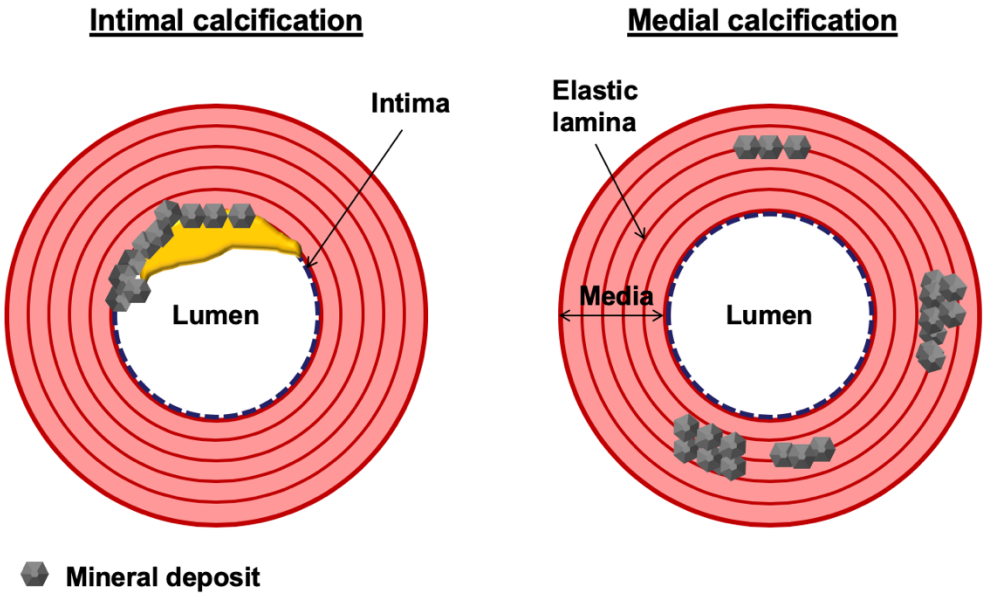

Figure 3.1. Schematic representation of intima and medial arterial calcification. Minerals deposit on the intima layer in association with the atherosclerotic plaque in intima calcification. In media calcification, mineral crystals are deposited on the elastic lamina. (Adapted from Dr. Murshed's lecture slides).

There is a considerable confusion in the literature due to the failure to properly distinguish intimal and medial calcification. Although there may be some common determinants mediating intimal and medial calcification, there are several basic lines of evidence showing that they follow distinct pathways, including histomorphological, clinical, epidemiological, genetic, and animal studies (32). Hence, intimal and medial calcification should be studied separately, and results of studies involving one of them

cannot be extrapolated to make general conclusions about the other one. The remainder of this review on vascular calcification will focus on medial arterial calcification.

3.1.2. Key determinants of vascular calcification

Mineral deposition in the vascular tissues has been traditionally considered as a passive phenomenon associated with aging or degenerative diseases (5, 6, 33). Growing evidence now suggests that vascular calcification is an actively regulated process that shares many common regulators with the physiological mineralization of bone. The major players of both bone mineralization and vascular calcification have been identified as the concentration of free calcium (Ca) ions and inorganic phosphate (P), a suitable ECM, and an environment free of calcification inhibitors (9, 10). Although these common factors govern mineral deposition in the arterial tissues, the exact molecular mechanism may differ depending on the type of vascular calcification.

3.1.2.1. Ca and P ions

The extracellular Ca and P ions are essential for ECM calcification. Alteration of serum Ca and P levels by genetic, metabolic, or therapeutic means can directly affect the initiation and progression of vascular calcification (34).

Elevated serum P levels have been associated with medial arterial calcification. Several *in vitro* studies have shown that when VSMCs were incubated in culture media with P concentrations close to those observed in hyperphosphatemia (> 1.5 mM), apatite phases precipitated into the ECM surrounding the cells (35-37). As a possible mechanism, it was suggested that this process was not just a passive precipitation of Ca-P phases, but rather a phenotypic change of VSMCs and the subsequent upregulation of genes commonly associated with bone differentiation (5, 36). Similar phenotypic changes

have also been observed *in vivo* both in human and in animal models of vascular calcification (36, 38, 39). Elevated P-induced phenotypic transition and calcification were shown to be dependent on a type III sodium-phosphate cotransporter, PiT-1, the most abundant transporter of P in human and rat VSMCs. High P levels stimulate the production of mineral molecules, such as matrix vesicles, Ca-binding proteins, alkaline phosphatase (ALPL), and collagen-rich ECM, which may in turn lead to vascular calcification (9, 40).

Likewise, elevating Ca levels in the culture medial of VSMCs *in vitro* to levels found in hypercalcemia (>2.6 mM) led to enhanced calcification and transdiferentiation of VSMCs (35, 41). Elevated Ca-induced calcification was also dependent on the function of PiT-1. Although elevated Ca did not significantly increase P uptake, it induced PiT-1 messenger ribonucleic acid (mRNA) expression (9). Hypercalcemia, along with the elevated serum P levels typically found in CKD, are considered to be the major cause of vascular calcification in CKD patients (42).

On the other hand, a reduced serum P level (hypophosphatemia) can prevent vascular calcification in mice lacking matrix gla protein (MGP), a potent mineralization inhibitor (43). The severe vascular calcification and associated abnormalities observed in $MGP^{-/-}$ mice are completely absent in $Mgp^{-/-}$; Hyp mice, who have hypophosphatemia due to *Phex* inactivation (44). Inactivation of *Phex* leads to an increase of fibroblast growth factor 23 (FGF23), a P regulating hormone in the serum. FGF23 acts on kidney proximal tubule cells to decrease the expression of type II sodium-phosphate cotransporters, resulting in renal P wasting and serum P level lower than normal (9.6 ± 0.2 vs 7.9 ± 0.3 mg/dl, $P < 0.001$) (45, 46).

Overall, these data show that Ca and P not only participate in Ca-P mineral formation but can also directly initiate both phenotypic changes and mineralization in vascular calcification.

3.1.2.2. Mineral scaffolding ECM

Initiation of ECM calcification requires a scaffold of fibrillar proteins such as collagen or ELN, within which critically sized nuclei of Ca-P compounds precipitate and become stable. These precipitates grow and mature into apatite phases over time. In bone, fibrillar type I collagen acts as mineral scaffold, and mineral deposition can take place both within the collagen fibrils and in the interfibrillar spaces (34, 47). In medial calcification, instead, the most abundant mineral nucleating protein appears to be ELN. Several studies have shown that mineral deposition occurs predominantly along and within the ELN-rich elastic laminae in humans and animal models (15-18). This process is increased when ELN is degraded by elastase and other proteases (48).

Recently, Khavandgar. *et al.* (10) showed that mineralization occurs almost exclusively along the ELN laminae in mouse model lacking MGP, and not in the collagen-rich regions. They also showed that the ELN content in arteries is critical for the initiation and progression of medial calcification in MGP-deficient mice. The amounts of accumulated minerals were significantly different within the same MGP-deficient aorta depending on the ELN content: the thoracic segment, which contains more ELN in comparison to the abdominal segment, is more mineralized than the latter. The critical role of ELN was further confirmed by the significant delays in mineral initiation and progression when decreasing the ELN gene dosage. While these studies show the

important role of ELN as main mineral nucleator in medial calcification, the molecular mechanism of mineral nucleation by ELN is still not understood.

3.1.2.3. Calcification inhibitors

In order for hard tissue ECM to properly mineralize, an environment free of calcification inhibitors is mandatory (43). On the contrary, these inhibitors are needed to prevent mineral deposition in vascular calcification. In fact, in absence of such inhibitors, spontaneous precipitation of Ca-P phases can occur since arterial media layer carries a suitable mineral scaffolding ECM, and that extracellular levels of Ca an P ions are supersaturated in blood serum in respect to apatite phases. Thus, calcification inhibitors are critical in the prevention of vascular calcification and a discussion on the mechanism of action of several key calcification inhibitors will be provided in the next section.

3.1.3. Molecular mechanisms of medial calcification

Based on the understanding of bone formation and of the regulators of ECM mineralization, several different mechanisms, not necessarily mutually exclusive, have been proposed for vascular calcification (Figure 3.2) (33).

The discovery of the expression of bone proteins such as osteopontin, osteocalcin, and bone morphogenetic protein (BMP2) in calcified vascular tissues has suggested the hypothesis that osteogenic mechanisms may play a role in vascular calcification (49). A variety of factors such as genetic mutations, apoptosis, renal abnormalities causing altered mineral homeostasis, or chronic inflammation, may induce the transdifferentiation of VSMCs into osteoblast or chondrocyte-like cells. These cells can modulate the levels of basic determinants of ECM mineralization to initiate vascular calcification. This

hypothesis was further reinforced with the observation of bone-forming events, including the production of matrix vesicles and apoptotic bodies in vascular calcification (50).

Although this was the most popular hypothesis on the mechanism of vascular calcification for many years, results from several groups supported an additional hypothesis, i.e. vascular calcification is due to the lack of specific calcification inhibitors, such as MGP, inorganic pyrophosphate (PPi), fetuin A, osteopontin, and osteoprontegerin (OPG). While both molecular mechanisms are not mutually exclusive, determining whether the transdiferentiation of VSMCs or the lack of inhibitors is the cause of the calcification process is critical, as medical treatments will differ depending on which mechanism is the initiating process.

3.1.3.1. Osteochondrogenic transdifferentiation of VSMCs

VSMCs are present in the medial layers of blood vessels and are usually responsible for regulating vascular tone. They also play a critical role in maintaining and remodelling the ECM of blood vessels (51). VSMCs and cells present in physiological mineralized tissues (i.e. chondrocytes and osteoblasts) share a common developmental precursor, the mesenchymal stem cell. This common developmental origin may facilitate the transdifferentiation of VSMCs into chondrocyte/osteoblast-like cells in response to a variety of stimuli, such as increased serum levels of Ca and P ions, lipid accumulation, and inflammatory responses, causing the induction of pro-chondrogenic/-osteogenic signaling pathways (Figure 3.2). In fact, the phenotypic plasticity of the mesenchymal-derived VSMCs allows them to transdifferentiate both *in vitro* and *in vivo*, thus gaining osteochondrogenic-like characteristics and expression of related genes (13).

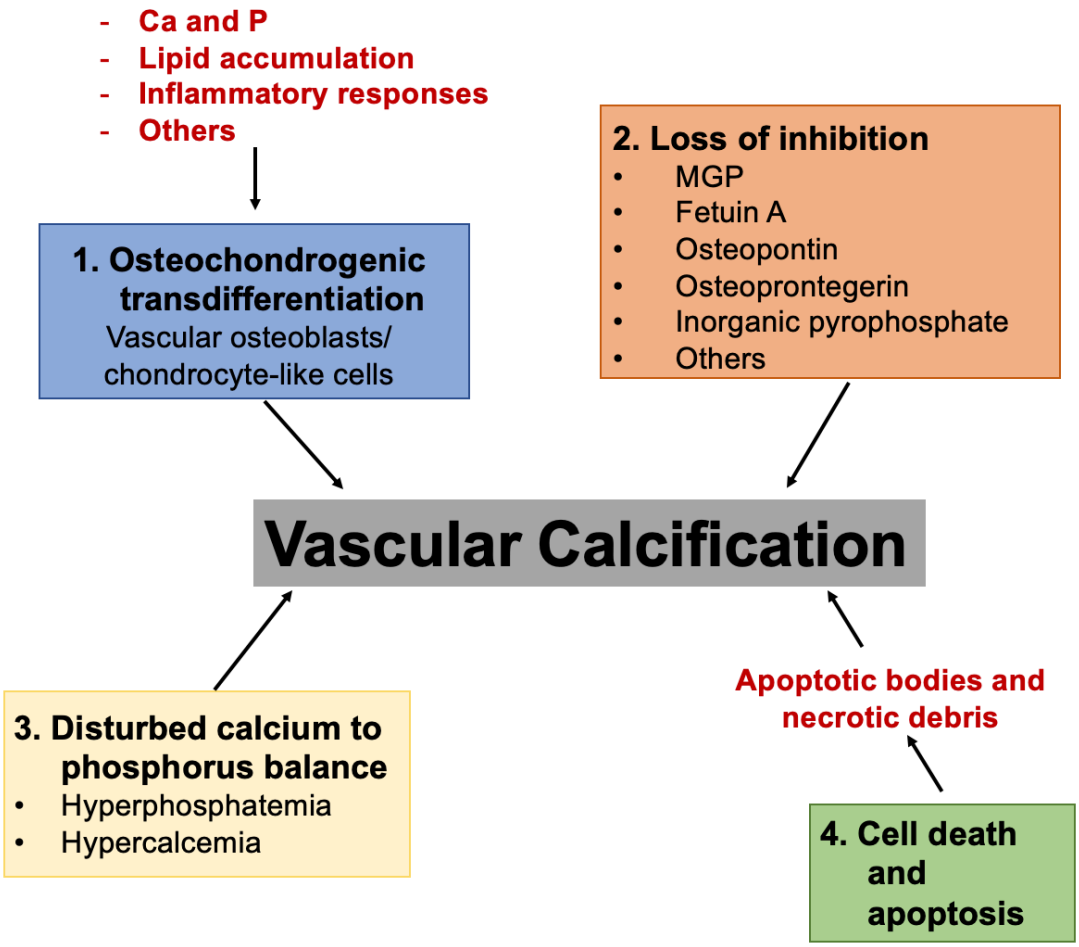

Figure 3.2. Schematic illustrating four non–mutually exclusive theories for vascular calcification: (1) osteochondrogenic transdifferentiation of VSMCs promotes mineral formation recapitulating bone development mechanisms, (2) loss of inhibition as a result of deficiency of constitutively expressed tissue-derived and circulating mineralization inhibitors leads to apatite deposition, (3) disturbed calcium to phosphorus balance, for example in case of hyperphosphatemia or hypercalcemia, and (4) cell death and apoptosis leading to release of apoptotic bodies and/or necrotic debris that may serve to nucleate apatite at sites of injury. (Adapted from (33)).

Transdifferentiation of VSMCs into osteoblasts-like cells has been reported in the mineralized medial layer of CKD patients. VSMCs in these patients express an early chondrogenic/osteogenic transcription factor RUNX2, followed by the upregulation of several other osteoblast markers such as type I collagen, osteopontin, bone sialoprotein, and ALPL (38, 39). Osteogenic transdifferentiation was also reported in the aortas of transgenic mice ubiquitously expressing *Msx2*, an osteoblast-specific transcription factor,

which were on a high-fat diet. The high-fat diet led to medial calcification in these transgenic mice, but not in their non-transgenic littermates. The results of these studies showed that in this model, *Mxs2* expression in the aortic media layer promoted vascular calcification by activating paracrine WNT signals (52, 53).

Also, calcified arteries in MGP-deficient mice contained chondrocyte-like cells in the medial layer (36, 54). Bostrom *et al*. and Zebboudj *et al.* suggested that MGP binds to BMPs, thus inhibiting the downstream signaling events and preventing the osteochondrogenic transdifferentiation of VSMCs (55, 56). Another study showed that the expression of RUNX2 is upregulated in the VSMCs of MGP-deficient mice (57). However, this study showed that RUNX2 upregulation can be detected at two weeks of age in the arterial tissues, and previous studies showed extensive medial arterial calcification at this age in MGP-deficient mice (54). It is thus not clear whether the observed osteochondrogenic differentiation in MGP-deficient mice takes place before or after the initiation of mineral deposition on the elastic lamina.

More recently, Khavandgar *et al.* showed that the osteochondrogenic transdifferentiation of VSMCs is not a prerequisite for medial arterial calcification in MGP-deficient mice (10). In fact, no upregulation of the expression of major osteochondrogenic markers was detected in young MGP-deficient mice prior to the initiation of medial calcification. They only observed upregulation of chondrogenic markers SOX9 and aggrecan in older mice that had heavily calcified arteries. They also showed that ablation of ALPL in *Mgp*$^{-/-}$*; Alpl*$^{-/-}$ mice had no effect on the vascular calcification phenotype. ALPL expression is mainly regulated by the BMP signaling pathways, thus these findings suggest that vascular calcification in MGP-deficient mice may not involve an induction of

BMP signaling. These results are in agreement with a previous *in vitro* study showing that the treatment of rat VSMCs with warfarin, an MGP antagonist, resulted in calcification of the cultures, but did not alter the levels of RUNX2 mRNA expression (58). Overall, these findings suggest that osteochondrogenic differentiation of VSMCs is not the initiating mechanism leading to medial calcification.

In addition, recent evidence shows that bone-related gene expression can be completely prevented *in vitro* with calcification inhibitors such as PPi or phosphonoformic acid, even in the presence of high Ca and P concentrations (59, 60). This suggests that osteochondrogenic expression can be a consequence of the nucleation of Ca-P minerals, rather than the cause.

3.1.3.2. Loss of calcification inhibitors

Under normal conditions, blood vessels are protected from calcification via the production and secretion of mineralization-inhibiting molecules. The loss of their expression gives rise to spontaneous calcification and increased mortality. Studies in both animals and humans have shown that the loss of a single calcification inhibitor can initiate medial calcification (61). VSMCs can dynamically express a range of proteins that both drive and inhibit calcification. The osteochondrogenic markers are balanced by inhibitors including MGP, fetuin A, osteopontin, OPG, and PPi (Figure 3.2).

MGP, a 14 kDa protein produced in both VSMCs and chondrocytes, belongs to a family of gamma (γ) carboxylated glutamic acid (Gla)-containing proteins (62). MGP has five Gla residues in humans and only four in mice (63). These Gla residues bind to Ca ions and apatite crystals and may prevent the nucleation and further growth of the nascent apatite crystals (63, 64). The glutamate residues are converted into Gla-residues during

a post-translational modification carried out by a vitamin-K dependent carboxylase (Figure 3.3). Upon oxidation of the co-factor-vitamin K hydroquinone (KH_2), the addition of an extra carboxyl group takes place at the γ-position of a glutamate residue (65). After reduction, vitamin K can be recycled by the vitamin K epoxide reductase (VKOR), which oxidizes it to reinitiate the cycle (Figure 3.3). The synthesis of Gla proteins can be blocked by 4-hydroxycoumarin derivates that block the VKOR enzyme, such as Warfarin, a commonly prescribed anticoagulant (Figure 3.3) (65). Additionally, MGP undergoes serine phosphorylation at the serine residues at positions 3, 6 and 9. Phosphorylation of ECM proteins has been recognized as a mechanism of activity regulation, however the impact of a such modification in MGP's anti-mineralization function is still unclear (65). Also, the kinase that phosphorylates the serine residues in MGP is still unknown.

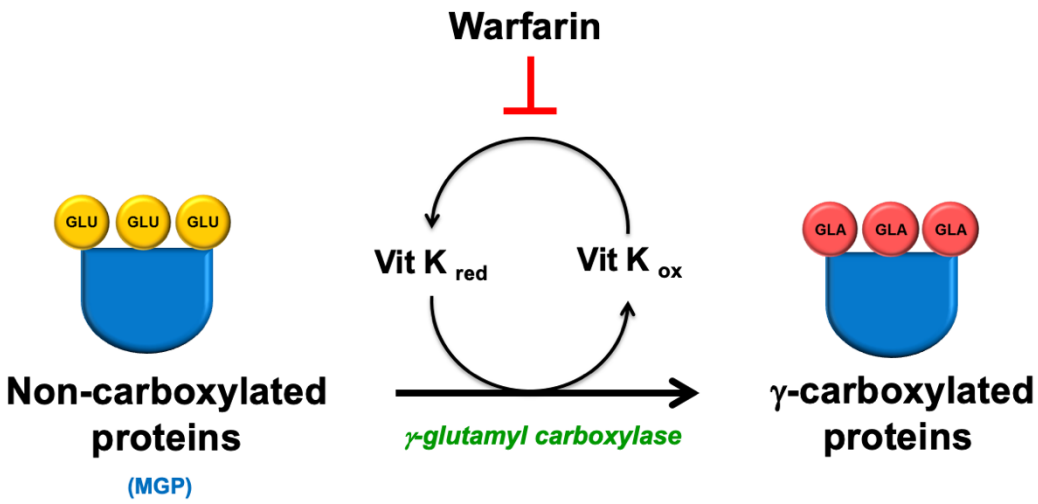

Figure 3.3. Schematic representation of the γ-carboxylation of Gla proteins such as MGP. The glutamate residues (GLU) are converted into GLA residues through the action of the γ-glutamyl carboxylase (GGCX) enzyme, using vitamin K as a co-factor. The oxidation and reduction of vitamin K is a continuous process dependent on the vitamin K epoxide reductase (VKORC) and can be inhibited by warfarin (Adapted from Dr. Murshed's lecture slides).

MGP deficiency in humans causes Keutel syndrome, a rare genetic disease characterized by extensive tissue calcification, pulmonary artery stenosis, brachytelephalangism, and facial dimorphism (66). *Mgp*$^{-/-}$ mice recapitulate most of the phenotypic abnormalities of the Keutel syndrome patients. In this model, the medial layer of the arteries quickly mineralizes, to the point that the animals die before 2 months of age because of complications caused by extensive mineral deposition (67).

Although MGP is one of the most potent mineralization inhibitors of vascular calcification *in vivo*, the molecular mechanism of its mode of action is still unknown. It was shown that the anti-mineralization function of MGP requires four Gla residues. While native MGP with four Gla residues, when overexpressed in bone caused severe mineralization defects, overexpression of MGP lacking all four Gla residues did not affect bone mineralization (68). However, the presence of Gla residues in osteocalcin, another Gla protein, was not sufficient to prevent arterial calcification in MGP-deficient mice. (68) This suggests that additional feature(s) in MGP is/are required for its anti-mineralization function. Based on atomistic molecular dynamics data, O'Young *et al.* suggested that both the Gla and phosphorylated N-terminal serine residues in MGP participate in the interaction of MGP with apatite crystals (69). This possibility is yet to be confirmed in cell culture and animal models.

A complementary inhibiting process could be the interaction between MGP and ELN, the mineral scaffolding ECM in medial calcification. By interaction with ELN on the same sites where Ca ions adsorb, MGP could prevent apatite nucleation and growth. Thus, a deficiency in MGP would lead to an unmasking of ELN and subsequent calcification. This

hypothesis is supported by immunohistochemical studies showing that MGP was present at the site of ELN fibres in healthy human arteries (70).

Fetuin A is a 60 kDa glycoprotein expressed in the liver and secreted into the blood, where it exerts its systemic anti-mineralization function. It has a high affinity for Ca-P compounds, forming soluble colloidal calciprotein particles (CCPs) that contain fetuin A, Ca, and P (71, 72). Fetuin accumulates in bone and sites of ectopic calcification such as atherosclerotic plaques (72); however, it is not known whether fetuin affects medial calcification.

The Fetuin A knockout mice show a severe calcification phenotype when generated on a genetic background that is prone to ectopic calcification. These mice manifest massive ectopic calcification in multiple tissues but not in the vascular media (71). Also, despite widespread soft tissue calcification in these mice, there has been no report of the presence of chondrocytes or osteoblasts at the sites of ectopic calcification (71). This observation strongly suggests that ectopic calcification may occur in the absence of any osteochondrogenic transdifferentiation.

Low levels of circulating Fetuin A have been detected in CKD patients and are associated with increased risk of death (73). Serum levels of Fetuin A are also reduced in patients suffering from Pseudoxanthoma elasticum (PXE), a genetic disease caused by a mutation of the *Abcc6* gene. The ectopic calcification in these patients is mainly localized in skin, eyes, and cardiovascular system (74). The overexpression of Fetuin A in a mouse model of PXE (i.e. *Abcc6*$^{-/-}$ mice), significantly reduces soft tissue calcification after 12 weeks of age (75). These data show the important role of Fetuin A as inhibitor of

vascular calcification, but its exact mechanism of action is still unclear and needs further investigation.

Osteopontin is an acidic phosphoprotein normally found in mineralized tissues such as bones and teeth, and regulates mineralization by inhibiting apatite crystal growth (76). Although osteopontin is not found in normal arteries, it is highly expressed at sites of calcification in human calcified arteries (77-79). It was shown that osteopontin levels are greatly elevated in calcified arteries from MGP-deficient mice (36). Also, mice deficient in both osteopontin and MGP (*Opn*$^{-/-}$*; Mgp*$^{-/-}$ mice) showed accelerated and enhanced medial calcification compared to those that were only MGP-deficient (80). These findings suggest that osteopontin is a powerful inhibitor of vascular calcification *in vivo* and may play an important role in the adaptive response of the body to injury or disease.

OPG is a phosphoprotein that regulates bone formation by inhibiting apatite crystal growth and osteoclast differentiation (81). It is produced by many tissues, including the cardiovascular system, lungs, kidney, and immune system (82). OPG was found to inhibit osteogenic differentiation and calcification in VSMCs (83), and OPG-deficient mice developed severe osteoporosis and vascular calcification (84). Clinical studies show that as the severity of vascular calcification increases in CKD patients, so does the serum OPG levels, thus indicating that this increase might be a compensatory response to the disease, rather than a risk factor (85, 86).

PPi is considered as one of the most potent inhibitors of ECM mineralization both in physiological and pathological calcification. PPi is formed by two P groups joined by an phosphoester bond and can bind to nascent Ca-containing crystals and inhibit further

crystal growth (87). It is generated by hydrolysis of adenosine triphosphate (ATP) induced by the enzyme ecto-nucleotide pyrophosphatase/phosphodiesterase 1 (Enpp1), and ECM-bound glycoprotein. When the Enpp1 gene is mutated and the enzyme is inactive, severe abnormal calcification of soft tissues, including medial arterial calcification, occurs both in mice and humans (87). This is one of the several demonstrations of the important role of PPi in preventing vascular calcification. In contrast, ALP which is induced by VSMC osteochondrogenic transdifferentiation, promotes vessel wall ECM mineralization (88). ALP hydrolyzes PPi, which in turn generates P ions and thus favors the development of vascular calcification.

3.1.3.3. Cell death and apoptosis

In addition to the two main molecular mechanisms of medial arterial calcification described above, it is believed that cell death and apoptosis can lead to vascular calcification (Figure 3.2). The vessel wall is damaged by inflammation processes and oxidative stress in CKD patients, which may induce cell apoptosis. During apoptosis, VSMCs release both matrix vesicles and apoptotic bodies. Although apoptotic bodies are larger than matrix vesicles, they both have the ability to concentrate Ca and nucleate Ca-P minerals (50).

3.1.4. *In vitro* models of medial arterial calcification

Vascular calcification is primarily studied *in vitro* using cultures of VSMCs. Many *in vitro* models using VSMCs from various sources (i.e. mouse, bovine, and human tissues) have been developed to explain vascular calcification, i.e. models described in the previous section (35-37, 40, 41, 50, 55, 58-60, 83). However, as discussed above, mineral deposition in medial calcification is most likely initiated by a physico-chemical process rather than a cell-mediated mechanism. Hence, an *in vitro* model based on ELN, the mineralization scaffolding ECM in medial calcification, may be more suitable to study the mechanism of medial calcification. Understanding how minerals nucleate and growth on ELN could greatly improve our understanding of the overall mechanism of medial calcification. Several acellular *in vitro* models based on ELN have been developed for medial calcification in the past 60 years.

To understand the approach used to develop *in vitro* models based on ELN, we first need to describe and comprehend the formation of ELN *in vivo*.

3.1.4.1. ELN and elastogenesis

The main difficulty for building *in vitro* models based on ELN is the highly water insoluble character of this protein. ELN is the major component of elastic fibers that allows stretching and reversible recoiling to many vertebrate tissues including major blood vessels, lung, and skin (89). ELN self-assembles from its monomeric precursor, tropoelastin.

Tropoelastin is a highly (>75%) non-polar protein characterized by hydrophobic sequences, or domains, that alternate with lysine-containing crosslinking domains (Figure 3.4). Hydrophobic domains are rich in glycine, valine, and proline residues that are

commonly arranged into repetitive motifs such as Val-Pro-Gly and Pro-Gly-Val-Gly (89, 90). Crosslinking domains contain lysine residues that are almost exclusively found in pairs spaced three or four residues apart (Figure 3.4). The formation of covalent crosslinkings by these lysine residues provides fibrous elastic networks with high resilience and structural integrity. Lysine residues in crosslinking domains are arranged either on a poly-alanine background (denoted KA-type), or within sequences rich in hydrophobic residues (denoted KP-type) (Figure 3.4) (90).

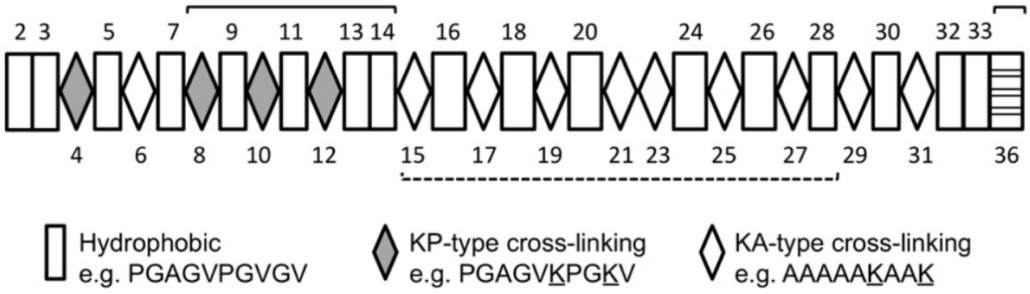

Figure 3.4. Schematic domain arrangement of human tropoelastin. Hydrophobic domains (open rectangles) alternate with cross-linking domains of KP-type (shaded diamonds) or KA-type (open diamonds). Representative sequence for each of these domain types is given. Motifs conserved across phylogeny are indicated by a solid bar. The C-terminal domain 36 (horizontal stripes) contains an RKRK motif. An expanded region that likely arose from the duplication of a KA-type cross-linking and hydrophobic exon pair is indicated by a dotted bar. Domain 22 is not observed in the most common isoform of mature tropoelastin. Genomic sequences corresponding to exons 34 and 35 have been lost in humans through evolution (90).

The process by which tropoelastin assembles into ELN *in vivo* is classically characterized by distinct stages of tropoelastin synthesis, coacervation, microfibrillar deposition and crosslinking. Human tropoelastin is expressed as an unglycosylated protein by elastogenic cells such as SMCs, endothelial cells, and fibroblasts in response to mechanical stress, glucocorticoids, cytokines, and growth factors (89). In the extracellular space, tropoelastin self-aggregates in a process known as coacervation.

Coacervation is a reversible thermosensitive liquid-liquid phase separation that is characterized by the formation of a dense protein-rich phase dispersed in a protein-poor solution phase (90). *In vivo*, this process is likely to be initiated by a rise in concentration concomitant with monomer secretion into a volume-restricted compartment (89). The soluble monomers (about 15 nm) are progressively aligned and concentrated into micrometer sized spheres which facilitate the formation of crosslinks (91). Hydrophobic domains are involved in the correct alignment of tropoelastin prior to assembly. The tropoelastin coacervates remain attached to cell-surface integrins and glycosaminoglycans until deposition on microfibrillar bundles (89). These microfibrillar bundles serve to orient the ELN in the formation of the elastic fibers.

Microfibrillar proteins recruit lysyl oxidase, which oxidatively deaminates specific tropoelastin lysine residues to form allysines (91). This triggers the spontaneous formation of intra and intermolecular crosslinks, thus forming three—dimensional networks of ELN fibers. Crosslinking imposes structural restrictions on ELN and renders elastic fibers insoluble (89).

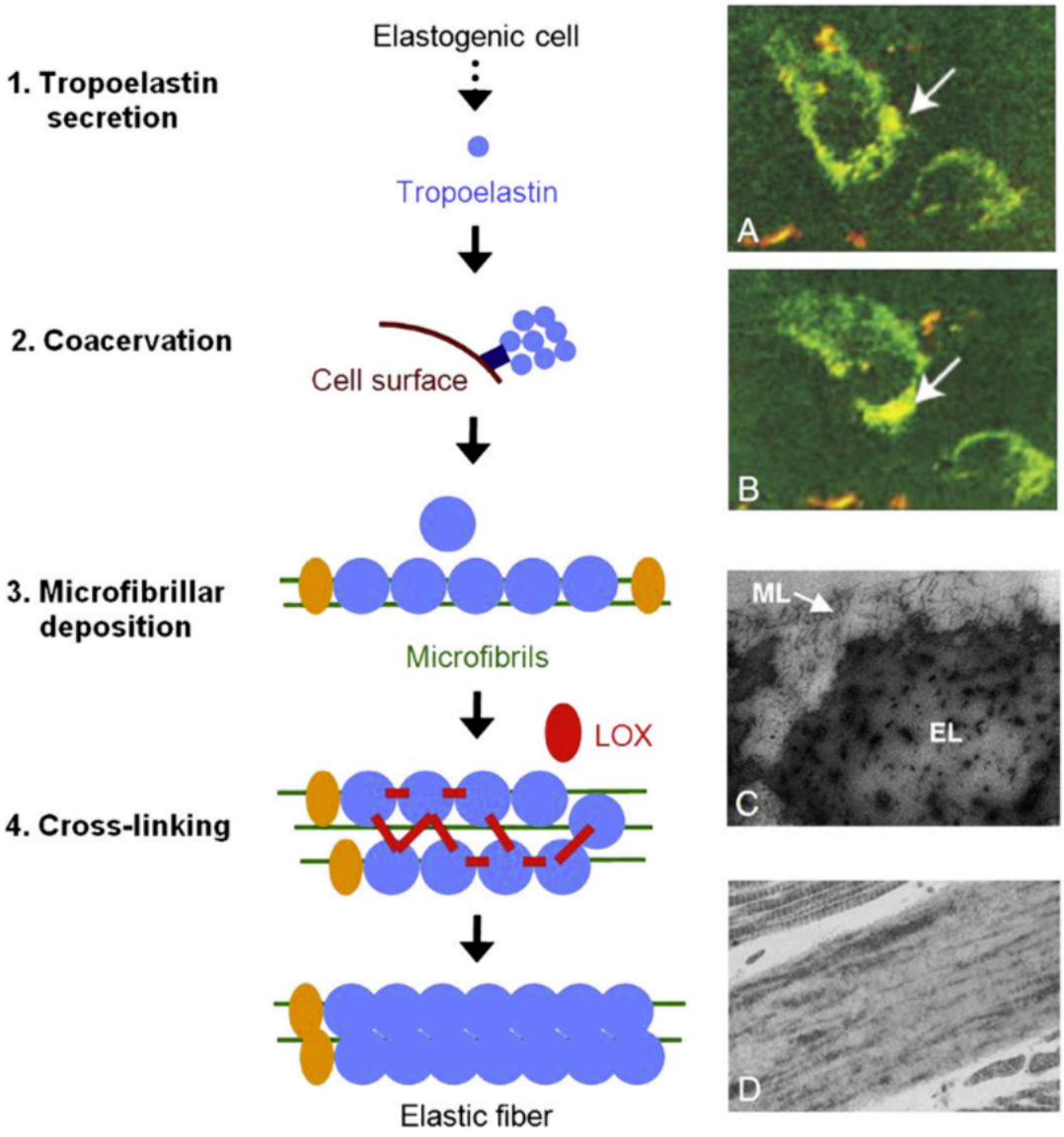

Figure 3.5. The classical model of elastic fiber assembly. Tropoelastin is secreted by elastogenic cells and coacervate into globules that remain attached to the cell surface until deposition on microfibrils. Microfibrillar proteins recruit lysyl oxidase (LOX), which modifies specific tropoelastin lysine residues. This triggers the formation of intramolecular and intermolecular crosslinks needed for the formation of stable and insoluble elastic fibers. (A) Secretion of tropoelastin particles (yellow particles shown by the arrows) by RFL-6 cells. (B) Tropoelastin aggregates into a large globule on the cell-surface. (C) Association of elastin (EL) with microfibrils (ML) in a human skin section stained with uranyl acetate and lead citrate. (D) Electron micrograph of elastic fibers in human dermis (89).

3.1.4.2. In vitro models based on ELN

Several methods were developed to obtain solubilized ELN from animal sources through partial hydrolysis of the protein chain (92). Agents used for hydrolysis include hot alkali, guanidine, oxalic acid, and potassium hydroxide (93, 94). Animal tissues rich in ELN, such as bovine ligamentum nuchae, are first extracted. Other macromolecules such as collagen, glycosaminoglycans, and carbohydrates, are removed, and ELN is fragmented by cleaving peptide bonds (95, 96). These fragmented peptides have properties similar to tropoelastin, such as the capacity to coacervate (97). Early studies published between 1964 and 1993 used solubilized ELN to build *in vitro* models for medial calcification.

Using solubilized ELN extracted from bovine nuchal ligament, Schiffmann *et al.* suggested sulfhydryl groups as nucleation sites in ELN (98, 99). However, it has been shown later that native ELN contains only few cysteines and other sources of sulfhydryl groups (100-102). Solubilized ELN is often contaminated by residual microfibrillar proteins, which are characterized by their high content of cysteine (103). The lack of a purification step after the extraction of ELN may thus explain the results obtained by Schiffmann *et al* (98, 99).

Carboxyl and amino groups have also been suggested as nucleation sites using *in vitro* models involving ELN. Molinari-Tosatti and Gotte showed that the binding of Ca ions to purified solubilized ELN was dependent on pH. In fact, Ca-ELN binding occurred only above pH 5.5 and increased with increasing pH (104). This could be due to electrostatic interactions between Ca ions and ionized groups on ELN, such as carboxyl groups. They also reported no binding of P at physiological pH, indicating that Ca rather than P ions

interacted first with ELN (104). Several studies have shown that blocking or altering amino groups by treatment with fluorodinitrobenzene, nitrous acid, or acetic anhydride, inhibited ELN calcification *in vitro*, thus suggesting their role as main nucleation sites (98, 105).

Although charged groups have been proposed as nucleation sites by several *in vitro* models of ELN calcification, these groups have been detected only in low concentrations in the amino acid composition of native ELN, which is mostly apolar (106). In addition, Starcher and Urry (107) showed that a solubilized form of ELN in which all the carboxyl and amino groups were blocked provided an excellent matrix for calcification *in vitro*. These findings suggest that ELN calcification involves the contribution of other groups.

Urry *et al.* proposed another type of nucleation sites in the absence of ionic interactions. The results of their *in vitro* study using solubilized ELN suggested that Ca ions bind at neutral binding sites (i.e. carbonyl groups) forming complexes with the acyl oxygens in ELN (108). When ELN was dissolved in trifluoroacetic acid, thus making all the functional groups on ELN either positively charged or neutral, a large conformation change was observed upon addition of Ca ions, thus indication that Ca ions can interact with neutral sites (108). The ability of neutral sites to coordinate and bind to Ca ions was further confirmed by Rucker *et al.* In their *in vitro* model, Ca-ELN binding was largely independent on changes in pH and ionic strength in solutions containing methanol (109). While these studies did not preclude the possibility that charged groups act as nucleation sites in ELN, they showed that Ca ions can also bind at neutral sites.

In agreement with previous studies, Mollinari and Gotte showed that in ELN calcification, apatite precipitation occurs with the prior binding of Ca rather than P (104). However, the results from Koutsopoulos *et al.* another study still using solubilized ELN

as *in vitro* model suggested that the formation of minerals on ELN was initiated via the adsorption of inorganic P (110). Possibly, one of the reasons behind these contradictory results is the heterogeneity of solubilized ELN. In fact, extraction and purification of solubilized ELN from animal sources result in a heterogeneous mixture of hydrophobic ELN fragments that are partially crosslinked, rather than the alternative domain structure observed in natural ELN (89, 111). Also, solubilized ELN shows evidence of degradation and contains high levels of contaminants (112).

An alternative to solubilized ELN are synthetic ELN-like polypeptides (ELPs) representative of the whole structure of the protein. Urry was the first to develop an artificial polypentapeptide (HCO-(Val-Pro-Gly-Val-Gly)$_n$-Val-OMe, where $10 \leq n \leq 15$) mimicking the repeated hydrophobic motifs found in tropoelastin (113). Since then, other groups have produced many ELP variants composed of segments of alternating hydrophobic and crosslinking domains (90, 114-120), or the full-length monomer (90, 91, 121, 122), using synthetic genes expressed in bacteria. ELPs self-organize into structures resembling native ELN through coacervation. Several researchers used ELPs with various combinations of hydrophobic and crosslinking domains to explore ELN structure and self-assembly *in vitro* (90, 114-120), thus overcoming the limitations of the previous studies based on solubilized ELN.

Not only do ELPs self-assemble *in vitro*, but they can also be crosslinked to form ELN-based matrices that have physical and elastic properties approaching those of native insoluble ELN (117, 118, 123). Many researchers have tested ELPs in this crosslinked form for tissue engineering, such as enamel, cartilage, and bone regeneration, and vascular grafts (124-134). In most of these studies, the ELN sequence was modified by

the addition of one or more bioactive sequences, for example to promote mineralization (i.e. Statherin-derived peptide) (125-129, 134), mesenchymal stem cell adhesion (i.e. RGDS sequence), or endothelial cell adhesion (i.e. REDV sequence) (126, 129, 130).

Despite the large literature on ELP-based materials, especially to promote hard tissue regeneration, ELP-based matrices have not been explored as models to understand medial arterial calcification. Even more surprisingly, no more *in vitro* models of ELN calcification have been reported since the early studies using solubilized ELN published between 1964 and 1993, and no one has brought new convincing evidence on the nucleation sites on ELN and the overall mechanism of mineral formation.

Currently, there is no available *in vitro* model that truly mimics arterial structure. *In vitro* models using natural tissues are the closest models to the *in vivo* situation; however, their complexity hampers a molecular understanding of the mechanism of vascular calcification.

3.2. Valvular calcification

While mineral deposition can occur in the four heart valves, AVC is the most common form of valvular calcification. AVC is the main intrinsic cause of valvular obstruction leading to AS, a pathologic condition characterized by a narrowing of the aortic valve opening that restricts blood flow from the heart to the aorta (135, 136). AS is the most common valvular heart disease affecting the aging population in developed nations and currently there are no therapies to treat this disease (19, 20). Once symptomatic and severe AS has developed, the only available therapeutic option is surgical aortic valve replacement or implantation, to which not all patients are suited (137).

AVC is present in about 25-30% of the population over the age of 65, and as many as half of those over 85 (138, 139). Until the early 1900s, AVC was regarded as a simple passive age-related degenerative process resulting in the deposition of mineral deposits in the ECM of the aortic valve leaflets. However, recent studies have shown that, instead, AVC is an active, highly complex process sharing common determinants with intimal arterial calcification, or atherosclerosis (19, 21, 22, 140). Both the latter and AVC result from a sequence of events initiated by inflammation, which stimulates the osteochondrogenic transdifferentiation of myofibroblasts and SMCs (140). They also share common risk factors including male sex, body mass index, smoking, arterial hypertension, and elevated lipid levels (141). Despite these recent findings, we still lack precise molecular insights into the mechanisms governing AVC and the extent to which AVC differs for atherosclerosis is currently unknown.

3.2.1. Pathophysiology and mechanism of AVC

AVC can be divided into two distinct phases: an early initiation phase dominated by valvular lipid deposition, injury, and inflammation, with many similarities with atherosclerosis, and a later propagation phase where pro-calcific and pro-osteogenic factors take over and drive mineral deposition (140) (Figure 3.6).

In normal conditions, aortic valve is composed of three leaflets that are at the same time strong and flexible to withstand the considerable mechanical stress and strain associated with valve opening and closing (142). In AVC, mineral deposition leads to reduced leaflet mobility and progressive valvular obstruction. Aortic valve homeostasis is tightly controlled by valvular interstitial cells (VICs) embedded in ECM, valvular

endothelial cells (VECs) covering the leaflets, and circulant and resident immune cells (3).

The initiation phase is usually triggered by increased mechanical stress and reduced shear stress in the valve causing endothelial activation and damage. The endothelial damage results in lipid infiltration, especially lipoprotein(a) and oxidized low-density lipoprotein (LDL) cholesterol. Progressive endothelial injury and lipid oxidization then initiate an inflammatory response within the valve that is characterized predominantly by infiltration of macrophages, T lymphocytes, and mast cells (143) (Figure 3.6). At this early stage, microcalcifications that co-localize with sites of lipid deposition are observed (143). The formation of these calcifications is likely mediated by cell death and the release of apoptotic bodies and extracellular vesicles (Figure 3.6). Such structures are similar to the matrix vesicles found in bone, and act as nucleating sites for Ca-P deposition (140, 144).

While the initiation phase is mainly mediated by inflammatory responses, the role of inflammation and lipid deposition is less prominent in the propagation phase. Instead, this phase is characterized by fibrotic thickening, followed by extensive calcification of the aortic valve leaflets (Figure 3.6). Bone formation is characterized by the initial deposition of collagen matrix, which provides scaffold for mineral deposits. Similar structural processes seem to occur in the aortic valve with many of the same cell mediators and proteins implicated (145). In fact, in AVC, collagen is deposited in anticipation of the pro-calcific processes that subsequently dominate. This fibrotic process with the valve may be regulated by reduced nitric oxide expression following endothelial injury (146). However, the up-regulation of the renin-angiotensin system and formation of angiotensin II are also believed to play a central role (147) (Figure 3.6).

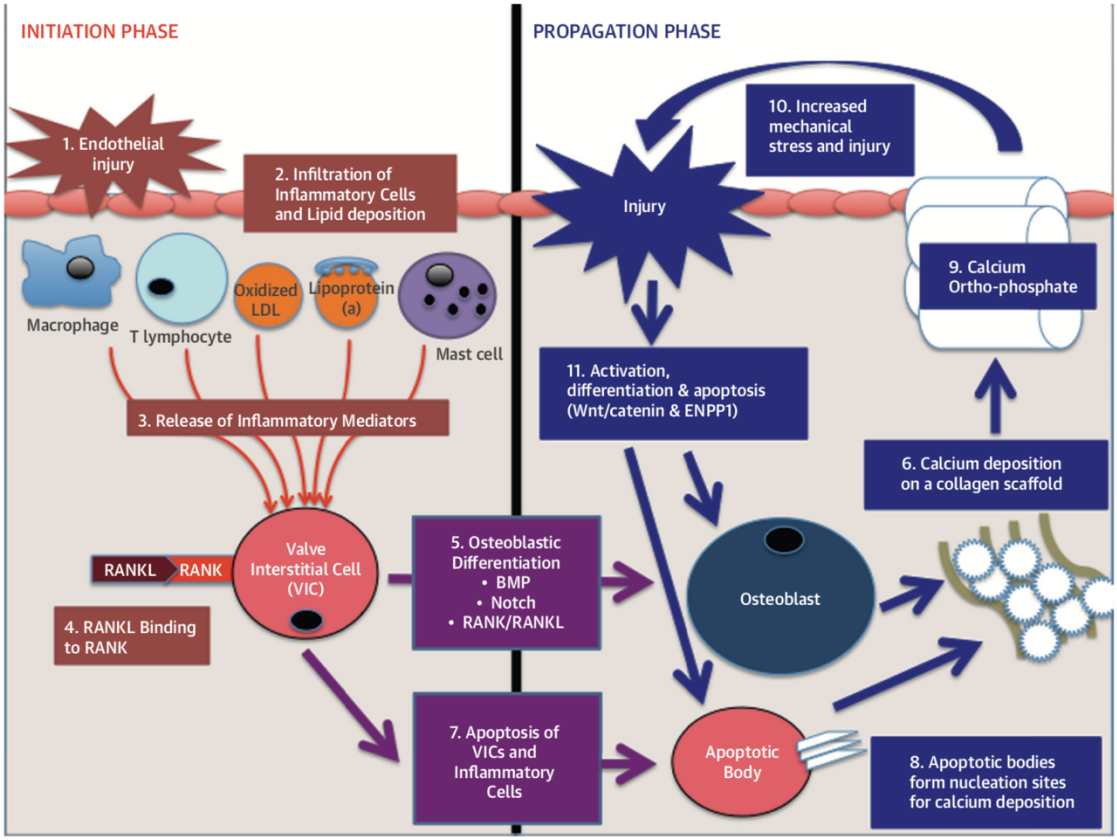

Figure 3.6. The pathophysiology of AVC. initiation phase: endothelial injury (1) facilitates the infiltration of oxidized lipids and inflammatory cells (2) into the valve and the release of proinflammatory mediators (3). These trigger the very early stages of AVC. The propagation phase: these proinflammatory processes subsequently induce VICs to undergo osteogenic differentiation (5) via several different mechanisms, including the binding of RANKL to RANK (4). Differentiated cells within the aortic valve first lay down a collagen matrix and other bone-related proteins causing valvular thickening and stiffening before producing calcium (6). Additionally, apoptotic remnants of some VICs and inflammatory cells (7) create a nidus for apoptosis-mediated calcification (8). Calcification of the valve (9) induces compliance mismatch, resulting in increased mechanical stress and injury (10). This results in further calcification via osteogenic differentiation and apoptosis (11). Hence, a self-perpetuating cycle of calcification, valve injury, apoptosis, and osteogenic activation is established that drives the propagation phase of the disease (147).

Beyond the initial fibrosis, once calcification is abundant, pro-osteogenic mechanisms become overwhelming, thus leading to severe calcification and valvular dysfunction. One mechanism implicated in the pathogenesis of AVC is the transdifferentiation of normally quiescent VICs into osteoblast-like bone-forming cells (148). This phenotypic switch is thought to be the fundamental step in the acceleration of AVC, initiated at least in part by inflammation (147). In the propagation phase, disease progression is driven by calcific regulatory pathways including Notch, receptor activator of nuclear kappa B (RANK)/receptor activator of nuclear factor kappa B ligand (RANKL), and BMPs (147, 148) (Figure 3.6).

Notch belongs to a family of cell surface receptors that are highly expressed in the aortic valve, playing a role in the morphological development. Patients with loss-of-function mutations in Notch-1 have higher rates of AVC and AS (149). Notch-1 was shown to be important in establishing osteogenic cells in the valve via the action of BMP2 (150). Expression of BMP2 is increased in both intimal arterial calcification and AVC, and plays a central role in the osteogenic transdifferentiation (151). *In vitro*, activated endothelial cells have been shown to secrete BMP2 in response to changes in laminar flow patterns, and BMP2 has been detected in VICs isolated from the aortic valve of aged rats (152, 153). BMP2 is up-regulated through binding of RANKL to RANK. Activation of the RANK/RANKL pathway results in the expression of proteins involved in calcification such as ALPL and osteocalcin and is involved in AVC (147).

Once calcification is established in the valve, it can initiate further mineral formation. This self-perpetuating cycle of calcification and valve injury appears to be the central driving force of disease progression (Figure 3.6). The mechanism for this may be

explained by the compliance mismatch caused by mineral deposits in the leaflets that results in increased mechanical stress and further osteoblast transdifferentiation (147). However, it could also be due to the action of membrane-bound ectonucleotidases. These enzymes are produced by VICs and regulate the extracellular production of inorganic P and PPi. Enpp1 is highly up-regulated in AVC. Hydrolysis of ATP by Enpp1 produces a significant increase in P, thus promoting calcification and production of further Enpp1 (154). Also, since ATP acts as a cell survival signal for VICs, its depletion also triggers apoptosis of these cells, thus providing a further key stimulus to calcification (154). Thus, ectonucleotidases may have a central role in amplifying pro-calcific processes in AVC.

3.2.2. The impact of sex in the pathogenesis of AVC

Consistent with many other cardiovascular diseases, male sex is an important risk factor for developing AVC (141, 155, 156). Although several studies have shown higher prevalence of AVC in men, investigations that focus on this issue have concentrated on sex differences in ventricular or vascular dysfunction caused by AVC, rather than the valve itself (157). Also, most of the *in vitro* studies investigating the mechanism of AVC use VICs that are not separated by sex or whose sex is unknown (157).

Only recently a significant step toward uncovering sex-specific differences in AVC was achieved in 2013. In fact, Aggarwal *et al.* provided initial evidence that male sex impacts not only the probability of developing AVC but also the nature of AVC (158). Specifically, they showed that, for the same AS severity, men present significantly higher AVC loads than women, as measured by multidetector computed tomographic (MDCT) imaging of valve patients. This difference in calcification amount remained significant even after adjusting for smaller body surface area and smaller aortic annulus area as typically

observed in women (158). This difference was further confirmed by other studies using both MDCT and echocardiography (23-27).

In 2017, Simard *et al*. confirmed the fundamental difference in AVC burden between men and women. Using a semiquantitative fibrosis score analysis, the also showed that for the same AS severity and same valve weight density, women have relatively more fibrosis than men (23). Since the two major mechanisms involved in AS are calcification and fibrosis of the valve, this may explain why women reach severe AS at a lower level of AVC loads. However, this is the only report showing differences in fibrosis between sexes, and the cause of different AVC loads between men and women is still unknown.

Some studies suggested that hormones may be involved. Estrogen signaling impacts several molecular processes and thus may have effects on osteogenic and fibrogenic signaling cascades (159). Physiological levels of estrogen have been shown to be essential for activation of endothelial nitric oxide signaling and increased nitric oxide bioavailability (160, 161), and suppression of RANKL signaling (162). This suggests that estrogen may be implicated in the production of excessive ECM through the activation of nitric oxide signaling, and in the protection against progression of AVC by suppression of RANKL signaling, a key signaling pathway in progression of AVC. Also, women tend to develop heart diseases and especially AVC later in life compared to men (163, 164); this could be attributable to the loss of estrogen during menopause.

Androgens, such as testosterone also initiate complex effects that could play a role in the initiation and progression of AVC. It was shown that androgens can have a significant positive effect on both osteoclast and osteoblast activity and function (165). Along the

same lines, *in vitro* studies showed that testosterone plays an important role in promoting calcification of VSMCs (27, 166).

In contrast, some studies proposed that intrinsic cell differences between sexes may be responsible of this pathophysiological difference. An *in vitro* study showed that male and female VICs behaved differently in a hormone-free environment: male VICs calcified more extensively than female VICs in hormone-free osteogenic medium (167). Another study showed that VICs derived from animals exhibited sex-specific molecular signatures *in vitro* that are likely to provide altered susceptibility to osteogenic and fibrogenic cell phenotypes *in vivo*. In fact, female VICs were less likely to express molecular signatures related to inflammation, apoptosis, and cellular proliferation compared with men cells (168). These data suggest that the biological explanation behind sexual differences in AVC is likely highly complex and may not rely only on hormonal differences between sexes.

3.3. Mineral deposits found in cardiovascular calcification

3.3.1. Ca-P phases in cardiovascular calcification

3.3.1.1. Apatite phases

The nature of the mineral deposits formed in cardiovascular calcification was found to be complex and non-uniform. For many years, minerals present in cardiovascular tissues have been identified predominantly as carbonated hydroxyapatite (CHA) with variable Ca/P ratios and substitutions (78, 169-175), similar in composition to the mineral component of bones and teeth (176-178).

HA is thermodynamically the most stable Ca-P salt with formula $Ca_{10}(PO_4)_6(OH)_2$. Its crystalline lattice symmetry is hexagonal belonging to space group $P6_3/m$, with 44 atoms per unit cell. Stoichiometric HA has a Ca to P (Ca/P) ratio of 1.67 (15). The structure of HA allows for compositional variations due to the presence of different ions that can be substituted on its three sub lattices. The main substitutions observed in biological apatites is the replacement of the PO_4^{3-} anions by CO_3^{2-} and HPO_4^{2-}. Carbonate ions can substitute either hydroxyls ions (type A carbonated-apatite; $Ca_{10}(PO_4)_6CO_3$) or phosphate ions (type B carbonated-apatite; Ca_{10-x} $[(PO_4)_{6-2x}$ $(CO_3)_{2x}]$ $(OH)_2$) (15). Numerically, one substitution of CO_3^{2-} for PO_4^{3-} results in a half Ca and one P deficiencies, thus giving a Ca/P ratio higher than 1.67 (Table 3.1) (179). Vice versa, one substitution of HPO_4^{2-} for PO_4^{3-} results only in a half Ca deficiency, to give a Ca/P ratio lower than 1.67 (Table 3.1) (179).

Several studies showed that the mineral deposits isolated from different cardiovascular tissues contained a non-negligible fraction of carbonate, which varied depending on the sample (172, 173, 175). Overall, the amount of carbonate was very similar to the carbonate content of bone (4 to 9 wt. % carbonate ions) (180).

Ca/P ratios can be used to characterize mineral deposits found in cardiovascular calcification. Fitzpatrick *et al.* quantified the Ca/P ratios in atherosclerotic arteries using energy dispersive x-ray (EDX) microanalysis and showed that they varied between 1.55 and 1.70, thus suggesting that the apatite phases with various ion substitutions was the main mineral phase present in the samples (78). Later, Cottignoli *et al.* showed chemical variability within a same calcified tissue by electron microprobe analysis (175). In fact, Ca/P ratios were significantly different from point to point within a same sample as well

as in different types of cardiovascular tissues. However, overall all of the Ca/P ratios fell in the CHA range, thus suggesting the chemical variability was likely regulated by the degree of carbonate substitution (175). Another study confirmed that Ca/P ratios varied not only among individual samples but also within the same sample. Indeed, using wet chemistry and EDX, Prieto *et al.* found very scattered Ca/P ratio values (174). Among of the values, they were able to distinguish two different groups of deposits: a group with high Ca/P ratios (average of 1.82) that indicate the presence of CHA, and a group with Ca/P ratio lower than 1.6 that were likely due to the presence of non-apatitic phases, such as amorphous calcium phosphate (ACP) (174). Danilchenko et al. reported much higher Ca/P ratios in a wide range of cardiovascular samples using the same technique (171). Ca/P ratios were all higher than 2.0 both in AVC and intimal calcification. They concluded that such high values were likely due to excess of Ca localized on the surface of apatite crystals.

Overall, these data show that Ca/P values vary significantly according to the method used to quantify the Ca/P ratios, the type of cardiovascular calcification, the degree of calcification, and even the localization within the sample. The amount of ion substitutions in the crystal apatite lattice has been seen as the main parameter that explain a such variability; however, the presence of non-apatitic Ca-P phases could also be responsible of this variability.

Table 3.1. List of Ca-P compounds found in pathological calcifications and their Ca/P molar ratios (179).

Name	Formula	Ca/P ratio
Amorphous calcium phosphate (ACP)	$Ca_3(PO_4)_2.3H_2O$	1.5
Octacalcium phosphate (OCP)	$Ca_8H_2(PO_4)_6.\ 5H_2O$	1.33
Dicalcium phosphate dihydrate (DCPD)	$Ca(HPO_4).2H_2O$	1.0
Magnesium- substituted β-tricalcium phosphate (β-TCMP)	$Ca_{18}(Mg)_2H_2(PO_4)_{14}$	1.29
Hydroxyapatite (HA)	$Ca_{10}(PO_4)_6(OH)_2$	1.67
Carbonated hydroxyapatite (CHA)	$Ca_{10-p}(PO_4)_{6-p}(OH)_{2-p}(CO_3)_p$ (0<p<1)	> 1.67
Calcium-deficient HA	$Ca_{10-x}(HPO_4)_x(PO_4)_{6-x}(OH)_{2-x}$ (0<x<1)	1.3 – 1.67

3.3.1.2. Precursor phases

More recently, several studies have suggested the presence of non-apatitic Ca-P phases, such as ACP, $Ca_3(PO_4)_2.3H_2O$), octacalcium phosphate (OCP, $Ca_8H_2(PO_4)_6.\ 5H_2O$), dicalcium phosphate dihydrate (DCPD, $Ca(HPO_4).2H_2O$), and magnesium-substituted β-tricalcium phosphate (β-TCMP, $Ca_{18}(Mg)_2H_2(PO_4)_{14}$), in addition to CHA (Table 3.1).

While HA is the most thermodynamically stable form of Ca-P at physiological pH, different phases can crystallize, and non-crystalline deposits can form too (181). ACP, OCP, DCPD, and β-TCMP were identified as the main Ca-P phases that can form and be transformed into apatite phases *in vitro*. The formation of each phase depends on a combination of pH, temperature, and solution composition (182). A similar process occurs also *in vivo*, during bone formation.

In vitro, ACP is the first phase that precipitates from a supersaturated solution prepared by mixing solutions containing Ca and P ions (183-185). ACP is a highly unstable phase that hydrolyzes almost instantaneously to more stable Ca-P phases. However, the life time of ACP in aqueous solutions was reported to be a function of the presence of additive ions and macromolecules, pH, ionic strength, and temperature (186, 187). For example, high pH and high Ca and P ion concentrations favor the formation of ACP. Also, magnesium and carbonate ions as well as pyrophosphate can stabilize ACP and prevent its further transformation to apatite phases (182). Thus, ACP may persist for appreciable periods under some specific conditions both *in vitro* and *in vivo*.

ACP was identified as the main precursor phase in newly formed bone and enamel, transforming over time into apatite phases (188-191). It was also recognized as one of the main precursor phases in both arterial and valve calcification. Using electron diffraction (ED) on human aortic valves, Kim *et al*. were the first to show the presence of ACP, in addition to apatite phases, in human non-skeletal tissues (192). Tomazic *et al*. (169) showed that the crystallinity of minerals found in human calcified deposits from different cardiovascular tissues was influenced by the composition of the tissue, the age of the deposit, and the relative exposure to blood flow. Using x-ray diffraction (XRD), they showed that youngest calcified deposits were largely apatitic but contained a non-negligible amorphous fraction, while well-aged deposits did not show the presence of ACP (169). These results, in agreement with ED data obtained by Kim *et. al* (192), indicate that mineral phases evolve over time and supported the presence of an amorphous precursor of apatite in cardiovascular calcification. Later, several other

studies suggested the presence of ACP in various calcified cardiovascular tissues where it was regarded as the main precursor of apatite phases. (174, 182, 193-195)

OCP has a significant biological relevance since it is recognized as a precursor during the formation of CHA in the hard tissues of vertebrates (196-199). It is also regarded as a precursor of HA i*n vitro* (186, 187). *In vitro* studies have shown that when pH > 5.4, the precipitation of HA is thermodynamically favorable, while OCP precipitation is thermodynamically favorable only when pH > 6.3 (200). The thermodynamic force of HA is always larger than that of OCP, although both increase with increasing pH. However, the nucleation rate of OCP is higher than that of HA under physiological conditions (200). Due to their mineralogical correlation, OCP can easily convert into HA, either through dissolution and subsequent reprecipitation into apatite phases, or by a direct solid-state transformation with reorganization of lattice ions and/or apatite clusters (186). It was also proposed that OCP could be an intermediate in the conversion of ACP to apatitic phases (201).

Using XRD, FTIR and SEM/EDS, Mikroulis *et al*. showed the presence of OCP, in addition to DCPD and HA, in mineral deposits from excised calcified natural and bioprosthetic aortic valves (202). XRD patterns and Ca/P ratios determined by chemical analysis showed the presence of both OCP and crystalline apatite among the mineral phases. They found lower Ca/P ratios in bioprosthetic valves compared to natural ones. This difference was ascribed to a higher content of precursor phases, such as OCP and DCPD in these samples, subsequently transformed into apatite phases. While XRD did not suggest the presence of DCPD, SEM/EDS analysis showed the presence of DCPD in addition to OCP and CHA (202).

The presence of OCP in calcified aortic valves was further confirmed by Raman spectroscopy. Pilarczyk *et al*. analyzed mineral phases present in calcified aortic valves by monitoring the shift of the Raman ν_1 phosphate band. They also correlated the chemical composition with the structural properties of the sample (203). Their results suggested that at very early stages of calcification, small deposits mainly composed of OCP (ν_1 phosphate band at 970 cm^{-1}) were formed. In intermediate stages, grain growth was observed with transformation of OCP into β-TCMP (ν_1 phosphate band at 985 cm^{-1}). Finally, in very advanced stages of calcification, CHA was the main compound found (ν_1 phosphate band at 960 cm^{-1}) (203). While these studies suggest that OCP is a precursor phase in valve calcification, the presence of OCP in both intimal and medial arterial calcification was never reported so far.

DCPD has been proposed as an intermediate in both bone mineralization and enamel dissolution (196). DCPD was also reported in some pathological calcifications, such as dental and urinary calculi (182). Studies on DCPD hydrolysis have shown that DCPD can transform into OCP and HA via dissolution and reprecipitation. This indicates that an DCPD can serve as a Ca and P ion reservoir for subsequent crystal growth of apatite phases (196).

As mentioned above, Mikroulis *et al.* suggested the presence of DCPD using SEM/EDS analysis, in addition to OCP and CHA in both natural and bioprosthetic calcified aortic valves (202). The presence of DCPD in AVC was also suggested by Raman spectroscopy, in addition to ACP, OCP, and CHA (174). However, to date, no convincing evidence of the presence of DCPD in AVC was reported. Also, DCPD was never reported so far in either intimal or medial arterial calcification.

Pure β-TCP never occurs in biological calcifications; only the magnesium-substituted form, β-TCMP or whitlockite, is found in dental calculus formation and in renal stones (196). However, it has not been observed in enamel, dentin, or bone, thus suggesting that it is not a precursor phase in physiological calcification (196).

Using synchrotron x-ray-micro-fluorescence and XRD, Verberckmoes *et al.* reported the presence of β-TCMP in addition to ACP and apatite phases in two rat models of uremia-related vascular calcification (193). Similarly, β-TCMP has been detected in addition to apatite phases in human vascular calcification (204). However, β-TCMP was not reported in non-uremic patients. The formation of β-TCMP in uremia-related vascular calcification may potentially be the result of the high concentration of Mg in these patients because of the presence of high levels of Mg ions in the dialysis solution. In rat models of uremia-related vascular calcification, vitamin D treatment was used to induce calcification. Vitamin D stimulates the gastrointestinal absorption of Mg, and can thus explain the formation of β-TCMP in this rat model.

More recently, Danilchenko *et al.* analyze the minerals found in several human cardiovascular deposits. Interestingly, they showed a correlation between mineral phase and localization of the deposit: a significant amount of β-TCMP was detected in human mitral valves, while the same mineral phase was not found in human tricuspid valves and aortas (171). Only one study suggested the presence of β-TCMP in calcified aortic valves using the shift of the Raman ν_1 phosphate band (203).

3.3.2. Morphology of mineral deposits found in cardiovascular calcification

Several studies have used scanning electron microscopy (SEM) to characterize the morphology of minerals deposited in several cardiovascular tissues. They showed that Ca-P phases can have several dense structures. Among them, the most common one is uneven and rough compact material of variable dimensions (171, 174, 175, 202, 205-207). Some studies showed that calcifications in the form of compact material were composed of smooth plate-like structures. These structures appeared as both single and stacked plates.

Some researchers also reported the presence of calcified fibers deposited in networks in addition to compact material (175, 206, 207). In addition to calcified fibers, several studies showed the presence of calcified spherical particles with sizes ranging from 100 nm to 5 μm (174, 175, 206, 207). These spherical particles have been observed in vascular and valvular calcification, independent of disease severity. Both single and coalescent spherical particles have been observed.

Using transmission electron microscopy (TEM) and selected area electron diffraction (SAED), Bertazzo *et al.* showed that the atoms that comprise these spherical particles are arranged in a highly ordered fashion, like a single HA crystal (207). Their SAED patterns are different from any different material found in the body, and they are far more crystalline than the minerals found in bone.

3.4. Clinical treatment of cardiovascular calcification

Despite the evidence that cardiovascular calcification induces cardiovascular mortality in patients suffering from life-threatening diseases, currently it is regarded as an untreatable disease. Once started, the process of mineral deposition in the cardiovascular

tissues becomes almost irreversible. The available therapeutic approaches are mainly focused on delaying disease progression. To date, treatments with PPi derivates, called bisphosphonates, and P binders are the most successful approaches to slow down the progression of cardiovascular calcification.

Bisphosphonates were first developed to prevent osteoclast-mediated bone resorption in osteoporotic patients. They inhibit bone resorption by binding to nascent mineral nuclei where they are ingested by osteoclasts (208-210). The uptake of these pyrophosphate analogs interferes with normal osteoclast functions, and reduces bone resorption. Pyrophosphate and bisphosphonates have been found to inhibit vascular calcification in a several animal studies (211). It has been hypothesized that this effect is due to lowered serum levels of Ca and P, and/or reduced nucleation and growth of Ca-P crystals. However, the efficacy of bisphosphonates for preventing vascular calcification in human is still controversial, and the results differ depending on the bisphosphonate molecule used (212, 213).

Hyperphosphatemia is a major factor contributing in the development of vascular calcification in CKD. Increased serum P in CKD patients may promote osteogenic transdifferentiation of the VSMCs but can also directly promote Ca-P deposition in the vascular walls (214). Several types of P binders are currently in use to control the elevated serum P levels. These compounds are taken orally together with food; they bind to dietary P and form an insoluble complex in the digestive system. This prevents the P from ever being absorbed. There are two main types of P binders: Ca-containing binders, such as Ca acetate, and Ca-free binders, such as lanthanum carbonate and sevelamer carbonate. Although both types are effective at regulating P levels, Ca-containing binders may

promote increased Ca loads in the gastrointestinal track and thus increase the circulatory Ca levels. This hypothesis is supported by several studies in human CKD patients (215). Most patients on dialysis are currently taking some form of P binder, but the data suggests that non-Ca containing P binders should be used in patients with high risk for vascular calcification.

Chapter 4. Multidisciplinary Approach to Understand Medial Arterial Calcification.

As described in **Chapter 3**, there are currently no available treatments to cure medial arterial calcification, mostly due to a lack of understanding of the underlying molecular mechanism. Despite recent evidence on the role of ELN as mineral nucleator in medial calcification, the physicochemical details of mineral nucleation and growth on the medial layer or arterial tissues are still unknown. This hinders our understanding of how minerals interact with ECM and mineralization inhibitors, and of the overall molecular mechanism of vascular calcification.

In this study, we analyze the evolution of medial calcification in an animal model that faithfully recapitulates medial arterial calcification in humans, to understand how pathological calcification is initiated on the vascular ECM. By combining traditional and synchrotron-based spectroscopies, we show that the mineral composition and crystallinity evolve over time and space, starting from the ELN-rich component of the arteries. We find that Ca is adsorbed first, and then ACP and OCP form, which then transform into HA and CHA. These events are repeated after each nucleation event, providing a snapshot of the overall mineral evolution at each time point analyzed. This work suggests the importance of analyzing mineral phases rather than just overall mineralization extent, to diagnose and possibly prevent disease development.

The findings of this study were published in the journal *Arteriosclerosis, Thrombosis, and Vascular Biology*, in 2018.

Ophélie Gourgas, Juliana Marulanda, Peng Zhang, Monzur Murshed, Marta Cerruti. (2018). Multidisciplinary Approach to Understand Medial Arterial Calcification. *Arteriosclerosis, Thrombosis, and Vascular Biology*, 38(2), 363-372.

4.1. Abstract

Objective: Vascular calcification significantly increases morbidity in life-threatening diseases, and no treatments are available because of lack of understanding of the underlying molecular mechanism. Here, we study the physicochemical details of mineral nucleation and growth in an animal model that faithfully recapitulates medial arterial calcification in humans, to understand how pathological calcification is initiated on the vascular extracellular matrix.

Approach and Results: MGP (matrix gla protein) is a potent mineralization inhibitor. We study the evolution of medial calcification in MGP-deficient mice over the course of five weeks using a combination of material science techniques and find that mineral composition and crystallinity evolve over time and space. We show that calcium is adsorbed first, and then amorphous calcium phosphate and octacalcium phosphate form, which then transform into hydroxyapatite and carbonated apatite. These events are repeated after each nucleation event, providing a snapshot of the overall mineral evolution at each time point analyzed.

Conclusions: Our results show that an interdisciplinary approach combining animal models and materials science can provide insights into the mechanism of vascular calcification, and suggest the importance of analyzing mineral phases, rather than just overall mineralization extent, to diagnose and possibly prevent disease development.

4.2. Introduction

Some of the most common pathologies worldwide, such as atherosclerosis, chronic kidney diseases (CKDs), and type 2 diabetes mellitus involve the calcification of vascular tissues (28, 216, 217). Vascular calcification is also associated with aging and genetic disorders (1). Vascular calcification can happen both in the intimal layer of arteries, along with atherosclerotic plaques, or in the medial layer, which is more common in CKD and diabetic patients (61, 216, 218).

When arteries calcify, calcium phosphate (Ca-P) minerals are deposited on the extracellular matrix (ECM) of their walls. This process may arise from several different and non- mutually exclusive mechanisms, such as loss of inhibitors, osteochondrogenic transdifferentiation of vascular smooth muscle cells (VSMCs), hyperphosphatemia, hypercalcemia, and cell death (31, 61). Matrix gla protein (MGP) is one of the most potent mineralization inhibitors that are normally present in the vascular tissues. Luo *et al*. (67) showed that genetically modified mice that do not express MGP develop extensive and progressive medial arterial calcification. Later, Khavandgar *et al.* (10) demonstrated the important role of elastin (ELN) as the main ECM protein regulating mineral deposition in the arteries of these mice and showed that ELN-rich thoracic aorta calcified more extensively than the abdominal aorta, which contains less ELN.

Despite this progress, the physicochemical details of mineral nucleation and growth inside blood vessels are still unknown; this hinders our understanding of how minerals interact with ECM and mineralization inhibitors and of the overall molecular mechanism of vascular calcification.

Several studies have characterized minerals formed in cardiovascular tissues and found that the major inorganic phase is poorly crystalline nonstoichiometric carbonated hydroxyapatite (CHA) with variable Ca/P ratios and substitutions (171, 172, 175, 182, 219), similar in composition and structure to the mineral component of bone (188, 220). More recently, other mineral phases were found at early stages of calcification, such as amorphous calcium phosphate (ACP), magnesium-substituted β-tricalcium phosphate (β-TCMP), octacalcium phosphate (OCP), and dicalcium phosphate dehydrate (DCPD) (169, 174, 193, 194, 202-204). The detection of such phases suggests that the vascular calcification shares common features with bone mineralization; however, a recent study reported the presence of highly crystalline, spherical hydroxyapatite (HA) particles in mineralized cardiovascular tissues and, thus, suggested that vascular calcification and bone mineralization follow completely different mechanisms (207).

To shed some light on this debate, in this study, we use MGP-deficient ($Mgp^{-/-}$) mice as an animal model of acute medial calcification. MGP deficiency in humans causes Keutel syndrome, a rare genetic disease characterized by extensive tissue calcification, pulmonary artery stenosis, brachytelephalangism, and facial dysmorphism (221). This phenotype is faith- fully recapitulated in $Mgp^{-/-}$ mice. Also, in this model, the medial layer of the arteries quickly mineralizes, to the point that the animals die before 2 months of age because of complications caused by extensive mineral deposition (67).

Thus, $Mgp^{-/-}$ mice provides us with a unique *in vivo* model to study the temporal evolution of medial calcification. We analyze mineral phases and crystallinity by combining traditional spectroscopic and microscopic techniques such as Fourier transform infrared (FTIR) spectroscopy, Raman spectroscopy, x-ray diffraction

spectroscopy, energy-dispersive x-ray spectroscopy (EDS), and scanning electron microscopy (SEM), with x-ray photoelectron spectroscopy (XPS) and synchrotron-based spectroscopy. This interdisciplinary approach combining genetically modified mouse models and materials science provides needed insights into the mechanism of ectopic calcification.

4.3. Results

Mgp$^{-/-}$ mice show progressive ectopic deposition of Ca-P minerals along the elastic laminae, reaching highly extensive mineralization after 5 weeks of age (Figure 4.1.A) (10). After 5 weeks, at some sites, minerals are also deposited on the surrounding ECM (54). At a very early stage (5 days), Ca adsorption is sparse in the aorta, and we detect only a punctate pattern primarily in the upper part of the thoracic aorta (Figure 4S.1).

Arterial mineral composition in *Mgp*$^{-/-}$ mice might be influenced by systemic Ca and P levels or abnormal glucose metabolism. However, we did not observe any change in serum Ca and phosphate levels in 5-week-old *Mgp*$^{-/-}$ mice in comparison to wild-type mice (Figure 4.1.B). Also, fasting glucose levels in 1- and 3-week-old *Mgp*$^{-/-}$ mice did not differ from age- and sex-matched control mice (Figure 4.1.C).

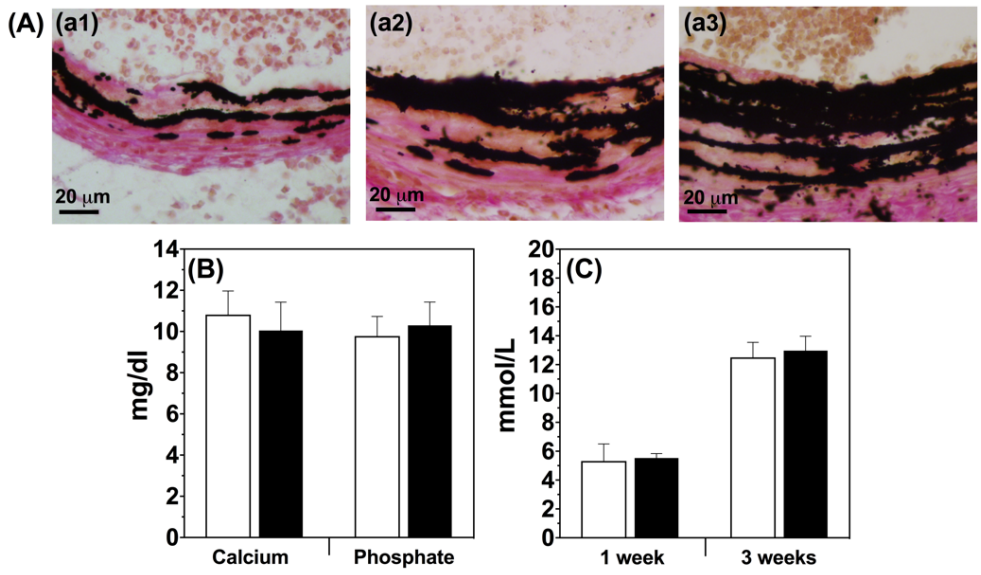

Figure 4.1. (**A**) Histological sections stained with von Kossa and van Gieson (stains phosphate) showing ectopic deposition of Ca-P minerals along the elastic lamina in the aortas from (**a1**) 1-week, (**a2**) 3-week, and (**a3**) 5-week-old *Mgp*$^{-/-}$mice. (**B**) Serum calcium and phosphate levels measured in 5-week old WT and *Mgp*$^{-/-}$ littermates show no difference between genotypes. (**C**) Glucose measurement in blood of 1-, and 3-week old WT and *Mgp*$^{-/-}$ littermates. At 1 week the pups were fasted for 2 hours and at 3 weeks the mice were fasted for 4 hours. There was no difference in the glucose level between the mutant and control mice at 1 and 3 weeks. The Student's *t* test was used for statistical analyses of 2-group comparisons.

An initial screening of the type of Ca compounds present in the mouse arteries, their crystallinity, and their amounts can be obtained by FTIR and Raman spectroscopies (Figure 4.2). FTIR spectra of aorta samples from *Mgp*$^{-/-}$ mice show peaks related to Ca-P phases starting from week 2, which become clearly indicative of HA at week 5 (Figure 4.2.A; see the degenerate v_3 vibration at 1031 and 1091 cm^{-1}, and the degenerate v_4 band at 564 and 602 cm^{-1}; Figure 4S.2.A; Table 4S.1). We estimate HA crystallinity by analyzing the relative intensities of the peaks and valleys in the v_4 envelope (Section 1 in the Supplement Material; Figure 4S.2.B) and find that the crystallinity of the deposits in 5-week-old mice is comparable to that of bone (Figure 4S.2.A).

Raman spectra confirm the presence of HA in *Mgp*$^{-/-}$ mice (Figure 4.2.B; Figure 4S.3.A; Table 4S.2): the intensity of the v_1 phosphate peak increases with the mice age, and the v_2 and v_4 bands of HA become clearly visible after 3 weeks, similar to what observed via FTIR (Figure 4.2.A).

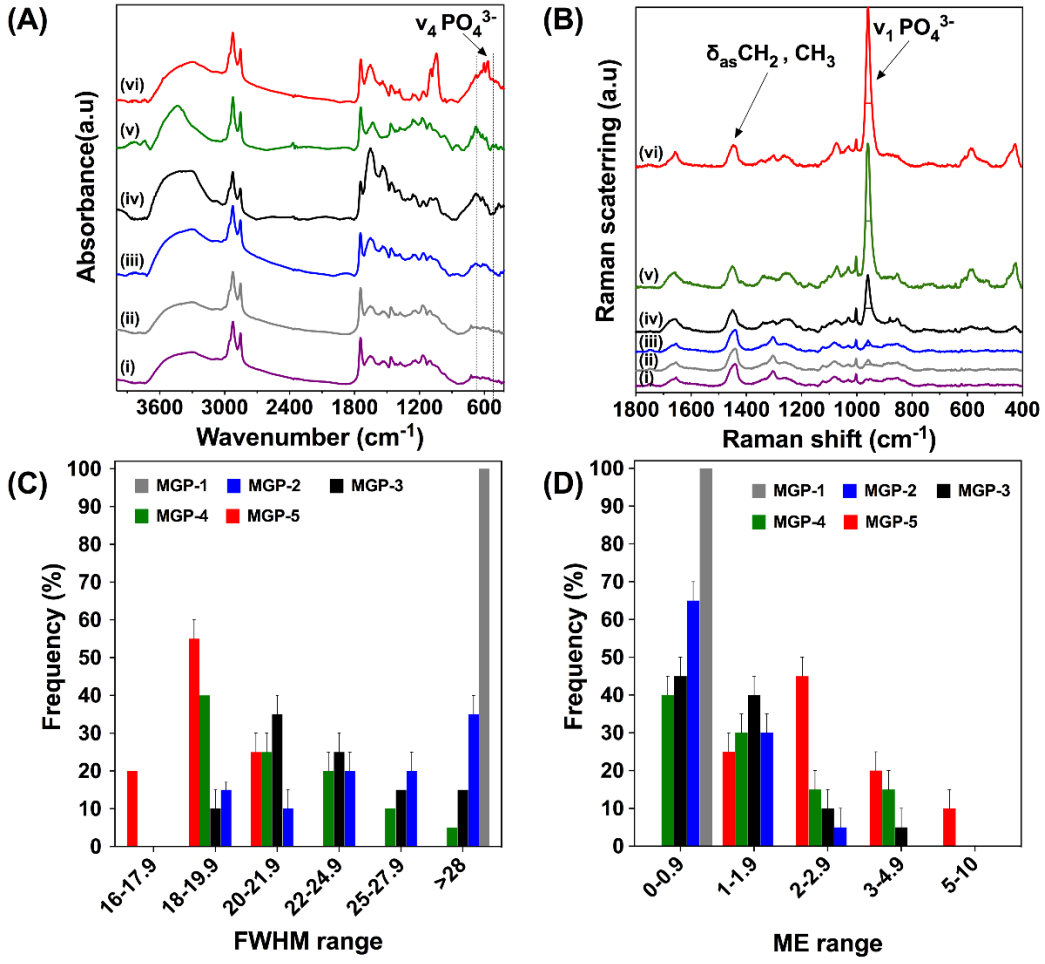

Figure 4.2. Representative FTIR (**A**) and Raman (**B**) spectra of aortas from (i) 5-week old WT mouse, (ii) 1-week, (iii) 2-week, (iv) 3-week, (v) 4-week, and (vi) 5-week-old *Mgp*$^{-/-}$ mice. FTIR spectra (**A**) were normalized based on the absorbance of the v C=O amide I band at 1654 cm^{-1}, while Raman spectra (**B**) based on the absorbance of the δ_{as} CH_2,CH_3 band at 1443 cm^{-1}. Distribution of FWHM values (**C**) measured on the Raman v_1 phosphate peak and of ME (**D**) based on Raman spectra collected on thoracic aortas from 1-week (grey), 2-week (blue), 3-week (black), 4-week (green), and 5-week-old (red) *Mgp*$^{-/-}$mice. For each age, 3 mice were analyzed, and 20 spectra were collected at different points for each sample.

Because the full width at half maximum (FWHM) of the v_1 phosphate peak inversely correlates with HA crystallinity (222) (Section 1 in the Supplement Material; Figure 4S.3.B), we can get a picture of the micron-scale distribution of mineral crystallinity as the mouse age increases (Figure 4.2.C for the thoracic segment; Figure 4S.4.A for the abdominal segment). FWHM values are highly heterogeneous in both segments. The median FWHM values decrease in both the thoracic and the abdominal segments as the mice age and reach values that are somewhat higher than those found for HA in mature bone (19.3±0.3 for the minerals found after 5 weeks in the thoracic segment versus 18±0.2 for bone).

By comparing the area underlying the v_1 phosphate peak between 945 and 962 cm^{-1} with that of the δ_{as} CH_2,CH_3 peak (223), we can also analyze the changes in inorganic-to-organic ratio, or mineralization extent (ME), as the mouse age increases (Figure 4S.3.C). Similar to FWHM values, the MEs found on aortas from 2- to 5-week-old mice are greatly scattered, suggesting that the mineral distribution on these tissues is highly uneven (Figure 4.2.D for the thoracic segment; Figure 4S.4.B for the abdominal segment). At each age analyzed, the median ME in the thoracic segment is significantly higher than that in the abdominal segment from the same mouse (P<0.05), thus confirming that for the same aorta the thoracic part is more calcified than the abdominal one, as expected based on the relative ELN content (10). Overall, the ME increases as the age of the mice increases in both thoracic and abdominal aortas.

The overall increase in mineral crystallinity over time is further confirmed by x-ray diffraction (Figure 4S.5; Table 4S.3): the FWHM of the peak corresponding to the HA planes (211), (121), and (300) decreases as the mouse age increases, reaching values similar to those found in mature bone.

XPS and Ca K-edge near-edge x-ray absorption fine structure (NEXAFS) spectroscopy (Figure 4.3) provide more details on the chemical composition and Ca-P phases present in the samples. Although only carbon (C), oxygen (O), and nitrogen (N) are present on the XPS survey spectra of wild- type mice aortas (Figure 4.3.A(i)), the spectra of *Mgp*$^{-/-}$ mice aortas show also Ca and P (Figure 4.3.A(ii, iii, iv)), confirming the presence of Ca-P phases in these samples. The Ca and P peaks are visible already after 1 week and increase in intensity in older mice, thus indicating that the mineral amounts increase with time. Indeed, Ca/N ratios are significantly higher in 5-week-old samples than in 3-week-old samples (Table 4S.4). The lack of significant differences between 1- and 3- and 3 and 5-week- old samples contrasts with the increasing ME found by Raman spectra. This may be because of the fact that XPS was performed on aorta sections, whereas with Raman spectra, we analyzed whole aortas—thus, Raman spectra results may be more representative.

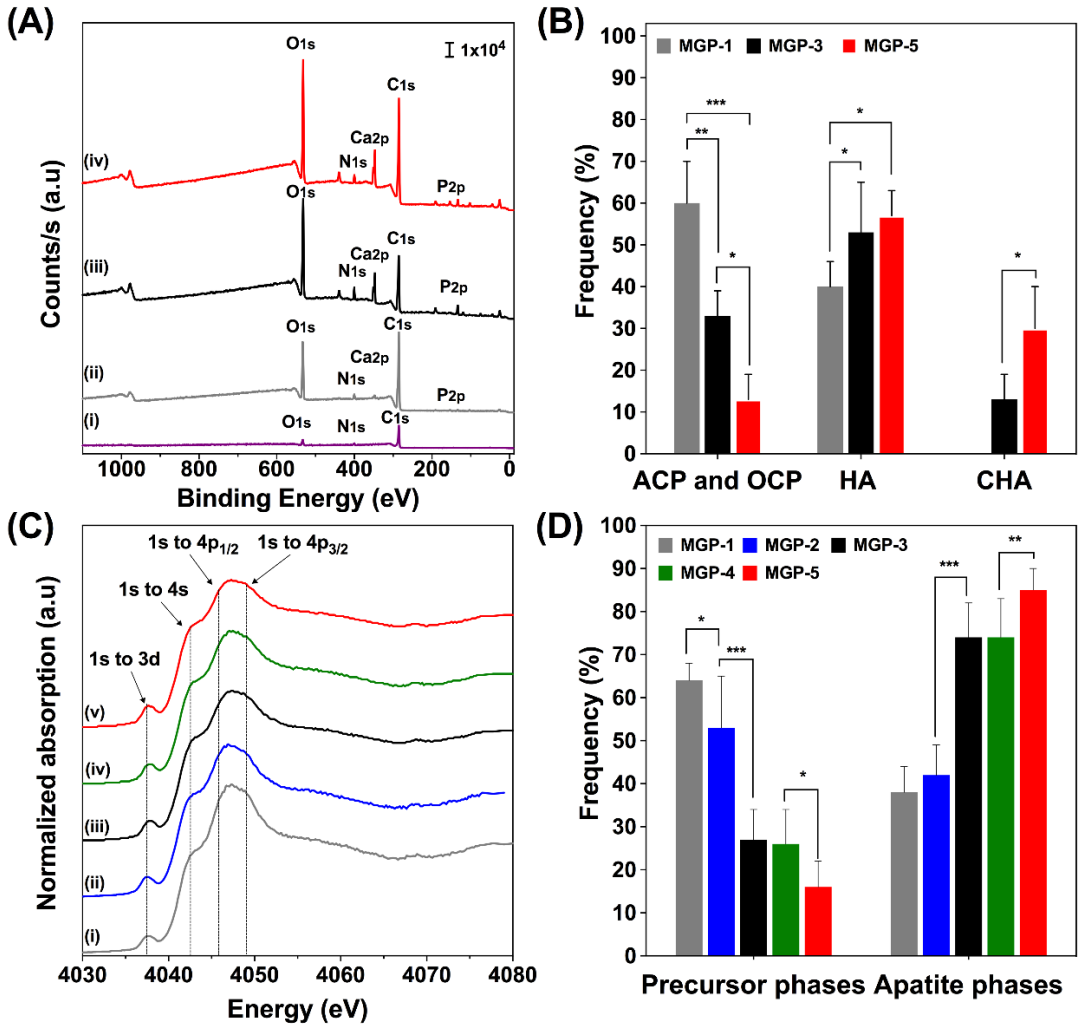

Figure 4.3. (**A**) Representative XPS survey spectra of aorta sections from (i) 5-week-old WT mice, and (ii) 1-week, (iii) 3-week and (iv) 5-week-old *Mgp*$^{-/-}$ mice. (**B**) Mineral phase distribution based on the Ca/P ratios determined by XPS on aorta sections from 1-week (grey), 3-week (black), and 5-week-old (red) *Mgp*$^{-/-}$ mice. ACP and OCP correspond to Ca/P ratios between 1.3 and 1.5, HA corresponds to Ca/P ratios between 1.6 and 1.8, and CHA corresponds to Ca/P > 1.8. For each age, 3 mice were analyzed. For each mouse, 10 Ca/P ratios were determined at different points. One-way ANOVA test was used for statistical analysis followed by Tukey's test correction for multiple comparisons. * indicate significant differences between the different ages, with * = P< 0.05, ** = P< 0.02, and *** = P< 0.0001. (**C**) Representative Ca K-edge NEXAFS spectra of calcified aortas from (i) 1-week, (ii) 2-week, (iii) 3-week, (iv) 4-week, and(v) 5-week-old *Mgp*$^{-/-}$ mice. (**D**) Relative amounts of precursor phases (ACP and OCP) and apatite phases (CHA and HA) in calcified aortas determined by LCF based on the reference sample spectra. 5 mice were analyzed for each age. The data are averages of 5 values ± the standard deviation. One-way ANOVA test was used for statistical analysis followed by Tukey's test correction for multiple comparisons. * indicate significant differences between the different ages, with * = P< 0.05, ** = P< 0.005, and *** = P< 0.0001.

Ca/P ratios vary greatly among point measurements within samples from the same age and even within the same sample, showing large differences in the composition of the minerals deposited (Table 4S.4). Overall, there is a significant increase in the average Ca/P ratios over time, with values going from 1.5 ± 0.2 after 1 week to 1.8 ± 0.3 after 5 weeks (P<0.05). This increase can be correlated to a change in Ca-P phases (174) (Figure 4.3.B; Table 4S.5). One-week-old aortas contain a larger amount of ACP and OCP than HA, but after 3 weeks, the amounts of ACP and OCP significantly decrease, the amount of HA significantly increases, and CHA appears. After 5 weeks, ACP and OCP further decrease, whereas HA remains constant, and CHA significantly increases (Figure 4.3.B).

A more precise identification of both crystalline Ca-P phases and precursors can be achieved with NEXAFS. NEXAFS is a local sensitive and chemically selective probe that is applicable to materials that are crystalline, poorly crystalline, or amorphous (224). All the reference and arterial sample spectra show 4 features that are typical of Ca-P compounds (Figure 4S.6; Figure 4.3.C, respectively). The small feature at the pre-edge (4039 eV) is because of electronic transitions from 1s to 3d orbitals (225, 226). The most intense absorption, that is, the absorption edge, shows a shoulder peak at 4044 eV, which is assigned to 1s to 4s transitions, and a double peak assigned to 1s to $4p_{1/2}$ and 1s to $4p_{3/2}$ transitions (225, 226). The relative intensities of the peaks assigned to 1s to $4p_{1/2}$ and 1s to $4p_{3/2}$ transitions depend on the atoms surrounding calcium atoms in the compounds (225, 226). Features at higher energies are related to transitions from 1s to higher unoccupied states, or multiple scattering contributions (225, 226).

To identify the Ca-P phases present in the samples, we perform linear combination fitting after the procedure explained in Section 1 in the Supplement Material.

Table 4S.6 shows the linear combination fitting results and the R-factors of each fit. All the R-factors are <0.02, thus indicating that all the fits are satisfactory (227).The results confirm that the calcified aortas are composed of a mixture of HA, CHA, ACP, and OCP. DCPD was not detected in any samples. Although HA and ACP are found as components of the spectra collected on all mice, OCP seems to be present only in the young mice (1 and 2-week-old), whereas CHA only in old mice.

To simplify the analysis of mineral evolution over time, we compare the amounts of precursor, nonapatitic Ca-P phases (ie, ACP and OCP), with the amounts of apatitic phases (ie, HA and CHA) at different time points (Figure 4.3.D). Larger amounts of precursor phases than apatite are found in 1-week-old mice. After 2 and 3 weeks, the amount of precursors significantly decreases, whereas apatitic phases increase. From 3 to 4 weeks, the composition of the calcified aortas does not significantly change. Finally, in 5-week-old samples, the Ca detected is mainly present in apatitic structures, and only a small amount of ACP can be detected. These results confirm XPS results, showing that although the amount of apatitic phases increases with the age of the mouse, the amounts of precursors decrease. Also, both techniques suggest that the conversion of precursor phases into apatite phases is rather fast in *Mgp*$^{-/-}$ mice model because a large amount of apatite (33 ± 6% by XPS and 38 ± 6% by NEXAFS) is already present in 1-week-old samples.

Next, we combine micro-x-ray fluorescence and μ-NEXAFS (Figure 4.4) to analyze the spatial distribution of the mineral phases in the thoracic sections of the aortas. Micro-x-ray fluorescence Ca maps (Figure 4.4.A through Figure 4.4.C) show an uneven mineral distribution. Ca/P ratios calculated based on micro-x-ray fluorescence spectral intensity lie between 1.3 and 1.8 for most of the spots analyzed on 1- and 3-week-old samples (see values reported on Figure 4.4.A and Figure 4.4.B) and between 1.6 and 2.3 for most spots analyzed on 5-week-old samples (Figure 4.4.C). Lower values can be seen on the less mineralized areas (values shown in yellow). These results show a conversion from precursor phases to hydroxy- apatite and CHA over the course of the 5 weeks of mice life, consistent with XPS.

The areas closer to the abdominal sections (to the left in Figure 4.4.A through Figure 4.4.C) show an overall lower Ca content, which was expected because of the lower ELN content of the abdominal section (10). On these areas, the Ca/P ratios measured were > 4 (values shown in red); this suggests that here Ca ions are only adsorbed on the samples and have yet to be transformed into Ca-P compounds.

μ-NEXAFS Ca K-edge spectra collected on the spots containing the larger amounts of Ca show the presence of OCP, ACP, and HA on the 1-week-old sample, and ACP and HA on the 3- and 5-week-old samples. This observation is consistent with bulk NEXAFS results, which showed the presence of OCP mostly on 1-week-old aortas (Table 4S.6).

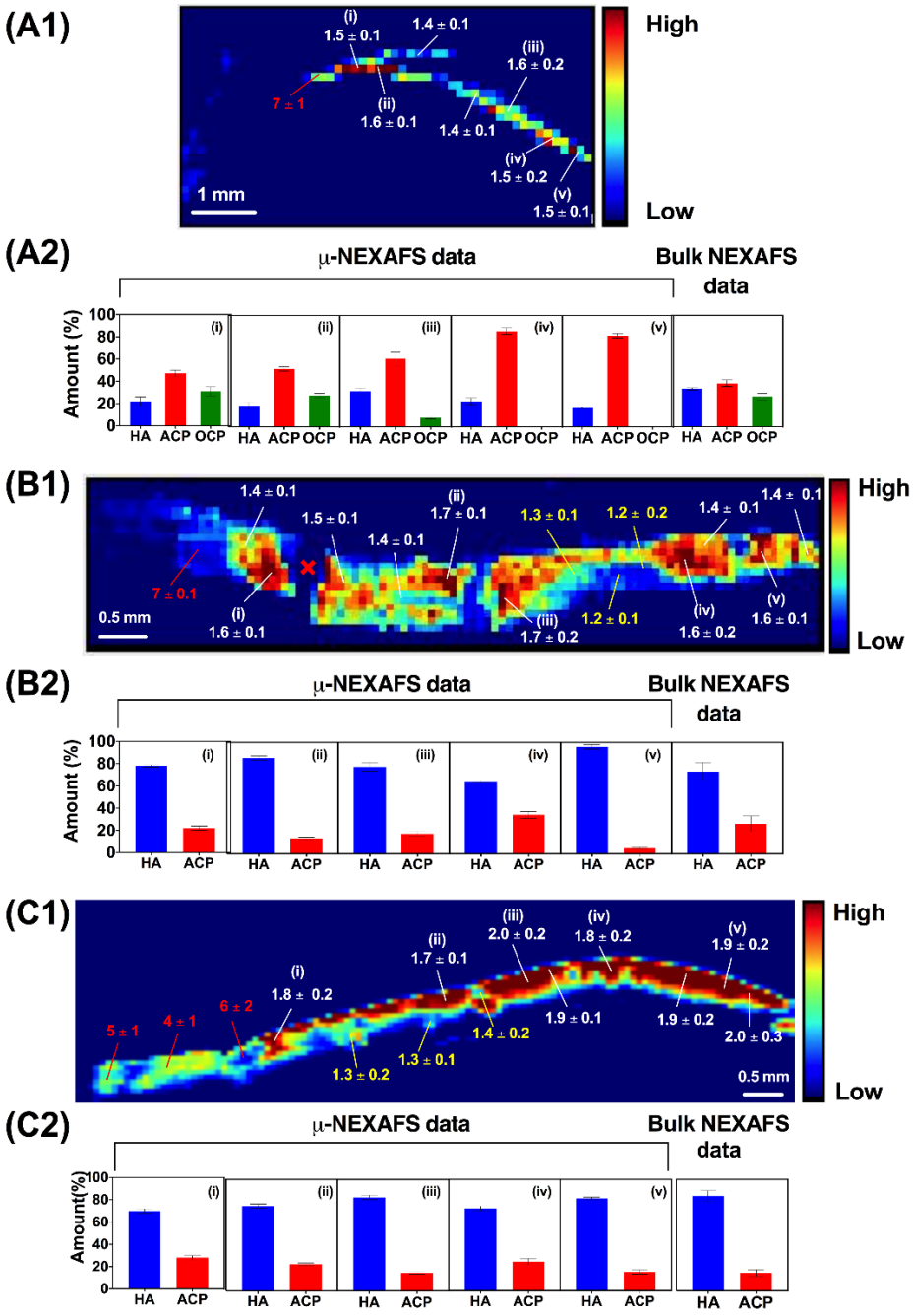

Figure 4.4. (**A1, B1 and C1**): μ-XRF Ca maps of calcified aortas from (**A1**) 1-week, (**B1**) 3-week, and (**C1**) 5-week-old *Mgp*$^{-/-}$ mice. The values indicated in **A1**, **B1** and **C1** are Ca/P ratios based on averaged μ-XRF spectral intensities of 4 pixels. The red cross shown in (**B1**) indicates that the aorta was broken at that location. Ca K-edge μ-NEXAFS spectra were collected on the spots that contained the highest amounts of Ca (20 pixels per spot), labeled as (i)-(v) in **A1**, **B1** and **C1**. (**A2, B2 and C2**): LCF results obtained from the analysis of the Ca K-edge μ-NEXAFS spectra collected at the corresponding locations indicated on the μ-XRF maps, reported along with the LCF results from bulk Ca K-edge spectra on the same samples.

The locations showing OCP on the 1-week old sample (points (i) through (iii) in Figure 4.4.A and Figure 4.4.D) are close to the abdominal section of the aortas. This observation suggests that the spatial distribution of mineral phases observed on the aortas at a specific time point follows the overall distribution observed with time: the least mineralized points are at earlier transformation stages, whereas the most mineralized points are at later stages. This is further confirmed on 3- and 5-week- old aortas. On the 3-week-old sample, most points analyzed by μ-NEXAFS show higher HA to ACP ratios than the bulk NEXAFS data, because the μ-NEXAFS spectra were collected on the spots showing the highest Ca concentration (Figure 4.4.E). On the 5-week-old sample, the differences between μ-NEXAFS and bulk NEXAFS spectra are less evident, because the aorta is overall heavily mineralized; still, even on this sample, the spots that show lower HA to ACP ratios (eg, points (i), (ii), and (iv) in Figure 4.4.F) are close to the least mineralized areas.

Finally, we combined SEM and EDS to examine the structure of the minerals and their interaction with the ECM. SEM images of calcified aortas from 1-, 3-, and 5-week-old *Mgp*$^{-/-}$ mice (Figure 4.5; Figure 4S.7) reveal 2 distinct mineral structures: compact material composed of smooth platelets and fibers deposited in networks. These 2 structures were previously reported in cardiovascular calcifications (171, 174, 175, 205-207, 219). Elemental analysis by EDS (Figure 4S.7) shows the presence of C, O, N, Ca, and P in the samples, confirming XPS data. However, EDS also shows small amounts of magnesium (Mg) in some spots (Figure 4S.7), not detected by XPS. Mg is frequently reported in calcified tissues in both organic and inorganic compounds (206).

Ca/P ratios determined by EDS (Figure 4.5; Figure 4S.8; Table 4S.7 through Table 4S.9) agree with those calculated by XPS and thus confirm the nature of the minerals. However, on aortas from 3- and 5-week-old mice, some spots show much higher Ca/P ratios, suggesting that Ca ions are adsorbed on the organic matrix (Figure 4.5.D, spots 1, 6, and 7 on Figure 4S.8.B and spots 2 and 4 on Figure 4S.8.C).

To further understand the relationship between the minerals and the ECM, we collected EDS maps of elemental distribution (Figure 4.6). In 1-week-old samples (Figure 4.6.C through Figure 4.6.G), Ca and P colocalize and are present only along the elastic laminae, in agreement with von Kossa staining (Figure 4.6.B). This is confirmed by the SEM/EDS spot analysis (Figure 4S.8.A; Table 4S.7) and further proves that mineral deposition first occurs on the elastic laminae.

After 5 weeks (Figure 4.6.J through Figure 4.6.N), EDS maps show Ca both along and between the elastic laminae, whereas P is mainly present along them, again in agreement with von Kossa staining (Figure 4.6.1). This suggests that at some point Ca started being adsorbed between the elastic laminae, whereas P did not.

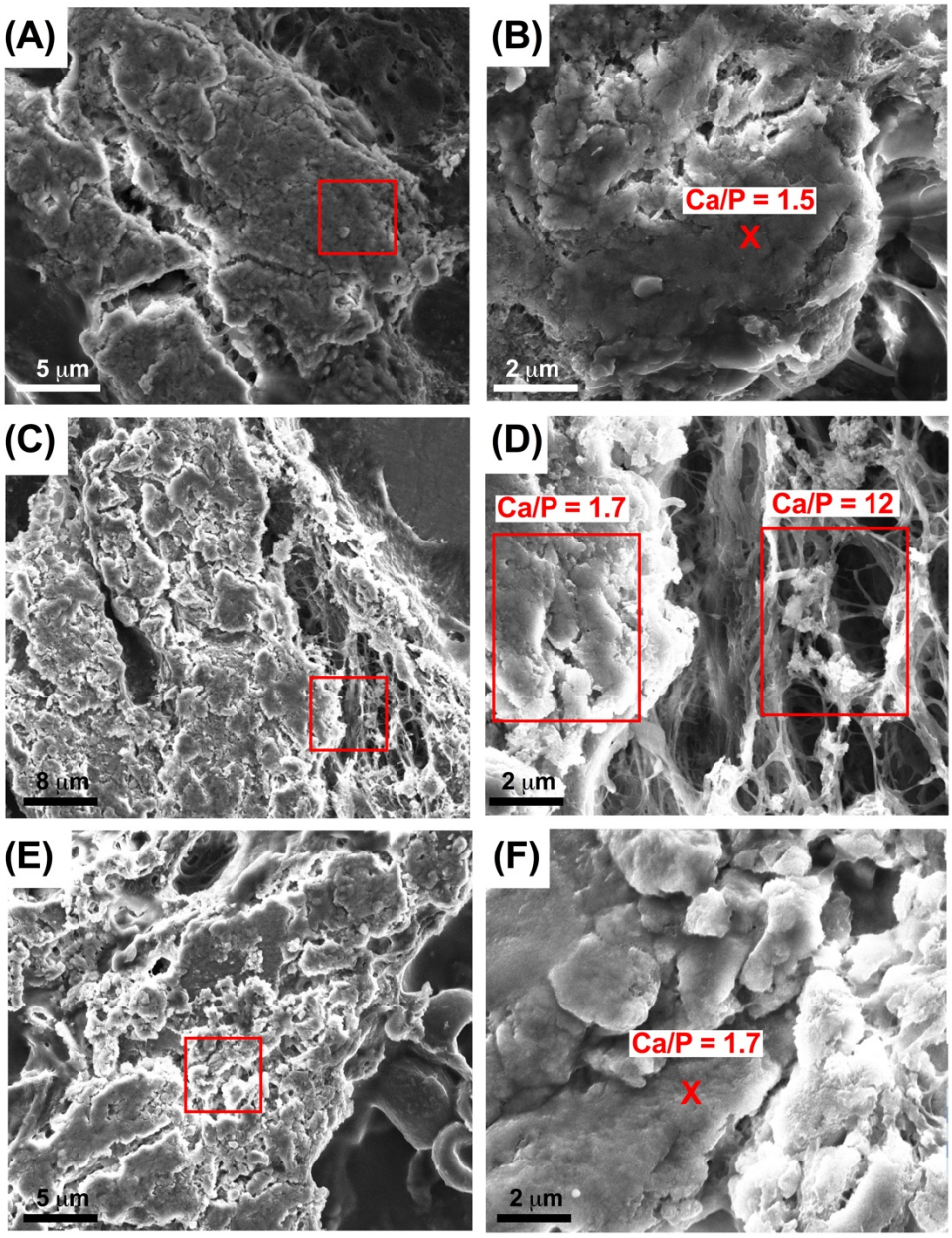

Figure 4.5. SEM images of aortas from (**A and B**) 1-week, (**C and D**) 3-week, and (**E and F**) 5-week-old *Mgp*$^{-/-}$ mice. **B**, **D**, and **F** are the magnified images of the regions highlighted by squares in **A**, **C**, and **E**, respectively. The Ca/P ratios indicated on **B**, **D**, and **F** are based on the elemental atomic percentages obtained by EDS.

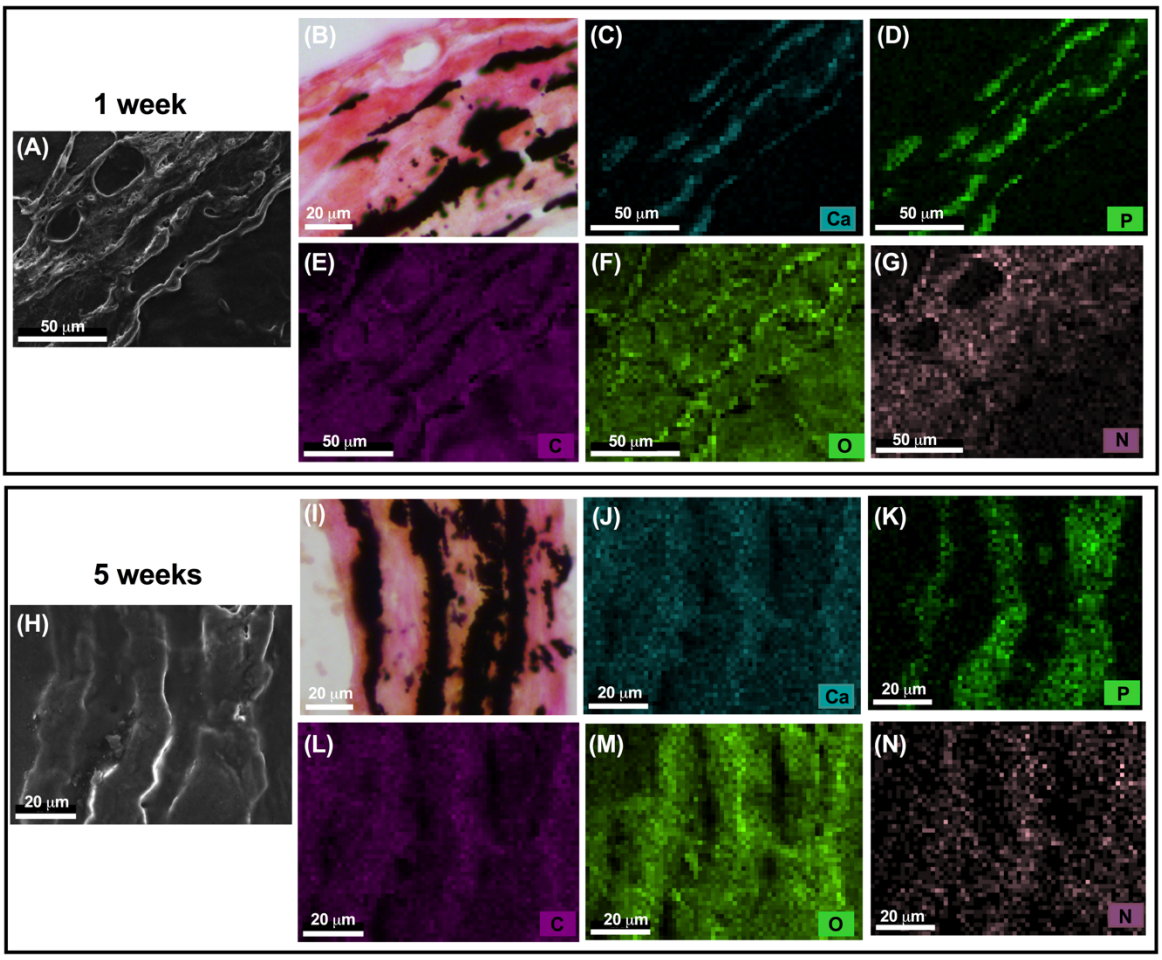

Figure 4.6. SEM images (**A** and **H**), histological sections stained with von Kossa and van Gieson (**B and I**) and EDS elemental mapping for Ca (**C** and **J**), P (**D** and **K**), C (**E** and **L**), O (**F** and **M**) and N (**G** and **N**) of calcified aortas from (**A-G**) 1-week and (**H-N**) 5-week-old *Mgp*$^{-/-}$ mice.

4.4. Discussion

Medial calcification is commonly seen in patients with CKD, diabetes mellitus, and some genetic diseases. Because of its rapid and fully penetrant elastic lamina calcification phenotype, *Mgp*$^{-/-}$ mice have become an attractive model to study medial calcification. VSMCs, the major cell type present in the arterial media, originate from both neural crest and mesoderm (228). Regardless of their origin, these cells coordinate the formation of the concentric elastic laminae that are the primary sites of mineral deposition in *Mgp*$^{-/-}$ mice. Genetic studies have established that arterial elastic content is a critical determinant of vascular calcification (10).

Although earlier studies analyzed the composition of medial calcifications (193, 204, 207), not much is known on how minerals nucleate, grow, and change in phase and crystallinity; this knowledge could be important in understanding disease development and potentially suggest ways to treat it. In this study, we strive to get to this understanding by analyzing mineral evolution in medial calcifications of *Mgp*$^{-/-}$ mice over the course of 5 weeks, using a variety of spectroscopic and microscopic techniques.

Raman spectroscopy shows that the amount of minerals significantly increases over time and that mineral deposition occurs predominantly on the elastic lamina, an ECM rich in ELN, which is more abundant in the thoracic than in the abdominal segment of aortas (10). Raman, FTIR, and x-ray diffraction spectroscopies show that although the mineral crystallinity is heterogeneous, overall it increases over time. These results confirm previous findings of lower crystallinity in ectopic deposits compared with physiological hard tissues (229) and show that Raman spectra is more reliable than FTIR and x-ray diffraction at evaluating small differences in HA crystallinity. The 3 techniques show that

Mgp$^{-/-}$ mice are a model for rapidly progressing medial arterial calcification because in few weeks vascular mineral deposits are almost as crystalline as minerals present in mature bone (230).

Both XPS and NEXAFS allowed us to identify mineral phase transformations. Although NEXAFS provided many more details, XPS was crucial in this study because it was the first time that NEXAFS was applied to the analysis of mineral phase transformations in arterial calcifications, and, thus, a more direct analysis was necessary to validate the results of linear combination fitting deconvolution of NEXAFS spectra.

The mineral phase identification enabled by XPS and NEXAFS confirms previous findings, while providing new insights. HA and CHA are the most abundant Ca-P phases of both physiological (220, 231) and pathological calcifications (171, 172, 175, 182). In vitro studies have shown that although HA is the most thermodynamically stable form of Ca-P at physiological pH, different phases can crystallize, and non-crystalline deposits can form too (181). ACP, OCP, DCPD, and β-TCMP were identified as the main Ca-P phases that can be formed and transformed into HA *in vitro*. The formation of each phase depends on a combination of pH, temperature, and solution composition (182). A similar process occurs also *in vivo*, during bone and enamel formation (190, 191).

In our samples, we did not detect either DCPD or β-TCMP. DCPD is considered a precursor of biological apatite in physiological and in some pathological calcifications, specifically dental and urinary calculi (182). Recently, few studies have identified DCPD in human valve calcified deposits (202, 203), but it was never found in arterial calcification. This may be because of different molecular mechanisms involved in arterial and valve calcifications, thus leading to the formation of different precursors of biological apatites

(182, 217). Our study confirms this point. β-TCMP has been reported to be a component of the mineral phase of several soft tissue calcifications, such as dental calculi and salivary stones (182). In arterial calcification, β-TCMP was detected in addition to HA in both human and rat uremic mineral deposits but not in nonuremic patients (193, 204). The formation of β-TCMP in uremia-related vascular calcification may potentially be the result of the high concentration of Mg in these patients because of the presence of high levels of Mg ions in the dialysis solution (182). In rat models of uremia-related vascular calcification, vitamin D treatment used to induce the calcification stimulates the gastrointestinal absorption of Mg (193). Because *Mgp*$^{-/-}$ mice did not receive any treatment that may increase the Mg concentration in their serum, it is not surprising that we did not find β-TCMP in this study.

The finding of ACP in *Mgp*$^{-/-}$ mice aortas is in line with previous findings showing ACP as the main precursor phase in newly formed bone and enamel, before apatitic phases (188-191); it was also found in both arterial and valve calcification, where it was regarded as a precursor of more crystalline phases (190, 191, 232).

The finding of OCP in arterial calcifications is new. Although previous studies have shown that OCP can be a precursor of biological apatite in normal calcified tissues (198) and in valve calcification (202, 203), this study reports the presence of OCP in arterial calcification. The high sensitivity of the synchrotron-based techniques we used might explain why we were able to identify OCP in this study. However, the presence of OCP might also be MGP related, and, thus, its formation might be indicative of another molecular mechanism involved. Analyzing the Ca-P phases present in calcified soft

tissues from patients with Keutel syndrome may help understand which explanation is the most likely.

Micro-x-ray fluorescence and μ-NEXAFS results suggest that the growth and phase transformation of Ca-P compounds occurs at different times depending on the location of the nucleation and that some locations are less prone to mineralization than others within the same aorta. Thus, by looking at the minerals found at a specific time point, one can get a snapshot of the overall, lifetime mineral phase transformation in the mouse aortas.

SEM/EDS data confirm the crucial role of ELN-rich elastin lamina as the main ECM scaffold onto which minerals deposit in medial arterial calcification. The results also show that while Ca starts accumulating between the elastic laminae after some time, P does not. Vascular calcification may induce both cell death and degradation of the ECM (10, 31). Dying cells may release Ca from the intracellular storages, whereas degraded ECM may expose Ca-binding peptides (eg, fibrillins), which could serve as substrate for Ca adsorption and, thus, explain the large amount of Ca found. However, the finding that P ions do not initially adsorb on this Ca-rich layer suggests that the substrate onto which Ca is adsorbed crucially determines the rate of mineral nucleation and growth.

SEM images did not show any of the highly crystalline HA spheres found in cardiovascular mineral deposits in a previous work (207). Thus, if any crystalline HA spheres were present in our samples, they would be much less prevalent. This difference may be because of the fact that we analyzed medial arterial calcification, which is associated with ELN, whereas the highly crystalline HA spheres were detected in intimal arterial and valve calcifications. These 2 types of calcification may not necessarily be associated with ELN and may be induced by a different mechanism, that is, chondro-

osteogenic transdifferentiation of VSMCs. Thus, this different mechanism and ECM substrate may be responsible for the formation of the highly crystalline spheres, whereas ELN may favor the mineralization process described in this work. Indeed, understanding how different calcification mechanisms affect mineral phase transformation remains to be explored. Thus, it will be important to compare the mineral properties in animal models and human patients with vascular calcification caused by other mechanisms. Overall, our results imply that medial calcification associated with ELN is a multistep process like bone mineralization, starting from amorphous precursors and leading to overall more crystalline deposits. This suggests that an effective strategy to prevent vascular calcification may involve preventing the transformation of metastable precursor phases, which are amorphous or poorly crystalline, into crystalline apatite deposits. Because the metastable precursors are more soluble than HA or CHA (196), it may be possible to selectively dissolve them with appropriately targeted drugs. This could become a viable treatment for vascular calcifications associated with ELN.

In summary, this study confirms the importance of multidisciplinary approaches combining genetically modified mouse models and material science (207, 232) to unravel the mystery of ectopic mineralization. We show that mineral deposition in medial arterial calcification happens through a precise series of events (adsorption of Ca ions on the elastic lamina, formation of ACP and OCP, and transformation to HA and CHA), which are reproduced after each nucleation event throughout the life of the mice. Although drawn from animal models, these conclusions may be highly relevant to humans as well: analyzing the mineral phases rather than just the overall amount of minerals may help

diagnose and possibly prevent disease development. To achieve this, it will be crucial to develop advanced techniques to analyze mineral phase transformation *in vivo* (233-235).

4.5. Acknowledgments

We acknowledge support from the Canadian Light Source (CLS), which is supported by the Canada Foundation for Innovation, the Natural Sciences and Engineering Research Council of Canada, the University of Saskatchewan, the Government of Saskatchewan, the Western Economic Diversification Canada, the National Research Council Canada, and the Canadian Institutes of Health Research. We also thank Dr. Yongfeng Hu, Dr. Qunfeng Xiao, and Dr. Aimee MacLennan of the CLS for their help with data analysis and technical support.

4.6. Sources of funding

This work was supported by the Heart and Stroke Foundation, the Jacques de Champlain award, the Fonds Québécois de la Recherche sur la Nature et les Technologies (FQRNT), the Canada Research Chair foundation, the Center for Self-Assembled Chemical Structures, and the McGill Engineering Doctoral Award.

4.7. Author contributions

M.M. and M.C. supervised the research; J.M. generated the *Mgp*$^{-/-}$ and WT mice and prepared the tissues for analysis; O.G. performed FTIR, Raman and XPS experiments; O.G., J.M. and P.Z. performed NEXAFS, micro-XRF and micro-XAFS experiments; O.G. analyzed FTIR, Raman, XPS, NEXAFS, micro-XRF and micro-XAFS data; O.G. and M.C. interpreted all the data; O.G. performed statistical analysis; O.G. and M.C. wrote the paper; O.G., J.M., P.Z., M.M., and M.C. approved the final version of the paper.

4.8. Highlights

- An interdisciplinary approach combining animal models and materials science can provide insights into the mechanism of vascular calcification
- Mineral composition and crystallinity evolve over time and space in medial arterial calcification.
- Mineral deposition happens through a series of events (adsorption of Ca ions on elastic lamina, formation of ACP and OCP, and transformation to HA and CHA), which are reproduced after each nucleation event throughout the life of the mice.
- Analyzing the mineral phases rather than just the overall amount of minerals may help diagnose and possibly prevent disease development.
- An effective strategy to prevent vascular calcifications associated with ELN may involve preventing the transformation of metastable and soluble precursor phases into crystalline apatite deposits.

4.9. Methods

4.9.1. Materials

All the powdered reference compounds (i.e. ACP, OCP, DCPD, HA, CHA, and Ca acetate) were purchased from Sigma-Aldrich (USA) and directly used without further modification.

4.9.2. Mice

Both male and female *Mgp*$^{-/-}$ mice are in C57Bl/6 background. All the knockout mice were whole-body knockouts. *Mgp*$^{-/-}$ mice lack exon 1 to 3 and part of exon 4 of the MGP gene (67). Mice were maintained in a pathogen-free standard animal facility. The animal use protocol and all procedures were reviewed and approved by the Shriners Hospitals for Children Animal Care Committee and the McGill Institutional Animal Care and Use Committee. Shriners Hospitals for Children - Canada and McGill University are accredited and followed the guidelines of the Canadian Council on Animal Care. Genotypes were determined by PCR on genomic DNAs isolated from tail biopsies. The nucleotide sequences of the primers used for genotyping are available upon request.

4.9.3. Tissue preparation

Thoracic and abdominal aorta segments were isolated from 1-week, 2-week, 3-week , 4-week , and 5-week-old *Mgp*$^{-/-}$ mice and from 3-week and 5-week old wild-type (WT) mice. For whole tissue analyses, aortas were fixed in 4% buffered paraformaldehyde overnight, washed in phosphate buffered saline (PBS), transferred to 70% ethanol, and dried under vacuum overnight before analysis. For cross section analyses, aortas were fixed overnight in freshly prepared 4% paraformaldehyde, washed in PBS, transferred to 70% ethanol, embedded in methyl methacrylate, sectioned (7-µm-thick), and deplastified with 2-methoxyethyl acetate before analysis.

Bones were isolated from 5-week-old WT mice. For the analyses, bones were fixed in 10% formalin overnight, washed in PBS, kept into 70% ethanol and then dried under vacuum overnight.

4.9.4. Histological analysis

Mouse aortas were fixed overnight in 4% buffered paraformaldehyde, embedded in methyl methacrylate, sectioned (7 μm), and stained by von Kossa and van Gieson (VKVG). All histological images were captured using a digital camera (DP72; Olympus Canada Inc), acquired with DP2-BSW software (XV3.0; Olympus Canada Inc) and processed using PhotoShop software (Adobe).

4.9.5. Alizarin red staining

For alizarin red staining of aortas, thoracic cages were fixed overnight in 95% ethanol, stained in 0.015% Alcian Blue dye (Sigma-Aldrich) in a 1:4 solution of glacial acetic acid and absolute ethanol for 24 hours. Tissues were then treated with 2% potassium hydroxide for another 24 hours (or until the soft tissues were dissolved) and then stained by 0.005% Alizarin Red (Sigma-Aldrich) in a 1% potassium hydroxide solution. Finally, the stained skeletal tissues were clarified in 1% potassium hydroxide /20% glycerol for 2 days.

4.9.6. Fourier Transform infrared (FTIR) spectroscopy

FTIR spectra of powdered aortas mixed with an appropriate 50% weight/weight ratio of KBr were collected on a Bruker Tensor 27 spectrometer equipped with a diffuse reflectance (DRIFT) accessory and a DTGS detector. The spectra were collected from 400 to 4000 cm^{-1} with 128 scans at 4 cm^{-1} resolution. The reflected signals were converted and reported as absorbance in the figures shown in this study. FTIR measurements were performed on three points per sample and three samples per condition were analyzed. The data was analyzed using OPUS software (OPUS 7.0.0, Bruker, Karlsruhe, Germany).

4.9.7. Raman spectroscopy

Whole aortas were analyzed by Raman spectroscopy using a Bruker Senterra confocal Raman spectrophotometer equipped with a 785nm diode laser coupled with an Olympus optical microscope, using a 40x objective. Spectra were collected at 100 mW laser power and spectral resolution of 3.5 cm^{-1}, between 400 and 1800 cm^{-1}, with an integration time of 60 seconds and 4 co-additions. In total, 3 thoracic and 3 abdominal samples were analyzed for each mouse age, and 20 points per sample were analyzed. The data was analyzed using OPUS software (OPUS 7.0.0, Bruker, Karlsruhe, Germany).

4.9.8. X-ray diffraction (XRD)

XRD data of grounded aortas were obtained with a Bruker D5000 diffractometer using a Cu Kα radiation source (Kα1 λ=1.54 Å), and a monochromator operated at 40 kV and 40 mA within the 10° to 80° range in 2θ. Three samples per condition were analyzed. The FWHM were analyzed using GraphPad software, Inc. (2016).

4.9.9. X-ray photoelectron spectroscopy (XPS)

The atomic composition of aorta cross sections was characterized using a Thermo Scientific Kα spectrometer, equipped with an Al Kα X-ray source (1486.6 eV, 0.843 nm), a micro-focused monochromator, and an ultrahigh vacuum chamber (10^{-9} Torr). Survey scans and high resolution spectra were acquired with an X-ray spot with a diameter of 50 μm. At least three survey scans were collected between 0 and 1200 eV with a step size of 1 eV for each sample. Elemental high resolution scans were acquired with a step size of 0.1 eV. Samples were hit with a flood gun shooting low energy electrons during the measurement to prevent charging. Ten points were randomly selected along the cross section of each aorta and three samples were analyzed per condition. Peak fitting and

quantitative analysis of the survey spectra were performed using the Thermo Advantage software (version 4.60).

4.9.10. Ca K-edge Near Edge X-ray absorption fine structure (Ca K-edge NEXAFS) spectroscopy

Ca K-edge NEXAFS spectra on whole aortas were collected at the bulk-XAFS end-station of the Soft X-ray Microcharacterization beamline (SXRMB) at the Canadian Light Source (CLS), Saskatoon, Saskatchewan. Powdered reference compounds of known chemical compositions were analyzed, including ACP, OCP, DCPD, hydroxyapatite (HA), CHA, and Ca acetate ($Ca(CH_3COO)_2$). Spectra were collected with energies between 1.7 and 10 keV in fluorescence mode and with a photon beam spot size of 2 mm x 6 mm. The spectra were calibrated, aligned, and normalized using Athena software (Demeter 0.9.20). Linear combination fitting (LCF) was performed on the NEXAFS regions of the aorta sample spectra using all the possible combinations of the reference samples. The quality of the fits was evaluated by the R-factor value: values below 0.02 indicate that the fitting results are satisfactory (227). For each spectrum, the best LCF combination (i.e. the combination giving the lowest R-factor) was retained. LCF was performed using Athena software.

4.9.11. Micro-X-ray fluorescence (μ-XRF) and μ-NEXAFS spectroscopy

μ-XRF Ca and P maps and μ-XAFS spectra were collected on whole aortas at the microprobe end-station of the Soft X-ray Microcharacterization beamline (SXRMB) at the Canadian Light Source (CLS), Saskatoon, Saskatchewan. μ-XRF maps were obtained by scanning the sample under a monochromatic beam with a spot size of 10 x 10 μm^2 at an X-ray energy of 4100 eV. μ-NEXAFS spectra were collected on hot spots, i.e. spots

that contain the highest amounts of Ca with energies between 1.7 and 10 keV in fluorescence mode and with a photon beam spot size of 10 x 10 μm^2. μ-XRF maps were created and analyzed using the SMAK software program and μ-NEXAFS spectra were analyzed using Athena software.

4.9.12. Scanning electron microscopy (SEM) and energy-dispersive X-ray spectroscopy (EDS)

Aorta cross sections were characterized using a combination of SEM and EDS. Samples were secured to an aluminium sample holder with carbon tape, and then coated with 8.5 nm carbon (carbon sputter coater, EMS150R ES, Electron Microscopy Sciences (EMS)). The samples were then imaged using an Inspect-50 field emission SEM (FEI, Japan), at 10 kV operating voltage under high vacuum. EDS spectra and elemental maps were obtained in the regions of interest using an EDX spectrometer (EDX, Thermo Scientific, USA).

4.9.13. Statistical analysis

Statistical data analysis was performed using GraphPad software, Inc. (2016). Mean values were expressed as average ± standard deviation. Statistical analysis on mean values were performed by Student's *t* test or one-way ANOVA test followed by Tukey's test correction for multiple comparisons, and $p < 0.05$ was considered significant. In the Raman experiments, median values instead of means were used because the data was not normally distributed. In this case, median values were expressed as median ± standard deviation; the statistical analysis was performed using Mood's median test followed by Tukey's test correction for multiple comparisons, and $p < 0.05$ was considered significant.

4.10. Supplemental Material

4.10.1. Section 1: Detailed methods

4.10.1.1. Determination of the crystallinity index (CI) of the minerals by FTIR

The splitting of the v_4 band can be used to estimate HA crystallinity index (CI) according to the formula introduced by Shemesh *et al.* (222):

$$CI = (A_{605} + A_{565}) / A_{595}, \qquad (i)$$

where A_x is the absorbance at wavenumber x (Figure 4S.2.B)

A higher degree of splitting and therefore a higher CI correspond to more crystalline materials (236). The CI of samples of synthetic HA, bone and calcified aortas are shown in the inset of Figure 4S.2.A. The CI of synthetic HA (3.4 ± 0.1, n = 3) is the highest ($p<0.005$), while no statistically significant differences are present between the minerals found in bone (2.4 ± 0.2, n = 3) and aorta (2.5 ± 0.1, n = 3).

4.10.1.2. Determination of the Full width at half maximum (FWHM) and mineralization extent (ME) by Raman spectroscopy

We analyzed changes in mineral crystallinity and in the amount of minerals deposited by measuring the full width at half maximum (FWHM) of the v_1 phosphate peak and the mineralization extent (ME), respectively. The FWHM is inversely proportional to HA crystallinity (Figure 4S.3.B) (222).

The ME is defined as the inorganic to organic ratio, i.e. the ratio between the areas under the peaks relative to the mineral component and those relative to the organic matrix (Figure 4S.3.C). While the v_1 phosphate peak between 945 and 962 cm^{-1} is always used as the mineral marker in the literature, different bands were used as organic markers, such as the amide I v C=O, the v CH, or the δ_{as} CH_2, CH_3 peak (223). Here we chose to

use the δ_{as} CH_2, CH_3 peak at 1443 cm^{-1} as marker of the organic matrix since it was well defined on all our spectra:

$$ME = A_{945\text{-}962} / A_{1443}, \qquad \text{(ii)}$$

where A_x is the area underneath the peak at the wavenumber x (Figure 4S.3.C)

The peak area calculation used to quantify the ME was performed by applying an integration profile to all spectra, i.e. by calculating the area between two manually selected points corresponding to the first and the last point of the peak. Only the area above the baseline was included in the measurements.

4.10.1.3. Linear combination fitting (LCF) procedure

To identify the Ca-P phases present in the samples, we first select six reference compounds (Figure 4S.5.): six Ca species that were identified in cardiovascular calcifications (ACP, OCP, DCPD, β-TCMP, HA, and CHA) (169, 174, 193, 194, 202-204), and Ca acetate ($Ca(CH_3COO)_2$), which may be a model of the very early stages of calcification if the Ca ions were first absorbed on the organic matrix by forming complexes with organic carboxyl groups. Then, we perform principal component analysis (PCA) to determine which reference compounds should be excluded; based on the PCA results, we exclude $Ca(CH_3COO)_2$ and β-TCMP from the reference samples for the fit. Finally, we perform LCF using all the possible combinations of the reference compounds that were selected by PCA, i.e. ACP, OCP, DCPD, HA, and CHA. We evaluate the quality of the fits using the R-factor: fitting results with R-factor values below 0.02 are considered satisfactory (227). We report the LCF combination giving the lowest R-factor for each sample analyzed.

4.10.1.4. Determination of the Ca/P ratios by micro-X-ray fluorescence (μ-XRF)

The Ca/P ratios are based on the ratio between the Ca and P μ-XRF spectral intensities (counts) ratio. μ-XRF spectral intensities were extracted from the Ca and P maps using the SMAK software program (Figure 4.4). For each map region, we calculated an averaged Ca/P ratio based on averaged μ-XRF spectral intensities of 4 pixels.

4.10.2. Section 2: Supplemental figures

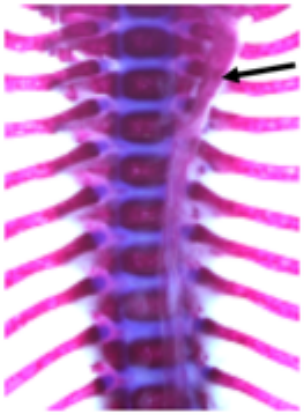

Figure 4S.1. Alizarin red (stains calcium) and alcian blue (stains proteoglycans) of the thoracic of 5-day-old *Mgp*$^{-/-}$ mouse showing the initial detection of calcified deposits in the upper part of the descending aorta (black arrow).

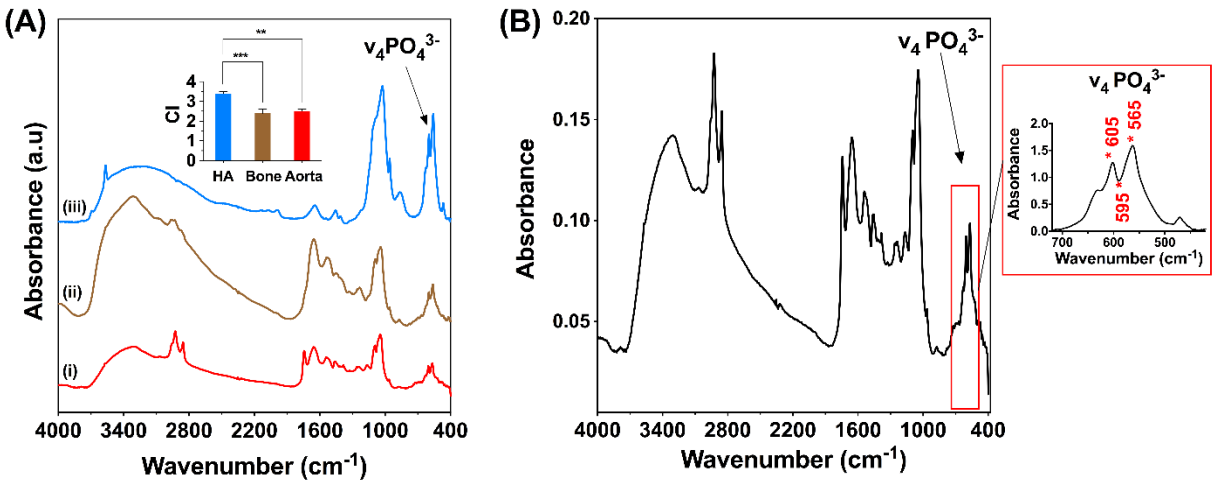

Figure 4S.2.(**A**) Representative FTIR spectra of (i) calcified aorta from a 5-week-old *Mgp*$^{-/-}$ mouse, (ii) bone, and (iii) HA showing the triply degenerated v_4 phosphate band used to determine the CI values. The inset shows the CI values for these three samples, (n = 3). * indicate significant differences between the different ages, with ** = P< 0.01, and *** = P< 0.002. (**B**) Representative FTIR spectrum of calcified aorta from 5-week-old *Mgp*$^{-/-}$ mouse showing the triply degenerated v_4 phosphate band used in Shemesh's method to determine the mineral crystallinity (222).

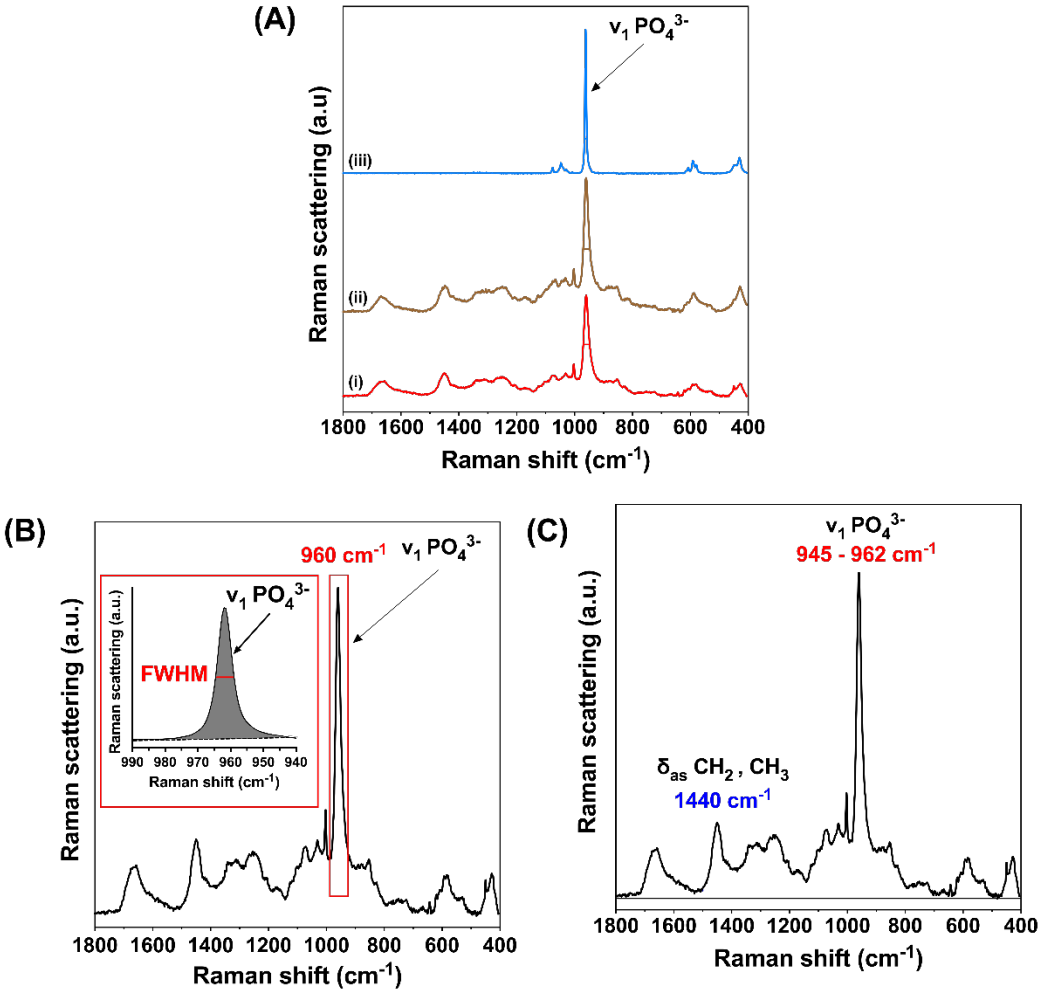

Figure 4S.3. (**A**) Representative Raman spectra of (i) calcified aorta from a 5-week-old *Mgp*$^{-/-}$ mouse, (ii) mature bone, and (iii) HA. Representative Raman spectra (**B** and **C**) of aorta from 5-week-old *Mgp*$^{-/-}$ mouse showing (**B**) the v_1 phosphate peak between 945 and 962 cm^{-1} and its FWHM, which was used to estimate mineral crystallinity, and (**C**) the two peaks used to estimate the ME: the v_1 phosphate peak at 960 cm^{-1} used as inorganic marker, and the $\delta_{as}CH_2,CH_3$ band used as organic marker. The inorganic to organic ratio was calculated as the ratio of the integrated areas of these two peaks.

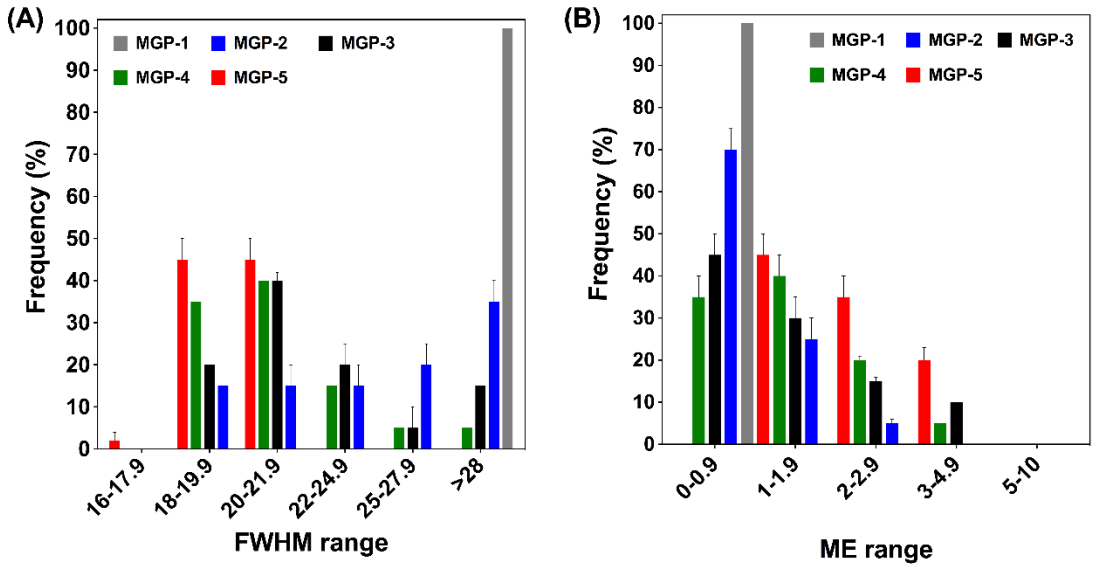

Figure 4S.4. Distribution of the FWHM measured on the ν_1 phosphate peak at 960 cm^{-1} (**A**) and of the ME (**B**) determined by Raman spectroscopy on abdominal aortas from 1-week (blue), 2-week (red), 3-week (orange), 4-week (green), and 5-week-old (purple) *Mgp*$^{-/-}$ mice. For each age, 3 mice were analyzed, and 20 spectra were taken at different points for each sample.

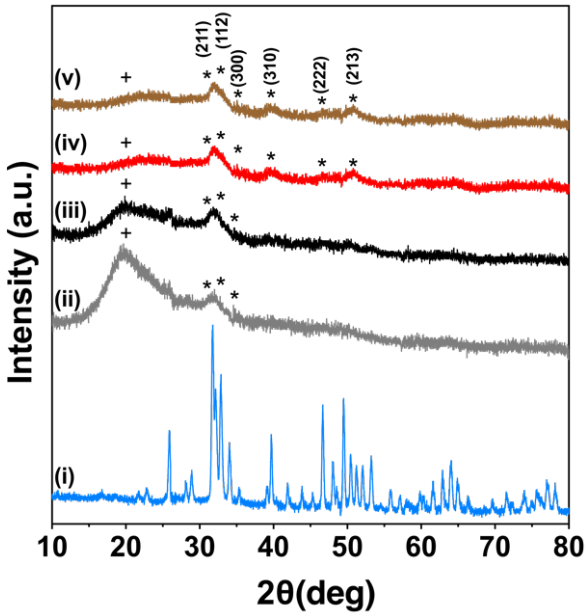

Figure 4S.5. Representative XRD patterns of aortas from (i) synthetic HA, calcified aortas from (ii) 1-week, (iii) 3-week, and (iv) 5-week-old *Mgp*$^{-/-}$ mice and from (v) bone. (+) and (*) signs indicate the peaks corresponding to collagen and HA, respectively. The labels on the spectra refer to the HA planes visible on aorta and bone samples. For each age, 3 mice were analyzed.

All the spectra of bone and aorta samples show a broad peak at about 20° characteristic of collagen (237) (Figure 4S.5). All the other peaks correspond to the diffraction peaks of HA (238). Only one well-defined diffraction peak centered at about 32° is present on 1-week and 3-week-old samples. This broad peak is the combination of the peaks corresponding to the crystallographic planes (211), (121), and (300) of HA and is indicative of a relatively low degree of crystallinity (239). In addition to this peak, mature bone and 5-week-old aorta samples show three other peaks at about 40°, 47°, and 51°, that correspond to the HA planes (310), (222), and (213), respectively (238). The presence of these peaks only after 5 weeks suggests that the crystallinity of the minerals in aorta samples increases with time. To confirm this, we estimated the degree of crystallinity by calculating the FWHM of the peak corresponding to the planes (211), (121), and (300). The FWHM decreases as the mice age increases, reaching the same value measured on mature bone (2.0 ± 0.1, 1.5 ± 0.1, and 1.1 ± 0.2 for the minerals found after 1, 3, and 5 weeks in aorta samples, respectively, vs. 0.9 ± 0.2 for bone) (Table 4S.3). The decrease in the collagen peak intensity over time may be explained by collagen remodeling induced by calcification.

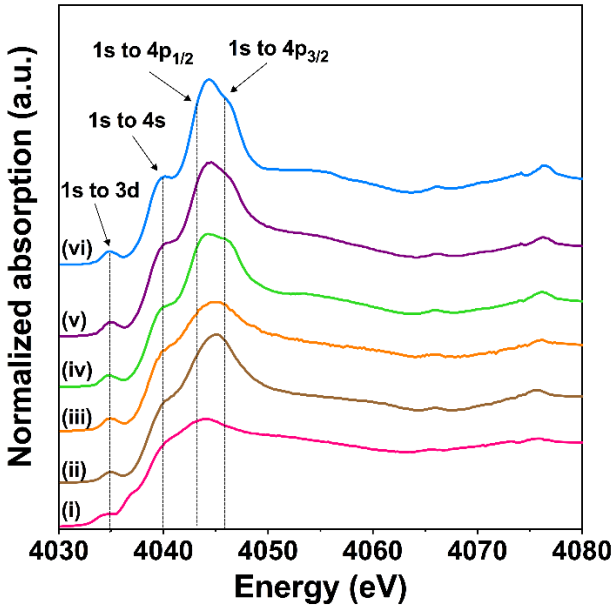

Figure 4S.6. Representative Ca K-edge NEXAFS reference spectra of (i) $Ca(CH_3COO)_2$, (ii) DCPD, (iii) ACP, (iv) OCP, (v) CHA and (vi) HA.

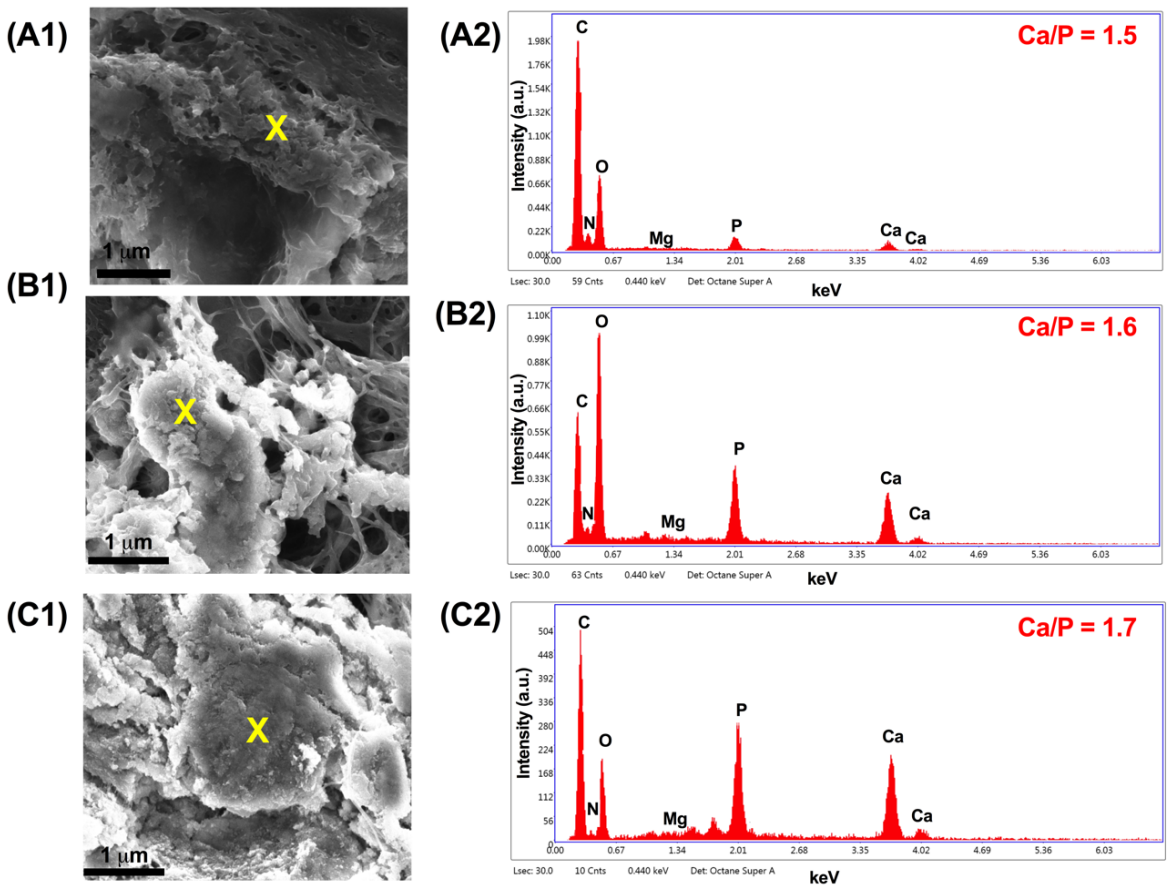

Figure 4S.7. (**A1**, **B1**, and **C1**): SEM images of aortas from (**A1**) 1-week, (**B1**) 3-week, and (**C1**) 5-week-old *Mgp*$^{-/-}$ mice. (**A2**, **B2**, and **C2**): Corresponding EDS spectra collected at the sites indicated by the crosses on the SEM images **A1**, **B1**, and **C1**, respectively. The Ca/P ratios were calculated based on the elemental atomic percentages.

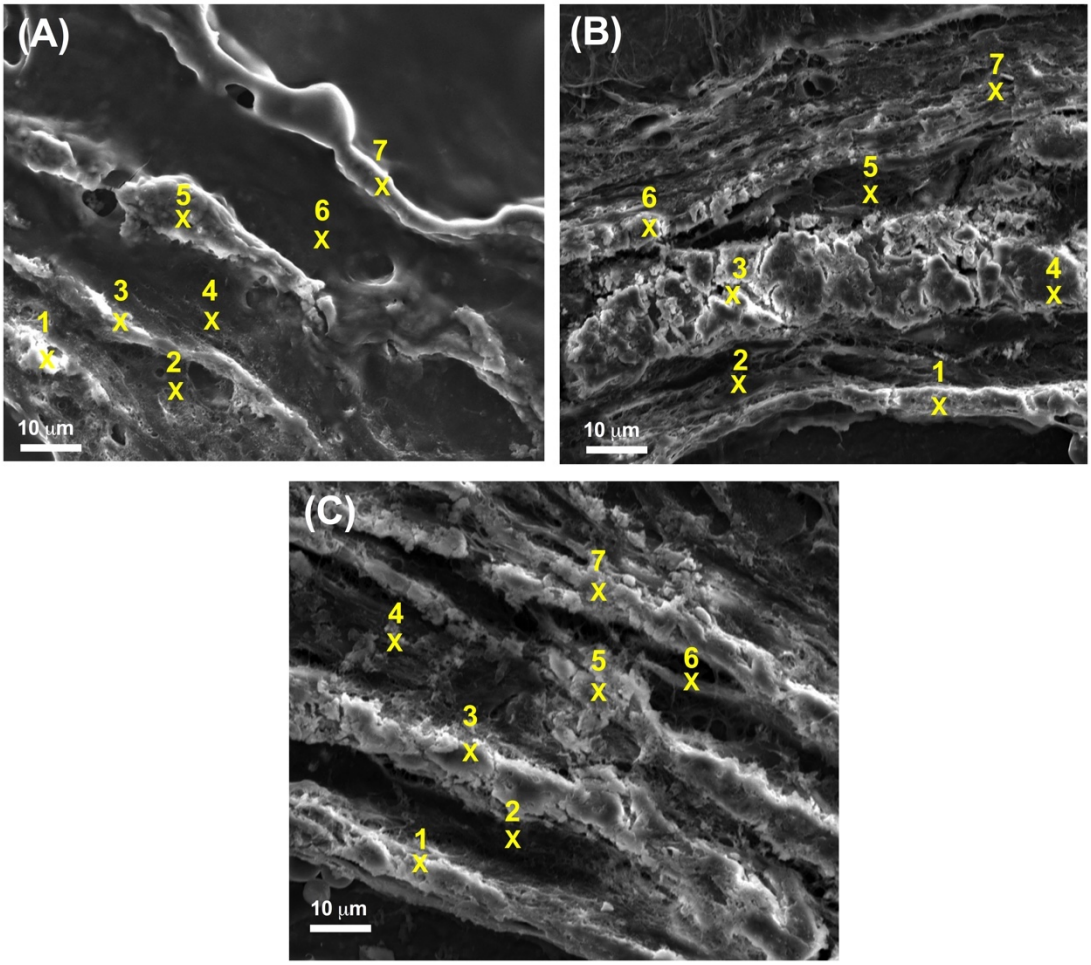

Figure 4S.8. SEM images of aortas from (**A**) 1-week, (**B**) 3-week, and (**C**) 5-week-old *Mgp*$^{-/-}$ mice. The numbered sites on **A**, **B**, and **C** indicate the spots where EDS spectra were collected and they correspond to the data presented in Table 4S.7, Table 4S.8, and Table 4S.9, respectively.

4.10.3. Section 3: Supplemental tables

Table 4S.1. FTIR peak assignments for HA, bone, and calcified aorta from a 5-week-old *Mgp*$^{-/-}$ mouse.

Peak (cm^{-1})	HA	Bone	Calcified aorta	References
v OH	3571	3322	3306	(194, 240)
v N-H		2960		(194)
v_{as} CH_2			2926	(194)
v_s CH_2			2855	(194)
v C=O (carbonyls)			1743	(194)
δ C=O (amide I)		1661	1654	(194, 240, 241)
v_3 CO_3^{2-}	1644			(173, 240)
v C-N (amide II)		1533	1534	(194, 240, 241)
v_3 CO_3^{2-}	1458	1449	1457	(173, 240)
δ C-H		1449	1457	(173, 240)
δ C-H (amide III)		1239	1241	(241)
v C-O			1165	(241)
v_3 PO_4^{3-}	1091	1094	1094	(173, 174, 194, 240, 241)
v_3 PO_4^{3-}	1031	1046	1046	(173, 174, 194, 240, 241)
v_1 PO_4^{3-}	962	955	963	(173, 174, 194, 240, 241)
v_2 CO_3^{2-}	863	869		(173, 174, 194, 240, 241)
v OH	633	626	628	(240)
v_4 PO_4^{3-}	602	603	604	(173, 174, 194, 240, 241)
v_4 PO_4^{3-}	564	566	588	(173, 174, 194, 240, 241)
v_2 PO_4^{3-}	473			(173, 174, 194, 240, 241)

v_{as}: antisymmetric stretching; v_s: symmetric stretching; δ: bending

Table 4S.2. Raman peak assignments for HA, bone, and calcified aorta from a 5-week-old *Mgp*$^{-/-}$ mouse.

Peak (cm^{-1})	HA	Bone	Calcified aorta	References
v C=O (amide I)		1659	1658	(235, 242, 243)
δ_{as} CH_2, CH_3 (proteins)		1448	1443	(203, 242, 243)
δ_s C-H (lipids)			1303	(242, 244)
δ_s N-H (amide III)		1250	1252	(235, 242, 243)
v_1 CO_3^{2-}		1104	1103	(203)
v_1 CO_3^{2-}		1086	1086	(242, 244)
v_3 PO_4^{3-}	1072	1070	1072	(203, 243, 244)
v_3 PO_4^{3-}	1046	1046	1046	(203, 243, 244)
v_3 PO_4^{3-}	1032	1035	1031	(203, 243, 244)
v C-C phenylalanine		1003	1003	(242, 244)
v_1 PO_4^{3-}	960	945-962	945-962	(203, 243, 244)
v C-C proteins		870	868	(235, 242)
v_4 PO_4^{3-}	602	602	602	(244)
v_4 PO_4^{3-}	591	592	591	(244)
v_4 PO_4^{3-}	560	561	561	(244)
v_2 PO_4^{3-}	462	460	460	(244)
v_2 PO_4^{3-}	425	427	428	(244)

v: stretching; v_s: symmetric stretching; δ_s: bending; δ_{as}: antisymmetric bending

Table 4S.3. Experimental FWHM values of the peak corresponding to the planes (211), (121), and (300) for calcified aortas from 1-week, 3-week, and 5-week-old *Mgp*$^{-/-}$ mice calculated from XRD data.

Age (week)	FWHM
1	2.0 ± 0.1** $^{+++}$
3	1.5 ± 0.1 ** $^{\#}$
5	1.1 ± 0.2 $^{+++}$ $^{\#}$

** indicates significant differences between 1- and 3-week-old samples with P< 0.005.
$^{+++}$ indicates significant differences between 1- and 5-week-old samples with P < 0.001.
$^{\#}$ indicates significant differences between 3- and 5-week-old samples with P < 0.02. (n=3)

Table 4S.4. Elemental Ca/N and Ca/P ratios determined by XPS on aorta sections from 1-week, 3-week, and 5-week-old *Mgp*$^{-/-}$ mice.

Age (week)	Ca/N	Ca/P
1	0.4 ± 0.1	1.5 ± 0.2 *
3	0.4 ± 0.2 $^{+++}$	1.6 ± 0.3 * $^{+}$
5	0.8 ± 0.2 $^{+++}$	1.8 ± 0.3 $^{+}$

* indicates significant differences between 1- and 3-week-old samples with P< 0.02.
$^{+}$ indicate significant differences between 3- and 5-week-old samples with $^{+}$ = P < 0.05 and $^{+++}$ = P< 0.0001. (n= 3)

Table 4S.5. List of Ca-P phases present in bone and their Ca/P molar ratios (179).

Name	Formula	Ca/P
Hydroxyapatite (HA)	$Ca_{10}(PO_4)_6(OH)_2$	1.67
Dicalcium phosphate dehydrate (DCPD)	$Ca(HPO_4).2H_2O$	1.0
Amorphous calcium phosphate (ACP)	$Ca_9(PO_4)_6$	1.5
Octacalcium phosphate (OCP)	$Ca_8H_2(PO_4)_6.\ 5H_2O$	1.33
Carbonated hydroxyapatite (CHA)	$Ca_{10-p}(PO_4)_{6-p}(OH)_{2-p}(CO_3)_p$ (0<p<1)	>1.67

Table 4S.6. Percentages of HA, CHA, ACP, and OCP in calcified aortas from 1-week, 2-week, 3-week, 4-week, and 5-week-old *Mgp*$^{-/-}$ mice determined by LCF using NEXAFS spectra of reference samples, and R-factors of the LCF.

		LCF results (%)				
Sample	Age (week)	HA	CHA	ACP	OCP	R-factor
1	1	40 ± 2	0	0	60 ± 2	0.001623
2	1	30 ±2	0	11 ± 2	59 ± 8	0.000283
3	1	34 ±1	0	37 ± 3	27 ± 3	0.000481
4	1	24 ± 3	16 ± 6	34± 3	27 ± 3	0.000836
5	1	46 ± 2	0	10 ± 1	53 ± 2	0.000883
6	2	40 ± 2	0	62 ± 2	0	0.001391
7	2	49 ± 1	0	33 ± 2	16 ± 2	0.000275
8	2	50 ± 3	0	43 ± 2	0	0.002424
9	2	35 ± 1	0	42 ± 3	17 ± 2	0.000451
10	2	38 ± 3	0	69 ± 3	0	0.003994
11	3	78 ± 1	0	21 ± 1	0	0.000447
12	3	80 ± 1	0	20 ± 1	0	0.000551
13	3	71 ± 1	0	27 ± 1	0	0.000412
14	3	82 ± 2	0	15 ± 1	0	0.000863
15	3	61 ± 1	0	38 ± 1	0	0.000186
16	4	74 ± 1	14 ± 3	15 ± 3	0	0.000312
17	4	59 ± 1	13 ± 2	28 ± 2	0	0.000157
18	4	44 ± 1	24 ± 1	31 ± 3	0	0.000502
19	4	42 ± 1	23 ± 2	33 ± 2	0	0.000237
20	4	57 ± 2	20 ± 2	23 ± 2	0	0.000902
21	5	90 ± 2	0	10 ± 1	0	0.000545
22	5	91 ± 7	0	7 ± 1	0	0.005459
23	5	83 ± 2	0	19 ± 2	0	0.000937
24	5	81 ± 1	0	21 ± 1	0	0.000538
25	5	86 ± 1	0	15 ± 1	0	0.000440

Table 4S.7. Relative elemental atomic percentages in aorta from a 1-week old *Mgp*$^{-/-}$ mouse. The spots 1-7 are shown in Figure 4S.8.A.

Spot	C (at%)	O (at%)	N (at%)	Ca (at%)	P (at%)	Mg (at%)	Ca/P	Ca/C
1	39.4	34	4.3	9.6	6.5	0	1.5	0.2
2	87.4	12.3	0.1	0.2	0	0	/	/
3	53.1	21.4	9.1	3.8	2.6	0	1.5	0.1
4	81.1	16	2.1	0.8	0	0	/	/
5	31.7	45.6	0.7	13.2	8.9	0	1.5	0.3
6	86.5	13.4	0,2	0.1	0	0	/	/
7	68.5	24.4	2.2	2.9	2	0	1.5	0.1

Table 4S.8. Relative elemental atomic percentages in aorta from a 3-week-old *Mgp*$^{-/-}$ mouse. The spots 1-7 are shown in Figure 4S.8.B.

Spot	C (at%)	O (at%)	N (at%)	Ca (at%)	P (at%)	Mg (at%)	Ca/P	Ca/C
1	52.6	16.2	14.2	16.1	0.7	0.2	23	0.3
2	52.4	15.1	11	12.9	8	0.9	1.6	0.3
3	36	36.3	2.3	16.3	8.8	0.7	1.9	0.5
4	50.5	19.1	13.6	10.6	6.5	0.1	1.6	0.2
5	59.4	13.6	8	11.2	7.6	0.4	1.5	0.2
6	60.7	13.3	9.5	15.9	0.4	0	40	0.3
7	57.8	12.5	11	18.1	0.5	0.2	36	0.3

Table 4S.9. Relative elemental atomic percentages in aorta from a 5-week-old *Mgp*$^{-/-}$ mouse. The spots 1-7 are shown in Figure 4S.8.C.

Spot	C (at%)	O (at%)	N (at%)	Ca (at%)	P (at%)	Mg (at%)	Ca/P	Ca/C
1	41	33.2	5.1	11.6	8.2	1.1	1.4	0.3
2	61.5	13.9	8.7	15.4	0.7	0.2	22	0.3
3	33.6	38.9	4.1	13.7	9	1	1.5	0.4
4	34.6	37.6	4	22.4	0.6	0.3	37	0.6
5	23.4	49.5	5.4	13.9	7.9	0.2	1.8	0.6
6	50.5	13.3	2.3	18.7	12.4	2.9	1.5	0.4
7	64.3	9.8	4.3	13.2	7.8	0.6	1.7	0.2

Chapter 5. Crosslinked Elastin-Like Polypeptide (ELP) Membranes as a Model for Medial Arterial Calcification.

In the previous chapter, we showed that mineral phase deposition in a mouse model of medial calcification occurs through a precise series of events including the formation of precursor phases and their further transformation into more crystalline apatite phases. This suggests that mineral formation associated with ELN is a multistep process like bone formation. However, the complexity of the artery's structure hampers a molecular understanding of this mechanism *in vivo*. Thus, *in vitro* models involving ELN could greatly improve our understanding of this process.

In this study, we propose crosslinked ELP membranes immersed in SBF as an *in vitro* model of medial calcification. We show that ELP fibers and filaments mineralize first, suggesting that the fiber-like nature of ELN makes it prone to mineralization. Ca-P phases form and evolve over time on ELP membranes similarly to what we previously reported in MGP-deficient mice, showing that a model based on ELP membranes immersed in SBF captures this crucial *in vivo* finding.

This work was published in the American Chemical Society journal *Biomacromolecules*, in 2019.

Ophélie Gourgas, Lisa D. Muiznieks, Dainelys Guadarrama Bello, Antonio Nanci, Simon Sharpe, Marta Cerruti. Crosslinked Elastin-Like Polypeptide (ELP) Membranes as a Model for Medial Arterial Calcification.

5.1. Abstract

Calcium phosphate minerals deposit on the elastin-rich medial layers of arteries in the majority of seniors, diabetic and chronic kidney disease patients, causing severe cardiovascular complications. There is no cure for medial calcification, and the mechanism of mineral formation on elastin layers is unknown. Here we propose crosslinked elastin-like polypeptide membranes as models to study medial calcification. Calcium phosphates deposit first on fibers and filaments and then spread to globular structures present in the membranes. Mineral phase evolution analyzed by near-edge x-ray spectroscopy matches that previously observed in a mouse model of medial calcification, showing that this simple system captures some of the key *in vivo* findings. This work shows how minerals form and evolve upon nucleation on elastin and provides an *in vitro* model that can be tuned to study hypotheses related to arterial calcification mechanisms and test drugs to stop or revert mineralization.

5.2. Introduction

Arterial calcification leads to the deposition of calcium phosphate (Ca-P) minerals on the extracellular matrix (ECM) of the arteries. This pathological condition significantly increases morbidity in patients suffering from life-threatening diseases, such as chronic kidney disease (CKD), type 2 diabetes, and atherosclerosis (28, 216, 245). It is also commonly seen in seniors and in patients with some genetic disorders (246). Currently, there is no cure to arterial calcification and the treatments available are aimed only at limiting its progression.

Mineral deposition occurs both in the intimal and medial layer of the arteries. Intimal calcification is mainly associated with atherosclerosis while medial calcification is mostly found in CKD and diabetic patients (14). Although they share common determinants, intimal and medial calcifications follow distinct pathways. For example, while intimal calcification involves osteochondrogenic transdifferentiation of vascular smooth muscle cells (VSMCs), this is not a prerequisite for medial calcification (10).

Although the molecular mechanism of medial arterial calcification is still unknown, several studies have shown the critical role of elastin (ELN) as mineral nucleator in this process (15, 16, 107, 247). Specifically, it was shown that mineral deposition occurs predominantly along and within the ELN-rich elastic laminae, and that collagen fibers are not required for the initiation of calcification (15, 16, 107, 247).This was confirmed more recently by Khavandgar *et al.* (248) who also showed that ELN haploinsufficiency significantly delays the progression of medial calcification. Still, the physicochemical details of mineral nucleation and growth and the sites of mineral deposition on ELN are

unknown. This impedes our understanding of how minerals interact with the ECM, especially ELN, and of the overall molecular mechanism of medial calcification.

Several studies have analyzed minerals formed in cardiovascular tissues and found that the major inorganic phase is poorly crystalline non-stoichiometric carbonated hydroxyapatite (CHA), similar in composition and structure to the mineral component of bone (171, 172, 175, 182, 207, 219). In addition to CHA, other Ca-P phases were found at early stages of calcification, such as amorphous calcium phosphate (ACP), octacalcium phosphate (OCP), dicalcium phosphate dehydrate (DCPD), and magnesium-substituted β-tricalcium phosphate (β-TCMP) (174, 193, 194, 202-204, 249). However, most of these studies examined intimal arterial and valve calcifications (171, 172, 175, 182, 207, 219), and only few works have been reported on medial calcification (193, 204, 249). Intimal arterial and valve calcifications may not necessarily be associated with ELN and may be induced by a different mechanism, thus leading to a different mineralization pathway. In our recent work (250), we analyzed minerals formed in matrix gla protein (MGP)-deficient mice, a mouse model for medial calcification. We showed that mineral deposition associated with ELN happens through a precise series of events: adsorption of Ca ions, formation of ACP and OCP, and further transformation to HA and CHA. This suggests that mineral formation in medial calcification is a multistep process like bone formation (188, 189, 251), starting from amorphous and poorly crystalline precursors and leading to more crystalline apatite deposits. However, more work is needed to confirm these results and to fully understand the ELN mineralization process. In fact, the complexity of the artery's structure hampers a molecular understanding of this

mechanism *in vivo*. Thus, *in vitro* models involving ELN could greatly improve our understanding of this process.

A major difficulty of this approach is that ELN is highly water insoluble (252). ELN self-assembles from its monomeric precursor, tropoelastin, through coacervation and subsequent formation of intermolecular crosslinks (89). Tropoelastin is a highly (>75%) non-polar protein characterized by hydrophobic sequences, or domains, that alternate with lysine-containing crosslinking domains. Hydrophobic domains are rich in glycine, valine, and proline residues that are commonly arranged into repetitive motifs such as Val-Pro-Gly and Pro-Gly-Val-Gly (89, 90). Early studies used solubilized ELN obtained from natural tissues through partial hydrolysis to build *in vitro* models for medial calcification (98, 99, 104, 105, 107-110). Among them, some suggested charged groups such as sulfhydryl, amino, and carboxyl groups as nucleation sites for ELN mineralization (98, 99, 104, 105); however, Starcher and Urry showed that a solubilized form of ELN in which all the carboxyl and amino groups were blocked provided an excellent matrix for calcification *in vitro* (107). This is consistent with the proposal that neutral binding sites (i.e. carbonyl groups) on ELN can bind Ca (108, 109). Although these studies suggested that Ca ions are adsorbed first on ELN, the results from another study also using solubilized ELN as an *in vitro* model suggested that the formation of minerals on ELN is initiated via adsorption of inorganic P (110). Possibly, one of the reasons behind these contradictory results is the heterogeneity of solubilized ELN. In fact, extraction and purification of solubilized ELN from animal sources result in a heterogenous mixture of hydrophobic ELN fragments that are partially crosslinked, rather than the alternative

domain structure observed in natural full-length ELN (89, 111). Also, solubilized ELN shows evidence of degradation and contains high levels of contaminants (112).

An alternative to solubilized ELN are synthetic ELN-like polypeptides (ELPs) representative of the whole structure of the protein. In 1974, Urry *et al.* first developed an artificial polypentapeptide (HCO-(Val-Pro-Gly-Val-Gly)$_n$-Val-OMe, $10 \leq n \leq 15$) mimicking the repeated hydrophobic motifs found in tropoelastin (113). After this, several ELPs composed of segments of alternating hydrophobic and crosslinking domains (90, 114-120), or the full-length monomer (90, 91, 121, 122), were produced through bacterial expression. ELPs self-organize into structures resembling native ELN through coacervation. Several researchers used ELPs with various combinations of hydrophobic and crosslinking domains to explore ELN structure and self-assembly *in vitro* (90, 114-120), thus overcoming the limitations of the previous studies based on heterogeneous and partially crosslinked solubilized ELN.

Not only do ELPs self-assemble *in vitro*, but they can also be crosslinked to form ELN-based matrices that have physical and elastic properties approaching those of native insoluble ELN (117, 118, 123). ELPs in this crosslinked form have been extensively used as biomaterials for tissue engineering applications, including enamel, cartilage, and bone regeneration, and vascular grafts (124-134). In most of these studies, the ELN sequence was modified by the addition of one or more bioactive sequences, for example to promote mineralization (i.e. Statherin-derived peptide) (125-129, 134), mesenchymal stem cell adhesion (i.e. RGDS sequence), or endothelial cell adhesion (i.e. REDV sequence) (126, 129, 130).

Despite the large literature on ELP-based materials, especially as platforms for promoting hard tissue regeneration, ELP-based matrices have not been explored as models to understand arterial calcification. Even more surprisingly, no new *in vitro* models of ELN calcification have been reported since the early studies using solubilized ELN such that the nucleation sites on ELN and the overall mechanism of mineral formation remain poorly understood.

To address this gap, in this study we use crosslinked ELP membranes as an *in vitro* model for medial arterial calcification. We induce ELP self-assembly by adding salt and heat; we do not use any organic solvent during this process. As crosslinker, we employ genipin, a natural plant-derived compound with excellent biocompatibility (253). We conduct the mineralization experiments in simulated body fluid (SBF) at physiological pH and temperature. This system allows us to more closely emulate the *in vivo* condition of ELN calcification, while providing us with a simple model for studying the temporal evolution of medial calcification. We analyze mineral phases formed on ELP membranes by combining traditional microscopic and spectroscopic techniques with synchrotron-based near-edge x-ray absorption fine structure spectroscopy (NEXAFS).

5.3. Materials and methods

5.3.1. Materials

Genipin (≥98.0% by HPLC) was purchased from Challenge Bioproducts (Taiwan, China). Sodium chloride (NaCl, ≥99.0%), and hydrochloric acid (HCl, ACS reagent, 36.5 to 38.0% (w/w)) were purchased from Fisher Scientific (Ottawa, ON, Canada). Sodium tetraborate decahydrate ($Na_2B_4O_7.10H_2O$, ACS reagent, 99.5-105.0%) sodium hydrogen carbonate ($NaHCO_3$, ≥99.0%), potassium chloride (KCl, BioXtra, ≥99.0%), potassium

phosphate dibasic trihydrate ($K_2HPO_4 \cdot 3H_2O$, ≥99.0%), magnesium chloride hexahydrate ($MgCl_2 \cdot 6H_2O$, BioXtra, ≥99.0%), calcium chloride ($CaCl_2$, ≥97.0%), sodium sulfate (Na_2SO_4, ACS reagent, ≥99.0%), tris(hydroxymethyl)aminomethane ($NH_2C(CH_2OH)_3$) (Tris), ACS reagent, ≥99.8%), amorphous calcium phosphate ($Ca_3(PO_4)_2.3H_2O$ (ACP)), dicalcium phosphate dihydrate ($Ca(HPO_4).2H_2O$, (DCPD)), and β-tricalcium phosphate ($Ca_{18}(Mg)_2H_2(PO_4)14$, β-TCMP)) were purchased from Sigma-Aldrich (Oakville, ON, Canada). Hydroxyapatite ($Ca_{10}(PO_4)_6(OH)_2$ (HA)) was obtained from the National Institute of Standards and Technology (NIST). The Epon resin kit was purchased from Electron Microscopy Sciences (EMS; Hatfield, PA, USA). All materials were used as received.

Carbonated hydroxyapatite ($Ca_{10-p}(PO_4)_{6-p}(OH)_{2-p}(CO_3)_p$ (0<p<1), (CHA)) and octacalcium phosphate ($Ca_8H_2(PO_4)_6. 5H_2O$, (OCP)) were prepared following methods previously described in (254) and (255), respectively.

5.3.2. ELP_3 expression and purification

ELP_3 in a pET-32b vector was cloned and overexpressed in *E.coli* BL21(DE3) cells as previously described (114). Briefly, expression was induced with isopropyl β-D-1-thiogalactopyranoside (0.1 mM) when the optical culture density (A_{600nm}) reached ~1. Cells were grown a further 3 h, (200 rpm, 37 °C) and harvested by centrifugation (6000 rpm, 15 min). Cell pellets were digested overnight (1g CnBr in 20 mL 70 % formic acid per liter culture) and dialysed (3500 MWCO dialysis tubing, Spectropor) against Na acetate (20 mM, pH 5.25) for 24 h. ELP_3 was purified from cleared cell lysate by ion exchange chromatography (SP Sepharose, Amersham Bioscience), eluted with a linear gradient of NaCl (0-220 mM) in 20 mM Na acetate buffer, pH 5.25. A final purification was carried out by HPLC (Jupiter C4 10 µm 300 Å column, Phenomenex), eluted with a linear

gradient of 25-50% acetonitrile. Purity, integrity and molecular weight of lyophilized proteins were confirmed by mass spectrometry (SPARC BioCentre, Hospital for Sick Children). Protein was stored lyophilized until use.

5.3.3. ELP_3 membrane preparation

Recombinant ELP_3-based membranes were prepared via coacervation and subsequent crosslinking by genipin as described previously (123). Briefly, purified and lyophilized ELP_3 was dissolved in 0.15 M sodium borate buffer (pH 8) to a final concentration of 10 mg/mL. The ELP_3 solution was incubated for 2 hours at 4 ^oC to allow complete dissolution. ELP_3 membranes were then prepared in the wells of Lab-Tek chamber slides: ELP_3 solution was added in the wells to a final concentration of 10 mg/mL; then, NaCl and genipin were added to final concentrations of 0.8 M and 10 mM, respectively. The sample chamber slide was then carefully placed into a styrofoam support and transferred to a flat-bottomed centrifuge bucket pre-warmed at 37 ^oC. Then, the bucket was inserted into a temperature-controlled swinging-bucket centrifuge pre-warmed at 37 ^oC and was spun at 3200 rpm for 7 min at 37 ^oC. The sample slide was then immediately placed in an incubator set at 37 ^oC and left overnight for the crosslinking reaction to occur. The membranes were removed from the chamber slide by gently flushing with distilled water and stored in water at pH 7 until use.

5.3.4. In vitro mineralization of ELP_3 membranes in simulated body fluid (SBF)

SBF with ionic concentration 1.5 times higher than serum (1.5xSBF) was prepared according to Kokubo *et al.* (256), and sterilized by filtering through a 0.2 µm polyethersulfone filter (Thermo Scientific, USA). ELP_3 membranes with lateral sizes of 0.5 cm x 0.5 cm were immersed vertically in Eppendorf tubes containing 500 µL of 1.5xSBF

and stirred at a speed of 50 rpm inside an incubator at 37 ± 0.5 ^{o}C. The SBF solution was changed every 3 days to mimic the constant ion concentrations present in body fluids. The membranes were sampled at 8, 16, 24, 28, and 32 days, and rinsed in deionized water for 3 times, 20 minutes each time, to remove the salts. The samples were then dried under vacuum overnight or kept hydrated in water, as needed for following analysis.

5.3.5. Scanning electron microscopy (SEM) and energy-dispersive X-ray spectroscopy (EDS)

ELP_3 membranes incubated in 1.5 x SBF for 8, 16, 24, 28, and 32 days were characterized using a combination of SEM and EDS. Samples were mounted on an aluminium SEM stub with carbon tape, and then coated with about 20nm carbon using a EMS 150R ES carbon sputter coater (EMS, Hatfield, USA). The samples were then imaged using an Inspect F50 field emission SEM (FE-SEM) (FEI, Japan), at 15 kV operating voltage under high vacuum. EDS spectra and elemental maps were obtained at 15 kV in the regions of interest using an Octane super 60 mm^2 EDS system (EDAX Inc., USA).

Further compositional and topographical information on the minerals present in 32 day-old samples were obtained using a Regulus 8230 ultra-high-resolution FE-SEM (Hitachi, Ltd., Japan) operated at 0.8 kV. EDS spectra and elemental maps of regions of interest were obtained at 10 kV using an X-Max Extreme EDS system (Oxford Instruments, Abingdon, UK).

Cross sections of 32 day-old samples were prepared using a IM4000Plus Ar Ion Milling System (Hitachi, Ltd., Japan). Images were obtained using the Regulus 8230 FE-

SEM operating at 0.5 kV and EDS spectra were acquired using the X-Max Extreme EDS system, as above.

5.3.6. Transmission electron microscopy (TEM) and selected area electron diffraction (SAED) analyses

5.3.6.1. Sample preparation

For resin embedding, air-dried 32 day-old samples were processed through a graded acetone series (30%, 50%, 70%, 90%, 95%, and two times 100% (v/v)) for 15 minutes in each solution. The samples were then infiltrated (a) overnight with a 1:1 mixture of pure acetone and epoxy resin (EMbed-812b, DDSA, NMA, DMP-30; EMS) prepared according to the manufacturer's instructions, (b) in a 1:3 mixture for 6 hours, (c) in pure epoxy resin overnight, and (d) in pure resin two times for 60 minutes. All these steps were performed under vacuum and at room temperature. Finally, the samples were embedded in pure resin, briefly passed under vacuum to remove any air bubbles, and finally transferred into an oven at 60 ^{o}C for two-day polymerization.

5.3.6.2. Focused ion beam (FIB), TEM AND SAED

Thin lamellae of the embedded samples (~ 100 nm thickness) were prepared using an Ethos NX5000 FIB system (Hitachi Ltd., Chiyoda, Japan) and examined in a JEM-2100F field emission TEM (JEOL, Akishima, Japan) operated ar 200 kV. SAED were obtained in the TEM operating at 200 kV. The Gatan Microscopy Suite® (GMS) 3 software was used for analysis of the SAED patterns.

5.3.7. Fourier Transform infrared (FTIR) spectroscopy

FTIR spectra of dried ELP_3 membranes were collected on a Spectrum 400 FT-IR spectrometer (PerkinElmer, Waltham, USA) equipped with an attenuated total reflection (ATR) accessory and a temperature stabilized fast-recovery deuterated triglycine sulphate (FR-DTGS) detector. The spectra were collected between 400 and 1800 cm^{-1} with a resolution of 4 cm^{-1} and using 64 scans. The collected spectra were baseline corrected and then normalized based on the absorbance of the ν C=O amide I band at 1634 cm^{-1} using Spectrum software (PerkinElmer, Waltham, USA). Three samples per condition were analyzed.

5.3.8. X-ray diffraction (XRD)

XRD diffractograms of dried ELP_3 membranes were obtained using a Bruker D8 Discover X-ray diffractometer (Bruker AXSS Inc., Fitchburg, USA) equipped with a Cu Kα source ($K\alpha_1$ λ=1.54 Å), and a monochromator operated at 40 mV and 40 mA within the 10^o to 80^o range in 2θ. Three samples per condition were analyzed.

5.3.9. X-ray photoelectron spectroscopy (XPS)

The atomic composition of the ELP_3 membranes was characterized using a Thermo Scientific Kα spectrometer (ThermoFisher Scientific, USA), equipped with an Al Kα X-ray source (1486.6 eV, 0.843 nm), a micro-focused monochromator, and an ultrahigh vacuum chamber (10^{-9}Torr). Survey scans and high-resolution spectra were acquired with an X-ray spot with a diameter of 400 μm. Three survey scans were collected for each sample, between 0 and 1200 eV with a step size of 1 eV. Elemental high-resolution scans were acquired with a step size of 0.1 eV. To prevent charging, samples were hit with a flood gun shooting low energy electrons during the measurement. For

each membrane, four points were randomly selected, and three samples were analyzed per condition. Peak fitting and quantitative analysis of the survey spectra were performed using the Thermo Advantage software (version 4.60).

5.3.10. Raman spectroscopy

The ELP_3 samples were analyzed using a Senterra Raman spectrophotometer (Bruker, Germany) equipped with 532, 633, and 785 nm diode lasers coupled with an Olympus optical microscope. The spectra were acquired using a 40x objective, in a spectrum range from 400 to 1800 cm^{-1} at a resolution of 3.5 cm^{-1}. The samples were also analyzed using a MultiRAM stand-alone FT-Raman spectrometer (Senterra, Bruker, Germany) equipped with a Nd:YAG laser sample excitation source of 1064 nm. The spectra were also acquired in a spectrum range from 400 to 1800 cm^{-1} at a resolution of 3.5 cm^{-1} The data was analyzed using OPUS software (OPUS 7.0.0, Bruker, Karlsruhe, Germany).

5.3.11. Uniaxial tensile testing

Genipin crosslinked ELP_3 membranes (0.5 x 0.5 cm) were mounted between the top and bottom grips of a Mach-1 mechanical tensile testing apparatus with a 1000 g load cell (Biosyntech, Montréal, Canada). Force-extension curves were obtained for membranes in deionized water using cycles of loading/ unloading to a strain of 25% initial resting length, L_0, and a rate of 103.6 μm/s. Membranes were preconditioned with 3 cycles of loading/ unloading and subsequently extended to break. Failure strain (extension) was calculated from strain at break as $\Delta L/L_0$, change in length normalized by the resting length of the material. Strength was measured as the stress at break, where stress was calculated as failure load/ cross-sectional area. As membranes were too thin to directly

measure cross-sectional area, normalized cross-sectional area was determined as [(dry weight/ elastin density) + dry weight x (water content/ water density)]/ L_0. Values for the density of insoluble elastin (1.3 g/m^3) and water content of genipin crosslinked ELPs (2.13%) were previously calculated (257). Dry weight of samples (i.e. mg protein exposed between grips) was determined using a ninhydrin colourimetric assay (Sigma Aldrich) following the method of Starcher (258) after overnight hydrolysis (HCl, 6N, 100C) of samples and ELP_3 standards of known concentration. Data are expressed as mean ± standard deviation, n=5-8. Statistical analyses were performed using an unpaired student's t-test with Welch's correction for unequal variance.

5.3.12. Ca K-edge near edge X-ray absorption fine structure (Ca K-edge NEXAFS) spectroscopy

Ca-P phases present in ELP_3 membranes were characterized using Ca K-edge NEXAFS spectroscopy at the bulk-XAFS end-station of the Soft X-ray Microcharacterization Beamline (SXRMB) at the Canadian Light Source (CLS), Saskatoon, Saskatchewan. Powdered reference compounds of known chemical compositions were also analyzed, including ACP, OCP, DCPD, HA, CHA, β-TCMP. We also analyzed ELP_3 membranes incubated in 3.8 mM of $CaCl_2$ solution (ELP_3-Ca^{2+}), as possible models of the early stages of calcification with only Ca ions adsorbed on the ELP_3 matrix. Spectra were collected with energies between 1.7 and 10 keV and with a photon beam spot size of 2 mm x 6 mm. Reference spectra were collected in transmission mode while spectra of ELP_3 membranes were collected in fluorescence mode. The spectra were calibrated, aligned, and normalized using Athena software (Demeter 0.9.20). Principle component analysis (PCA) was first performed on the spectra to avoid

using an excessive number of references in the fitting. Then, linear combination fitting (LCF) was performed on the NEXAFS regions of the spectra using combinations of the reference samples selected by the PCA. The quality of the fits was evaluated by the R-factor value: values below 0.02 indicate that the fitting results are satisfactory (227). For each spectrum, the best LCF combination (i.e. the combination giving the lowest R-factor) was retained. PCA and LCF were performed using Athena software.

5.3.13. Statistical analysis

Statistical data analysis was performed using GraphPad software, Inc. (2016). Mean values were expressed as average ± standard deviation. Statistical analysis on mean values was performed by Student's t-test or one-way ANOVA test followed by Tukey's test correction for multiple comparisons, and $p < 0.05$ was considered significant.

5.4. Results and Discussion

Recombinantly expressed ELP_3 contains an alternating arrangement of crosslinking and hydrophobic domains that are simplified representations of repetitive sequence motifs commonly found in human tropoelastin (Figure 5S.1) (259). ELP_3 coacervates and forms a protein-rich liquid phase in presence of NaCl at 37 ^{o}C (120). After overnight crosslinking with genipin, we obtain elastic dark blue ELP_3 membranes (see inset in Figure 5.1.A). SEM images show that the membranes mainly consist of clusters of spherical droplets about 1 to 6 μm in diameter, either smooth or rough (Figure 5.1). Thin filaments (about 5 nm in diameter) and fiber-like structures (about 100 to 300 nm in diameter) link the droplets to one another (Figure 5.1). The atomic composition of droplets, thin filaments, and fiber-like structures are not significantly different (Figure 5S.2

and Table 5S.1). The spherical droplets were already reported in *in vitro* assembly of both full-length tropoelastin (89, 91, 122, 252) and ELPs (90, 119, 120, 257, 260). It was shown that droplets grow by coalescence over time and that droplet size and long-term morphology can be influenced by the primary sequence of the ELP used (90). Similar tropoelastin-rich globules of 1 to 6 μm diameter are a feature of elastogenesis *in vivo* where they are transformed over time into a more fibrous appearance (261, 262). Both thin filaments and fibers seem to be more advanced self-assembled structures compared to ELN droplets, and are similar in morphology and diameter to those observed in previous studies of elastogenesis (91, 263, 264).

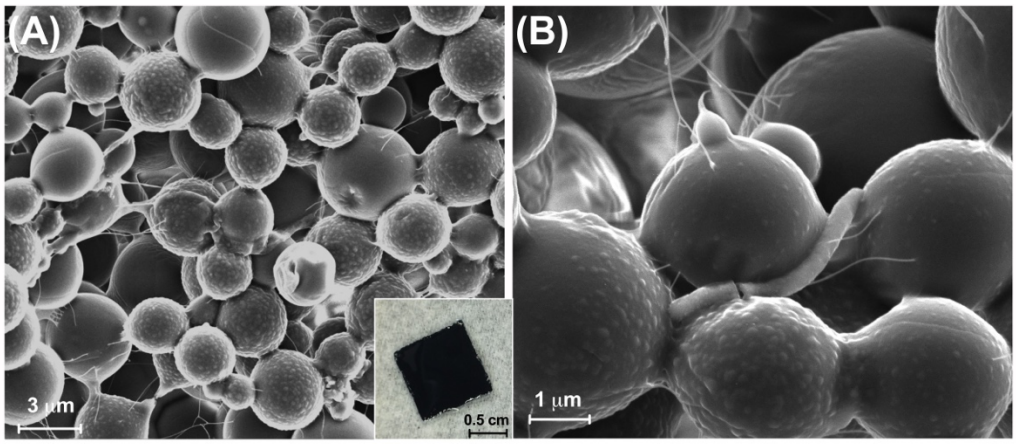

Figure 5.1. (**A-B**) Scanning electron microscopy (SEM) images of ELP_3 membranes. Inset figure on (**A**) is a photo of a hydrated ELP_3 membrane.

After 8 days of incubation in 1.5 x SBF, relatively few minerals deposits are observed on the droplets (Figure 5.2.A and Figure 5.2.B). Ca/P ratios determined by EDS vary between 1.3 and 1.5 (Figure 5S.3.A and Figure 5S.3.B; Table 5S.2). Although EDS is more reliable on flat and homogenous samples due to the influence of the surface roughness on the x-ray intensity, these results suggest that minerals are composed of

mixed Ca-P phases but do not contain HA or CHA at this stage (Table 5S.3) (179). Several spots show much higher Ca/P ratios (Figure 5S.3.A, spots 1 and 3) or only Ca and no P (Figure 5S.3.B, spot 6) suggesting that Ca ions are adsorbed on the ELN membranes. Overall, elemental analysis on the filaments and fiber-like structures show higher atomic percentages of Ca and P than on the droplets (Figure 5S.3.B, spots 4 and 5), implying that they are the first structures to be mineralized. This is confirmed by lower N/Ca ratios measured on these spots (Table 5S.2). However, the Ca/P ratios are similar to those found on the globules, indicating that the minerals formed on these structures are also a mix of non-apatitic Ca-P phases (Figure 5.2.B; Figure 5S.3.A and Figure 5S.3.B; Table 5S.2).

No significant changes in mineral deposition and Ca/P ratios are observed after 16 days, suggesting that apatite phases are still not formed at this stage (Figure 5.2.C and Figure 5.2.D; Figure 5S.3.C and Figure 5S.3.D; Table 5S.4); however, the filaments and fiber-like structures are much more mineralized than at 8 days (Figure 5S.3.C, spots 1 and 2 and Figure 5S.3.D, spots 4 and 6).

Overall, the SEM/EDS data on samples incubated in SBF for 8 and 16 days show that Ca ions are first adsorbed on the ELP_3 membranes. This finding is in agreement with some of the early *in vitro* studies showing that mineral formation starts with the initial adsorption of Ca on the ELN matrix (108, 109). This also agrees with the results of our *in vivo* study showing that medial calcification is initiated by the deposition of Ca ions (250). These results also show that mineral deposition first occurs on the filaments and fiber-like structures.

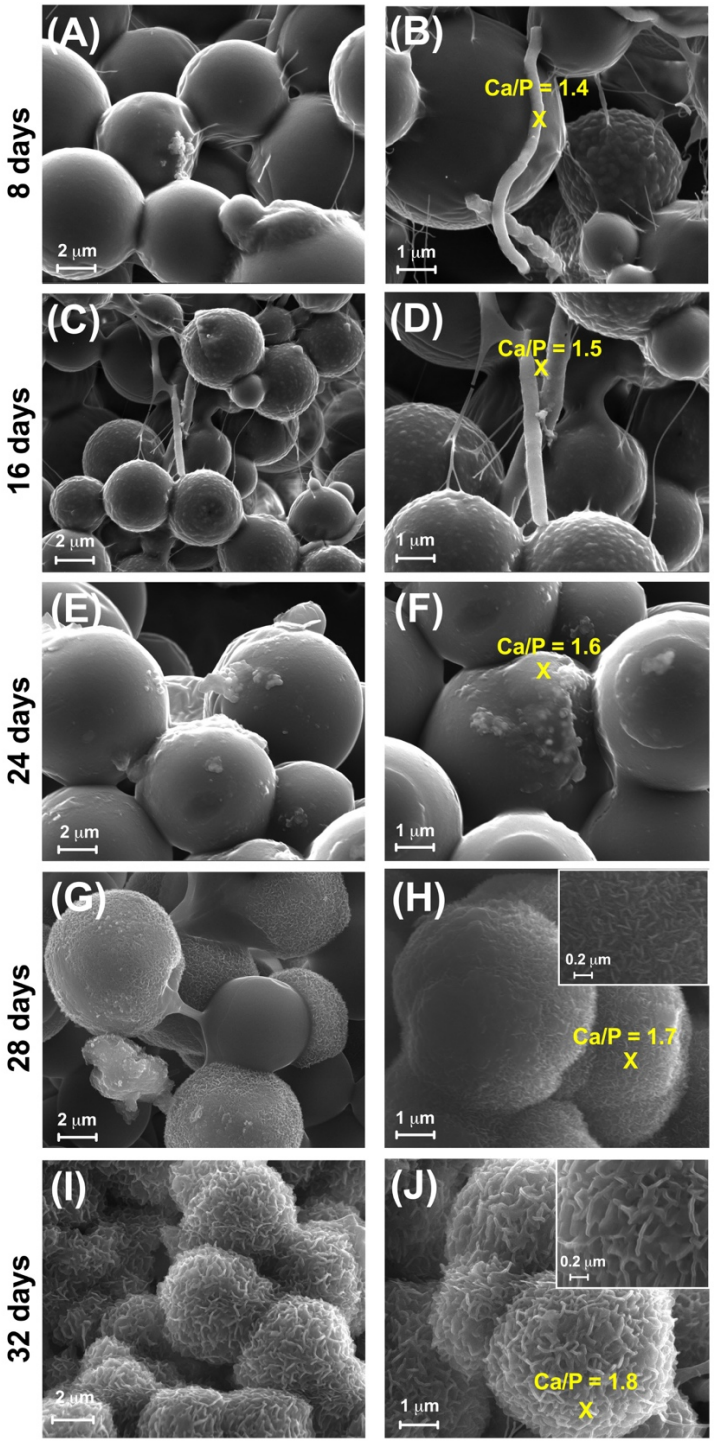

Figure 5.2. Scanning electron microscopy (SEM) images of ELP_3 membranes after incubation in 1.5 x SBF for (**A** and **B**) 8, (**C** and **D**) 16, (**E** and **F**) 24, and (**G** and **H**) 28 days. The Ca/P ratios indicated on **B**, **D**, **F**, and **H** are based on elemental atomic percentages obtained by energy-dispersive x-ray spectroscopy (EDS). Inset on **H** is an SEM image showing the morphology of the minerals deposited on the ELP_3 membranes after 28 days.

This finding emphasizes that ELN is highly vulnerable to calcification. Indeed, to perform its function and provide elasticity and flexibility to blood vessels, ELN has to be assembled into fibers; however, these self-assembled fibers and filaments seem to be the structures that are more prone to mineralization, as if this configuration exposed a larger fraction of nucleation sites for interaction with Ca ions. Further work will be needed to understand this intriguing result.

After 24 days, more minerals form on the droplets, with Ca/P ratios going from 1.5 to 1.7, implying that at this stage the minerals are likely composed of both non-apatitic and apatitic phases (Figure 5.2.E and Figure 5.2.F; Figure 5S.3.E and Figure 5S.3.F; Table 5S.5). After 28 days, minerals in the form of thin flakes in radial arrangement are observed on the droplets (Figure 5.2.G and Figure 5.2.H). This is the typical microstructure of HA *in vitro* and is reported in many other studies (265-268). Except for few spots where Ca/P ratios are lower than 1.6 (Figure 5S.4.A, spots 1 and 2), most of the Ca/P ratios are in the range of HA and CHA, suggesting that more apatite phases are formed (Figure 5S.4.A and Figure 5S.4.B; Table 5S.6). However, not all the globules are coated by HA flakes, and some of them are only partially covered (see spot 1 on Figure 5S.4.A). The filaments and fiber-like structures contain very high atomic Ca and P percentages and are highly mineralized (Figure 5S.4.B, spot 5).

After 32 days, all the globules are covered by aggregates of HA and the Ca/P ratios are all higher than 1.6, indicating that at this stage the minerals are mainly composed of HA and CHA (Figure 5.3.A and Figure 5.3.E; Figure 5S.4.C and Figure 5S.4.D; Table 5S.7). The globules, filaments, and fiber-like structures contain very high Ca and P atomic percentages, and thus very low N/Ca ratios (Table 5S.7). EDS mapping reveals that Ca,

P, and oxygen (O) co-localize (Figure 5.3.B-Figure 5.3.D) and are primarily present within the mineral particles (seen as lighter areas in the backscattered electron image; Figure 5.3.A). On the contrary, carbon (C) and nitrogen (N) are mainly localized within the parts of the globules that are not coated by HA (Figure 5S.5.B and Figure 5S.5.C, respectively). Cross section backscattered electron images of 32 day-old ELP_3 membranes show lighter regions only around the ELN droplets, thus suggesting that the minerals are not penetrating inside the globules (Figure 5.3.F and Figure 5S.6.A). This is further confirmed by EDS analysis showing Ca and P only on the external surface of the ELP_3 globules (Figure 5S.6.B and Figure 5S.6.C). This indicates that the mineral layers deposited on the surface prevent the diffusion of Ca and P ions into the ELN globules from the SBF solution.

High-resolution TEM images of FIB sections from 32 day-old ELP_3 membranes confirm the presence of rod-shaped mineral crystals deposited on the ELN droplets (Figure 5.3.G). At even higher resolution, several sets of lattice fringes with predictable spacings can be seen over a whole area of minerals (Figure 5.3.H). The SAED patterns reveal diffraction rings corresponding to poorly crystalline HA, similar to what observed in native bone (Figure 5.3.I) (JCPDS# 09-0432) (269).

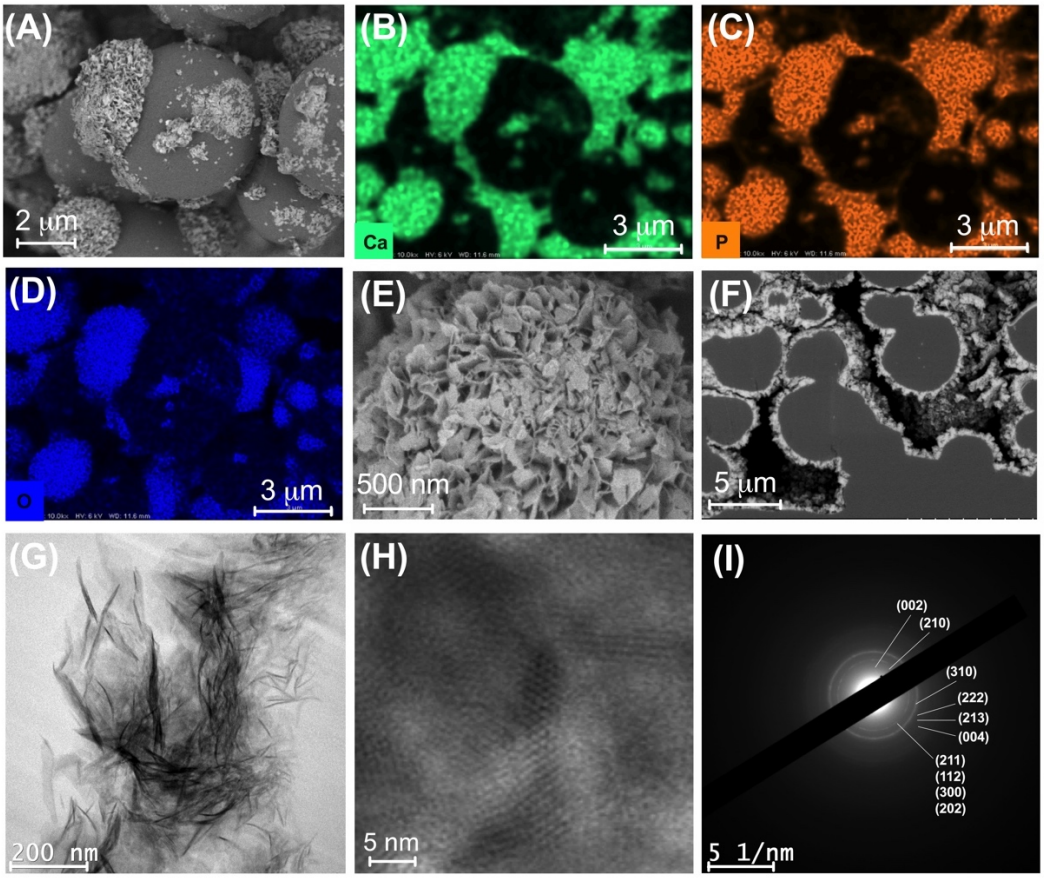

Figure 5.3. (**A – F**): Scanning electron microscopy (SEM) image (**A**) and energy-dispersive x-ray spectroscopy (EDS) elemental mapping for Ca (**B**), P (**C**), and O (**D**) of ELP_3 membranes after incubation in 1.5 x SBF for 32 days. (**E**) High magnification SEM image showing the morphology of the minerals deposited on the ELP_3 membranes after 32 days. (**F**) Cross section view of ELP_3 membranes incubated in 1.5 x SBF for 32 days. (**G** and **H**) High-resolution transmission electron microscopy (TEM) images of an ultrathin section of ELP_3 membranes incubated in 1.5 x SBF for 32 days showing the crystals deposited on the membranes. (**I**) Selected area electron diffraction (SAED) image from mineral region imaged in (**G**).

We further analyzed the mineral phases present in the calcified ELP_3 samples, their crystallinity, and their amounts by FTIR, XRD, and XPS (Figure 5.4.A-Figure 5.4.D). FTIR spectra of ELP_3 membranes incubated in SBF show the ν_1 phosphate band at 963 cm^{-1} and the degenerate ν_3 vibration at 1030 and 1109 cm^{-1} related to HA starting from 24 days; they become more and more visible with time (Figure 5.4.A) (191, 240). While the ν_3 peak at 1030 cm^{-1} is characteristic of highly crystalline apatite, the ν_3 peak at 1109 cm^{-}

^{1} has been assigned to poorly crystalline apatite (191, 270, 271). Thus, we estimated mineral crystallinity by analyzing the area ratio 1030/1109 cm^{-1} (272). This ratio significantly increases from 24 to 32 days, suggesting that the minerals become more crystalline over time (Table 5S.8). By comparing the area underlying the ν_3 phosphate peak between 1030 and 1109 cm^{-1} with that of the $\nu_{C=O}$ peak for amide I, we can also analyze the changes in inorganic to organic ratio over time (Table 5S.8). The ratios found after 8 and 16 days are very low and do not significantly increase over time. After 16 days, the inorganic to organic ratios significantly increase over time, thus showing that overall more minerals are deposited. A complete list of peak assignments is presented in Table 5S.9.

XRD spectra confirm the presence of HA starting from 24 days (Figure 5.4.B; see the broad peak centered at about 32° that is the combination of the peaks corresponding to the crystallographic planes (211), (121), and (202) of HA) (JCPDS# 09-0432). In addition to this peak, after 32 days, the XRD spectra show six other peaks corresponding to the planes (002), (210), (212), (222), (213), and (304) of HA. The presence of these peaks only after 32 days confirms that the HA crystallinity increases with time (238). We estimated the crystallinity of the HA deposits by calculating the full width at half maximum (FWHM) of the peak corresponding to the HA planes (211), (121), and (202); this value inversely correlates with HA crystallinity. FWHM values significantly decrease between 24 and 32 days (1.4 ± 0.1 vs 1.0 ± 0.2, $p = 0.0059$), confirming the increase in mineral crystallinity.

Although only C, O, and N are present on the XPS survey spectra of ELP_3 membranes before incubation in SBF, the XPS surveys of samples immersed in SBF show additional Ca and P (Figure 5S.7; Table 5S.10). This confirms the presence of Ca-P phases in the samples incubated in 1.5 x SBF starting from 8 days. While the N/Ca ratios are constant between 8 and 16 days, they significantly decrease between 16 and 32 days, thus confirming that mineral amounts increase significantly after 16 days (Figure 5.4.C; Table 5S.10). Also, average Ca/P ratios significantly increase over time after 16 days, with values increasing from 1.4 ± 0.1 to 1.8 ± 0.2 after 32 days incubation (Figure 5.4.D; Table 5S.10). This increase is correlated to a change in Ca-P phases (Table 5S.3) and is in agreement with changes in mineral morphologies and Ca/P ratios observed by SEM/EDS. Overall, these data suggest that more apatite is formed over time.

We attempted to use Raman spectroscopy to characterize the minerals present in the ELP_3 samples; however, we were not able to get a good Raman signal due to a large fluorescent background (Figure 5S.8). ELN is one of the main fluorophores in biological tissues (273), and several other studies have already reported difficulties in getting Raman spectra of ELN samples due to the high fluorescence background (274, 275).

Tensile tests on non-calcified ELP_3 membranes show that the mechanical properties of the membranes are similar to native elastic fibers, with ultimate tensile strength (~ 0.8 MPa) of the same order of magnitude to that of native elastic fibers (Figure 5.4.E) (276).

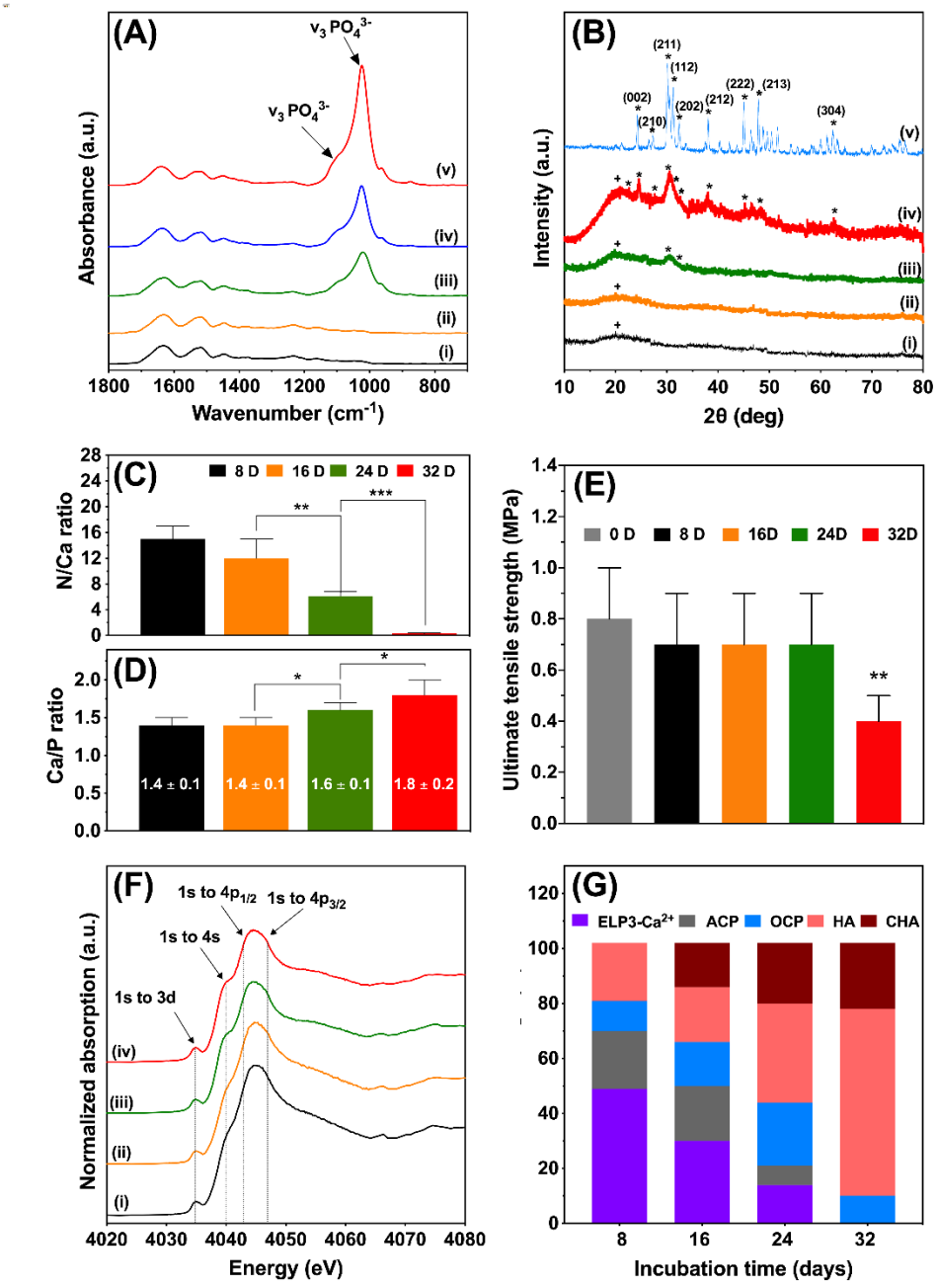

Figure 5.4. (**A**) Representative Fourier transform infrared (FTIR) spectra of ELP_3 membranes after incubation in 1.5 x SBF for (i) 8, (ii) 16, (iii) 24, (iv) 28, and (v) 32 days. Arrows show ν_3 PO_4^{3-} vibration bands discussed in the text. The spectra were normalized based on the absorbance of the ν C=O amide I band at 1634 cm^{-1}. For each time point, 3 samples were analyzed. (**B**) Representative x-ray diffraction (XRD) patterns of ELP_3 membranes after incubation in 1.5 x SBF for (i) 8, (ii) 16, (iii) 24, and (iv) 32 days, and from (v) synthetic HA. (+) and (*) signs indicate the peaks corresponding to ELN and HA, respectively. The labels on the spectra refer to the HA planes present on ELP_3 membrane samples. For each time point, 3 samples were analyzed. N/Ca (**C**) and Ca/P ratios (**D**) determined based on x-ray photoelectron spectroscopy (XPS) surveys in ELP_3

membranes incubated in 1.5 x SBF. For each time point, 3 samples were analyzed, and 4 XPS surveys were collected at different points for each sample. One-way ANOVA test followed by Tukey test correction for multiple comparisons were used for statistical analysis. * indicate significant differences between the different time points, with * = P< 0.05, ** = P< 0.005, and *** = P< 0.0001 (**E**) Ultimate tensile strength calculated based on the stress-strain curve in control samples and ELP_3 membranes incubated in SBF. T-test was used for statistical analysis. ** indicate significant differences with the 32-days old samples, with P< 0.02. (**F**) Representative Ca K-edge near-edge x-ray absorption fine structure spectroscopy (NEXAFS) spectra of ELP_3 membranes incubated in 1.5 x SBF for (i) 8, (ii) 16, (iii) 24, and (iv) 32 days. The labels on the spectra refer to the different electronic transitions. (**G**) Relative percentages of ELP_3-Ca^{2+}, ACP, OCP, HA, and CHA in ELP_3 membranes incubated in 1.5 x SBF determined by linear combination fitting (LCF) based on the reference spectra. Two samples were analyzed for each time point and three spectra by sample were collected.

Both ultimate tensile strength and extension (~ 0.5 mm/mm) values are in the normal range for materials formed from both ELPs and tropoelastin (Figure 5.4.E and Figure 5S.9, respectively) (120, 257, 277, 278). Results on calcified samples show no significant differences in mechanical properties for the ELP_3 samples incubated in SBF for 8, 16, and 24 days, compared to the non-incubated membranes. However, both the extension and ultimate tensile strength of the calcified ELP_3 membranes decrease after 32 days of incubation in SBF (Figure 5.4.E and Figure 5S.9). This correlates well with the drastic increase both in mineral amount and crystallinity.

Overall, SEM/EDS, FTIR and XPS show that the amount of mineralization significantly increases over time from 16 to 32 days. No significant increase in mineralization is shown by FTIR and XPS between 8 and 16 days; however, SEM/EDS analyses on the different ELN structures reveal that while the amounts of Ca and P are not significantly different between 8 and 16 days on the ELN droplets, they significantly increase both on the thin filaments and fiber-like structures, which are the first ones to mineralize. Both SEM/EDS and XPS show that the increase in mineral amount over time is associated with an overall

increase in Ca/P ratios, thus suggesting a change in mineral phases. On average, Ca/P ratios lower than 1.6 are reported before 24 days, indicating non-apatitic phases. Both techniques show that after 24 days, apatite phases dominate with Ca/P ratios higher than 1.6. The ratios further increase with time, implying that more apatite is formed. This is further confirmed by FTIR and XRD, which show HA only after 24 days and an increase in mineral crystallinity over time. All techniques show a drastic difference in mineral amount and crystallinity after 32 days. This is supported by the significant loss of mechanical resistance of the ELP_3 membranes only in the 32 day-old samples.

While SEM/EDS, FTIR, XRD, and XPS show that overall minerals evolve from non-apatitic to more crystalline apatite phases over time, these techniques cannot determine the nature of Ca-P phases present in the calcified ELP_3 membranes. To identify and quantify the mineral phases present in the samples, we further analyzed the calcified ELP_3 membranes using Ca K-edge NEXAFS (Figure 5.4.F and Figure 5.4.G). NEXAFS analyzes how x-rays absorption by an atom is affected by its neighboring atoms, thus acting as local chemical/structural probe. NEXAFS is well suited for our samples since crystallinity is not required (224); thus, enabling identification of the amorphous and poorly crystalline phases present in the ELP_3 membranes, in addition to the crystalline apatite phases.

To identify the compounds present in ELP_3 membranes, we selected as reference samples: ELP_3 membranes incubated in Ca solution (ELP_3-Ca^{2+}), ACP, OCP, DCPD, β-TCMP, HA, and CHA. We then performed principle component analysis (PCA) and linear combination fitting (LCF) following the procedure explained in Section 1 of the supplemental material. NEXAFS spectra of reference samples and ELP_3 membranes

show four features that are typical of Ca-P compounds (Figure 5S.10 and Figure 5.4.F, respectively) (225, 226). The small feature at the pre-edge around 4035 eV is due to electronic transitions between 1s and 3d orbitals. The absorption edge, the most intense peak, shows a shoulder around 4040 eV assigned to 1s to 4s transitions, and a more intense double peak centered at around 4045 eV, which is assigned to 1s to $4p_{1/2}$ and 1s to $4p_{3/2}$ transitions (225, 226). The features at higher energies are due to multiple scattering contributions.

The LCF results and the associated R-factors are presented in Table 5S.11 and Figure 5.4.G. All the R-factor values are < 0.02, thus suggesting that all the fits are satisfactory (227). The results show that the calcified ELP_3 samples are composed of a mixture of adsorbed Ca ions (ELP_3 -Ca^{2+}), ACP, OCP, HA, and CHA. DCPD and β-TCMP were not detected in any sample.

After 8 days of incubation in SBF, nearly 50% of the Ca atoms show a neighboring environment like that of Ca atoms in ELP_3 membranes immersed in $CaCl_2$ solution, thus indicating that about 50% of the Ca present is just adsorbed on the samples. The other Ca atoms are present as ACP (21 ± 4), OCP (11 ± 2), and HA (21 ± 3) (Figure 5.4.G). From 8 to 16 days, the amount of adsorbed Ca ions significantly decreases, the amounts of ACP and HA remains the same, OCP increases, and CHA is formed. After 24 days, there is a drastic change in mineral phase proportions: while the amount of adsorbed Ca ions and ACP significantly decreases, both HA and CHA drastically increase. Meanwhile, the amount of OCP slightly increases. Finally, in the 32 day-old samples, the Ca detected is mainly present in apatitic structures (HA and CHA), and only a small amount of OCP can be detected. Adsorbed Ca ions and ACP are not present anymore at this stage. These

results confirm the SEM and EDS data, showing that while the fraction of Ca in apatite phases increases with time, the amounts of ELP_3-Ca^{2+}, ACP, and OCP decrease. This suggests that ACP and OCP are the precursor phases of apatite in this *in vitro* model of medial calcification.

The presence of HA and CHA in our samples is in agreement with the literature since they are the most abundant Ca-P phases found in both physiological (176, 220) and pathological (171, 172, 175, 182) calcifications. HA is the most thermodynamically stable Ca-P phase at physiological pH; however, other mineral phases that are amorphous or poorly crystalline can also form under these conditions (181). In pathological calcifications, it was shown that ACP, OCP, DCPD, and β-TCP are the main phases that can be formed and transformed into HA (182).

The finding of ACP and OCP as precursor phases is in line with our previous study where both ACP and OCP were found in medial calcification of mice arteries (250). Both ACP and OCP have been identified as precursors of biological apatite in normal calcified tissues, such as bone and enamel (190, 198, 220, 279). Although ACP was described as one of the main precursor phases in arterial calcification (182), the presence of OCP in arterial calcification was first reported in our recent *in vivo* study (250). The use of highly sensitive synchrotron-based NEXAFS spectroscopy may explain why we were able to identify OCP both in our *in vivo* study and in this present work.

We did not find either DCPD or β-TCMP in our samples. Although DCPD was identified as a precursor phase in valve calcification (202, 203), it was never reported in arterial calcification. This can be explained by the different molecular mechanisms in arterial and valve calcifications, which may lead to the formation of different precursor phases of

apatite. β-TCP was reported in two studies of uremia-related medial calcification (193, 204) but was never detected in non-uremic patients. The presence of β-TCMP in human uremic minerals may be due to the high magnesium (Mg) concentration in the dialysis solution. In rat models of uremia-related arterial calcification, vitamin D treatment used to induce calcification stimulates the gastrointestinal absorption of Mg and thus leads to the formation of β-TCMP. Since ion concentration in SBF matches that of serum and there is no excess of Mg, it is not surprising that we did not detect β-TCMP in our samples.

5.5. Conclusion

Using genipin crosslinked ELP_3 membranes we show that mineral deposition on ELP_3 membranes happens through a precise series of events starting with the adsorption of Ca ions, in agreement with our *in vivo* findings (250). Fibers and filaments mineralize first, showing that the fiber-like nature of elastin makes it prone to mineralization. Ca-P phases form and evolve over time on ELP_3 membranes similarly to what was previously reported in calcified mice arteries (250), showing that a model based on ELP_3 membranes immersed in SBF captures this crucial *in vivo* finding.

This model could be used in the future to study hypotheses related to arterial calcification mechanisms and to test drugs designed to stop or revert calcification. For example, by changing the ELP sequence and analyzing the interactions between different ELP membranes with Ca and P ions, the sequence(s) in ELN that are involved in mineral nucleation could be investigated. This *in vitro* model could also be used to understand the interactions between ELN and calcification inhibitors, leading to design and testing of new therapeutic agents to block the initiation and progression of medial calcification.

Finally, this study further shows the power of a material science approach to understand vascular calcification and highlights the importance of NEXAFS in mineral analysis.

5.6. Acknowledgments

We acknowledge support from the Canadian Light Source (CLS), which is supported by the Canada Foundation for Innovation, the Natural Sciences and Engineering Research Council of Canada (NSERC) the University of Saskatchewan, the Government of Saskatchewan, the Western Economic Diversification Canada, the National Research Council Canada, and the Canadian Institutes of Health Research. We also thank Dr Yongfeng Hu and Dr Qunfeng Xiao of the CLS for their help with data analysis and technical support. We also acknowledge the Canada Research Chair foundation, the Heart and Stroke Foundation and NSERC for providing funding for this research, and Prof. Monzur Murshed for very useful scientific discussions. We thank Katia Ponce for expert technical assistance in sample embedding and the Hitachi High Technologies America for assisting with SEM analyses and preparation of lamellae for TEM characterization. TEM images was taken at the $(CM)^2$ center of the Polytechnique Montreal.

5.7. Funding sources

This work was supported by the Heart and Stroke Foundation, the Jacques de Champlain Award, the Fond Québécois de la Recherche sur la Nature et les Technologies (FQRNT), the Canada Research Chair Foundation, the Center for Self-Assembled Chemical Structures, the Canadian Institutes of Health Research (CIHR), the

Réseau de Recherche en Santé Buccodentaire et Osseuse (RSBO) doctoral award, and the McGill Engineering Doctoral Award (MEDA).

5.8. Supplemental material

5.8.1. Section 1: Detailed methods

5.8.1.1. Determination of the inorganic to organic ratio by Fourier Transform Infrared (FTIR) Spectroscopy

We analyzed changes in mineral amount by calculating the inorganic to organic ratio, i.e. the ratio between the areas under the peaks relative to the mineral component and those relative to the organic matrix. We choose the v_3 phosphate peak between 1030 and 1109 cm^{-1} as the mineral marker, and the $v_{C=O}$ band at 1634 cm^{-1} as organic marker since it is well defined on all the spectra.

The inorganic to organic ratio is defined as: $A_{1030\text{-}1109}/A_{1634}$ (i)

where A_x is the area underneath the peak at the wavenumber x

The peak area calculation used to quantify the inorganic to organic ratio was performed by applying an integration profile to all spectra, i.e. by calculating the areas between two manually selected points corresponding to the first and the last point of the peak. Only the area above the baseline was included in the measurements.

5.8.1.2. Ca K-edge Near Edge X-ray absorption fine structure (Ca K-edge NEXAFS) spectroscopy

Spectra acquisition

To identify and quantify the Ca-P phases present in the samples, we applied NEXAFS spectroscopy. It is a synchrotron-based technique that allows analyzing how x-rays are absorbed by an atom at energies near the core-level binding energies of that atom

depending on its chemical and physical environment (224). Because of crystallinity is not required for NEXAFS measurements, this technique is well suited for analysis of non-crystalline or poorly crystalline phases (224). Also, NEXAFS is more sensitive than traditional spectroscopic techniques, with a detection limit that can be as low as few ppm. Thus, NEXAFS is an excellent tool to analyze et differentiate the Ca-P phases present in our samples.

Ca K-edge spectra were collected in fluorescence mode with energies between 1.7 and 10 keV and with a photon beam spot size of 2 mm x 6 mm. The storage ring energy during data collection was 2.9 GeV ant the current around 200 mA. The X-ray beam was monochromated by Si (111) crystals with energy resolution ($\Delta E/E$) of 10^{-4}.

Data analysis

We first selected seven reference compounds (Figure 5S.10). The first one is ELP_3 membranes incubated in 3.8 mM of $CaCl_2$ solution for 16 days (ELP_3-Ca^{2+}) which may be a model of the very early stages of calcification if the Ca ions were first adsorbed on the ELP_3 matrix. The other five references are Ca species that are known to be present in pathological calcifications: amorphous calcium phosphate (ACP), octacalcium phosphate (OCP), dicalcium phosphate dihydrate (DCPD), hydroxyapatite (HA), carbonated hydroxyapatite (CHA), and β-tricalcium phosphate (β-TCP) (174, 175, 182, 193, 204, 250).

To determine and quantify the Ca-P phases in the ELP_3 samples, we performed linear combination fitting (LCF) analysis using Athena software (Demeter 0.9.20). LCF is justified because the x-ray absorption from different species in a sample is additive (280). The total absorption coefficient calculated by LCF can be written as:

$$M = \Sigma_i f_i (STD_i), \text{ (ii)}$$

where M is the least square fit to the sample spectrum, (STD_i) represents the absorption coefficient of the standard reference spectra, and f_i is the fraction of each reference spectrum in the sample spectrum, summed over the number of references, i. Thus, with appropriate standard references, LCF can identify and quantify the fraction of chemical species in an unknown sample (280).

We first performed principal component analysis (PCA) to determine which reference compounds should be excluded for the LCF fitting and thus avoid using an excessive number of standard compounds. PCA results showed that DCPD and β-TCP were not likely present in the calcified membranes. Thus, we used ELP_3-Ca^{2+}, ACP, OCP, HA, and CHA as references for the LCF analysis. We performed LCF using all the possible combinations of the selected reference compounds. We evaluated the quality of the fits using the R-factor: fitting results with R-factor values below 0.02 are considered satisfactory (227). We reported the LCF combination giving the lowest R-factor for each sample analyzed.

5.8.2. Section 2: Supplemental figures and tables

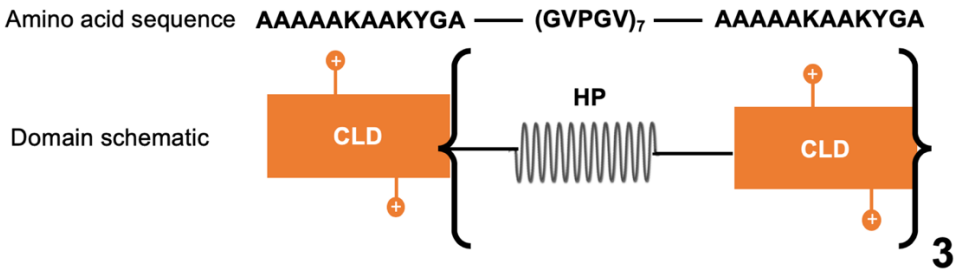

Figure 5S.1. The repeating amino acid sequence and alternating domain architecture of ELP_3. Crosslinking domains (CLD) and hydrophobic domains (HP) are represented as orange rectangles and springs, respectively.

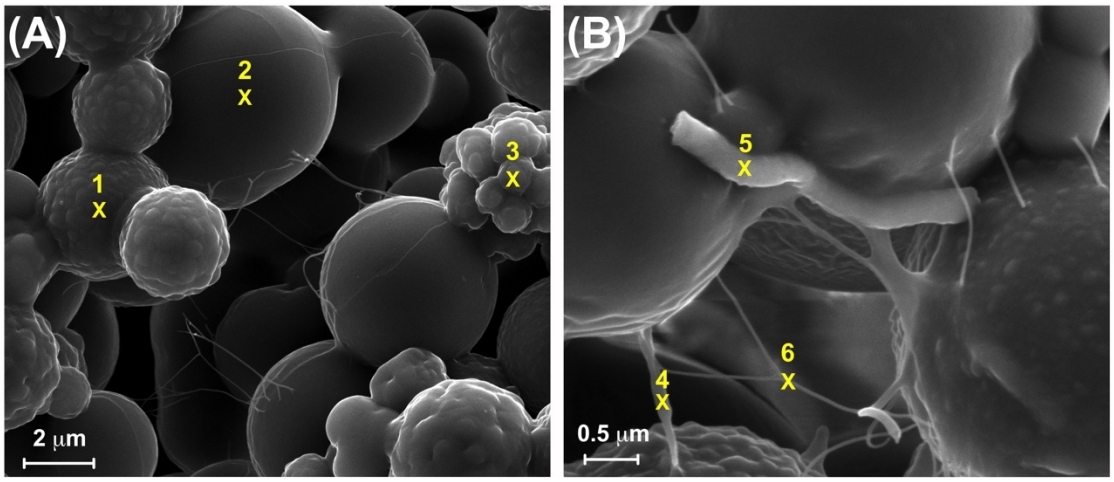

Figure 5S.2. (**A** and **B**) Scanning electron microscopy (SEM) images of non-calcified ELP_3 membranes. The numbered sites on **A** and **B** indicate the spots where energy-dispersive x-ray spectroscopy (EDS) spectra were collected and they correspond to the data presented in Table 5S.1.

Table 5S.1. Relative elemental atomic percentages in ELP_3 membranes non-incubated in SBF. The spots 1-6 are shown in Figure 5S.2.A and Figure 5S.2.B.

Spot	C (at%)	O (at%)	N (at%)	O/C	N/C
1	64.8	20.4	14.8	0.31	0.23
2	64.4	19.8	15.8	0.31	0.25
3	65.7	17.4	16.9	0.26	0.26
4	63.3	20.1	16.6	0.32	0.26
5	64.5	18.2	17.4	0.28	0.27
6	63.6	20.4	16.0	0.32	0.25

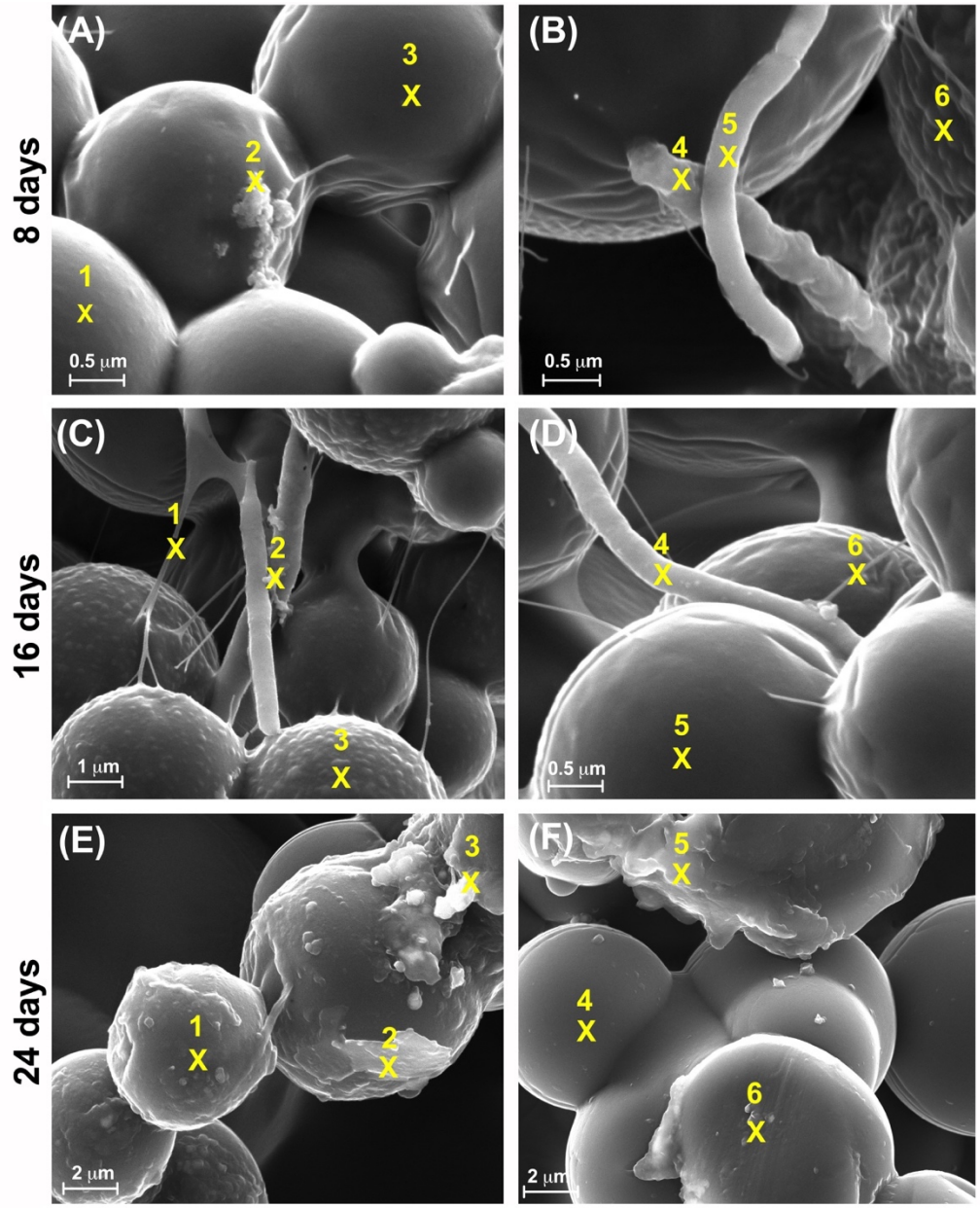

Figure 5S.3. SEM images of ELP_3 membranes after incubation in 1.5 x SBF for (**A** and **B**) 8, (**C** and **D**), and (**E** and **F**) 16 days. The numbered sites on **A** and **B, C** and **D,** and **E** and **F** indicate the spots where EDS spectra were collected and they correspond to the data presented in Table 5S.2, Table 5S.4,and Table 5S.4, respectively.

Table 5S.2. Relative elemental atomic percentages in ELP_3 membranes incubated in SBF for 8 days. The spots 1-6 are shown in Figure 5S.3.A and Figure 5S.3.B.

Spot	C (at%)	O (at%)	N (at%)	Ca (at%)	P (at%)	O/C	N/C	Ca/P	N/Ca
1	65.4	18	15.4	1.1	0.1	0.28	0.24	11	14.1
2	61.9	26.9	8.8	1.4	1.0	0.43	0.14	1.4	6.3
3	65.3	17.1	15.7	1.9	0.2	0.26	0.24	9.5	8.3
4	62.8	20.8	10.4	3.6	2.4	0.33	0.17	1.5	2.9
5	52.4	35.2	6.8	3.2	2.4	0.67	0.13	1.3	2.1
6	67.2	15.9	16.3	1.6	0	0.24	0.24	/	10.2

Table 5S.3. List of Ca-P compounds found in pathological calcifications and their Ca/P molar ratios (179).

Name	Formula	Ca/P ratio
Amorphous calcium phosphate (ACP)	$Ca_3(PO_4)_2.3H_2O$	1.5
Octacalcium phosphate (OCP)	$Ca_8H_2(PO_4)_6.\ 5H_2O$	1.33
Dicalcium phosphate dihydrate (DCPD)	$Ca(HPO_4).2H_2O$	1.0
Magnesium- substituted β-tricalcium phosphate (β-TCMP)	$Ca_{18}(Mg)_2H_2(PO_4)_{14}$	1.29
Hydroxyapatite (HA)	$Ca_{10}(PO_4)_6(OH)_2$	1.67
Carbonated hydroxyapatite (CHA)	$Ca_{10-p}(PO_4)_{6-p}(OH)_{2-p}(CO_3)_p$ (0<p<1)	> 1.67

Table 5S.4. Relative elemental atomic percentages in ELP_3 membranes incubated in SBF for 16 days. The spots 1-6 are shown in Figure 5S.3.C and Figure 5S.3.D.

Spot	C (at%)	O (at%)	N (at%)	Ca (at%)	P (at%)	O/C	N/C	Ca/P	N/Ca
1	56.8	21.4	16.2	3.4	2.2	0.38	0.29	1.5	4.8
2	38.6	41.4	4.3	9.5	6.2	1.07	0.11	1.5	0.45
3	61.1	22.2	17.3	0.6	0	0.36	0.28	/	28.8
4	43.1	32.5	9.5	8.8	6.1	0.75	0.22	1.4	1.08
5	64.8	18.8	12.5	3.8	0.1	0.29	0.19	38	3.29
6	54.3	21.4	18	3.7	2.6	0.39	0.33	1.4	4.86

Table 5S.5. Relative elemental atomic percentages in ELP_3 membranes incubated in SBF for 24 days. The spots 1-6 are shown in Figure 5S.3.E and Figure 5S.3.F.

Spot	C (at%)	O (at%)	N (at%)	Ca (at%)	P (at%)	O/C	N/C	Ca/P	N/Ca
1	47.5	39	4.5	5.6	3.4	0.82	0.09	1.6	0.80
2	38.2	41.5	8.8	7.3	4.2	10.9	0.23	1.7	1.21
3	31.8	32.5	9.9	12.4	7.3	1.02	0.31	1.7	0.80
4	62.1	25.1	10.5	2.2	1.5	0.40	0.17	1.5	4.77
5	49.5	31.3	14.5	2.8	1.9	0.63	0.29	1.5	5.18
6	60.7	21.1	10.2	4.1	2.5	0.35	0.17	1.6	2.49

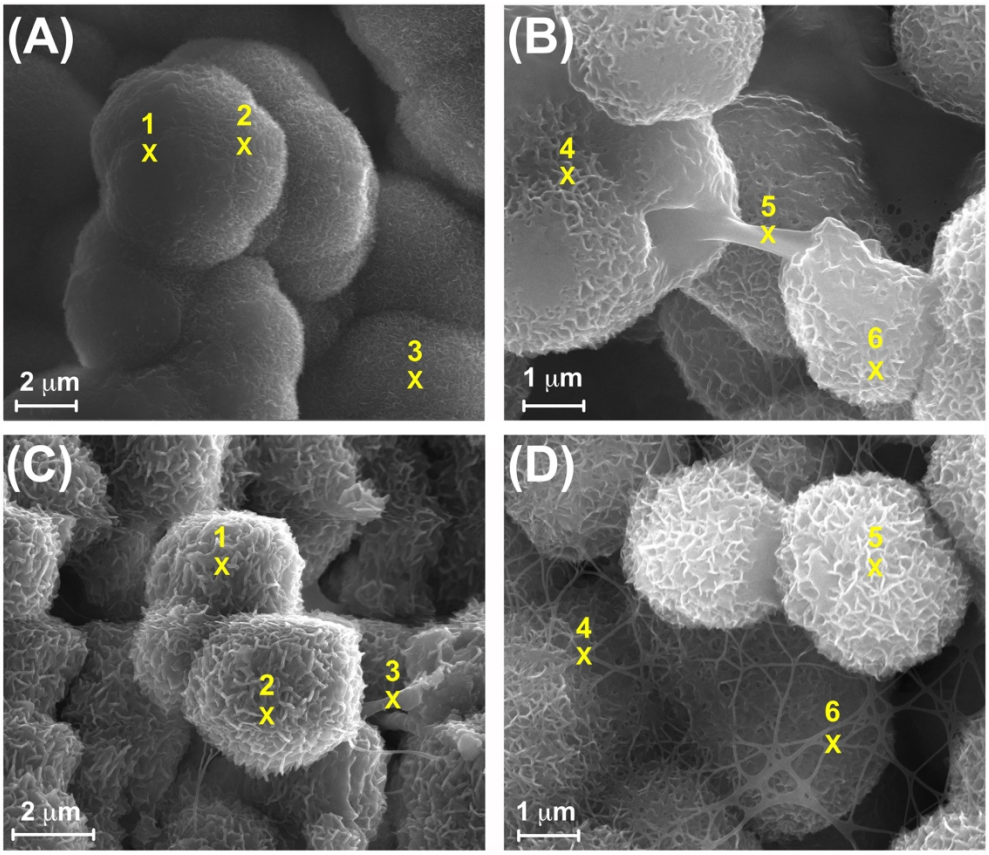

Figure 5S.4. SEM images of ELP_3 membranes after incubation in 1.5 x SBF for (**A** and **B**) 28, and (**C** and **D**) 32 days. The numbered sites on **A** and **B,** and **C** and **D** indicate the spots where EDS spectra were collected and they correspond to the data presented in Table 5S.6, and Table 5S.7, respectively.

Table 5S.6. Relative elemental atomic percentages in ELP_3 membranes incubated in SBF for 28 days. The spots 1-6 are shown in Figure 5S.4.A and Figure 5S.4.B.

Spot	C (at%)	O (at%)	N (at%)	Ca (at%)	P (at%)	O/C	N/C	Ca/P	N/Ca
1	27.4	47.0	2.7	13.9	9.0	1.72	0.10	1.5	0.19
2	23.6	50.0	1.9	14.8	9.7	2.12	0.08	1.5	0.13
3	21.3	56.8	3.8	11.7	6.4	2.67	0.18	1.8	0.32
4	19.5	58.1	3.6	11.8	7.0	2.98	0.18	1.7	0.31
5	22.6	28.9	0.1	31.4	17.1	1.28	0.01	1.8	0.01
6	20.4	52.7	1.2	16.1	9.6	2.58	0.06	1.7	0.07

Table 5S.7. Relative elemental atomic percentages in ELP_3 membranes incubated in SBF for 32 days. The spots 1-6 are shown in Figures Figure 5S.4.C and Figure 5S.4.D.

Spot	C (at%)	O (at%)	N (at%)	Ca (at%)	P (at%)	O/C	N/C	Ca/P	N/Ca
1	12.6	17.4	2.1	44.8	23.1	1.38	0.17	1.9	0.05
2	14.6	40.3	3.9	26.6	14.6	2.76	0.27	1.8	0.15
3	2.2	3.0	0.1	63.2	31.5	1.36	0.05	2.0	/
4	5.4	8.2	0.2	57.6	28.6	1.52	0.04	2.0	/
5	10.2	11.1	0.6	49.5	28.6	1.09	0.06	1.7	0.01
6	2.9	8.5	0.1	55.0	33.5	2.93	0.03	1.6	/

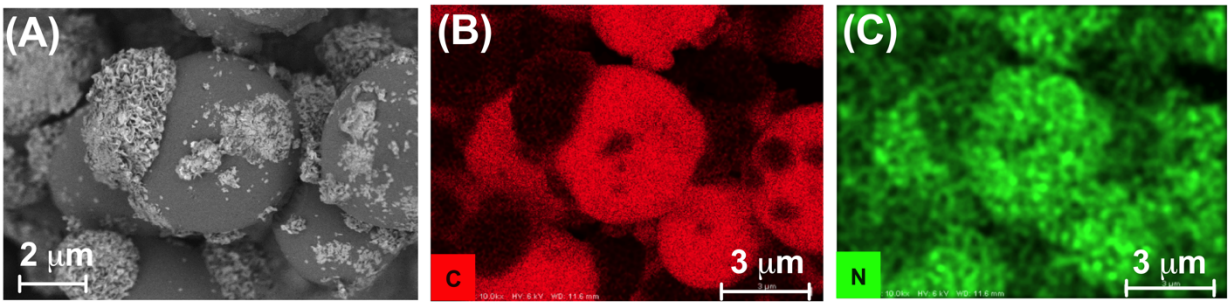

Figure 5S.5. SEM image (**A**) and EDS elemental mapping for oxygen (**B**) and nitrogen (**C**) of ELP_3 membranes after incubation in 1.5 x SBF for 32 days.

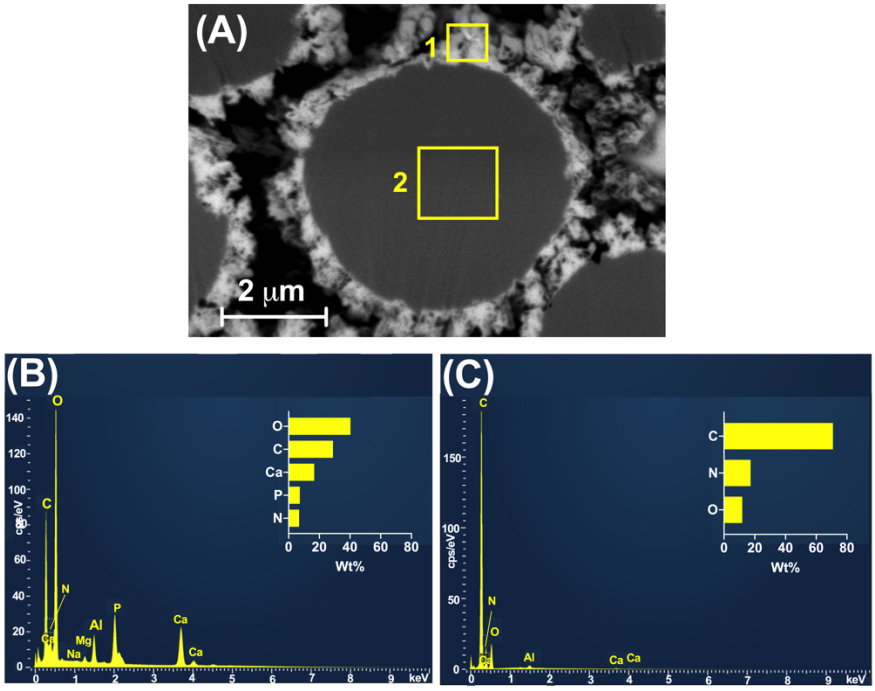

Figure 5S.6. (A) Cross section view of ELP_3 membranes incubated in 1.5 x SBF for 32 days. (**B - C**) EDS spectra collected on areas shown by rectangles 1 and 2 on (**A**), respectively.

Table 5S.8. Experimental FTIR area ratio 1030/1109 cm^{-1} and inorganic to organic ratio measured in ELP_3 membranes at 24, 28, and 32 days based on the FTIR ν_3 vibration peaks.

Time point (days)	FTIR area ratio 1030/1109 cm^{-1}	FTIR
8	/	0.1 ± 0.06
16	/	0.3 ± 0.1$^{###}$
24	1.29 ± 0.1***	3.0 ± 0.3$^{### \dagger}$
28	1.31 ± 0.2^{++}	3.7 ± 0.4$^{+++ \dagger}$
32	1.43 ± 0.2$^{*** ++}$	8.0 ± 0.3^{+++}

$^{###}$ indicates significant difference between 16- and 24- days old samples with P< 0.0001.
*** indicates significant differences between 24- and 32-days old samples with P< 0.0001.
† indicates significant differences between 24- and 28-days old samples with P< 0.05.
$^{+}$ indicates significant differences between 28- and 32-days old samples with ++ = P< 0.005, and $^{+++}$ = P< 0.0001.
Three samples per time point were analyzed.

Table 5S.9. FTIR peak assignments for calcified ELP_3 membranes.

Peak (cm^{-1})	Calcified ELP_3 membrane	References
v C=O (amide I)	1634	(281), (282), (283)
v C-N, δ N-H (amide II)	1516	(281), (282), (283)
δ CH_2	1447	(284)
δ CH_3	1372	(281), (283), (284)
δ C-H (amide III)	1236	(281)
v C-O	1162	(281)
v_3 PO_4^{3-}	1109	(282), (242), (240), (285)
v_3 PO_4^{3-}	1030	(282), (242), (240), (285)
v_1 PO_4^{3-}	963	(282), (242), (240), (285)
v_2 CO_3^{2-}	874	(282), (242), (240), (279)

v : symmetric stretching; δ : bending

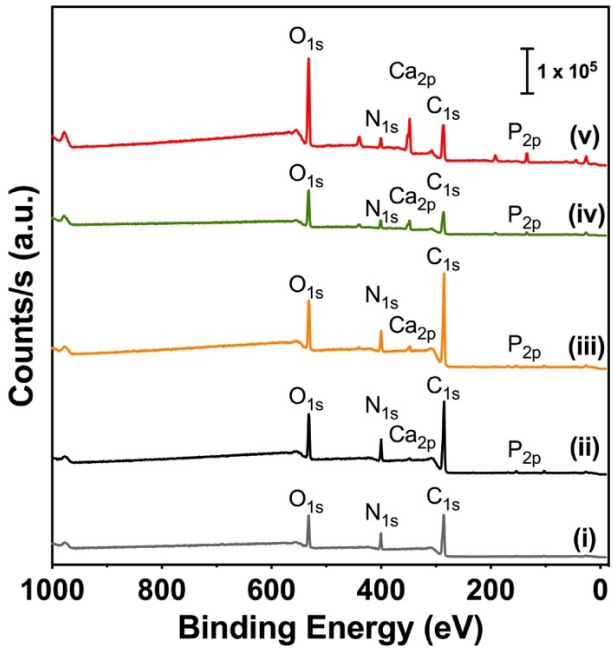

Figure 5S.7. Representative x-ray photoelectron spectroscopy (XPS) survey spectra of non-calcified ELP_3 membranes (i) and ELP_3 membranes incubated in 1.5 x SBF for (i) 8, (ii) 16, (iii) 24, and (iv) 32 days.

Table 5S.10. Relative atomic percent of C, O, N, Ca, and P, and Ca/P and N/Ca ratios on ELP_3 membranes after incubation in 1.5 x SBF, measured by XPS survey.

Time point (days)	C (at%)	O (at%)	N (at%)	Ca (at%)	P (at%)	Ca/P	N/Ca
0	68 ± 3	19 ± 3	13 ± 1	N	N	/	/
8	70 ± 1	20 ± 1	8.7 ± 0.2	0.6 ± 0.1	0.4 ± 0.1	1.4 ± 0.1	15 ± 2
16	68 ± 1	21 ± 1	9.6 ± 0.7	0.9 ± 0.2^{+}	0.6 ± 0.1^{+}	1.4 ± 0.1^{+}	12 ± 3^{++}
24	68 ± 1	19 ± 1	9.7 ± 0.4	1.6 ± 0.2$^{+\#\#\#}$	1.0 ± 0.2$^{+\#\#\#}$	1.6 ± 0.1$^{+\ \#}$	6.1 ± 0.7$^{++\#\#\#}$
32	57 ± 6	32 ± 5	1.8 ± 0.3	6.0 ± 0.4$^{\#\#\#}$	3.8 ± 0.3$^{\#\#\#}$	1.7 ± 0.1$^{\#}$	0.3 ± 0.1$^{\#\#\#}$

+ indicates significant differences between 16- and 24-days old samples with + = P< 0.05 and ++ = P< 0.005
# indicates significant differences between 24- and 32-days old samples with # = P< 0.05 and ### = P< 0.0001
For each time point, 3 samples were analyzed and 4 surveys were taken at different spots for each sample

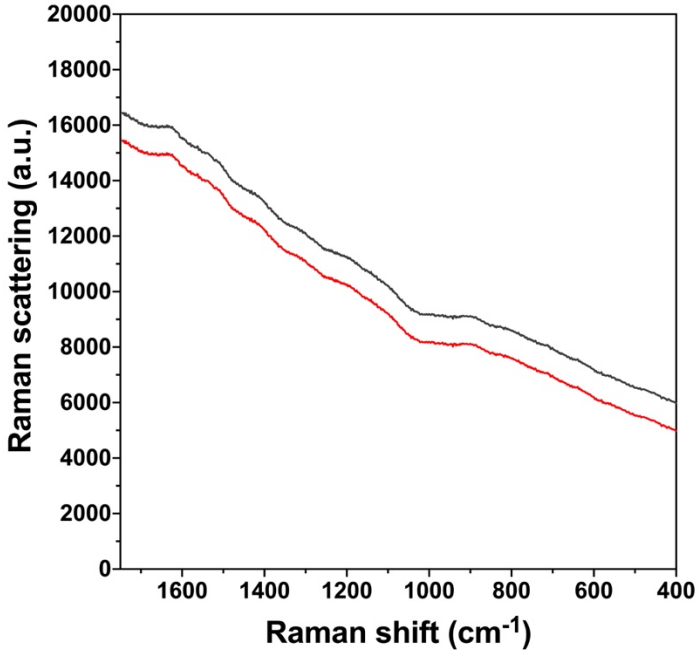

Figure 5S.8. Representative Raman spectra of non-calcified ELP_3 membranes (grey spectrum) and ELP_3 membranes incubated in 1.5 x SBF for 32 days (red spectrum) obtained using a near-infrared (1064 nm) excitation laser.

We analyzed the ELP_3 membranes using Raman spectroscopy either with a visible (532 and 633 nm) or a near-infrared (NIR) (785 or 1064 nm) excitation laser. We were not able to get a good Raman signal with either of the laser, even though the 1064 nm laser is supposed to drastically reduce fluorescence in biological samples (Figure SVII). This is due to the highly fluorescent signal of ELN which is known as one of the main fluorophores in biological tissues, along with collagen (273). Several other studies have discussed the difficulty of getting Raman ELN peaks due to its high fluorescence background (274, 275).

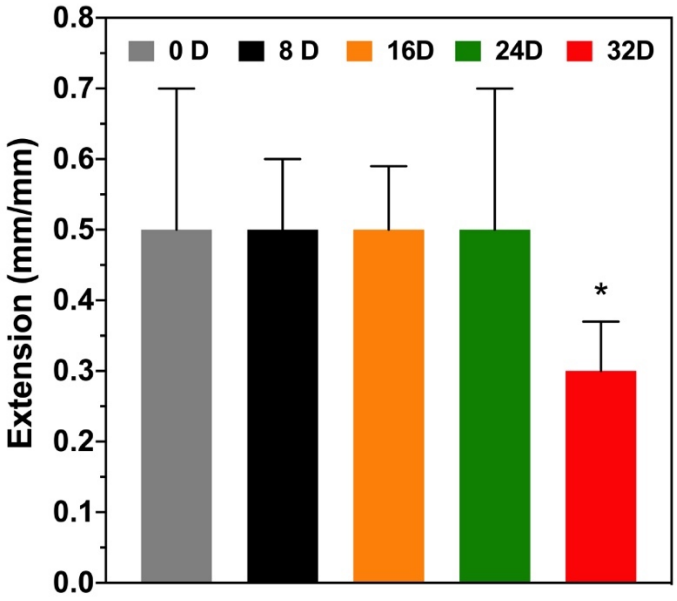

Figure 5S.9. Extension calculated based on the stress-strain curve in control samples and ELP_3 membranes incubated in SBF. T-test was used for statistical analysis. * indicate significant differences with the 32-days old samples, with $P< 0.05$.

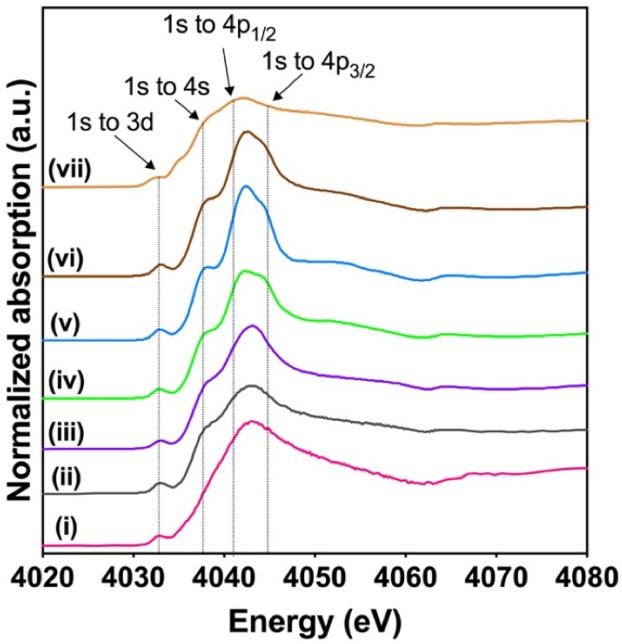

Figure 5S.10. Representative Ca K-edge NEXAFS reference spectra of (i) ELP_3-Ca^{2+}, (ii) ACP, (iii) DCPD, (iv) OCP, (v) HA, (vi) CHA, and (vii) β-TCP.

Table 5S.11. Percentages of ELP_3-Ca^{2+}, ACP, OCP, HA, and CHA in ELP_3 membranes incubated in SBF for 8, 16, 24, and 32 days determined by LCF using Ca K-edge NEXAFS spectra of reference samples, and R-factors of the LCF.

Time point (days)	ELP_3-Ca^{2+} (%)	ACP (%)	OCP (%)	HA (%)	CHA (%)	R-factor
8	48 ± 4***	21 ± 4	11 ± 2*	21 ± 3	0***	0.000396
16	30 ± 5*** +++	20 ± 5+++	18 ± 5* +	20 ± 5+++	17 ± 5*** +	0.000404
24	14 ± 2+++ ###	7 ± 1+++ ##	25 ± 3+ ###	39 ± 4+++ ###	21 ± 4+	0.000313
32	0###	0##	10 ± 2###	68 ± 6###	23 ± 2	0.000910

* indicates significant differences between 8- and 16-days old samples with * = P< 0.05 and *** = P< 0.0001
\+ indicates significant differences between 16- and 24-days old samples with + = P< 0.05 and +++ = P< 0.0001
\# indicates significant differences between 24- and 32-days old samples with ## = P< 0.005 and ### = P< 0.0001
For each time point, 2 samples were analyzed and 3 different spectra were collected for each sample

Chapter 6. Effect of the Ionic Concentration of Simulated Body Fluid on the Minerals Formed on Crosslinked Elastin-Like Polypeptide Membranes.

In the previous chapter, we developed an *in vitro* model of medial calcification based on ELP membranes immersed in SBF. Our results show that this simple system captures some of the *in vivo* findings, however, the long incubation time required to follow mineral nucleation and growth is a practical limitation of this model. Using an accelerated process with higher SBF ion concentration could be a good alternative to enhance the kinetics of mineral deposition in this model; however, the effect of increasing SBF ion concentration on mineral nucleation and growth is still not well understood.

To understand if our ELP membranes remain a biomimetic system if immersed in higher ion concentration SBF, we analyze mineral nucleation and phase transformation *in vitro* on ELP membranes immersed in high concentration SBF. We show that while mineral deposition is significantly accelerated in these conditions, both the mineral phase evolution as well as the final composition and structure of apatite formed are strongly affected. While the use of low concentration seems more appropriate to study medial calcification associated with the loss of calcification inhibitors, higher SBF ion concentration may be more relevant to study medial calcification in patients with life-threatening diseases, such as chronic kidney disease.

An article based on these findings is currently in preparation for submission to a peer-reviewed journal.

Ophélie Gourgas, Lisa D. Muiznieks, Simon Sharpe, Marta Cerruti. Effect of the Ionic Concentration of Simulated Body Fluid on the Minerals Formed on Crosslinked Elastin-Like Polypeptide Membranes.

6.1. Abstract

Deposition of calcium phosphate minerals on the elastin-rich medial layers of arteries can cause severe cardiovascular complications. There are no available treatments for medial calcification, and the mechanism of mineral formation on elastin layers is still unknown. We recently developed an *in vitro* model of medial calcification using crosslinked elastin-like polypeptide (ELP) membranes immersed in simulated body fluid (SBF). While mineral phase evolution matched that observed in a mouse model of medial calcification, the long incubation required was a practical limitation of this model. Using higher SBF ion concentrations could be a solution to speed up mineral deposition, but its effect on the mineralization process is still not well understood. Here we analyze mineral nucleation and phase transformation on ELP membranes immersed in high concentration SBF. We show that while mineral deposition is significantly accelerated in these conditions, the chemistry and morphology of the minerals deposited on the ELP membranes and the overall mineralization process are strongly affected. Overall, this work suggests that while the use of low concentration SBF in this *in vitro* model is more appropriate to study medial calcification associated with the loss of calcification inhibitors, higher SBF ion concentration may be more relevant to study medial calcification in patients with life-threatening diseases, such as chronic kidney disease.

6.2. Introduction

Arterial calcification involves nucleation and growth of calcium phosphate (Ca-P) minerals on the extracellular matrix (ECM) of the arteries. There is no therapy to stop or reverse arterial calcification and the medical treatments available are aimed only at slowing down its progression.

Mineral deposition occurs both in the intimal and medial layer of the arteries. Intimal calcification is commonly associated with atherosclerotic plaques and results from a sequence of events initiated by inflammation, which stimulates the osteochondrogenic transdifferentiation of vascular smooth muscle cells (VSMCs) (14, 61). On the contrary, medial calcification occurs in the absence of inflammation and is associated with aging, CKD and type II diabetes (14, 61).

While the processes leading to intimal calcification are quite well understood, the molecular mechanism of medial calcification is still elusive (13, 216). Several researchers have shown that medial calcification occurs predominantly within and along the elastic lamina, the concentric layers rich in elastin (ELN) (10, 15, 16, 107, 247). However, the mechanism of mineral nucleation and growth on ELN is still unknown.

To help understanding ELN mineralization process, researchers have developed *in vitro* models of medial calcification (286). *In vivo*, the ELN-rich layers are formed through coacervation of tropoelastin and subsequent crosslinking (89). Tropoelastin is a highly (>75%) non-polar protein characterized by hydrophobic domains alternating with lysine-containing crosslinking domains (89, 90). Early *in vitro* models were based on what is known as “solubilized ELN”, i.e. ELN fragments obtained by hydrolysis of the elastic layers of natural tissues (98, 99, 104, 105, 108-110). Since solubilized ELN consists of a

heterogeneous mixture of partially crosslinked hydrophobic ELN fragments rather than the alternating domain structure of full-length tropoelastin (89, 111), these early models were only partially biomimetic and sometimes led to contradictory results (98, 99, 104, 105, 108-110).

To overcome these drawbacks, we recently developed an *in vitro* model of medial calcification based on a synthetic elastin-like polypeptide (ELP) composed of alternating crosslinking and hydrophobic domains that mimic the motifs found in human tropoelastin (259). ELPs self-assemble and can be crosslinked to form gels and membranes with microstructural and tensile properties approaching those of native insoluble ELN (117, 118, 123). In our model, ELP is coacervated by adding salt and heating, and the coacervate crosslinked via genipin, a natural plant-derived compound with excellent biocompatibility (253). We then analyzed mineral nucleation and growth by immersing the crosslinked ELP membranes in 1.5 x simulated body fluid (SBF), at physiological pH and temperature. We showed that mineral phase evolution matches that previously observed in a mouse model of medial calcification (250), suggesting that this simple system captures some of the key *in vivo* findings (286). Although we used a solution with 1.5 times the ion concentration of the original 1 x SBF, long incubation times (i.e. 32 days) were needed to follow mineral nucleation and growth in this *in vitro* model. Using higher SBF ion concentrations could be a good alternative to enhance the kinetics of mineral deposition in this model.

The use of highly concentrated SBF was already proposed by several researchers to shorten the time needed to form Ca-P phases on various types of substrates *in vitro* (267, 287-294). SBF is a supersaturated solution with respect to several Ca-P phases, with

ionic concentration very similar to that of human blood plasma. It was first introduced by Kobuko *et al*. three decades ago as a way to perform *in vitro* simulations of *in vivo* conditions (295, 296). Since then, several modifications to the original SBF composition have been adopted to better match the ionic concentration of blood plasma (256, 297-300). More recently, it was shown that incubation times can be significantly reduced by incubating various types of substrates in SBF solutions with 2 to 10 times the ion concentration of original SBF (2 x to 10 x SBF) (267, 287-294). While increasing ion concentrations in SBF enhances the kinetics of mineral deposition, mineral nucleation and growth may also be affected in these higher supersaturation conditions.

A few studies have investigated the effect of increasing SBF ion concentration on the chemical and morphological properties of minerals deposited on metallic and polymeric substrates for bone tissue engineering (267, 287-291). For example, Barrere *et al*. accelerated mineral deposition on titanium alloys from 7 days to 1 day by immersing substrates in 5 x SBF instead of 1.5 x SBF (287, 288). However, they did not compare the minerals formed in this system with those formed in 1.5 x SBF. Kim *et al*. studied the composition and structure of apatite phases formed on polyethyleneterephtalate substrates in SBFs with concentrations from 0.75 to 2 x SBF (289). They showed that both the Ca/P ratio and the lattice constant *c* of the apatite formed significantly decreased with increasing ionic concentration and attributed this to an increase in the number of PO_4^{3-} to HPO_4^{2-} substitutions, which caused the formation of Ca-deficient apatites. In agreement with this, Shin *et al.* showed that less crystalline and more Ca-deficient carbonated hydroxyapatite (CHA) was formed on poly(lactide-*co*-glycolide) scaffolds when SBF ion concentration increased from 0.75 to 2 x SBF (267). All the minerals in this

study were flake-like and composed of sub-micrometer sized structures, thus suggesting that the increase in SBF ion concentration did not affect the mineral morphologies (267). Chen *et al.* also found no differences in morphology between the apatite particles formed on poly($_L$-lactic acid) films and poly(glycolic acid) scaffolds using 1.5 x or 5 x SBF (291). However, differently from Kim (289) and Shin (267), they found no compositional differences among the minerals formed in the two solutions. In another study, Chesnutt *et al.* showed profound differences in the morphology of minerals formed on phosphorylated chitosan films in 1 x and 1.5 x SBF, and yet they did not find significant compositional differences between minerals formed in the two SBFs (290).

These contradictory results may be explained by the different substrates used, which may have caused different mineral formation mechanisms. Also, some of these studies pre-treated the samples before immersing them in SBF to favor mineral formation, such as soaking in a saturated $Ca(OH)_2$ solution or putting them in contact with particles of bioactive glass-ceramics (289, 290). This might have affected the mineral formation process.

Also, while all these studies focused on morphological and compositional changes of the minerals, none of them investigated the effect of SBF concentration on mineral nucleation and growth. No studies analyzed the precursor phases formed and the overall process of mineral phase transformation in the different SBFs used. In fact, while hydroxyapatite (HA) and CHA are the most thermodynamically stable Ca-P phases formed at physiological pH and temperature, non-apatitic phases can form too (181). Amorphous calcium phosphate (ACP), octacalcium phosphate (OCP), dicalcium phosphate (DCPD), and magnesium-substituted β-tricalcium phosphate (β-TCMP) can

be formed *in vitro* before HA and CHA, depending on the pH, temperature, and solution composition (182). A similar process occurs *in vivo*, for both physiologic and pathologic calcification (182, 188, 189, 250, 251). None of these precursor phases were reported in the studies cited above (267, 287-291). One reason could be that, in an accelerated process, Ca-P phase transformation on these substrates is so fast that the precursor phases cannot be detected. Another reason could be that the techniques used in (267, 287-291) were not sensitive enough to detect them. Understanding how precursor phases form and evolve over time *in vitro* when using high SBF ion concentrations would be critical to determine whether such models can still be used to emulate *in vivo* situations.

To shed some light on these open questions, as well as understand if our ELP membranes remain a biomimetic system if immersed in higher concentration SBF, we analyze mineral nucleation and phase transformation on ELP membranes immersed in high concentration SBF using several techniques, including highly sensitive synchrotron-based near-edge x-ray absorption fine structure spectroscopy (NEXAFS) to study mineral phase evolution. While this study focuses on mineral formation on ELP, its conclusions on the effect of increasing SBF ion concentration on mineralization are relevant for any *in vitro* model involving SBF.

6.3. Materials and methods

6.3.1. Materials

Genipin (≥98.0% by HPLC) was purchased from Challenge Bioproducts (Taiwan, China). Sodium chloride (NaCl, ≥99.0%), and hydrochloric acid (HCl, ACS reagent, 36.5 to 38.0% (w/w)) were purchased from Fisher Scientific (Ottawa, ON, Canada). Sodium

tetraborate decahydrate ($Na_2B_4O_7.10H_2O$, ACS reagent, 99.5-105.0%) sodium hydrogen carbonate ($NaHCO_3$, ≥99.0%), potassium chloride (KCl, BioXtra, ≥99.0%), potassium phosphate dibasic trihydrate ($K_2HPO_4 \cdot 3H_2O$, ≥99.0%), magnesium chloride hexahydrate ($MgCl_2 \cdot 6H_2O$, BioXtra, ≥99.0%), calcium chloride ($CaCl_2$, ≥97.0%), sodium sulfate (Na_2SO_4, ACS reagent, ≥99.0%), tris(hydroxymethyl)aminomethane ($NH_2C(CH_2OH)_3$) (Tris), ACS reagent, ≥99.8%), amorphous calcium phosphate [$Ca_3(PO_4)_2.3H_2O$, (ACP)], dicalcium phosphate dihydrate [$Ca(HPO_4).2H_2O$, (DCPD)], and β-tricalcium phosphate [$Ca_{18}(Mg)_2H_2(PO_4)14$, (β-TCMP)] were purchased from Sigma-Aldrich (Oakville, ON, Canada). Hydroxyapatite [$Ca_{10}(PO_4)_6(OH)_2$, (HA)] was obtained from the National Institute of Standards and Technology (NIST). All materials were used as received.

Carbonated hydroxyapatite [$Ca_{10-p}(PO_4)_{6-p}(OH)_{2-p}(CO_3)_p$ ($0<p<1$), (CHA)] and octacalcium phosphate [$Ca_8H_2(PO_4)_6. 5H_2O$, (OCP)] were prepared following methods previously described in (254) and (255), respectively.

6.3.2. ELP_3 expression and purification

ELP_3 (Figure 6S.1) in a pET-32b vector was cloned and overexpressed in *E.coli* BL21(DE3) cells as previously described (114). Briefly, expression was induced with isopropyl β-D-1-thiogalactopyranoside (0.1 mM) when the optical culture density (A_{600nm}) reached ~1. Cells were grown a further 3 h, (200 rpm, 37 °C) and harvested by centrifugation (6000 rpm, 15 min). Cell pellets were digested overnight (1g CnBr in 20 mL 70 % formic acid per liter culture) and dialysed (3500 MWCO dialysis tubing, Spectropor) against Na acetate (20 mM, pH 5.25) for 24 h. ELP_3 was purified from cleared cell lysate by ion exchange chromatography (SP Sepharose, Amersham Bioscience), eluted with a linear gradient of NaCl (0-220 mM) in 20 mM Na acetate buffer, pH 5.25. A final

purification was carried out by HPLC (Jupiter C4 10 μm 300 Å column, Phenomenex), eluted with a linear gradient of 25-50% acetonitrile. Purity, integrity and molecular weight of lyophilized proteins were confirmed by mass spectrometry (SPARC BioCentre, Hospital for Sick Children). Protein was stored lyophilized until use.

6.3.3. ELP_3 membrane preparation

Recombinant ELP_3-based membranes were prepared via coacervation and subsequent crosslinking by genipin as described previously (123). Briefly, purified and lyophilized ELP_3 was dissolved in 0.15 M sodium borate buffer (pH 8) to a final concentration of 10 mg/mL. The ELP_3 solution was incubated for 2 hours at 4 ^oC to allow complete dissolution. ELP_3 membranes were then prepared in the wells of Lab-Tek chamber slides: ELP_3 solution was added in the wells to a final concentration of 10 mg/mL; then, NaCl and genipin were added to final concentrations of 0.8 M and 10 mM, respectively. The sample chamber slide was then carefully placed into a styrofoam support and transferred to a flat-bottomed centrifuge bucket pre-warmed at 37 ^oC. Then, the bucket was inserted into a temperature-controlled swinging-bucket centrifuge pre-warmed at 37 ^oC and was spun at 3200 rpm for 7 min at 37 ^oC. The sample slide was then immediately placed in an incubator set at 37 ^oC and left overnight for the crosslinking reaction to occur. The membranes were removed from the chamber slide by gently flushing with distilled water and stored in water at pH 7 until use.

6.3.4. In vitro mineralization of ELP_3 membranes in simulated body fluid (SBF)

Modified SBF solutions (Table 6S.1) were prepared following procedures described by Kokubo *et al.* (256). The concentrations of ionic species (Na^+, K^+, Mg^{2+},

Ca^{2+}, Cl^{-}, HPO_4^{2-}, SO_4^{2-}) were adjusted to produce SBF solutions with ionic concentrations 1.5 (1.5 x SBF), 2 (2 x SBF), and 3 (3 x SBF) times higher than those of blood plasma. Each SBF solution was prepared by sequentially dissolving reagent-grade chemical NaCl, $NaHCO_3$, KCl, $K_2HPO_4 \cdot 3H_2O$, $MgCl_2 \cdot 6H_2O$, $CaCl_2$, and Na_2SO_4 in deionized water. Since SBF solutions are supersaturated at physiological pH, increasing the concentrations is limited by the low solubility of Ca and P. To maintain thermodynamic conditions conducive to heterogeneous nucleation and avoid any homogeneous nucleation, SBFs were buffered to three different pH values (7.4 for 1.5 x SBF, 7.0 for 2 x SBF, and 6.8 for 3 x SBF) with 1M HCl and Tris at 36.5 ^{o}C. All the SBF solutions were sterilized by filtering through a 0.2 µm polyethersulfone filter (Thermo Scientific, USA). ELP_3 membranes with lateral sizes of 0.5 cm x 0.5 cm were immersed vertically in Eppendorf tubes containing 500 µL of 1.5 x SBF, 2 x SBF, or 3 x SBF and stirred at a speed of 50 rpm inside an incubator at 37 ± 0.5 ^{o}C. The membranes were removed from the solutions after 3, 5, and 7 days, and rinsed in deionized water for 3 times, 20 minutes each time. Membranes incubated in 1.5 x SBF were also sampled after 21 days. The samples were then dried under vacuum overnight or kept hydrated in water, as needed for following analysis.

6.3.5. Scanning electron microscopy (SEM) and energy-dispersive X-ray spectroscopy (EDS)

ELP_3 membranes incubated in 1.5 x, 2 x, and 3 x SBF were characterized using a combination of SEM and EDS. Samples were mounted on an aluminium SEM stub with carbon tape, and then coated with about 20nm carbon using an EMS 150R ES carbon sputter coater (EMS, Hatfield, USA). The samples were then imaged using an Inspect F50 field emission SEM (FE-SEM) (FEI, Japan), at 15 kV operating voltage under high

vacuum. EDS spectra and elemental maps were obtained at 15 kV in the regions of interest using an Octane super 60 mm^2 EDS system (EDAX Inc., USA).

6.3.6. X-ray photoelectron spectroscopy (XPS)

The atomic composition of the ELP_3 membranes was characterized using a Thermo Scientific Kα spectrometer (ThermoFisher Scientific, USA), equipped with an Al Kα X-ray source (1486.6 eV, 0.843 nm), a micro-focused monochromator, and an ultrahigh vacuum chamber (10^{-9} Torr). Survey scans and high-resolution spectra were acquired with an X-ray spot with a diameter of 400 μm. Three survey scans were collected for each sample, between 0 and 1200 eV with a step size of 1 eV. To prevent charging, samples were hit with a flood gun shooting low energy electrons during the measurement. For each membrane, four points were randomly selected, and three samples were analyzed per condition. Peak fitting and quantitative analysis of the survey spectra were performed using the Thermo Advantage software (version 4.60).

6.3.7. Fourier Transform infrared (FTIR) spectroscopy

FTIR spectra of dried ELP_3 membranes were collected on a Spectrum Two FT-IR spectrometer (PerkinElmer, Waltham, USA) equipped with an attenuated total reflection (ATR) accessory and a temperature stabilized fast-recovery deuterated triglycine sulphate (FR-DTGS) detector. The spectra were collected between 400 and 4000 cm^{-1} with a resolution of 4 cm^{-1} and using 64 scans. The collected spectra were baseline corrected and then normalized based on the absorbance of the ν C=O amide I band at 1634 cm^{-1} using Spectrum software (PerkinElmer, Waltham, USA). Three samples per condition were analyzed.

6.3.8. X-ray diffraction (XRD)

XRD diffractograms of dried ELP_3 membranes were obtained using a Bruker D8 Discover X-ray diffractometer (Bruker AXSS Inc., Fitchburg, USA) equipped with a Cu Kα source ($K\alpha_1$ λ=1.54 Å), and a monochromator operated at 40 mV and 40 mA within the 10º to 80º range in 2θ. Three samples per condition were analyzed.

6.3.9. Ca K-edge near edge X-ray absorption fine structure (Ca K-edge NEXAFS) spectroscopy

Ca-P phases present in ELP_3 membranes were characterized using Ca K-edge NEXAFS spectroscopy at the bulk-XAFS end-station of the Soft X-ray Microcharacterization Beamline (SXRMB) at the Canadian Light Source (CLS), Saskatoon, Saskatchewan. Powdered reference compounds of known chemical compositions were also analyzed, including ACP, OCP, DCPD, HA, CHA, β-TCMP. We also analyzed ELP_3 membranes incubated in 3.8 mM of $CaCl_2$ solution (ELP_3-Ca^{2+}), as possible models of the early stages of calcification with only Ca ions adsorbed on the ELP_3 matrix. Spectra were collected with energies between 1.7 and 10 keV and with a photon beam spot size of 2 mm x 6 mm. Reference spectra were collected in transmission mode while spectra of ELP_3 membranes were collected in fluorescence mode. The spectra were calibrated, aligned, and normalized using Athena software (Demeter 0.9.20). Principle component analysis (PCA) was first performed on the spectra to avoid using an excessive number of references in the fitting. Then, linear combination fitting (LCF) was performed on the NEXAFS regions of the spectra using combinations of the reference samples selected by the PCA. The quality of the fits was evaluated by the R-factor value: values below 0.02 indicate that the fitting results are satisfactory (227). For

each spectrum, the best LCF combination (i.e. the combination giving the lowest R-factor) was retained. PCA and LCF were performed using Athena software. Three samples were analyzed for each condition and two spectra by sample were collected.

6.3.10. Statistical analysis

Statistical data analysis was performed using GraphPad software, Inc. (2016). Mean values were expressed as average ± standard deviation. Statistical analysis on mean values was performed by Student's t-test or one-way ANOVA test followed by Tukey's test correction for multiple comparisons, and $p < 0.05$ was considered significant.

6.4. Results and Discussion

ELP_3 peptides form elastic dark blue membranes after coacervation in presence of NaCl at 37 °C and overnight crosslinking with genipin (see inset in Figure 6.1.A) (286). Crosslinked ELP_3 membranes form clusters of spherical droplets about 1 to 6 μm in diameter, either smooth or rough (Figure 6.1). Thin filaments and fibre-like structures link the droplets to one another (Figure 6.1). These results are consistent with previous studies showing that droplets, filaments, and fibers are the three self-assembled structures that formed during *in vitro* assembly of both full-length tropoelastin (89, 91, 122, 252, 263, 264) and ELPs (90, 119, 120, 257, 260, 286).

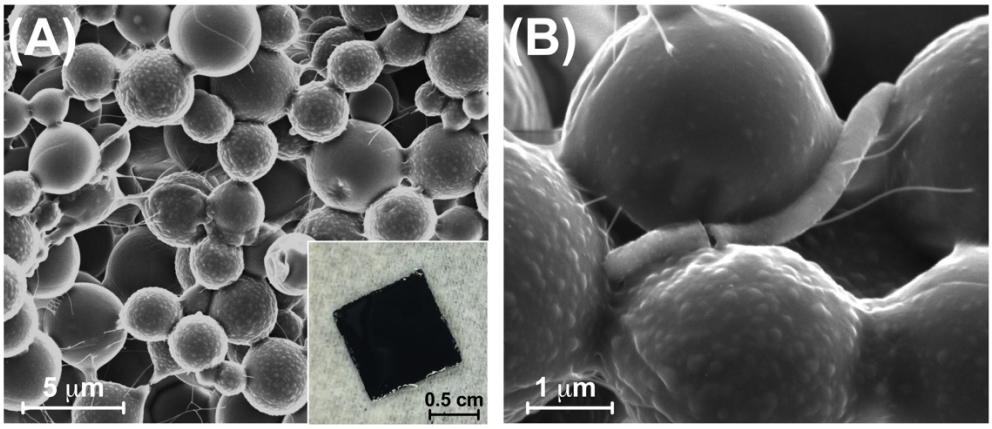

Figure 6.1. (**A**-**B**) Scanning electron microscopy (SEM) images of ELP_3 membranes. Inset figure on (**A**) is a digital picture of a hydrated ELP_3 membrane.

After 3 days of incubation in 1.5 x SBF, no minerals are deposited on the ELN droplets, but some Ca-P deposits are found on the filaments and fiber-like structures (Figure 6.2.A; Figures 6S.2.A and 6S.2.B; Table 6S.2). Ca/P ratios on filaments and fibers vary between 1.3 and 1.4, suggesting that minerals are composed of mixed Ca-P phases but do not contain apatite phases, such as HA and CHA, at this stage (Table 6S.3) (179). Some spots show much higher Ca/P ratios (Figure 6S.2.B; Table 6S.2), suggesting Ca ion adsorption (286). After 5 days in 1.5 x SBF, Ca and P ions start depositing on the ELN droplets and more minerals are formed on the thin filaments and fibers with Ca/P ratios between 1.4 and 1.6, suggesting the presence of both non-apatitic and apatitic phases at this stage (Figure 6.2.B; Figure 6S.2.C and 6S.2.D; Table 6S.4). Overall the N/Ca ratios decrease from 3 to 5 days, indicating that more minerals are formed overtime. The ELN droplets start being covered by HA flakes after 7 days in 1.5 x SBF with Ca/P ratio between 1.6 and 1.7, suggesting formation of stochiometric HA (Figure 6.2.C; Figures 6S.2.E and 6S.2.F; Table 6S.5). These apatites are flake-like in radial arrangement and composed of sub-micrometer sized platelets, which is the typical microstructure of HA *in*

vitro (Figure 6S.3.A) (265-268). The amount of minerals further increases after 7 days, as shown by overall lower N/Ca ratios (Table 6S.5). However, some spots on ELN globules still show higher Ca/P ratios, implying that Ca ions are adsorbed on the surface and have yet to be transformed into Ca-P compounds (Table 6S.5). Also, many droplets do not show yet the presence of Ca or P at this stage. This implies that mineral nucleation and growth on the ELN droplets occur at different times depending on the location and that after 7 days, only partial mineral deposition has occurred. After 21 days of incubation in 1.5 x SBF, most of the ELP globules are fully covered with thin HA flakes (Figures 6S.4.A-6S.4.D) and most of the minerals are composed of apatitic phases at this stage (Figure 6S.4.C). The minerals exhibit the same morphology than at earlier time point in 1.5 x SBF (Figure 6S.4.D).

A similar but faster process happens for samples incubated in 2 x SBF (Figures 6.2.D-6.2.F; Figure 6S.5). Indeed, for each time point analyzed, the N/Ca ratios are overall lower for samples incubated in 2 x SBF compared to those immersed in 1 .5 x SBF (Tables 6S.6-6S.8). After 3 days, the 2 x SBF samples already show the presence of minerals with flake-like morphology in radial arrangement, similar to those found in 1.5 x SBF at longer time points (Figure 6S.3.B). This finding is in agreement with a previous study showing no significant differences in the size and shape of the minerals deposited on polymeric substrates incubated in 1.5 and 2 x SBF (267). However, the Ca/P ratios on the apatite flakes in 2 x SBF are all between 1.4 and 1.6 (Table 6S.8). These values are overall lower than those for 1.5 x SBF samples at the same time point and suggest that apatite phases formed in 2 x SBF are mostly Ca-deficient (Table 6S.3).

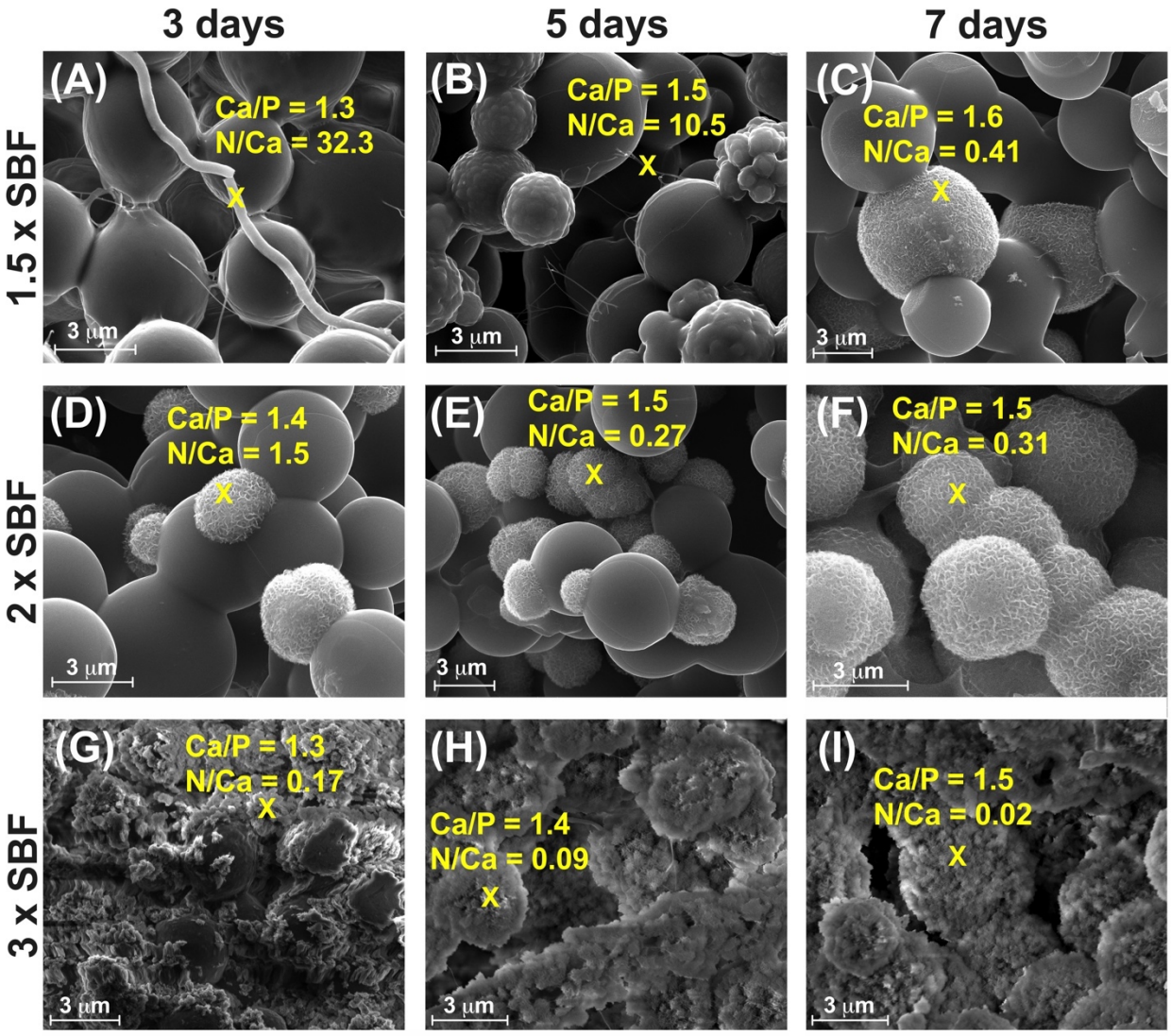

Figure 6.2. Scanning electron microscopy (SEM) images of ELP_3 membranes after incubation in (**A - C**) 1.5 x SBF, (**D** - **F**) 2 x SBF, and (**G - I)** 3 x SBF for 3, 5, and 7 days. The Ca/P and N/Ca ratios indicate on **A**, **B**, **C**, **D**, **E**, **F**, **G**, **H** and **I** are based on elemental atomic percentages obtained by energy-dispersive x-ray spectroscopy (EDS).

Mineral deposition is even faster on samples incubated in 3 x SBF. After 3 days, most of the ELN globules are already covered by Ca-P deposits (Figure 6.2.G; Figures 6S.6.A and 6S.6.B). The greater mineral deposition in 3 x SBF is confirmed by the lower N/Ca ratios measured on 3 x SBF samples compared to those found in both 1.5 x and 2 x SBF samples (Figure 6S.6; Tables 6S.9-6S.11). While all of the apatites deposited on samples

incubated in 1.5 x and 2 x SBF solutions after 7 days are flake-like in radial arrangement and composed of sub-micrometer sized platelets (Figures 6S.3.A and 6S.3.B), those formed on samples incubated in 3 x SBF are substantially different. The mineral flakes are more disordered and densely packed compared to those formed in 1.5 and 2 x SBF solutions (Figure 6S.3.C). Similar to what was observed in 2 x SBF, the Ca/P ratios measured on 3 x SBF samples are all lower than 1.67, thus suggesting that the apatites formed in this system are also mostly Ca-deficient (Figures 6.2.G-6.2.H; Table 6S.3). This result agrees with previous findings of Ca/P ratios lower than 1.67 for minerals formed in 2 x SBF and higher concentration SBF, thus suggesting that the apatite formed through this accelerated process is mostly Ca-deficient (267, 291, 293).

Overall, these results show that the rate of mineralization can be significantly accelerated by increasing the SBF ionic concentration. A uniform HA layer can be deposited on ELP_3 membranes in 7 days by immersing the samples in 3 x SBF, while this takes about 21 days in 1.5 x SBF solution. However, while no major differences in mineral morphology are found between 1.5 x and 2 x SBF samples, apatite particles formed on ELP membranes incubated in 3 x SBF are greatly different.

We further analyzed the mineral deposits by XPS (Figures 6.3.A and 6.3.B). XPS data confirm that the atomic percent of Ca deposited on ELP_3 membranes, and thus the amount of minerals, significantly increases with both the incubation time and ion concentration ($P < 0.05$) (Figure 6.3.A; Table 6S.12). While there are no significant differences in average Ca/P ratios between 3 and 5 days in all SBF solutions, the ratio significantly increases after 7 days for the 1.5 x SBF samples only ($P < 0.05$) (Figure 6.3.B). This increase is correlated with the overall higher Ca/P ratios found by EDS after

7 days. In higher concentration SBF, the Ca/P values measured by XPS match those obtained by EDS, and are lower than the value for stochiometric apatite, in agreement with previous literature (267, 291, 293).

We estimated mineral crystallinity using FTIR and XRD (Figures 6.3.C and 6.3.D). All FTIR spectra of ELP_3 membranes incubated in 1.5, 2, and 3 x SBF for 7 days show peaks related to HA (Figure 6.3.C; see the ν_1 phosphate band at 963 cm^{-1}, the degenerate ν_3 vibration at 1030 and 1109 cm^{-1}, and the degenerate ν_4 band at 562 and 602 cm^{-1}; a complete list of peak assignments is presented in Table 6S.13). We estimated apatite crystallinity by analyzing the relative intensities of the peaks and valley in the ν_4 envelope (Section 1 in the supplemental material; Figure 6S.7). A higher degree of splitting and therefore a higher crystallinity index (CI) correspond to more crystalline materials (236). After 7 days, the CIs of the mineral deposits in samples incubated in 2 x and 3 x SBF solutions are significantly lower than those formed in 1.5 x SBF ($P < 0.05$) (Figure 6.3.C; Table 6S.14). These data suggest that apatite phases formed in an accelerated SBF process are not only Ca-deficient but also less crystalline, confirming results from Shin *et al*. (267) on poly(lactide-*co*-glycolide) scaffolds. The CI of HA deposits in samples incubated in 1.5 x SBF further increases from 7 to 21 days ($P < 0.02$) (Figure 6.3.C), as previously observed (286). All the CIs are significantly lower than that of synthetic HA (Figure 6.3.C).

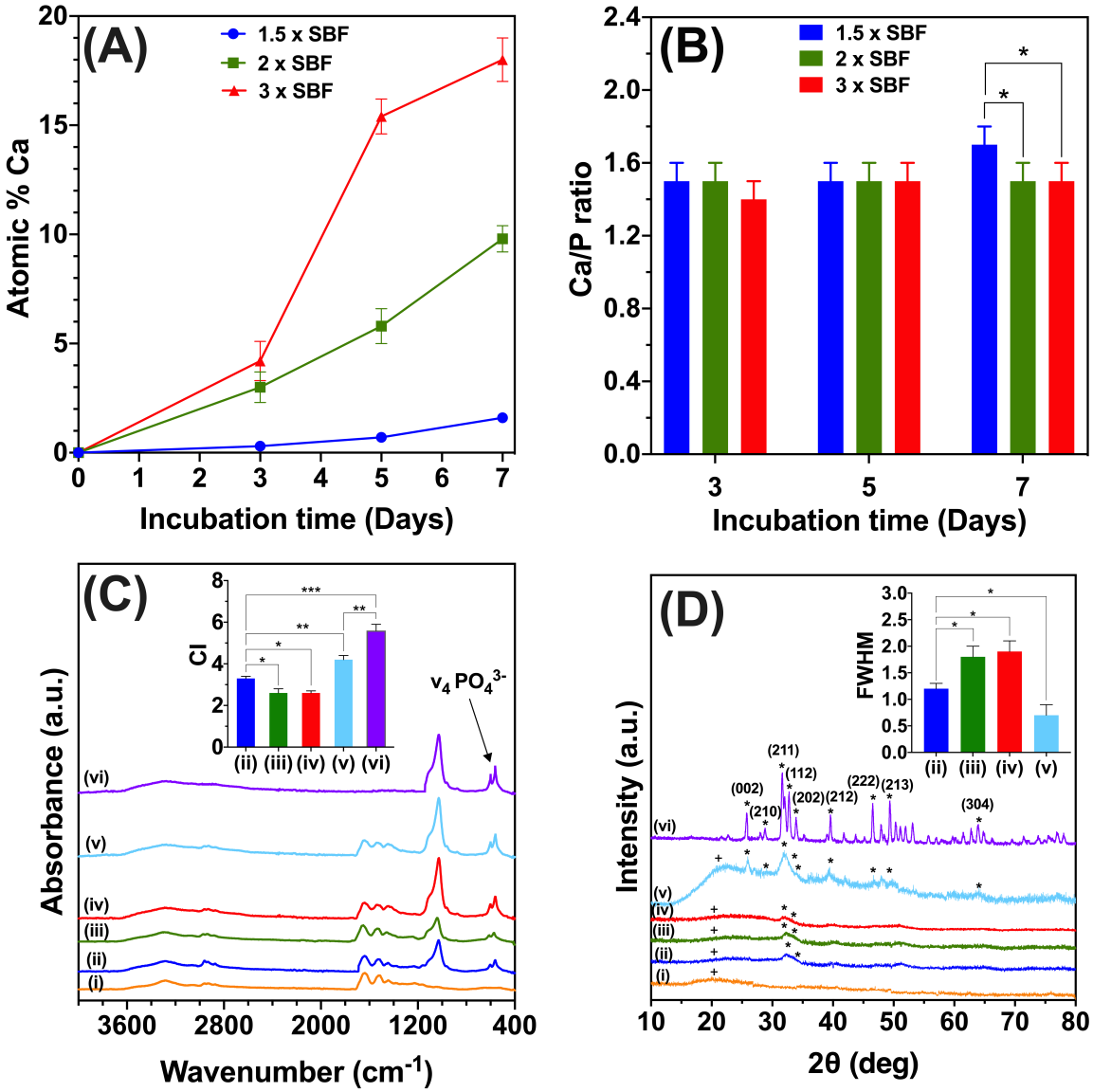

Figure 6.3. Atomic percentages of calcium (**A**) and Ca/P ratios (**B**) determined by x-ray photoelectron spectroscopy (XPS) surveys on ELP_3 membranes incubated in 1.5 x (blue), 2 x (green), and 3 x SBF (red) for 3, 5, and 7 days. For each time point, 3 samples were analyzed, and 4 XPS surveys were collected at different points for each sample. One-way ANOVA test followed by Tukey test correction for multiple comparisons were used for statistical analysis. * indicates significant differences between the different SBF solutions with P< 0.05. (**C**) Representative Fourier transform infrared (FTIR) spectra of ELP_3 membranes (i) before incubation in SBF, after incubation in (ii) 1.5 x, (iii) 2 x, and (iv) 3 x SBF for 7 days, and in (v) 1.5 x SBF for 21 days, and from (vi) synthetic HA. The arrow shows ν_4 PO_4^{3-} vibration bands used to estimate the mineral crystallinity. The spectra were normalized based on the absorbance of the ν C=O amide I band at 1638-1642 cm^{-1}. The inset shows the CI values for samples (ii) to (vi). * indicate significant difference between the different samples, with * = P < 0.05, ** = P< 0.02, and *** = P <

0.001. For each time point, 3 samples were analyzed. (**D**) Representative x-ray diffraction (XRD) patterns of ELP_3 membranes (i) before incubation in SBF, after incubation in (ii) 1.5 x, (ii) 2 x, and (iii) 3 x SBF for 7 days, and in (iv) 1.5 x SBF for 21 days, and from (vi) synthetic HA. ($^+$) and (*) signs indicate the peaks corresponding to ELN and HA, respectively. The labels on the spectra refer to the HA planes present on ELP_3 membrane samples. The inset shows the FWHM values for samples (ii) to (v). * indicates significant difference between the different samples, with * = $P < 0.05$. For each time point, 3 samples were analyzed.

XRD spectra confirm the presence of HA in ELP_3 membranes incubated in the three different SBF ionic concentrations for 7 days (Figure 6.3.D; see the broad peak centered at about 32° that is the combination of the peaks corresponding to the crystallographic planes (211), (121), and (202) of HA) (JCPDS# 09-0432). Full width at half maximum (FWHM) values of the peak corresponding to the HA planes (211), (121), and (202) are significantly lower in samples incubated in 1.5 x SBF compared to those found in 2 x and 3 x SBF samples ($P < 0.05$) (Figure 6.3.D;Table 6S.15). Since FWHM inversely correlates with HA crystallinity, this confirms the higher mineral crystallinity in 1.5 x SBF samples compared to 2 x and 3 x samples. FWHM values further decrease from 7 to 21 days in 1.5 x SBF, thus confirming the increase in mineral crystallinity shown by FTIR ($P < 0.05$) (Figure 6.3.D).

Overall, SEM/EDS, XPS, FTIR, and XRD show that as the ionic concentration in SBF increases, minerals grow faster and more abundantly on the ELP_3 membranes, but the apatite phases become Ca-deficient and less crystalline. The faster precipitation in high SBF ion concentration is consistent with the results of a theoretical analysis of Ca-P precipitation in SBF showing that the activation energy for nucleation (i.e. the free energy change, ΔG) decreases with increasing Ca and P ion concentrations in SBF (200). The increase in the nucleation rate with increasing SBF ion concentrations can be attributed to an increase in the HA ionic activity product (IP) and degree of supersaturation (S).

Indeed, while the three SBF solutions are supersaturated with respect to HA (S > 0), the degree of supersaturation increases with the SBF ionic concentration (S= 20, 26, and 45 in 1.5, 2, and 3 x SBF, respectively) (Section 1 in the supplemental material, Table 6S.1). This increase is non-linear, and the sudden increase in S between 2 x and 3 x SBF matches the drastic changes in mineral amount and morphology observed in 3 x SBF.

Once the mineral nuclei are formed, less energy and time are required to add ions or ion clusters to already existing mineral nuclei than to form the initial mineral crystals (49). They grow spontaneously by consuming the Ca, and P ions from the surrounding fluid. SBF solutions with high degree of supersaturation provide a large supply of Ca and P ions in the area surrounding the nuclei, leading to an accelerated growth of the minerals. Since minerals grow much faster in SBF with higher degree of supersaturation, the ions have less time to re-organize themselves within the apatite lattice, thus leading to an overall lower degree of structural order. This explains the differences in mineral crystallinity and morphology observed between minerals formed on samples incubated in SBF with different degree of supersaturation. The presence of larger amounts of Mg^{2+} in high ion concentration SBFs compared to 1.5 x SBF also contributes to the formation of less crystalline, Ca-deficient apatite (301-303). In fact, while Mg^{2+} ions hardly incorporate into the apatite lattice, as confirmed in our experiments by the absence of Mg based on both EDS and XPS results, they can be adsorbed on existing mineral nuclei and temporarily block these sites.

Although Ca/P ratios determined by EDS and XPS give some indications about the Ca-P phases present in our samples, they cannot unequivocally identify these phases. Indeed, the variability in Ca/P values can be explained by the presence of non-apatitic

phases in addition to apatite phases, but it can also be due to ion substitutions within the crystal apatite lattice. To show whether differences in amounts and types of non-apatitic and apatitic phases exist in samples incubated in different SBF ionic concentrations, we further analyzed the calcified ELP_3 membranes using Ca K-edge NEXAFS (Figure 6.4). NEXAFS is a local chemical/structural probe analyzing how x-rays absorption by an atom is affected by its neighboring atoms. Since crystallinity is not required for NEXAFS (224), it can identify the amorphous and poorly crystalline phases present in the ELP_3 membranes, in addition to the crystalline apatite phases.

To identify the Ca-P phases present in our samples, we selected as reference samples ELP_3 membranes incubated in Ca solution (ELP_3-Ca^{2+}), ACP, OCP, DCPD, β-TCMP, HA, and CHA. We then performed principle component analysis (PCA) and linear combination fitting (LCF) following the procedure explained in Section 1 of the supplemental material. NEXAFS spectra of reference samples and ELP_3 membranes incubated in 1.5 x, 2 x, and 3 x SBF solutions show four features that are typical of Ca-P compounds (Figure 6S.8 and Figures 6.4.A-6.4.C, respectively) (225, 226). The small feature at the pre-edge around 4035 eV is due to electronic transitions between 1s and 3d orbitals. The absorption edge, the most intense peak, shows a shoulder around 4040 eV assigned to 1s to 4s transitions, and a more intense double peak centered at around 4045 eV, which is assigned to 1s to $4p_{1/2}$ and 1s to $4p_{3/2}$ transitions (225, 226). The features at higher energies are due to multiple scattering contributions.

The LCF results and the associated R-factors are presented in Table 6S.16 and Figure 6.4.D. All the R-factor values are < 0.02, thus suggesting that all the fits are satisfactory (227). The results show that the calcified ELP_3 samples are composed of a

mixture of adsorbed Ca ions (ELP_3 -Ca^{2+}), ACP, OCP, HA, and CHA. DCPD and β-TCMP were not detected in any sample.

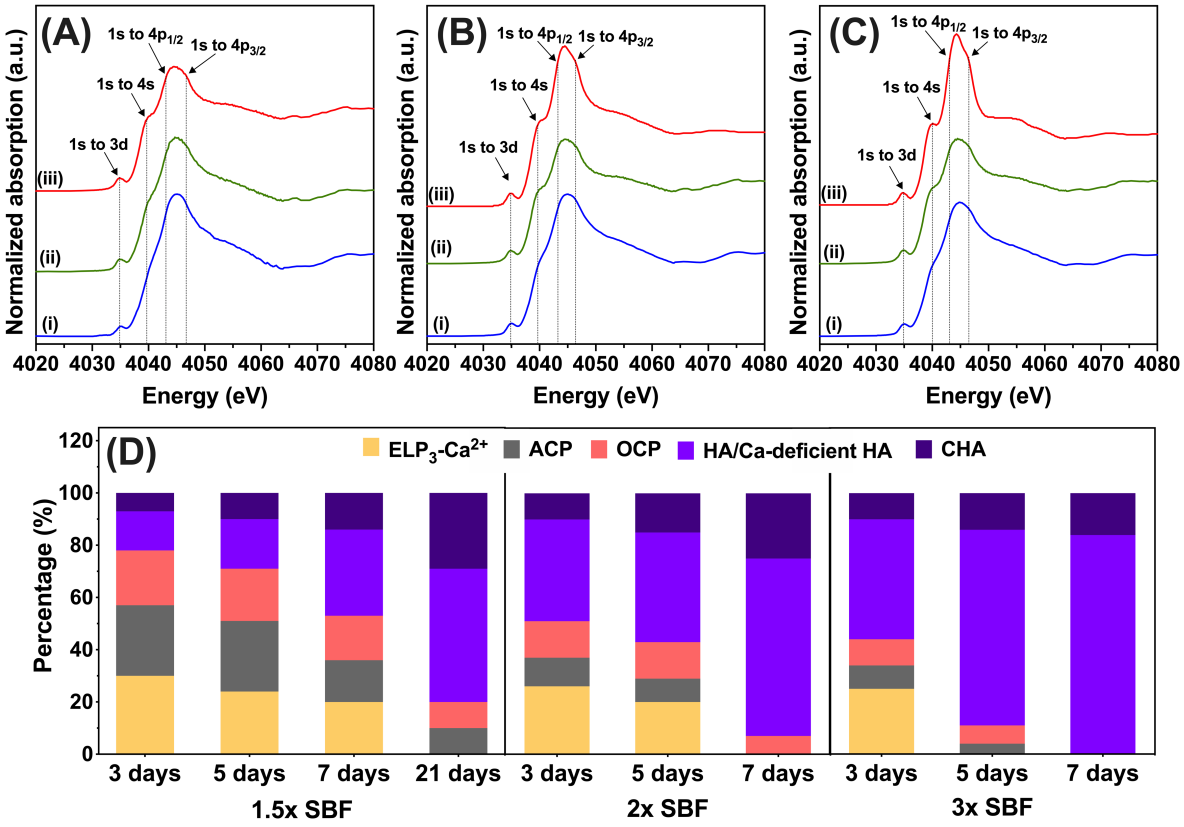

Figure 6.4. Representative Ca K-edge near-edge x-ray absorption fine structure spectroscopy (NEXAFS) spectra of ELP_3 membranes incubated in 1.5 x (blue), 2 x (green), and 3x SBF (red) for (**A**) 3, (**B**) 5, and (**C**) 7 days. The labels on the spectra refer to the different electronic transitions. (**D**) Relative percentages of ELP_3-Ca^{2+}, ACP, OCP, HA, and CHA in ELP_3 membranes incubated in 1.5 x, 2x, and 3x SBF solutions determined by linear combination fitting (LCF) based on the reference spectra. Three samples were analyzed for each condition.

After 3 days of incubation in 1.5 x SBF, nearly 30% of the Ca atoms show a neighboring environment like that of Ca atoms in ELP_3 membranes immersed in $CaCl_2$ solution, thus indicating that about 30% of the Ca present is just adsorbed on the samples. The other Ca atoms are mostly present as non-apatitic phases, while only about 20% of the Ca atoms are part of apatite phases. There are not many differences in the relative

percentages of Ca-P phases in ELP_3 membranes incubated in 1.5 x SBF between 3 and 5 days (Figure 6.4.D). This finding is in agreement with SEM/EDS and XPS data showing no significant differences in Ca/P ratios between these two time points. Ca/P ratios determined by SEM/EDS and XPS are between 1.4 and 1.6 at this stage; this reflects well the NEXAFS data showing a mix of non-apatitic and apatitic phases. After 7 days, the ELP_3 membranes show larger amounts of ACP and apatite phases, while the amounts of adsorbed Ca and OCP remain the same. After 21 days in 1.5 x SBF, small amounts of ACP and OCP are still detected, showing that not all the precursor phases have yet been transformed into apatite phases (Figure 6.4.D). NEAXFS data show the presence of both stochiometric HA and CHA at this stage. This is consistent with the Ca/P ratios higher than 1.6 determined by EDS and XPS on these samples.

The relative amount of adsorbed Ca ions in ELP3 membranes incubated in 2 x SBF for 3 days is not significantly different from that measured on 1.5 x SBF samples (Figure 6.4.D). However, the amounts of non-apatitic phases (i.e. ACP and OCP) are significantly lower and about 50% of the Ca ions are already present as apatite phases (Figure 6.4.D; Table 6S.16). In agreement with SEM/EDS results, there are not many differences between 3 and 5 days for these samples. After 7 days in 2 x SBF, about 95% of the Ca ions are present in apatitic structures (HA and CHA), and only a small amount of OCP is still present (Figure 6.4.D). Since Ca-deficient HA and stoichiometric HA have very similar spectra in NEXAFS (304), to understand which type of HA is formed on these samples we have to look at results obtained with other techniques. Since both SEM/EDS and XPS showed Ca/P ratios between 1.4 and 1.6 on 2 x SBF samples at all time points analyzed,

the HA found by NEXAFS as the most abundant mineral phase deposited on these samples after 7 days of immersion is Ca-deficient HA.

The relative percentages of Ca-P phases on ELP_3 membranes incubated in 3 x SBF for 3 days are very similar to those measured on 2 x SBF samples. However, different from 2 x SBF samples, after 5 days the Ca detected on 3 x SBF is mainly present in apatitic structures, and ACP and OCP are only present in small amounts. There is no more evidence of adsorbed Ca ions, suggesting that there are no more available nucleation sites on the ELP_3 membranes at this stage (Figure 6.4.D). After 7 days, the samples are exclusively composed of apatite phases (HA and CHA). Like what discussed for 2 x SBF samples, considering that both EDS and XPS results indicate Ca/P ratios close to 1.5, these samples are mostly composed of Ca-deficient apatite, indicated as HA in the NEXAFS results, and a small percentage of CHA.

The finding of ACP and OCP as precursor phases in these three *in vitro* systems is in line with our previous study where we found both ACP and OCP in the medial layer of calcified arteries from genetically modified mice lacking a specific calcification inhibitor (matrix gla protein, MGP) (250). We showed that ACP and OCP are slowly transformed into HA and CHA and these mineral phase transformations are reproduced after each nucleation event throughout the life of the mice (250). Although these precursor phases are detected in the three *in vitro* systems, the kinetics of mineral phase formation and transformation is much faster in the models using 2 and 3 x SBF. In fact, ACP and OCP are hardly detected on samples incubated in 2 x SBF after 7 days, and they are almost completely absent in 3 x SBF samples. Also, while apatite phases formed in 1.5 x SBF are mostly stochiometric HA and CHA, those formed in higher degree of supersaturation

are mainly Ca-deficient HA, which were not present among the minerals formed in the medial layer of MGP-deficient mice (250). Thus, the *in vitro* model using 1.5 x SBF more closely matches mineral transformation related to MGP deficiency (250).

MGP deficiency is found in humans with Keutel syndrome, a rare genetic disease (221). It is possible that mineral formation and growth occur similarly in patients suffering from diseases associated with the deficiency of other calcification inhibitors, such as type 2 diabetes and idiopathic infantile arterial calcification, marked by lower levels of Fetuin A and pyrophosphate, respectively (305-308). However, the mineral formation process in medial calcification may be completely different in other diseases, such as CKD. CKD patients usually suffer from hypercalcemia and/or hyperphosphatemia, i.e. their serum Ca and P levels are higher than those found in healthy people (42). Also, patients with end-stage CKD on dialysis usually present high Mg concentration in their serum because of the presence of high levels of Mg ions in the dialysis solution (182). The presence of higher Ca, P, and Mg levels in CKD patients may lead to an overall mineralization process quite different from the one observed in the MGP-deficient mouse model we previously studied, and may be in fact more similar to what observed here on the ELP membranes immersed in 2 and 3 x SBF. Thus, different SBF ion concentrations could be used in conjunction with ELP membranes as *in vitro* models of different *in vivo* pathological situations.

6.5. Conclusion

The formation of Ca-P phases on ELP_3 membranes incubated in SBF solutions with different ionic concentrations can be significantly accelerated by increasing SBF ionic concentration. However, the chemical and morphological properties of the minerals

deposited on the ELP_3 membranes and the overall mineralization process are strongly affected. We show that SBF ion concentration influences both the mineral phase evolution and the final composition and structure of apatite formed.

Mineral phase formation and transformation on ELP_3 membranes immersed in 1.5 x SBF matches that previously observed in a mouse model of medial calcification associated with the loss of MGP. However, mineral phase evolution on samples incubated in 2 x and 3 x SBFs is substantially different. While the same precursor phases are involved, they are much less prevalent and very quickly transformed into apatite phases. The final apatites are less crystalline and mostly Ca-deficient HA in these two systems, rather than stochiometric HA and CHA. In 3 x SBF, the mineral deposits are overall more disordered and densely packed compared to those formed in 1.5 and 2 x SBF solutions.

The findings obtained using 2 or 3 x SBF might more closely match mineral nucleation and transformation happening in the arteries of patients with life-threatening diseases such as CKD. This hypothesis could be tested by analyzing mineral phase formation and transformation in medial calcification associated with CKD, which is yet to be explored. If mineral formation and transformation found in CKD patients actually matched those observed in our *in vitro* system using 2 x and/or 3 x SBF, then different strategies should be developed to stop or reverse calcification for these patients compared to seniors or patients affected by loss of calcification inhibitors.

For example, an effective approach to prevent medial calcification associated with the loss of calcification inhibitors may involve preventing the transformation of metastable precursor phases, which are amorphous or poorly crystalline, into crystalline apatite

phases. However, this approach may not be a viable treatment for CKD patients where mineral phase transformation is likely accelerated in the presence of high serum Ca and P levels and almost no precursor phases are formed, as shown in this study. Thus, another option should be considered for these patients.

6.6. Acknowledgments

We acknowledge support from the Canadian Light Source (CLS), which is supported by the Canada Foundation for Innovation, the Natural Sciences and Engineering Research Council of Canada (NSERC) the University of Saskatchewan, the Government of Saskatchewan, the Western Economic Diversification Canada, the National Research Council Canada, and the Canadian Institutes of Health Research. We also thank Dr Yongfeng Hu and Dr Qunfeng Xiao of the CLS for their help with data analysis and technical support. We also acknowledge the Canada Research Chair foundation, the Heart and Stroke Foundation and NSERC for providing funding for this research.

6.7. Funding sources

This work was supported by the Heart and Stroke Foundation, the Jacques de Champlain Award, the Fond Québécois de la Recherche sur la Nature et les Technologies (FQRNT), the Canada Research Chair Foundation, the Center for Self-Assembled Chemical Structures, the Canadian Institutes of Health Research (CIHR), and the McGill Engineering Doctoral Award (MEDA).

6.8. Supplemental material

6.8.1. Section 1: Detailed methods

6.8.1.1. Determination of the apatite ionic activity products (IP) and degree of supersaturation (S)

An increase in concentration of calcium (Ca) and phosphate (P) ions in the simulated body fluid (SBF) leads to an increase in the apatite ionic activity product (IP) of the SBF.

Formation of hydroxyapatite (HA) from its constituent ions is given by the following equilibrium (309):

$$Ca_{10}(PO_4)_6(OH)_2 \Leftrightarrow 10Ca^{2+} + 6PO_4^{3-} + 2OH^-, \text{ (i)}$$

The ionic activity product (IP) of HA in an aqueous solution is this given by the following equation (309):

$$IP = (\gamma_{Ca^{2+}})^{10} (\gamma_{PO4^{3-}})^{10} (\gamma_{OH^-})^2 [Ca^{2+}]^{10} [PO_4^{3-}]^6 [OH^-]^2, \text{ (ii)}$$

Where γ is the activity coefficient, and [ ] represents ionic concentration.

The activity coefficients were calculated based on the modified Debye-Hückel equation proposed by Davies (310). The IP of each SBF solution is given in Table 6S.1.

The relative degree of supersaturation S with respect to apatite phases was calculating using the following equation (309):

$$S = (IP/K_{sp})^{1/n}, \text{ (iii)}$$

Where IP is the ionic activity, K_{sp} the solubility product, and n the number of ions in a formula unit (i.e. 18 for apatite). K_{sp} of apatite in water is 5.5×10^{-118} at 37 °C (311).

The degree of supersaturation S of each SBF solution in respect to apatite is given in Table 6S.1.

6.8.1.2. Determination of the crystallinity index (CI) of the minerals by FTIR

The splitting of the v_4 PO_4^{3-} band can be used to estimate HA crystallinity index (CI) according to the formula introduced by Shemesh *et al*. (222):

$$CI = (A602 + A562) / A588, \text{ (iv)}$$

where A_X is the absorbance at wavenumber x (Figure 6S.7)

A higher degree of splitting and therefore a higher CI correspond to more crystalline materials (236).

6.8.1.3. Ca K-edge Near Edge X-ray absorption fine structure (Ca K-edge NEXAFS) spectroscopy

To identify and quantify the Ca-P phases present in the samples, we applied NEXAFS spectroscopy. It is a synchrotron-based technique that allows analyzing how x-rays are absorbed by an atom at energies near the core-level binding energies of that atom depending on its chemical and physical environment (224). Because of crystallinity is not required for NEXAFS measurements, this technique is well suited for analysis of non-crystalline or poorly crystalline phases (224). Also, NEXAFS is more sensitive than traditional spectroscopic techniques, with a detection limit that can be as low as few ppm. Thus, NEXAFS is an excellent tool to analyze et differentiate the Ca-P phases present in calcified ELP_3 membranes.

Ca K-edge spectra were collected in fluorescence mode with energies between 1.7 and 10 keV and with a photon beam spot size of 2 mm x 6 mm. The storage ring

energy during data collection was 2.9 GeV ant the current around 200 mA. The X-ray beam was monochromated by Si (111) crystals with energy resolution ($\Delta E/E$) of 10^{-4}.

Data analysis

We first selected seven reference compounds (Figure 6S.6). The first one is ELP_3 membranes incubated in 3.8 mM of $CaCl_2$ solution for 16 days (ELP_3-Ca^{2+}) which may be a model of the very early stages of calcification if the Ca ions were first adsorbed on the ELP_3 matrix. The other five references are Ca species that are known to be present in pathological calcifications: amorphous calcium phosphate (ACP), octacalcium phosphate (OCP), dicalcium phosphate dihydrate (DCPD), HA, carbonated hydroxyapatite (CHA), and β-tricalcium phosphate (β-TCMP) (174, 175, 182, 193, 204, 250, 286).

To determine and quantify the Ca-P phases in the ELP_3 samples, we performed linear combination fitting (LCF) analysis using Athena software (Demeter 0.9.20). LCF is justified because the x-ray absorption from different species in a sample is additive (280). The total absorption coefficient calculated by LCF can be written as:

$$M = \Sigma_i f_i (STD_i), (v)$$

where M is the least square fit to the sample spectrum, (STD_i) represents the absorption coefficient of the standard reference spectra, and f_i is the fraction of each reference spectrum in the sample spectrum, summed over the number of references, i. Thus, with appropriate standard references, LCF can identify and quantify the fraction of chemical species in an unknown sample (280).

We first performed principal component analysis (PCA) to determine which reference compounds should be excluded for the LCF fitting and thus avoid using an excessive

number of standard compounds. PCA results showed that DCPD and β-TCMP were not likely present in the calcified membranes. Thus, we used ELP_3-Ca^{2+}, ACP, OCP, HA, and CHA as references for the LCF analysis. We performed LCF using all the possible combinations of the selected reference compounds. We evaluated the quality of the fits using the R-factor: fitting results with R-factor values below 0.02 are considered satisfactory (227). We reported the LCF combination giving the lowest R-factor for each sample analyzed (Table 6S.16).

6.8.2. Section 2: Supplemental figures and tables

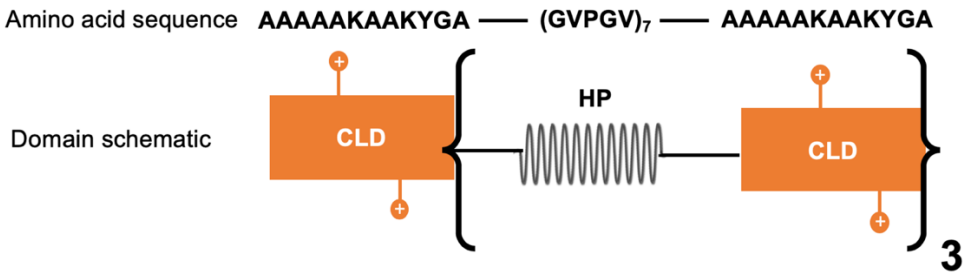

Figure 6S.1. The repeating amino acid sequence and alternating domain architecture of ELP_3. Crosslinking domains (CLD) and hydrophobic domains (HP) are represented as orange rectangles and springs, respectively.

Table 6S.1. Ion concentrations, apatite ionic activity products (IP), and degree of supersaturation (S) of human blood plasma, 1 x, 1.5 x, 2 x, and 3 x simulated body fluid (SBF) solutions.

	Ion concentration (mM)									
Solution	Na^+	K^+	Mg^{2+}	Ca^{2+}	Cl^-	HCO_3^-	HPO_4^{2-}	SO_4^{2-}	Log IP	S
Blood plasma	142.0	5.0	1.5	2.5	103.0	27.0	1.0	0.5	-96.6	14
1 x SBF	142.0	5.0	1.5	2.5	147.8	4.2	1.0	0.5	-96.6	14
1.5 x SBF	211.5	7.5	2.4	3.8	228.0	6.3	1.5	0.8	-93.8	20
2 x SBF	282.0	10.0	3.0	5.0	304.0	8.4	2.0	1.0	-91.9	26
3 x SBF	423.0	15.0	4.8	7.6	456.0	12.6	3.0	1.6	-87.5	45

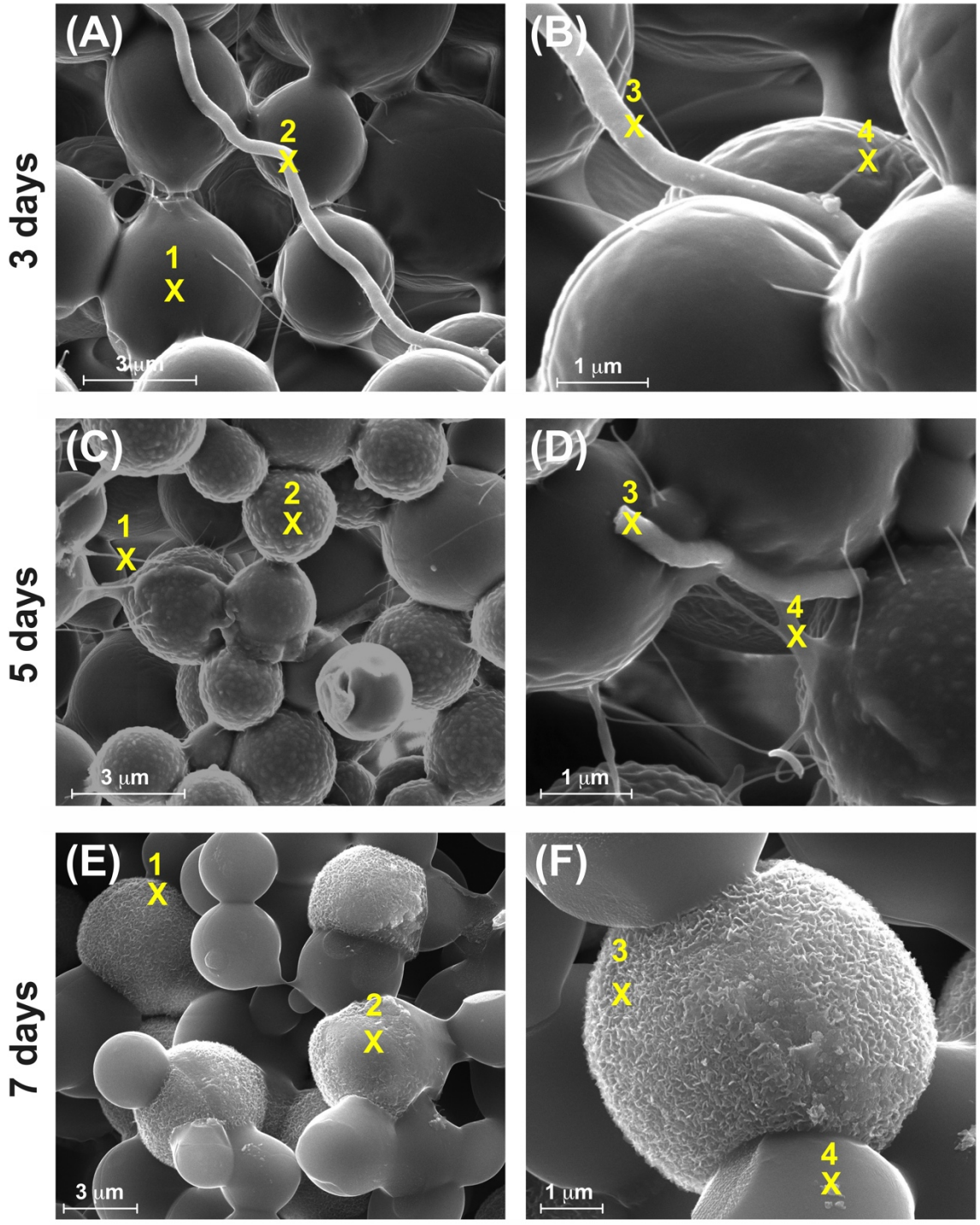

Figure 6S.2. SEM images of ELP_3 membranes after incubation in 1.5 x SBF for (**A** and **B**) 3, (**C** and **D**) 5, and (**E** and **F**) 7 days. The spots marked with "X" on all panels indicate the spots where EDS spectra were collected and they correspond to the data presented in Tables SII (spots in **A, B**), SIV (spots in **C, D**), and SV (spots in **E, F**).

Table 6S.2. Relative elemental atomic percentages measured by EDS in ELP_3 membranes incubated in 1.5 x SBF for 3 days. The spots 1-4 are shown in Figures 6S.2.A and 6S.2.B.

Spot	C (at%)	O (at%)	N (at%)	Ca (at%)	P (at%)	O/C	N/C	Ca/P	N/Ca
1	67.2	17.8	15.0	0	0	0.26	0.22	/	/
2	64.8	21.6	12.9	0.4	0.3	0.33	0.20	1.3	32.3
3	64.4	26.3	7.4	1.3	0.9	0.41	0.11	1.4	5.7
4	68.1	20.8	10.4	0.6	0.1	0.31	0.15	6.0	17.3

Table 6S.3. List of Ca-P compounds found in pathological calcifications and their Ca/P molar ratios (179).

Name	Formula	Ca/P ratio
Amorphous calcium phosphate (ACP)	$Ca_3(PO_4)_2.3H_2O$	1.5
Octacalcium phosphate (OCP)	$Ca_8H_2(PO_4)_6.\ 5H_2O$	1.33
Dicalcium phosphate dihydrate (DCPD)	$Ca(HPO_4).2H_2O$	1.0
Magnesium- substituted β-tricalcium phosphate (β-TCMP)	$Ca_{18}(Mg)_2H_2(PO_4)_{14}$	1.29
Hydroxyapatite (HA)	$Ca_{10}(PO_4)_6(OH)_2$	1.67
Carbonated hydroxyapatite (CHA)	$Ca_{10-p}(PO_4)_{6-p}(OH)_{2-p}(CO_3)_p$ (0<p<1)	> 1.67
Calcium-deficient HA	$Ca_{10-x}(HPO_4)_x(PO_4)_{6-x}(OH)_{2-x}$ (0<x<1)	1.3 – 1.67

The stoichiometric apatite is given by the chemical formula $Ca_{10}(PO_4)_6(OH)_2$, with a Ca/P atomic ratio of 1.67 (179). When apatite forms, both *in vivo* and *in vitro*, some sites for the PO_4^{3-} ion can be partially substituted by CO_3^{2-} and HPO_4^{2-} ions. Numerically, one substitution of CO_3^{2-} for PO_4^{3-} results in a half Ca and one P deficiencies, thus giving a

Ca/P ratio higher than 1.67. On the contrary, one substitution of HPO_4^{2-} for PO_4^{3-} results only in a half Ca deficiency, to give a Ca/P ratio lower than 1.67 (179).

Table 6S.4. Relative elemental atomic percentages measured by EDS in ELP_3 membranes incubated in 1.5 x SBF for 5 days. The spots 1-4 are shown in Figures 6S.2.C and 6S.2.D.

Spot	C (at%)	O (at%)	N (at%)	Ca (at%)	P (at%)	O/C	N/C	Ca/P	N/Ca
1	60.4	21.3	15.7	1.5	1.1	0.35	0.26	1.4	10.5
2	65.1	21.8	12.4	0.6	0.1	0.33	0.19	6	20.7
3	52.8	25.4	17.7	2.5	1.6	0.48	0.34	1.6	7.1
4	61.2	20.9	16.7	1.0	0.2	0.34	0.27	5	16.7

Table 6S.5. Relative elemental atomic percentages measured by EDS in ELP_3 membranes incubated in 1.5 x SBF for 7 days. The spots 1-4 are shown in Figures 6S.2.E and 6S.2.F.

Spot	C (at%)	O (at%)	N (at%)	Ca (at%)	P (at%)	O/C	N/C	Ca/P	N/Ca
1	30.3	46.0	6.1	10.9	6.6	1.52	0.20	1.7	0.56
2	33.0	48.6	3.6	9.0	5.8	1.47	0.05	1.6	0.40
3	40.4	40.0	3.9	9.6	6.1	0.99	0.10	1.6	0.41
4	67.4	17.4	13.6	1.4	0.3	0.26	0.20	4.7	9.7

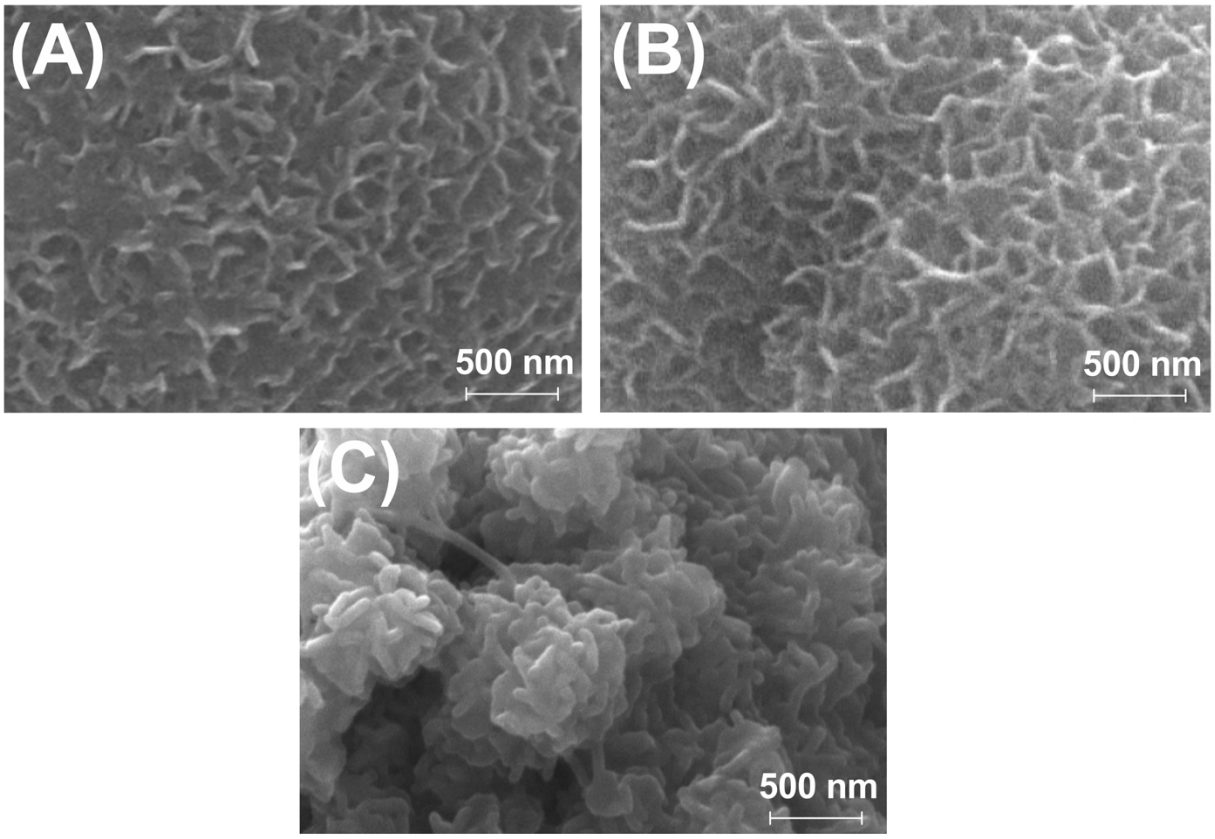

Figure 6S.3. (**A** - **C**) Highly magnified nanoscale structures of the minerals after 7 days in (**A**) 1.5 x, (**B**) 2 x, (**C**), 3 x SBF solutions.

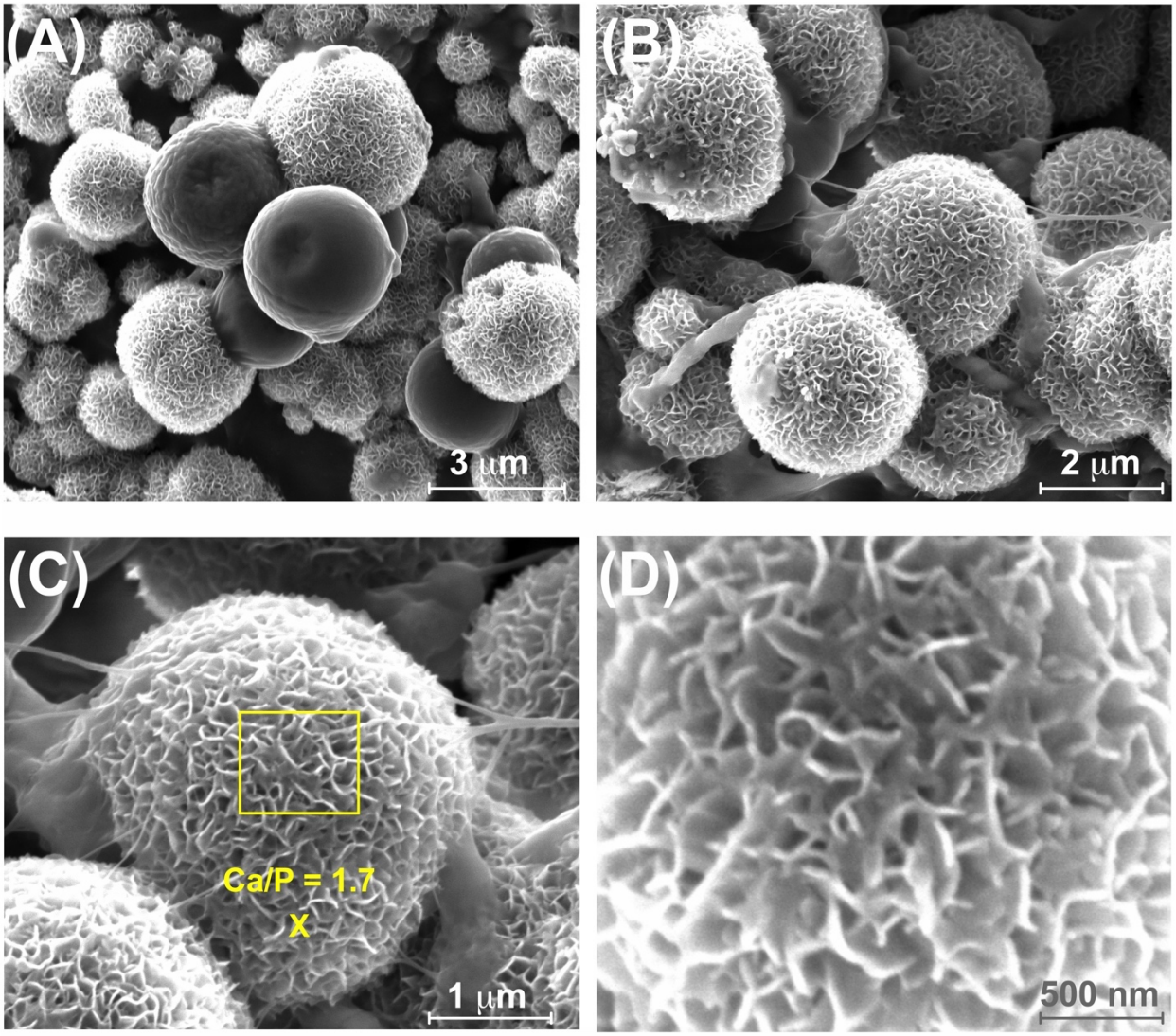

Figure 6S.4. SEM images of ELP_3 membranes after incubation in 1.5 x SBF for 21 days. The Ca/P ratio indicated on **C** is based on elemental atomic percentages obtained by ED and (**D**) is the magnification of the highlighted region in (**C**).

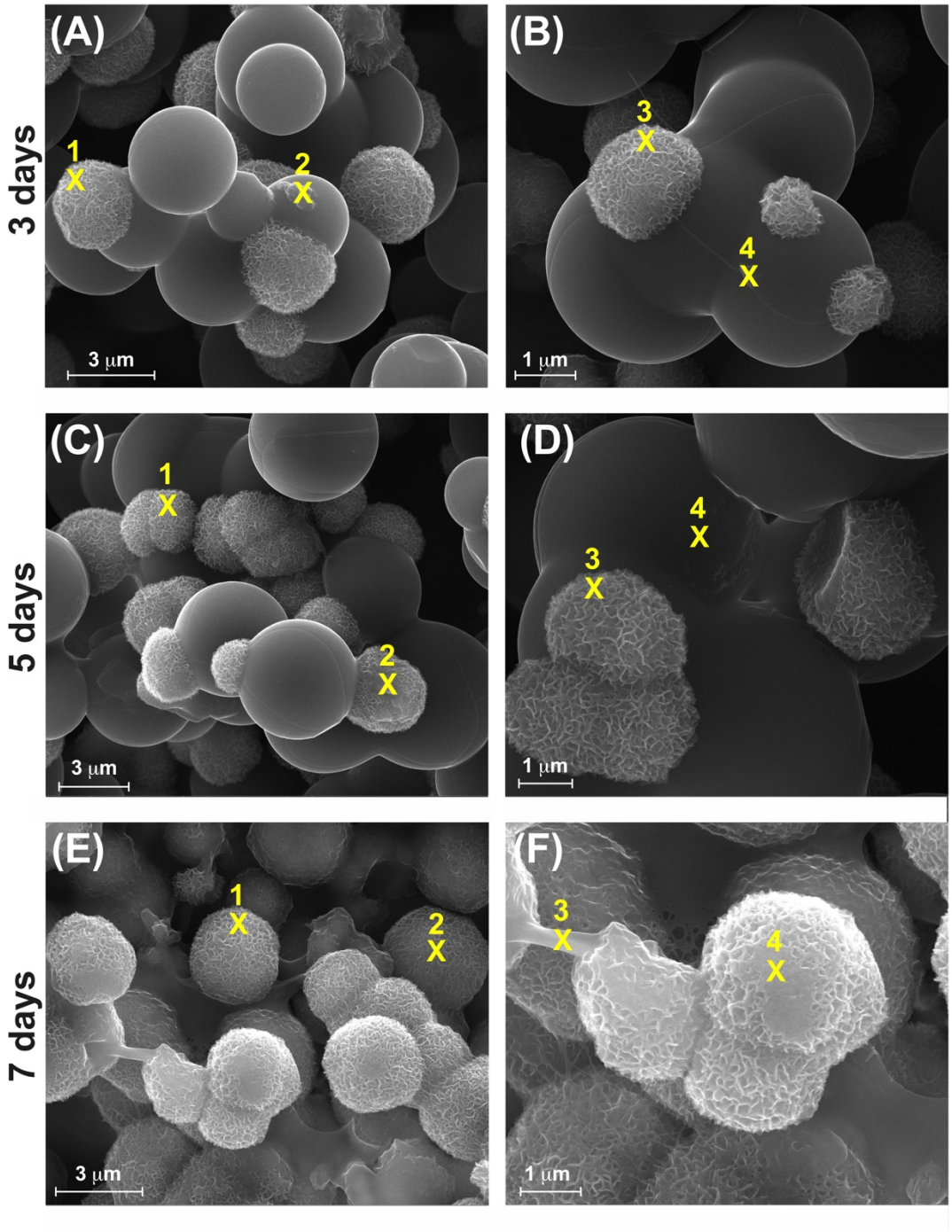

Figure 6S.5. SEM images of ELP_3 membranes after incubation in 2 x SBF for (**A** and **B**) 3, (**C** and **D**) 5, and (**E** and **F**) 7 days. The spots marked with "X" on all panels indicate the spots where EDS spectra were collected and they correspond to the data presented in Tables SVI (spots in **A, B**), SVII (spots in **C, D**), and SVIII (spots in **E, F**).

Table 6S.6. Relative elemental atomic percentages measured by EDS in ELP_3 membranes incubated in 2 x SBF for 3 days. The spots 1-4 are shown in Figure 6S.5.A and 6S.5.B.

Spot	C (at%)	O (at%)	N (at%)	Ca (at%)	P (at%)	O/C	N/C	Ca/P	N/Ca
1	36.0	44.6	3.2	9.7	6.5	1.24	0.09	1.5	0.33
2	61.8	17.7	18.7	1.7	0.2	0.29	0.30	8.5	11.0
3	67.5	19.3	6.2	4.1	2.9	0.29	0.09	1.4	1.5
4	59.9	22.1	17.0	0.9	0.1	0.37	0.28	9.0	18.9

Table 6S.7. Relative elemental atomic percentages measured by EDS in ELP_3 membranes incubated in 2 x SBF for 5 days. The spots 1-4 are shown in Figures 6S.5.C and 6S.5.D.

Spot	C (at%)	O (at%)	N (at%)	Ca (at%)	P (at%)	O/C	N/C	Ca/P	N/Ca
1	45.8	38.1	1.9	7.1	4.8	0.83	0.04	1.5	0.27
2	52.4	30.2	11.7	3.4	2.3	0.58	0.22	1.5	3.44
3	27.5	51.5	5.0	9.3	6.6	1.87	0.18	1.4	0.54
4	60.0	23.2	15.8	0.8	0.2	0.39	0.26	4.0	19.8

Table 6S.8. Relative elemental atomic percentages measured by EDS in ELP_3 membranes incubated in 2 x SBF for 7 days. The spots 1-4 are shown in Figures 6S.5.E and 6S.5.F.

Spot	C (at%)	O (at%)	N (at%)	Ca (at%)	P (at%)	O/C	N/C	Ca/P	N/Ca
1	22.9	56.1	3.2	10.7	7.1	2.45	0.14	1.5	0.31
2	38.3	41.0	2.1	11.4	7.3	1.07	0.05	1.6	0.18
3	20.4	50.7	1.2	17.1	10.6	2.48	0.06	1.6	0.07
4	25.6	52.0	2.7	11.4	8.3	2.03	0.11	1.4	0.24

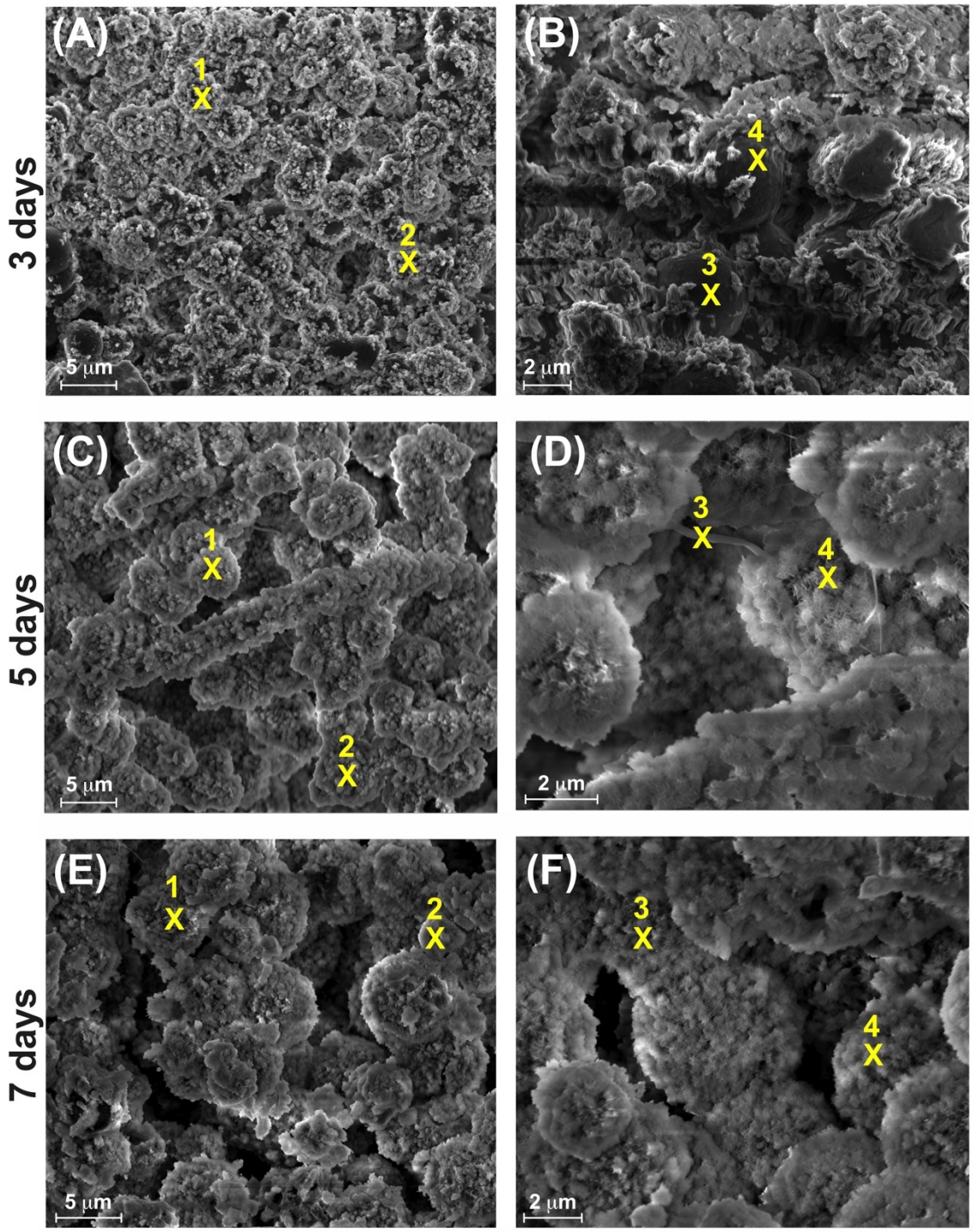

Figure 6S.6. SEM images of ELP_3 membranes after incubation in 3 x SBF for (**A** and **B**) 3, (**C** and **D**) 5, and (**E** and **F**) 7 days. The spots marked with "X" on all panels indicate the spots where EDS spectra were collected and they correspond to the data presented in Tables SIX (spots in **A, B**), SX (spots in **C, D**), and SXI (spots in **E, F**).

Table 6S.9. Relative elemental atomic percentages measured by EDS in ELP_3 membranes incubated in 3 x SBF for 3 days. The spots 1-4 are shown in Figures 6S.6.A and 6S.6.B.

Spot	C (at%)	O (at%)	N (at%)	Ca (at%)	P (at%)	O/C	N/C	Ca/P	N/Ca
1	21.4	57.6	1.8	10.7	8.3	2.69	0.08	1.3	0.17
2	35.7	45.0	1.2	8.2	5.9	1.26	0.03	1.4	0.15
3	51.9	28.8	6.0	11.4	1.8	2.69	0.12	6.3	0.52
4	48.8	33.4	2.2	15.7	0.1	0.68	0.05	157	0.14

Table 6S.10. Relative elemental atomic percentages measured by EDS in ELP_3 membranes incubated in 3 x SBF for 5 days. The spots 1-4 are shown in Figures 6S.6.C and 6S.6.D.

Spot	C (at%)	O (at%)	N (at%)	Ca (at%)	P (at%)	O/C	N/C	Ca/P	N/Ca
1	13.4	59.5	2.9	13.3	10.0	4.44	0.22	1.3	0.22
2	17.2	55.7	3.2	13.3	10.6	3.24	0.19	1.3	0.24
3	11.5	38.4	2.2	30.6	17.3	3.34	0.19	1.8	0.07
4	15.5	57.0	4.7	13.7	9.1	3.68	0.30	1.5	0.34

Table 6S.11. Relative elemental atomic percentages measured by EDS in ELP_3 membranes incubated in 3 x SBF for 7 days. The spots 1-4 are shown in Figures 6S.6.E and 6S.6.F.

Spot	C (at%)	O (at%)	N (at%)	Ca (at%)	P (at%)	O/C	N/C	Ca/P	N/Ca
1	18.4	43.0	3.1	21.3	14.2	2.34	0.17	1.5	0.15
2	6.4	44.7	0.7	29.1	19.2	6.98	0.11	1.5	0.02
3	15.9	55.2	1.4	16.6	11.0	3.47	0.09	1.5	0.08
4	17.8	46.8	2.5	20.1	12.9	2.63	0.14	1.6	0.12

Table 6S.12. Relative atomic percent of C, O, N, Ca, and P, and Ca/P and N/Ca ratios on ELP_3 membranes after incubation in 1.5 x, 2 x, and 3 x SBF, measured by XPS survey. No other elements were detected.

SBF solution	Time point (days)	C (at%)	O (at%)	N (at%)	Ca (at%)	P (at%)	Ca/P	N/Ca
/	0	68 ± 3	19 ± 3	13 ± 1	N	N	/	/
1.5 x SBF	3	67 ± 2	22 ± 3	11 ± 1	0.3 ± 0.1*** $^{+++}$	0.2 ± 0.1	1.5 ± 0.2	37 ± 8
	5	67 ± 1	21 ± 2	11 ± 1	0.7 ± 0.1*** $^{+++}$	0.5 ± 0.1	1.5 ± 0.1	17 ± 3
	7	66 ± 4	21 ± 2	11 ± 2	1.6 ± 0.2*** $^{+++}$	0.9 ± 0.2	1.7 ± 0.1	7 ± 2
	21	59 ± 3	23 ± 3	10 ± 1	4.8 ± 0.8	3.0 ± 0.9	1.8 ± 0.3	2.2 ± 0.6
2 x SBF	3	65 ± 2	20 ± 3	9 ± 2	3 ± 0.7***	2.1 ± 0.4	1.4 ± 0.1	3.0 ± 1.0
	5	52 ± 4	30 ± 2	8 ± 2	5.8 ± 0.8*** †	3.9 ± 0.7	1.5 ± 0.1	1.4 ± 0.6
	7	30 ± 3	49 ± 2	5 ± 1	9.8 ± 0.6*** †	6.4 ± 0.5	1.5 ± 0.1	0.6 ± 0.2
3 x SBF	3	55 ± 5	30 ± 4	8 ± 2	4.2 ± 0.9^{+++}	2.8 ± 0.8	1.5 ± 0.1	1.9 ± 0.7
	5	24 ± 3	47 ± 2	1.7 ± 0.5	15.4 ± 0.8^{+++} †	10.6 ± 0.7	1.5 ± 0.2	0.1 ± 0
	7	22 ± 3	46 ± 3	1.5 ± 0.5	18 ± 1^{+++} †	11.8 ± 0.6	1.5 ± 0.2	0.1 ± 0

* indicates significant differences between samples incubated in 1.5 x and 2 x SBF with * = P<0.02, ** = P<0.001, *** = P<0.0005.
$^{+}$ indicates significant difference between samples incubated in 1.5 x and 3 x SBF with $^{++}$ = P< 0.005, $^{+++}$ = P< 0.0001.
† indicates significant differences between samples incubated in 2 x and 3 x SBF with †† = P< 0.005, and ††† = P< 0.0001.

Table 6S.13. FTIR peak assignments for calcified ELP_3 membranes and HA.

Peak (cm^{-1})	Calcified ELP_3 membrane	HA	References
v OH	3290-3300	3300	(281), (282), (283)
v N-H	2958-2964		(281), (282), (283)
v_{as} CH_2	2926-2929		(281), (282), (283)
v_s CH_2	2865-2868		(281), (282), (283)
v C=O (amide I)	1638-1642		(281), (282), (283)
v C-N, δ N-H (amide II)	1535-1540		(281), (282), (283)
δ CH_2	1443-1451		(284)
δ CH_3	1365-1372		(281), (283), (284)
δ C-H (amide III)	1232-1236		(281)
v_3 PO_4^{3-}	1109-1110	1091	(282), (242), (240), (285)
v_3 PO_4^{3-}	1027-1031	1031	(282), (242), (240), (285)
v_1 PO_4^{3-}	960-963	962	(282), (242), (240), (285)
v_2 CO_3^{2-}	864-867		(282), (242), (240), (279)
v_4 PO_4^{3-}	600-602	602	(281), (282), (283)
v_4 PO_4^{3-}	561-563	564	(281), (282), (283)

v_{as}: antisymmetric stretching; v_s: symmetric stretching; δ: bending

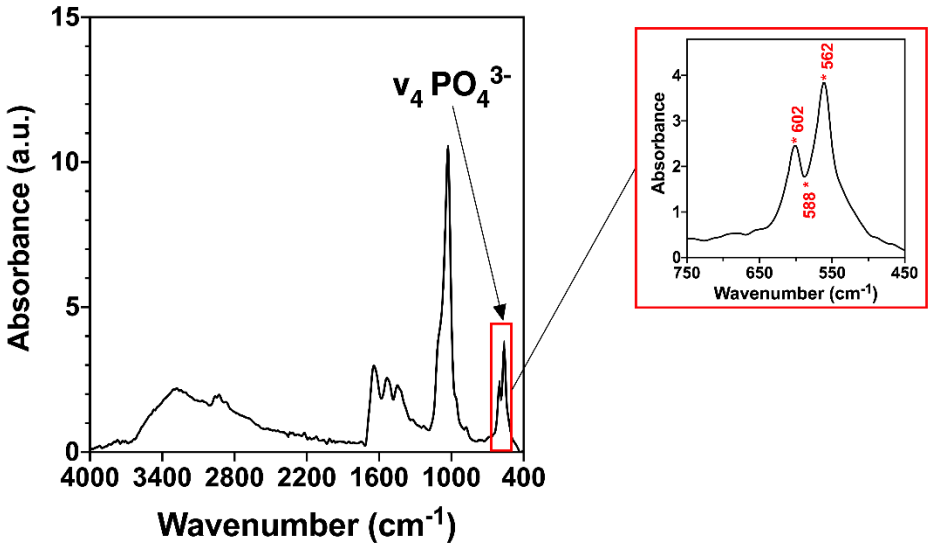

Figure 6S.7. Representative FTIR spectrum of calcified ELP3 membraned incubated in 1.5 x SBF for 21 days showing the degenerated ν_4 phosphate band used in Shemesh's method to determine the mineral crystallinity (222).

Table 6S.14. Experimental mineral crystallinity indexes (CI) measured in calcified ELP_3 membranes and HA based on the FTIR ν_4 vibration peaks.

SBF solution	Time point (days)	CI
1.5 x SBF	7	3.3 ± 0.1* + ##
	21	4.2 ± 0.2 ##
2 x SBF	7	2.6 ± 0.2*
3 x SBF	7	2.6 ± 0.1+
HA	/	5.6 ± 0.3

* indicates significant differences between samples incubated in 1.5 x and 2 x SBF for 7 days with P<0.05.
+ indicates significant difference between samples incubated in 1.5 x and 3 x SBF for 7 days with P< 0.05.
indicates significant differences between samples incubated in 1.5 x SBF for 7 and 21 days with P< 0.02.
Three samples per condition were analyzed.

Table 6S.15. Experimental XRD FWHM values of the peak corresponding to the planes (211), (121), and (202) in ELP_3 membranes incubated in 1.5 x SBF for 7 and 21 days, and in 2 x SBF and 3 x SBF for 7 days.

SBF solution	Time point (days)	XRD FWHM
1.5 x SBF	7	1.2 ± 0.1* $^{+}$ #
	21	0.7 ± 0.2#
2 x SBF	7	1.8 ± 0.2*
3 x SBF	7	1.9 ± 0.2^{+}

* indicates significant differences between samples incubated in 1.5 x and 2 x SBF for 7 days with P<0.05.
$^{++}$ indicates significant difference between samples incubated in 1.5 x and 3 x SBF for 7 days with P< 0.05.
# indicates significant differences between samples incubated in 1.5 x SBF for 7 and 21 days with P< 0.05.
Three samples per condition were analyzed.

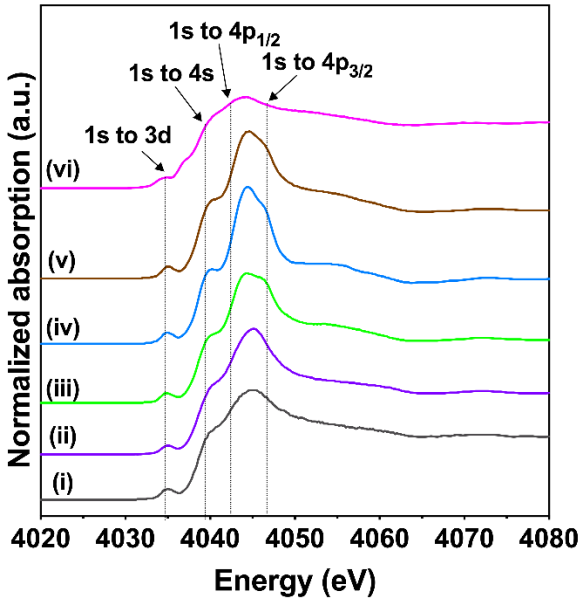

Figure 6S.8. Representative Ca K-edge NEXAFS reference spectra of (i) ELP_3-Ca^{2+}, (ii) ACP, (iii) DCPD, (iv) OCP, (v) HA, (vi) CHA, and (vii) β-TCMP.

Table 6S.16. Percentages of ELP_3-Ca^{2+}, ACP, OCP, HA, and CHA in ELP_3 membranes incubated in 1.5 x, 2 x, and 3 x SBF solutions determined by LCF using Ca K-edge NEXAFS spectra of reference samples, and R-factors of the LCF.

SBF solution	Time point (days)	ELP_3-Ca^{2+} (%)	ACP (%)	OCP (%)	HA (%)	CHA (%)	R-factor
1.5 x SBF	3	30 ± 5	27 ± 7$^{*\,++}$	21 ± 5^{++}	15 ± 5$^{**\,++}$	7 ± 2	0.007 ± 0.003
	5	24 ± 4^{+++}	19 ± 3$^{**\,++}$	20 ± 6^{++}	19 ± 3$^{**\,+++}$	10 ± 4	0.003 ± 0.001
	7	20 ± 4^{***+++}	16 ± 3$^{***\,+++}$	17 ± 3$^{*\,+++}$	33 ± 3$^{**\,+++}$	14 ± 5*	0.005 ± 0.002
	21	0	10 ± 3	10 ± 2	51 ± 6	29 ± 2	0.0003 ± 0.0001
2 x SBF	3	26 ± 4	11 ± 2*	14 ± 3	39 ± 6**	10 ± 4	0.005 ± 0.0002
	5	20 ± 4†††	9 ± 3**	14 ± 4	42 ± 5$^{**\,\dagger\dagger}$	15 ± 3	0.0002 ± 0.0001
	7	0***	0***	7 ± 3$^{*\,\dagger}$	68 ± 5$^{**\,\dagger}$	25 ± 5*	0.003 ± 0.001
3 x SBF	3	25 ± 4	9 ± 3^{++}	10 ± 5^{++}	46 ± 3^{++}	10 ± 4	0.002 ± 0.0005
	5	0$^{+++\,\dagger\dagger\dagger}$	4 ± 1^{++}	7 ± 3^{++}	75 ± 4$^{+++\,\dagger\dagger}$	14 ± 3	0.0004 ± 0.0001
	7	0^{+++}	0^{+++}	0†	84 ± 6†	16 ± 5	0.0004 ± 0.0001

* indicates significant differences between samples incubated in 1.5 x and 2 x SBF with * = P<0.05, ** = P<0.005, ***=P<0.0001.
$^{+}$ indicates significant difference between samples incubated in 1.5 x and 3 x SBF with $^{++}$ = P< 0.005, $^{+++}$ = P< 0.0001.
† indicates significant differences between samples incubated in 2 x and 3 x SBF with † = P< 0.05, †† = P< 0.005, and ††† = P< 0.0001.
Three samples per condition were analyzed.

Chapter 7. Aortic Valve Calcification Follows Different Mineralization Pathways in Men and Women.

While in **Chapters 4**, **5**, and **6**, we studied the molecular mechanism of mineral formation and evolution in medial arterial calcification, in this chapter we studied the process involved in another type of cardiovascular calcification, AVC.

AVC is the most common intrinsic mechanism of valvular obstruction leading to AS. It is a major health issue with high morbidity and mortality. Currently, there is no approved effective treatment and the only available therapeutic option is invasive valve replacement, to which not all patients are suited. The main reason for such lack of treatment options is our lack of understanding of the calcification mechanism. Recently, several studies have shown that for the same aortic stenosis severity, women present significantly lower calcification loads than men. However, the causes of this sex-related differences are still unknown.

To understand sex-dependent differences in AVC, we analyzed mineral deposits from surgically excised calcified human aortic valves from men and women. We show profound differences in mineral composition and morphology between sexes, suggesting that aortic valve calcification follows different mineralization pathways in men and women.

The findings of this study have been submitted to *Proceedings of the National Academy of Sciences of the United States of America* and are currently under review.

Ophélie Gourgas, Kashif Khan, Adel Schwertani, Marta Cerruti. Aortic Valve Calcification Follows Different Mineralization Pathways in Men and Women.

7.1. Abstract

Aortic valve calcification is a pathologic condition resulting in the deposition of calcium phosphate minerals in the extracellular matrix of the aortic valve leaflets. The mineral deposits can severely narrow the opening of the aortic valve, thus leading to aortic stenosis. Currently, there are no therapies to halt or slow down disease progression and the mechanisms governing aortic valve calcification are still poorly understood. Recently, several studies have shown that for the same aortic stenosis severity, women present significantly lower calcification loads than men. However, the causes of this sex-related differences are still unknown, and more work need to be done to understand these mechanisms. Also, while previous studies analyzed minerals present in aortic valve calcification, the impact of sex on the chemical composition and morphology of minerals was never studied.

To address these gaps, in this study we analyzed mineral deposits from surgically excised calcified human aortic valves from men and women. We first assessed the calcified aortic valves for overall levels of calcification and fibrosis using semi-quantitative methods. Then, using a combination of material characterization techniques we analyzed the composition and structure of the minerals. We found profound differences in mineral composition and morphology between sexes, which strongly suggest that minerals form slower in women than in men and follow a different mineralization pathway. These results pave the way for new, sex-specific methods to diagnose, prevent and treat aortic valve calcification.

7.2. Statement of significance

Aortic valve calcification is a health disorder with increasing prevalence and high morbidity and mortality. Currently there is no approved effective treatment; the only available therapeutic option is invasive valve replacement, to which not all patients are suited. The main reason for such lack of treatment options is our lack of understanding of the calcification mechanism. In this study, we show profound differences in mineral composition and morphology between sexes, suggesting that aortic valve calcification follows different mineralization pathways in men and women. These findings pave the way for new approaches specifically geared towards men or women in the diagnosis and treatment of aortic valve calcification.

7.3. Introduction

Aortic stenosis (AS) is the most common valvular heart disease affecting the aging population in developed nations (19, 20). Although several medical treatments are on clinical trials, none of them convincingly halted or slowed down disease progression, and currently there are no therapies for AS (312). Once symptomatic and severe AS has developed, the only available treatment is surgical aortic valve replacement or implantation, to which not all patients are suited (137).

Aortic valve calcification (AVC) is the main intrinsic mechanism of valvular obstruction leading to AS (135, 136) and is present in about 25-30% of the population over the age of 65, and as many as half of those over 85 (138, 139). Until the early 1900s, AVC was regarded as a simple passive age-related degenerative process resulting in the deposition of calcium phosphate (Ca-P) phases in the extracellular matrix (ECM) of the aortic valve leaflets. However, recent studies have shown that AVC is an active, highly

complex process sharing common determinants with intimal arterial calcification, or atherosclerosis (19, 21, 22). Both the latter and AVC result from a sequence of events initiated by inflammation, which stimulates the osteochondrogenic transdifferentiation of myofibroblasts and smooth muscle cells (SMCs) (140). They also share common risk factors including male sex, body mass index, smoking, arterial hypertension, and elevated lipid levels (141). Despite these recent findings, we still lack precise molecular insights into the mechanisms governing AVC.

Although male sex is a well-known risk factor for developing AVC(141, 155, 156), only recently a significant step toward unraveling sex-specific differences in AVC was made. Aggarwal *et al.* (158) provided initial evidence that male sex impacts not only the probability of developing AVC but also the nature of AVC. Specifically, they showed that men present significantly higher AVC loads than women for an equivalent degree of AS, as measured by multi detector computed tomographic (MDCT) imaging (158). This finding was further confirmed by several other studies using both MDCT and echocardiography (23-27).

While the causes of this sex-related difference are still unknown, some studies suggested that hormones may be involved. On one hand, it was shown that estrogen may protect against the progression of valvular calcification (159). Indeed, women tend to develop heart diseases and especially AVC later in life compared to men (163, 164); this could be attributable to the loss of estrogen during menopause. On the other hand, androgens have been reported to have a significant effect on both osteoclast and osteoblast activity and function (165). Along the same lines, it was shown that testosterone plays an important role in promoting calcification of vascular SMCs *in vitro*

(27, 166). However, another *in vitro* study showed that male and female valvular interstitial cells (VICs) behaved differently in a hormone-free environment: male VICs calcified more extensively than female VICs in hormone-free osteogenic medium (167). Another work from Simard *et al.* suggested that the sex-related difference in AVC may be explained by more valvular fibrosis and relatively less valvular calcification in women than men (23). Overall, this shows that the biological explanation for the sexual difference in AVC is likely highly complex and may not rely only on hormonal differences between sexes. Clearly, more work needs to be done to understand the pathophysiological differences between sexes.

To shed some light on the sex differences in AVC, here we analyze the mineral deposits from surgically excised calcified aortic valves from both men and women patients. We first assessed the calcified aortic valves for overall levels of calcification and fibrosis using semi-quantitative methods. Then, using a combination of material characterization techniques including Raman and near edge x-ray absorption fine structure (NEXAFS) spectroscopies, scanning electron microscopy (SEM) and energy-dispersive spectroscopy (EDS), we analyzed the composition and structure of the minerals.

7.4. Methods

7.4.1. Materials

Amorphous calcium phosphate [$Ca_3(PO_4)_2.3H_2O$, (ACP)], dicalcium phosphate dihydrate [$Ca(HPO_4).2H_2O$, (DCPD)], and magnesium-substituted β-tricalcium phosphate [$Ca_{18}(Mg)_2H_2(PO_4)14$, (β-TCMP)]. were purchased from Sigma-Aldrich (Oakville, ON, Canada). Hydroxyapatite [$Ca_{10}(PO_4)_6(OH)_2$, (HA)] was obtained from the National Institute of Standards and Technology (NIST). All materials were used as received.

Carbonated hydroxyapatite [$Ca_{10-p}(PO_4)_{6-p}(OH)_{2-p}(CO_3)_p$ $(0<p<1)$, (CHA)] and octacalcium phosphate [$Ca_8H_2(PO_4)_6. 5H_2O$, (OCP)] were prepared as previously described in (254) and (255), respectively.

7.4.2. Human aortic valve samples

Archived human aortic valve tissues were obtained in accordance with the McGill University Health Centre guidelines. These aortic valves were originally obtained from cardiac valve replacement surgeries from patients with severe AS between 2009 and 2012 at the McGill University Health Centre. The samples were collected in ice cold saline and washed with cold 1x phosphate-buffered saline (PBS) before being snap frozen in liquid nitrogen and transferred to -80 °C freezer for long storage. A total of 109 calcified human aortic valves from both sexes and different ages (71 $\pm$ 13 years old) were collected for valve histology analysis along with a detailed clinical history (Table 7S.1). Lipid profile, aortic valve area (AVA), jet velocity through the aortic valve (jet), the maximum pressure gradient across the valve (Pmax), the mean pressure gradient across the valve (Pmean) and the left ventricular ejection fraction (LVEF) were all noted.

For mineral analysis, 33 calcified human aortic valves were selected (Table SII). The samples were kept in 70% ethanol and then dried under vacuum overnight for mineral characterization.

The study was approved by the McGill University Health Centre and the Montreal Heart Institute ethics committees; we have obtained informed consent from all participants involved in this study.

7.4.3. Human aortic valve histology

The 109 calcified aortic valves were fixed in formalin and embedded in paraffin for histological analysis. The paraffin-embedded tissue blocks were cut into 4 μm sections using a microtome and placed on glass slides. Five sections were examined per lesion. A total of 6 images were analyzed per section.

The degree of valvular calcification was attributed by a visual semi-quantitative score (313, 314): score 0: no calcium deposition; score 1: calcium deposition in < 25% of tissue; score 2: calcium deposition in 25-50% of tissue; score 3: calcium deposition in > 50% of tissue.

The degree of valvular tissue fibrosis was also assessed using a semi-quantitative method (314, 315): score 0: no fibrotic tissue on the section surface; score 1: fibrotic tissue representing < 25% of the section surface; score 2: fibrotic tissue representing 25-50% of the section surface; score 3: fibrotic tissue representing > 50% of the aortic surface.

7.4.4. Raman spectroscopy

The valve samples were analyzed using a Raman spectrophotometer (Senterra, Bruker, Germany) equipped with a 785 nm diode laser of 100 mW power coupled with an Olympus optical microscope. Raman spectra were acquired using a 40x objective, in a spectrum range from 400 to 1800 cm^{-1} at a resolution of 3.5 cm^{-1}. Ten different spots were scanned for each sample with an integration time of 60 seconds and 2 co-additions. The data was analyzed using OPUS software (OPUS 7.0.0, Bruker, Karlsruhe, Germany).

7.4.5. Ca K-edge Near Edge X-ray absorption fine structure (Ca K-edge NEXAFS) spectroscopy

The samples were characterized using Ca K-edge NEXAFS spectroscopy at the bulk-XAFS end-station of the Soft X-ray Microcharacterization Beamline (SXRMB) at the Canadian Light Source (CLS), Saskatoon, Saskatchewan. Powdered reference compounds of known chemical compositions were also analyzed, including ACP, OCP, DCPD, HA, CHA, and β-TCMP. Spectra were collected with energies between 1.7 and 10 keV in fluorescence mode and with a photon beam spot size of 2 mm x 6 mm. Reference spectra were collected in transmission mode while spectra of calcified aortic valves were collected in fluorescence mode. The spectra were calibrated, aligned, and normalized using Athena software (Demeter 0.9.20). Principle component analysis (PCA) was first performed on the spectra to avoid using an excessive number of references in the fitting. Then, linear combination fitting (LCF) was performed on the NEXAFS regions of the spectra using combinations of the reference samples selected by the PCA. The quality of the fits was evaluated by the R-factor value: values below 0.02 indicate that the fitting results are satisfactory (227). For each spectrum, the best LCF combination (i.e.

the combination giving the lowest R-factor) was retained. PCA and LCF were performed using Athena software.

7.4.6. Scanning electron microscopy (SEM) and energy-dispersive X-ray spectroscopy (EDS)

Calcified human aortic valves were characterized using a combination of SEM and EDS. Samples were mounted on an aluminium SEM stub with carbon tape, and then coated with about 20nm carbon (carbon sputter coater, EMS150R ES, Electron Microscopy Sciences (EMS)). The samples were then imaged using an Inspect-50 field emission SEM (FEI, Japan), at 15 kV operating voltage under high vacuum. EDS spectra and elemental maps were obtained in the regions of interest using an EDX spectrometer (EDX, Thermo Scientific, USA).

7.4.7. Statistical analysis

Statistical data analysis was performed using GraphPad software, Inc. (2016). Mean values were expressed as average ± standard deviation. A generalized linear regression model was used to assess the statistical significance of gender and age on all clinical variables including lipid profile and echocardiographic parameters. Significance level was set at $p<0.05$. For Raman and NEXAFS data, statistical analysis on mean values was performed by unpaired t-tests, and $p< 0.05$ was considered statistically significant

7.5. Results and Discussion

Generalized linear regression model shows that there were no significant clinical differences between men and women. Only age was significant for creatinine concentration when adjusting for gender ($P < 0.01$) (Table 7S.1). This is in agreement with previous literature showing that serum creatinine concentration significantly increases with age (316).

We first assessed calcified aortic valves for overall levels of calcification and fibrosis using semi-quantitative methods (313-315). Overall, the calcification score was significantly lower in females compared to males ($P = 0.0004$) (Figure 7.1.A). This is in agreement with previous studies showing lower AVC loads in females than males for the same AS severity (23-27, 158). However, the degree of valvular tissue fibrosis was not significantly different between sexes ($P = 0.6911$) (Figure 7.1.B). This result disagrees with the work from Simard *et al.* (23). While we used only a semi-quantitative method to measure fibrosis in aortic valves, Simard *et al.* used both semi-quantitative scoring and quantitative methods based on histological staining. However, they did not quantify fibrotic tissue in the entire series of samples but only in a small subset of histological sections (24 samples) (23). To the best of our knowledge, Simard's *et al.* is the only report showing significantly higher amounts of fibrotic tissues in women compared to men. Clearly, additional work is required to accurately quantify fibrotic tissue in addition to histological staining, but it seems likely that other mechanisms in addition or alternative to fibrosis may be involved in the observed sex differences in AVC.

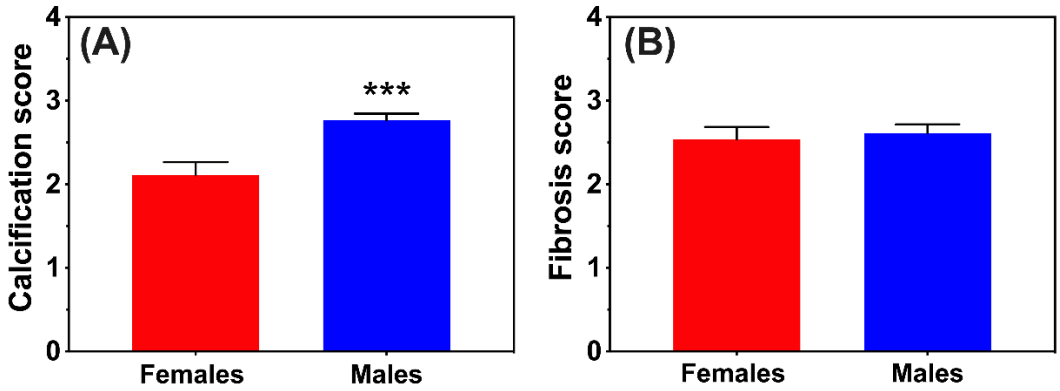

Figure 7.1. Distribution of the **(A)** calcification score and **(B)** fibrosis score in females and males. Welch's t test was used for statistical analysis. ***indicates significant difference between females and males with $P < 0.0005$.

To understand sex-specific differences in AVC we characterized mineral deposits in a subset of 33 calcified aortic valves from men and women with severe AS (Table 7S.2). We first analyzed the composition and crystallinity of the mineral deposits using Raman spectroscopy. The main spectral features of the Raman spectra of calcified aortic valves are related to HA, thus confirming the presence of minerals in the samples (Figure 7.2.A, see the ν_1, ν_4 and ν_2 phosphate peaks; Table 7S.3) (203, 317, 318). Peaks related to the ν_1 and ν_2 carbonate (CO_3^{2-}) stretching modes are also visible on the spectra, thus suggesting that some carbonate ions were incorporated into the HA lattice (Table 7S.3) (203, 233, 317, 318). In agreement with previous studies, these results show that the main mineral phase present in the valve samples is carbonated hydroxyapatite (CHA), similar in composition to the minerals in bone (174, 175, 229, 319). The other peaks visible on the spectra are related to the organic components of the valves (Table 7S.3). The peaks around 1292 and 1661 cm^{-1} are ascribed to the amide III and amide I, respectively (203, 233, 320, 321). The peak around 1003 cm^{-1} is assigned to the C-C stretching of the phenylalanine residue of collagen (320). While most samples show

similar Raman spectra with no strong differences in the mineral region of the spectra, we could not identify distinguishable phosphate or carbonate peaks in five samples (Figure 7S.1.A), implying that the amount of mineral deposits in these samples was too low to be detectable by Raman.

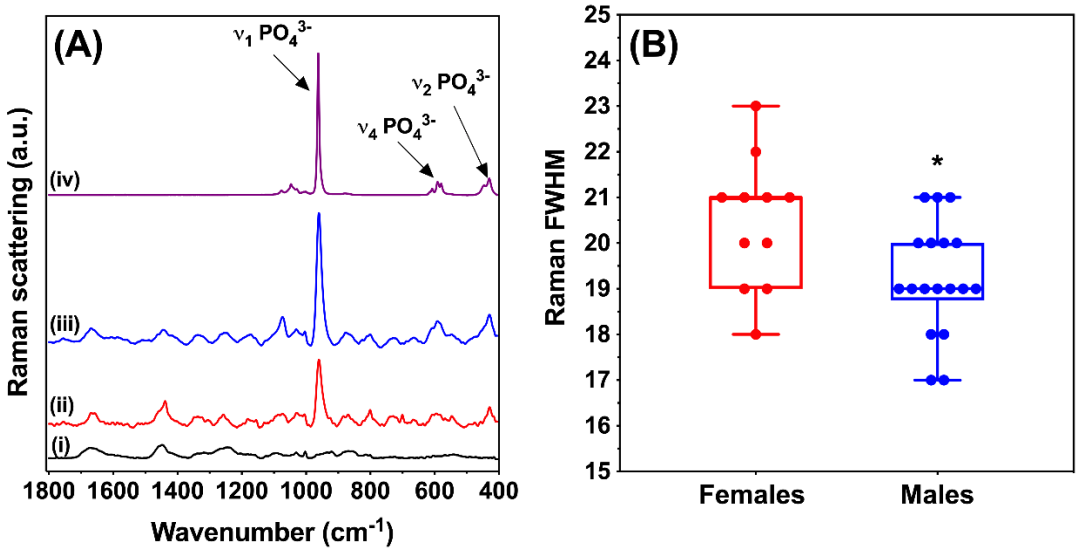

Figure 7.2. (A) Representative Raman spectra of (i) a non-calcified aortic valve, (ii) a calcified aortic valve from female, (iii) a calcified aortic valve from male, and (iv) HA. Arrows point at the ν_1, ν_4 and ν_2 phosphate vibration bands of HA. The spectra were normalized based on the absorbance of the C=O amide I band at 1634 cm^{-1}. **(B)** Distribution of Raman FWHM values in females and males measured on the Raman ν_1 phosphate peak. For each sample, we analyzed 10 different spots and we plotted the value corresponding to the mean of the values measured on the 10 spots. Unpaired t-test was used for statistical analysis. * indicates significant difference between females and males with $P< 0.05$.

By measuring the full width at half maximum (FWHM) of the ν_1 phosphate peak, we estimated the degree of crystallinity of the mineral deposits (see section 1 of the Supplementary Material; Figure 7S.1.B). A wider peak indicates a less crystalline material, while sharper peaks relate to higher crystallinity (222). Although the FWHM values were overall homogeneous within the same sample, they varied greatly between

samples (Table 7S.4). Consistent with previous findings (229, 250), the crystallinity measured on all samples was lower than that found in bone; however, FWHM values were significantly lower in men than women ($P < 0.05$), indicating more crystalline apatite deposits in men (Figure 7.2.B). In fact, while in women the minerals were much less crystalline than the minerals present in mature bone, the apatite deposits in men were almost as crystalline as minerals found in bone (230).

Although apatite phases are the most thermodynamically stable forms of Ca-P at physiological pH, different phases can crystallize, and non-crystalline deposits can form too (181). In fact, several researchers reported the presence of non-apatitic phases such as amorphous calcium phosphate (ACP), octacalcium phosphate (OCP), and dicalcium phosphate dehydrate (DCPD) in AVC (171, 174, 194, 202, 203, 322-324). Our previous analysis of medial calcifications in mice showed that mineral deposition started with amorphous precursors such as ACP and OCP and progressively transformed into more and more crystalline deposits (250). A similar trend is observed during mineral deposition in bone (188, 189, 251). Should a similar process happen in AVC, our finding that minerals are less crystalline in women than in men would imply that mineral deposition in women occurs more slowly than in men.

While Raman spectroscopy shows mineral crystallinity differences between sexes, it cannot determine the nature of Ca-P phases deposited on the valve leaflets. Theoretically, Raman can identify different mineral phases based on the position of the ν_1 phosphate vibration (325). However, this band is sensitive to the local surroundings, the substitution of anionic groups, and the changes in degree of crystallinity; thus, the frequency of the ν_1 phosphate band varies according to several parameters in addition to

Ca-P phase (326). Also, in the valve samples we did not detect distinct peaks, but only a peak centered between 959 and 962 cm^{-1}. This suggests that Raman is not sensitive enough to discriminate different phases in mixed samples. We made a similar observation in our previous analysis of mixed Ca-P phases present in medial calcifications (250)

To identify and quantify the mineral phases present in the samples, we analyzed the calcified aortic valves using Ca K-edge NEXAFS. NEXAFS analyzes how x-rays absorption by an atom is affected by its neighboring atoms, thus acting as local chemical and structural probe. NEXAFS is well suited for our samples since crystallinity is not required (224); thus, it allows us to identify the amorphous and poorly crystalline phases present in the calcified valves, in addition to crystalline HA. To identify the compounds present in the valve samples, we selected as reference samples ACP, OCP, DCPD, β-TCMP, HA, and CHA. We then performed PCA and LCF following the procedure explained in Supplementary Material. NEXAFS spectra of reference samples and calcified aortic valves show four features that are typical of Ca-P compounds (Figure 7S.2 and Figure 7.3.A, respectively) (225, 226). The most intense peak, also called the absorption edge, shows a shoulder peak around 4044 eV assigned to 1s to 4s transitions, and a double peak more intense centered at around 4046 eV, which is assigned to 1s to $4p_{1/2}$ and 1s to $4p_{3/2}$ transitions (225, 226). The small feature at the pre-edge around 4039 eV is due to electronic transitions between 1s and 3d orbitals. Features at higher energies are related to transitions from 1s to higher unoccupied states, or multiple scattering contributions (225, 226).

The LCF results and associated R-factors are presented in Table 7S.5. All the R-factor values were lower than 0.02, thus suggesting that all the fits were satisfactory. We found ACP, OCP, DCPD, HA and CHA in the samples; however, not all these phases were present in all the valves, and the amount of each phase was very variable between samples (Table 7S.5.). We did not detect β-TCMP in any sample.

To simplify the analysis of valve composition, we compared the amount of non-apatitic phases (i.e. ACP, OCP, and DCPD) with that of apatitic phases (i.e. HA and CHA) in the two sexes. Significantly larger amounts of non-apatitic phases were detected in women compared to men ($P< 0.05$) (Figure 7.3.B). A more detailed analysis showed that women had significantly higher amounts of ACP and DCDP than men (Figure 7.3.C and Figure 7.3.D), while the amounts of OCP were not significantly different between sexes (Figure 7S.3). Specifically, DCPD was much more prevalent in women than in men ($P < 0.0002$), with only 3 male samples showing this phase out of the 20 analyzed (Figure 7.3.D).

While in five samples we could not detect apatite deposits by Raman spectroscopy, NEXAFS showed the presence of Ca-P phases in all samples. This confirms that NEXAFS is more sensitive than Raman spectroscopy, and highlights the importance of using NEXAFS in addition to traditional spectroscopic techniques for mineral analysis.

The presence of non-apatitic phases such as ACP, OCP, and DCPD is in line with the literature. ACP and OCP have been identified as the main precursors of biological apatite in physiological calcifications (198, 220) and they have been reported several times in valve calcification (190, 202, 203, 322-324). DCPD is also regarded as a precursor of biological apatite in physiological and in some pathological calcifications, such as dental and urinary calculi (182). Recently, it was also reported in human AVC (202, 203).

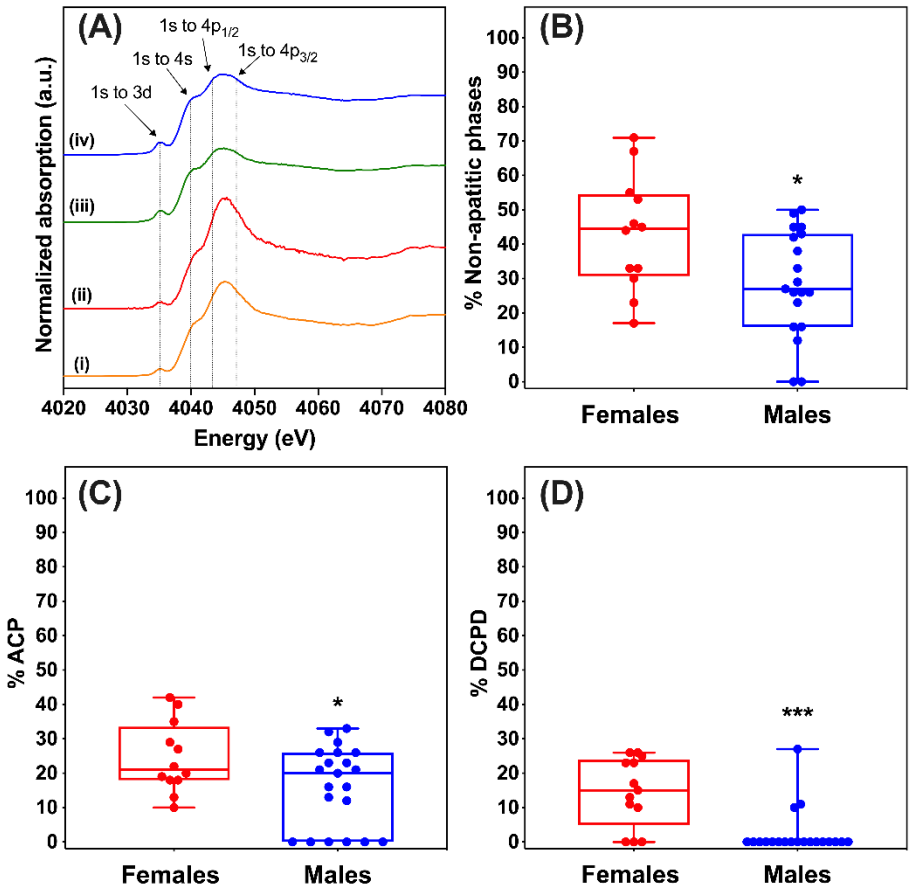

Figure 7.3. (A) Representative Ca K-edge NEXAFS spectra of calcified aortic valves from females ((i): spectrum for sample W103 and (ii): spectrum for sample W100) and males ((iii): spectrum for sample W99 and (iv): spectrum for sample W83). Distribution of the percentage of **(B)** non-apatitic phases, **(C)** ACP, **(D)** and DCPD in females and males determined by LCF based on reference Ca K-edge NEXAFS spectra. Unpaired t-test was used for statistical analysis. * indicate significant differences between females and males with * = P< 0.05 and *** = P<0.0005.

We did not detect β-TCMP in any sample. β-TCMP has been reported as a component of the minerals found in several soft tissue calcifications, such as dental calculi and salivary stones (182). While it was detected in addition to HA in mineral deposits from calcified human mitral valves (171, 327), only one study suggested its presence in AVC (203). However, the presence of β-TCMP in this study was only shown by the shift of the ν_1 phosphate peak from 960 for HA to 970 cm^{-1} by Raman spectroscopy; no other

characterization technique was used to confirm this result and only 11 samples were analyzed (203), thus suggesting that further work will be required to unequivocally determine if β-TCMP is present in AVC.

NEXAFS data show that women are prone to have greater amounts of non-apatitic phases than men for the same AS severity. Since mineralization in both physiological (188, 189, 251) and pathological (250) conditions usually starts from non-apatitic, less crystalline precursors and develops into more crystalline deposits, this result along with the lower HA crystallinity found by Raman strongly suggests that the process of mineral deposition in women occurs more slowly than in men. This would explain why women are found to have lower AVC loads than men for similar AS severity. Also, NEXAFS shows that DCPD is found almost exclusively in women; this implies that the mineralization process in women is not only slower but follows a different mineralization pathway than in men.

To further prove whether different mineralization pathways exist between sexes, we analyzed the morphology and composition of the minerals at a nanoscale level by SEM/EDS. Previous studies have shown that the minerals present in AVC are remarkably different from the platelets found in bone (328, 329). They can be classified as compact materials, calcified fibers, and spherical particles (171, 174, 205, 207, 232). The composition and formation mechanisms of these three distinct structures are still unknown. Only recently, a study showed that the spherical particles are highly crystalline HA (207). Such highly crystalline structures are not found in bone, which is composed only of poorly crystalline CHA. This implies that there are profound differences in mineralization pathways between AVC and bone.

SEM images of calcified valves containing only apatite phases, as determined by NEXAFS, revealed only one distinct mineral structure: compact material (Figure 7.4.A and Figure 7.4.B, Figure 7S.4). This is the typical morphology of HA deposits in AVC (171, 194, 205, 207, 324). Ca/P ratios determined by EDS on these structures are between 1.7 and 1.9, thus confirming the HA nature of the minerals (Figure 7S.4; Table 7S.6 and Table 7S.7) (179). These are the samples with the most uniformly distributed Ca/P ratios.

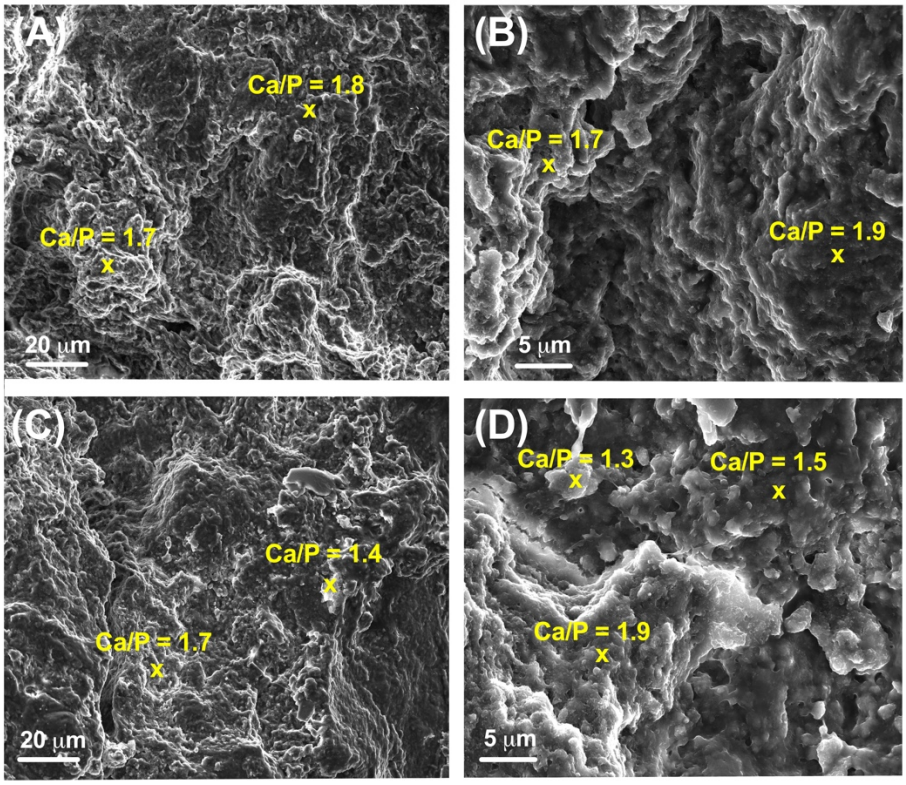

Figure 7.4. SEM images of calcified human aortic valves containing only apatite phases **(A** and **B),** or a combination of non-apatitic and apatite phases but no DCPD **(C** and **D)**. The Ca/P ratios indicated on the SEMs are based on elemental atomic percentages obtained by EDS.

SEM images of calcified valves containing ACP, OCP, HA, and CHA showed the same compact material structure of the minerals (Figure 7.4.C and Figure 7.4.D; Figure 7S.5). However, the Ca/P ratios varied greatly among the same sample, ranging from 1.3 to 1.9, confirming that there is a mix of several phases in these samples (Figure 7.4.C and Figure 7.4.D; Figure 7S.5; Table 7S.8).

Samples containing DCPD, and thus almost exclusively female samples, showed the presence of two other mineral morphologies in addition to compact materials: mineralized fibers forming networks and coalesced spherical particles (Figure 7.5). The latter have variable sizes, with diameters ranging from 100 nm to 5 μm (Figure 7.5.C and Figure 7.5.D). Both calcified fibers and spherical particles were already reported by several studies of AVC (171, 174, 205, 207, 232). While the nature and mineral formation processes of these two structures are still unknown, a recent report showed that the spherical particles are highly crystalline HA, and suggested that these are the first mineralized structures forming in pathological calcifications (207). If this is the case, the observation that spherical particles occur predominantly in female samples supports our previous suggestion that mineral deposition occurs more slowly in women than in men.

EDS measured on the spherical particles confirmed that they are HA (Figure 7.5.D), in agreement with (207) ; however, Ca/P ratios on the fibers were lower than 1.5 (Figure 7.5.A and Figure 7.5.C), suggesting that they could be rich in precursor phases, specifically DCPD (Figure 7S.6;Table 7S.9). The concurrent presence of both highly crystalline spherical particles and fibers containing precursor phases explains the overall lower apatite crystallinity in women than men measured by Raman spectroscopy.

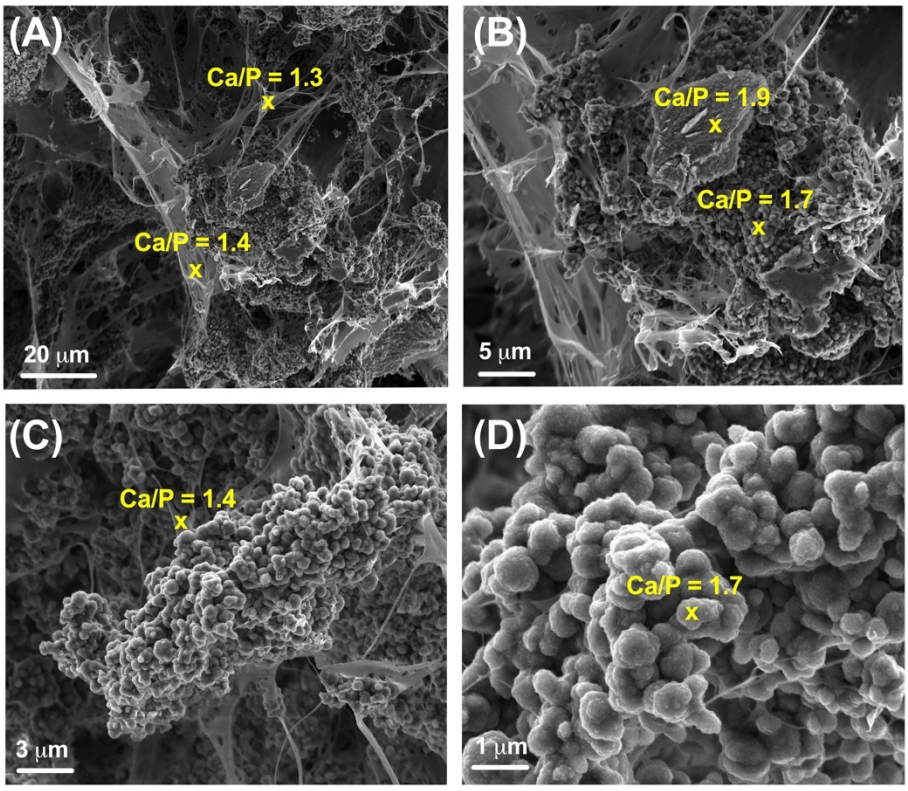

Figure 7.5. SEM images of calcified human aortic valves containing DCPD in addition to other non-apatitic and apatite phases **(A - D)**. The Ca/P ratios indicated on the SEMs are based on elemental atomic percentages obtained by EDS.

7.6. Conclusions

Minerals in AVC have different composition and morphology in men than in women. Calcifications in women are less crystalline and contain larger amounts of ACP and DCPD than in men. In fact, hardly any male sample showed any DCPD. These phase differences are mirrored by differences in morphology. While compact material, calcified fibers, and spherical particles were already identified as the three main mineral morphologies in AVC, here we show that their presence is sex-dependant. Compact material is the only mineral morphology we identify in male calcified aortic valves. In female aortic valve samples,

instead, we show the presence of fibers and spherical particles in addition to HA compact material.

These results suggest that mineralization is slower in women and follows a different pathway than in men: minerals would start from ACP, convert to OCP and further transform into crystalline HA in men, while in women minerals would take longer to transform from ACP to OCP, and transition to DCPD before becoming HA.

Understanding the mechanisms of nucleation and growth of spherical particles and fibers and what stabilizes ACP and DCPD as precursors in women will be crucial to understanding the pathophysiological differences between sexes in AVC. The reasons behind these mineral differences may be biological and intrinsic to tissues, or dependant on hormone levels. But they may be also due to physical chemistry, and relate to different levels of mineralization or phase transformation inhibitors circulating in the blood of female and male patients. To understand this, it will be crucial to perform further experiments, and explore mineral formation and transformation *in vitro* and possibly *in vivo*, in animal models.

Although this mineral analysis was conducted on a small number of patients, the difference between precursor phases and especially DCPD in women vs. men was remarkable. This shows the power of analyzing mineral phases rather than just the overall level of calcification and suggests mineral phase analysis as a new method to diagnose and possibly prevent disease development.

Last but not least, the observed mineral differences may lead to the development of sex-specific treatments: DCPD and the less crystalline deposits found in women may be

easier to eliminate than the crystalline ones found in men. Future treatments may consider exploiting such likely differences in stability.

7.7. Acknowledgments

We acknowledge support from the Canadian Light Source (CLS), which is supported by the Canada Foundation for Innovation, the Natural Sciences and Engineering Research Council of Canada (NSERC) the University of Saskatchewan, the Government of Saskatchewan, the Western Economic Diversification Canada, the National Research Council Canada, and the Canadian Institutes of Health Research. We also thank Dr Yongfeng Hu and Dr Qunfeng Xiao of the CLS for their help with data analysis and technical support. We also acknowledge the Canada Research Chair foundation, the Heart and Stroke Foundation and NSERC for providing funding for this research. Dr. Schwertani is supported by a Discovery grant from NSERC.

7.8. Author Contributions

M.C. and A.S. supervised the research; K.K. prepared the histological sections and run the semi-quantitative analyses; O.G. performed Raman, NEXAFS, SEM, and EDS experiments. O.G. analyzed Raman, NEXAFS, SEM, and EDS data; O.G. and M.C. interpreted all the data; O.G. and K.K. performed statistical analysis; O.G. and M.C. wrote the paper; O.G., K.K., A.S. and M.C. approved the final version of the paper.

7.9. Supplemental material

7.9.1. Section 1: Detailed methods

7.9.1.1. Determination of the full width at half maximum (FWHM) by Raman spectroscopy

We determined the crystallinity of mineral deposits present in calcified aortic valves by measuring the full width at half maximum (FWHM) of the v_1 phosphate peak at around 960 cm^{-1} (Figure 7S.1.B). This peak is of particular interest because of its good resolution. It corresponds to apatitic phosphate environment and gives direct information on the crystallinity index of the sample. The narrower the peak is, the higher the crystallinity index (222, 330).

7.9.1.2. Ca K-edge Near Edge X-ray absorption fine structure (Ca K-edge NEXAFS) spectroscopy

Spectra acquisition

To identify and quantify the Ca-P phases present in the samples, we applied NEXAFS spectroscopy. NEXAFS is a synchrotron-based technique that allows analyzing how x-rays are absorbed by an atom at energies near the core-level binding energies of that atom depending on its chemical and physical environment (224). This technique is suitable for analysis non-crystalline and poorly crystalline mineral phases present in valve calcification since crystallinity is not required for NEXAFS measurements (224). Also, NEXAFS is more sensitive than traditional spectroscopic techniques, with a detection limit that can be as low as few ppm.

Ca K-edge spectra were collected in fluorescence mode with energies between 1.7 and 10 keV and with a photon beam spot size of 2 mm x 6 mm. The storage ring energy during data collection was 2.9 GeV ant the current around 200 mA. The X-ray beam was monochromated by Si (111) crystals with energy resolution ($\Delta E/E$) of 10^{-4}.

Data analysis

We first selected six reference calcium (Ca) species that were already reported in cardiovascular calcifications: amorphous calcium phosphate (ACP), octacalcium phosphate (OCP), dicalcium phosphate dihydrate (DCPD), hydroxyapatite (HA), carbonated hydroxyapatite (CHA), and magnesium-substituted β-tricalcium phosphate (β-TCMP) (171, 174, 175, 194, 202, 203, 319, 322-324).

To determine and quantify the Ca phosphate (Ca-P) phases present in the valve samples, we performed linear combination fitting (LCF) analysis using Athena software (Demeter 0.9.20). LCF is justified because the x-ray absorption from different species in a sample is additive (280). The total absorption coefficient calculated by LCF can be written as:

$$M = \Sigma_i f_i (STD_i), \text{ (i)}$$

where M is the least square fit to the sample spectrum, (STD_i) represents the absorption coefficient of the standard reference spectra, and f_i is the fraction of each reference spectrum in the sample spectrum, summed over the number of references, i. Thus, with appropriate standard references, LCF can identify and quantify the fraction of chemical species in an unknown sample (280).

We first performed principal component analysis (PCA) to determine which reference compounds should be excluded for the LCF fitting and thus avoid using an excessive

number of reference compounds. PCA results did not exclude any reference compounds for the LCF. Thus, we used all the reference compounds we first selected for the LCF analysis. We performed LCF using all the possible combinations of the selected reference compounds. We evaluated the quality of the fits using the R-factor: fitting results with R-factor values below 0.02 are considered satisfactory (227). We reported the LCF combination giving the lowest R-factor for each sample analyzed (Table 7S.5).

7.9.2. Section 2: Supplemental tables and figures

Table 7S.1. Clinical data of patients with aortic valve diseases included for the calculation of calcium and fibrosis scores (total of 109 patients).

Clinical parameter	Females (N=43) (Mean ± SD)	Males (N=66) (Mean ± SD)
Age (years)	71 ± 11	69 ± 13
Total cholesterol (mmol/L)	4 ± 1	4 ± 1
LDL (mmol/L)	2.3 ± 0.9	2.3 ± 0.9
HDL (mmol/L)	1.2 ± 0.3	1.0 ± 0.4
Triglycerides (mmol/L)	1.5 ± 0.9	1.4 ± 0.9
Creatinine (μmol/L)	83 ± 54	100 ± 35 *
Calcium (mmol/L)	2.0 ± 0.3	2.0 ± 0.2
Albumin (mmol/L)	29 ± 8	28 ± 7
AVA (cm^2)	1.0 ± 0.5	1.0 ± 0.7
Jet velocity (cm/s)	390 ± 137	395 ± 122
Pmax (mmHg)	68 ± 39	68 ± 34
Pmean (mmHg)	42 ± 27	41 ± 22
LVEF (%)	61 ± 12	58 ± 14

Abbreviations: SD: standard deviation; LDL: low density lipoprotein; HDL: high density lipoprotein; AVA: aortic valve area; Pmax and Pmean: P-wave duration; LVEF: left ventricular ejection fraction
*P < 0.01 for age when adjusting for gender using a generalized linear model.

Table 7S.2. Clinical data of patients with aortic valve diseases included for the mineral analysis (total of 33 patients, 13 females and 20 males).

Study ID	Age (years)	Sex (F=0, M=1)
W5	71	0
W45	68	1
W46	68	0
W51	35	1
W53	72	1
W54	75	1
W57	74	0
W59	59	1
W60	82	1
W63	65	0
W65	82	1
W66	68	1
W71	74	0
W72	79	1
W73	73	0
W74	78	1
W75	83	1
W77	62	1
W78	78	1
W81	69	1
W82	65	1
W83	55	1
W93	82	0
W94	66	0
W95	75	0
W97	78	0
W98	73	1
W99	71	1
W100	78	0
W101	67	0
W102	74	1
W103	73	0
W104	80	1

Table 7S.3. Raman peak assignments for normal human aortic valve, calcified human aortic valve, and HA.

Peak (cm^{-1})	Normal aortic valve	Calcified aortic valve	HA	References
v C=O (amide I)	1661	1661		(203, 233, 320, 321)
C-H deformation proteins	1444	1444		(203, 233, 320)
δ C-H proteins	1331	1331		(320)
δs N-H (amide III)	1262	1262		(203, 233, 320)
v C-H Tyrosine, Phenylalanine	1182	1182		(320)
v C-C, v C-N in proteins	1155	1155		(320)
v_3 PO_4^3		1073		(203, 317, 318)
v_1 CO_3^{2-}		1071	1072	(233, 317, 318)
v_3 PO_4^{3-}		1046	1046	(317, 318)
v_3 PO_4^{3-}		1031	1032	(203, 317, 318)
v C-C phenylalanine	1003	1003		(320)
v_1 PO_4^{3-}		959-962	960	(203, 233, 317, 318)
v C-C proteins	871	871		(320)
v_2 CO_3^{2-}		826		(203, 317)
U, A, C (DNA)	796	796		(331)
Tryptophan	758	758		(320)
v C-C Phenylalanine	621	621		(320)
v_4 PO_4^{3-}		602	602	(317, 318)
v_4 PO_4^{3-}		591	591	(203, 317, 318)
v_4 PO_4^{3-}		561	560	(317, 318)
v_2 PO_4^{3-}		462	460	(317, 318)
v_2 PO_4^{3-}		426	425	(203, 317, 318)

v: symmetric stretching; δ : bending

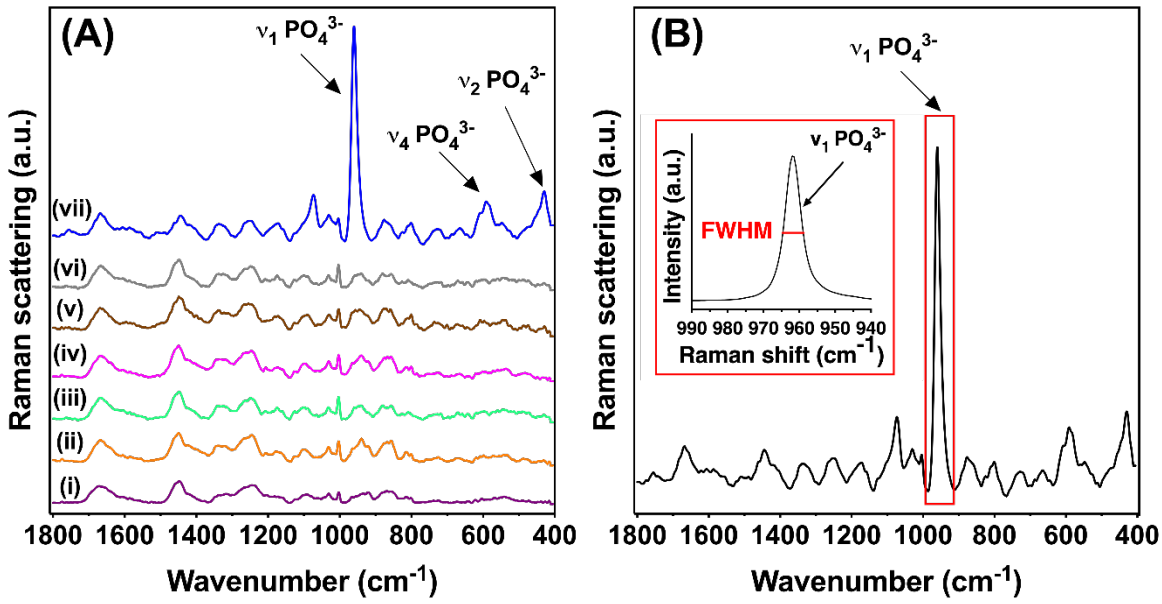

Figure 7S.1. (A) Representative Raman spectra of (i) a non-calcified human aortic valve sample, (ii) W53, (iii) W57, (iv) W60, (v) W94, (vi) W99, and (vii) W66. This figure shows the absence of ν_1, ν_2, and ν_4 phosphate peaks in samples W53, W57, W60, W94, and W99. The spectra were normalized based on the absorbance of the C=O amide I band at 1634 cm^{-1}. **(B)** Raman ν_1 phosphate peak between 945 and 962 cm^{-1} and its FWHM, which was used to estimate mineral crystallinity.

Table 7S.4. Raman FWHM values for calcified human aortic valves.

Study ID	Sex (F=0, M=1)	Raman FWHM
W5	0	19 ± 1
W45	1	19 ± 2
W46	0	21 ± 2
W51	1	21 ± 1
W53	1	/
W54	1	20 ± 2
W57	0	/
W59	1	20 ± 1
W60	1	/
W63	0	20 ± 1
W65	1	19 ± 1
W66	1	19 ± 2
W71	0	22 ± 3
W72	1	20 ± 2
W73	0	21 ± 2
W74	1	17 ± 1
W75	1	21 ± 2
W77	1	18 ± 2
W78	1	19 ± 1
W81	1	19 ± 2
W82	1	18 ± 2
W83	1	18 ± 0.5
W93	0	21 ± 1
W94	0	/
W95	0	20 ± 2
W97	0	21 ± 2
W98	1	19 ± 1
W99	1	/
W100	0	19 ± 1
W101	0	18 ± 0.5
W102	1	19 ± 0.7
W103	0	23 ± 2
W104	1	21 ± 2

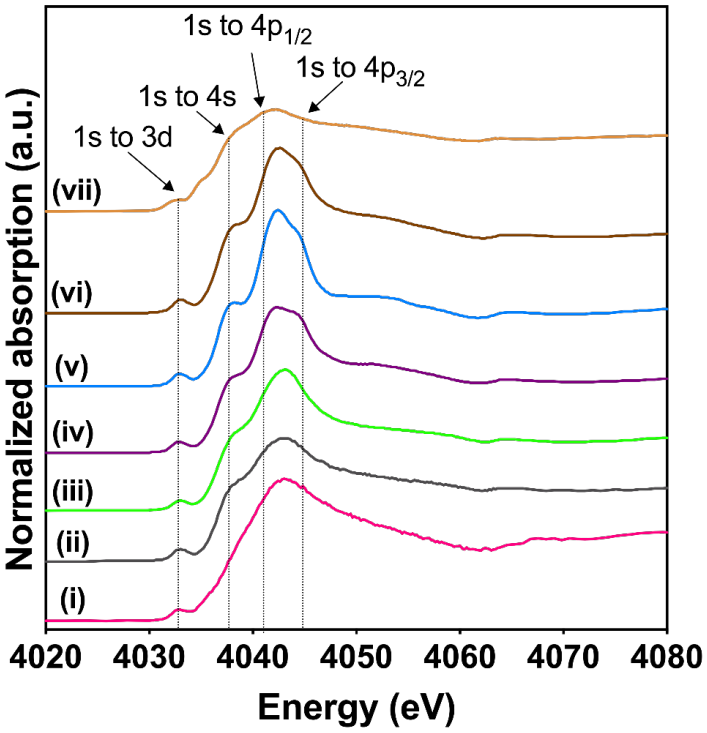

Figure 7S.2. Representative Ca K-edge NEXAFS reference spectra of (i) ACP, (ii) DCPD, (iii) OCP, (iv) HA, (v) CHA, and (vi) β-TCMP.

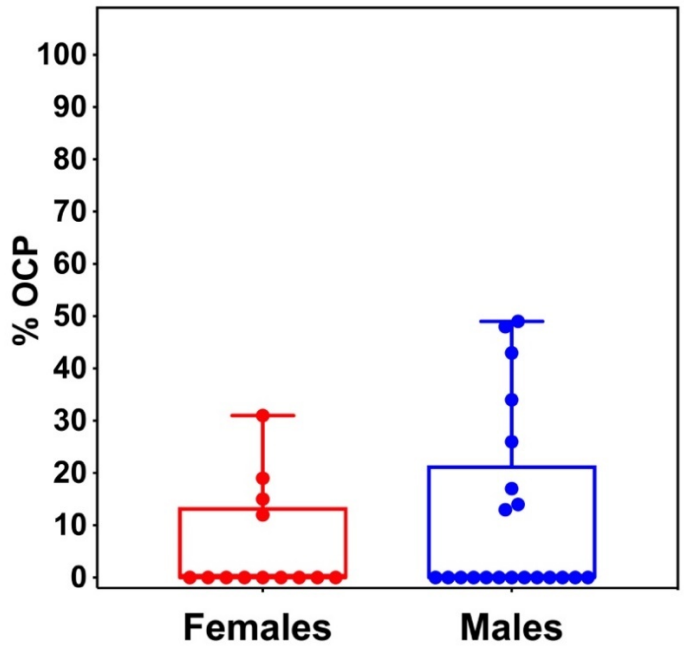

Figure 7S.3. Distribution of the percentage of OCP in females and males determined by LCF based on reference Ca K-edge NEXAFS spectra. Unpaired t-test was used for statistical analysis.

Table 7S.5. Percentages of ACP, OCP, DCPD, HA, and CHA in calcified aortic valves determined by LCF using Ca K-edge NEXAFS spectra of reference samples, and R-factors of the LCF.

Study ID	Sex (F=0, M=1)	ACP (%)	OCP (%)	DCPD (%)	HA (%)	CHA (%)	R-factor
W5	0	40 ± 4	31 ± 6	0	6 ± 1	24 ± 2	0.001903
W45	1	26 ± 4	0	0	61 ± 4	17 ± 5	0.001730
W46	0	42 ± 3	0	25 ± 4	34 ± 3	0	0.001682
W51	1	23 ± 2	0	0	77 ± 1	0	0.002533
W53	1	21 ± 1	53 ± 5	0	26 ± 2	0	0.004378
W54	1	23 ± 2	0	27 ± 3	42 ± 5	9 ± 2	0.001204
W57	0	18 ± 2	15 ± 1	0	27 ± 5	39 ± 7	0.001040
W59	1	16 ± 1	0	0	86 ± 10	0	0.000774
W60	1	0	34 ± 5	11 ± 3	17 ± 2	39 ± 5	0.001301
W63	0	22 ± 8	0	22 ± 3	47 ± 4	9 ± 2	0.002691
W65	1	26 ± 5	17 ± 6	0	30 ± 3	28 ± 5	0.000871
W66	1	0	0	0	52 ± 2	48 ± 1	0.002653
W71	0	35 ± 3	0	11 ± 1	42 ± 3	13 ± 3	0.002259
W72	1	13 ± 1	14 ± 2	0	64 ± 8	10 ± 3	0.002989
W73	0	18 ± 4	12 ± 3	23 ± 5	48 ± 4	0	0.003510
W74	1	33 ± 6	0	0	67 ± 4	0	0.001566
W75	1	32 ± 2	0	10 ± 4	42 ± 2	16 ± 5	0.001582
W77	1	0	13 ± 2	32 ± 5	49 ± 8	7 ± 2	0.001762
W78	1	0	26 ± 3	0	23 ± 2	51 ± 4	0.000358
W81	1	29 ± 5	0	0	50 ± 3	22 ± 9	0.001487
W82	1	26 ± 5	0	0	12 ± 1	63 ± 5	0.001017
W83	1	0	0	0	97 ± 4	0	0.001818
W93	0	0	0	17 ± 3	86 ± 6	0	0.001862
W94	0	27 ± 5	69 ± 8	0	0	0	0.002811
W95	0	20 ± 2	0	10 ± 2	39 ± 6	32 ± 8	0.001983
W97	0	13 ± 3	0	23 ± 6	71 ± 7	0	0.000755
W98	1	12 ± 3	0	0	87 ± 8	0	0.000804
W99	1	20 ± 3	48 ± 6	0	13 ± 4	19 ± 5	0.005657
W100	0	10 ± 2	0	13 ± 3	18 ± 6	60 ± 5	0.000177
W101	0	19 ± 6	0	26 ± 7	40 ± 4	13 ± 3	0.002773
W102	1	0	49 ± 9	0	51 ± 8	0	0.013143
W103	0	29 ± 7	0	26 ± 3	0	45 ± 4	0.001997
W104	1	16 ± 4	0	0	86 ± 9	0	0.000635

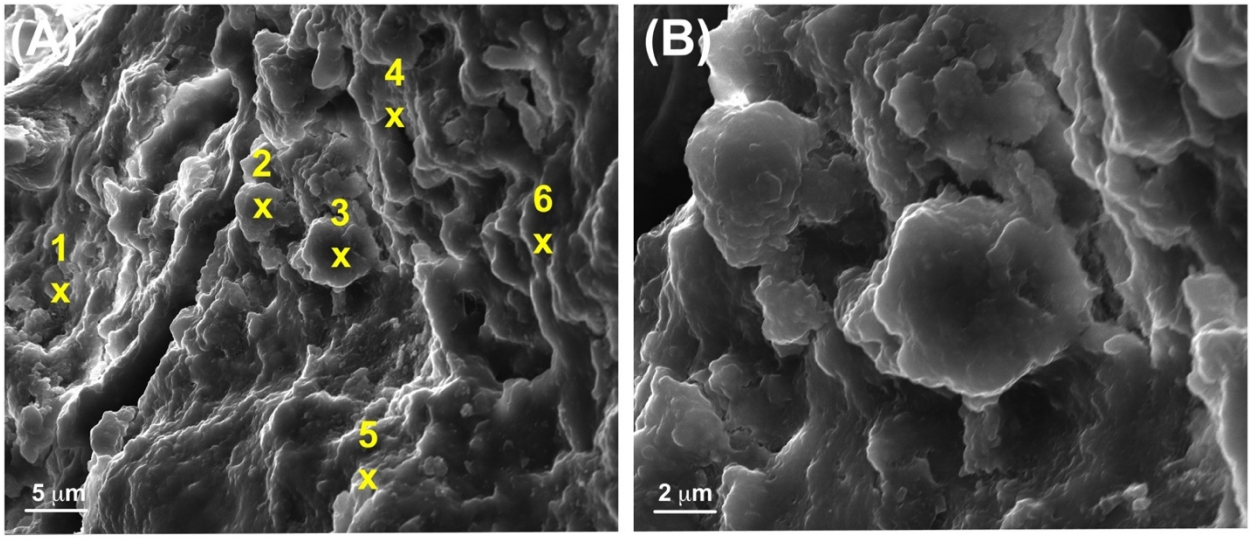

Figure 7S.4. (A and B) scanning electron microscopy (SEM) images of calcified human aortic valves containing only apatite phases as determined by NEXAFS. The numbered sites on **A** indicate the spots where energy dispersive spectroscopy (EDS) spectra were collected and they correspond to the data presented in Table 7S.6.

Table 7S.6. Relative elemental atomic percentages in calcified human aortic valves containing only apatite phases. The sports 1-6 are shown in Figure 7S.4.

Spot	C (at%)	O (at%)	N (at%)	Ca (at%)	P (at%)	Mg (at%)	Na (at%)	Ca/P	Ca/Mg	Ca/Na
1	37.0	39.6	4.7	10.4	5.9	0.6	1.9	1.8	17	5
2	32.5	31	4	18.9	11.1	0.2	0.5	1.7	95	38
3	29.3	39.5	1.0	19.1	10.9	0	0	1.8	/	/
4	36.9	30	1.2	20.6	11.2	0.1	0	1.8	206	/
5	26.8	36.9	1.1	20.4	11.4	0.3	0.1	1.8	68	204
6	32.1	44.3	10.3	6.8	4.1	0.5	1.9	1.7	14	4

Table 7S.7. List of Ca-P compounds found in pathological calcifications and their Ca/P molar ratios (179).

Name	Formula	Ca/P ratio
Amorphous calcium phosphate (ACP)	$Ca_9(PO_4)_6$	1.5
Octacalcium phosphate (OCP)	$Ca_8H_2(PO_4)_6.\ 5H_2O$	1.33
Dicalcium phosphate dihydrate (DCPD)	$Ca(HPO_4).2H_2O$	1.0
Hydroxyapatite (HA)	$Ca_{10}(PO_4)_6(OH)_2$	1.67
Carbonated hydroxyapatite (CHA)	$Ca_{10-p}(PO_4)_{6-p}(OH)_{2-p}(CO_3)_p$ (0<p<1)	> 1.67

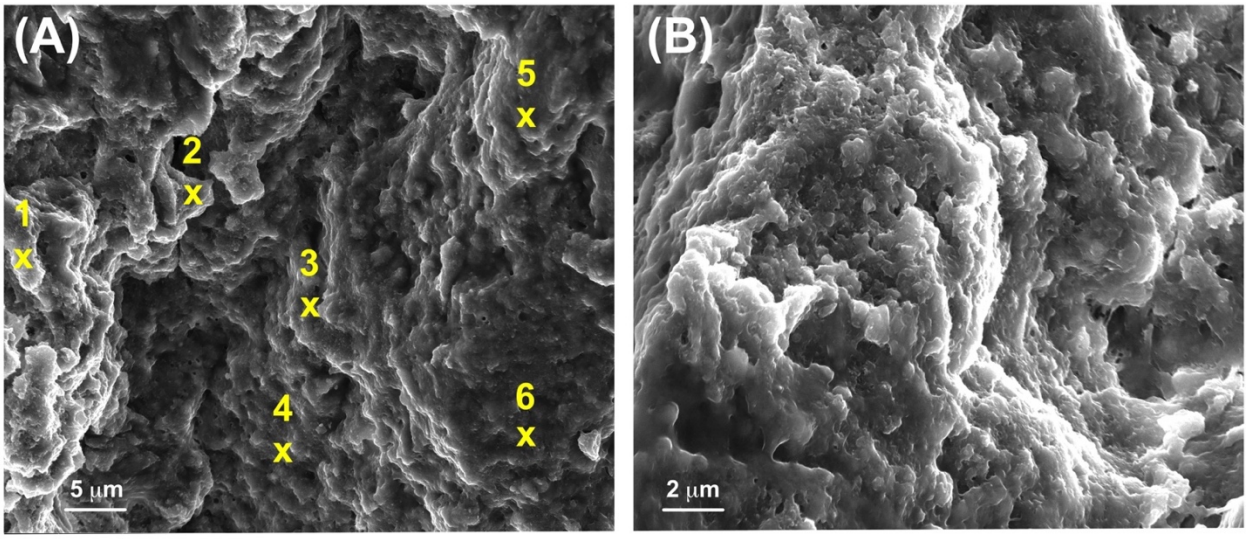

Figure 7S.5. (A and B) SEM images of calcified human aortic valves containing ACP, OCP, HA, and CHA as determined by NEXAFS. The numbered sites on **A** indicate the spots where EDS spectra were collected and they correspond to the data presented in Table 7S.8.

Table 7S.8. Relative elemental atomic percentages in calcified human aortic valves containing ACP, OCP, HA, and CHA. The sports 1-6 are shown in Figure 7S.5.

Spot	C (at%)	O (at%)	N (at%)	Ca (at%)	P (at%)	Mg (at%)	Na (at%)	Ca/P	Ca/Mg	Ca/Na
1	38.6	28.3	3.2	17.6	9.9	0.6	1.8	1.8	29	10
2	39.5	35.8	9.1	8.5	5.1	0.5	1.5	1.7	17	6
3	35.9	39.0	15.1	5.2	3.6	0.2	1.1	1.4	26	5
4	33.6	35.9	12.0	10.3	6.7	0.4	1.1	1.5	26	9
5	28.7	41.2	6.6	14.4	7.6	0.3	0.2	1.9	48	72
6	37.7	39.2	13.8	4.6	3.0	0.3	0.6	1.5	15	8

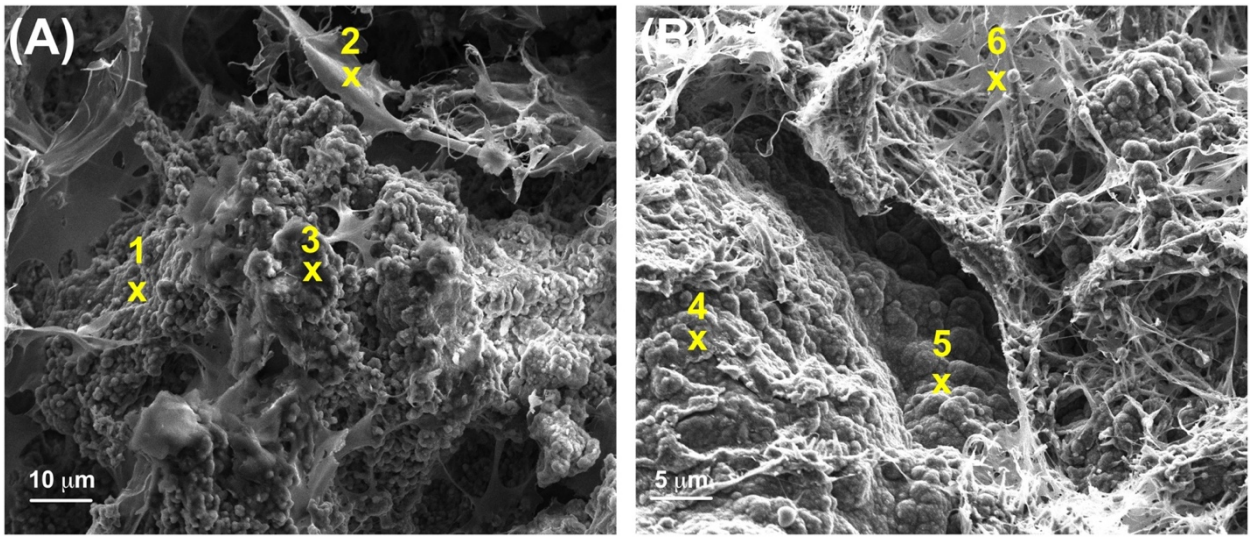

Figure 7S.6. (A and B) SEM images of calcified human aortic valves containing DCPD in addition to other non-apatitic and apatite phases as determined by NEXAFS. The numbered sites on **A** and **B** indicate the spots where EDS spectra were collected and they correspond to the data presented in Table 7S.9.

Table 7S.9. Relative elemental atomic percentages in calcified human aortic valves containing DCPD in addition to other non-apatitic and apatite phases. The sports 1-6 are shown in Figure 7S.6.

Spot	C (at%)	O (at%)	N (at%)	Ca (at%)	P (at%)	Mg (at%)	Na (at%)	Ca/P	Ca/Mg	Ca/Na
1	31.9	43.3	0.7	14.3	7.8	0.8	1.2	1.8	18	12
2	44.5	28.2	5.5	10.4	8.1	1.5	1.8	1.3	7	6
3	20.9	33.0	1.2	28.5	15.9	0.5	0.9	1.8	57	32
4	31.8	42.3	5.9	10.9	6.4	1.1	1.5	1.7	10	7
5	27.2	47.2	3.9	11.9	8.6	1.5	1.1	1.4	8	11
6	29.4	46.5	4.5	10.4	8.1	0.5	0.5	1.3	21	21

Chapter 8. Original contributions

The main motivation of this doctoral project was to study the physico-chemical properties of the mineral deposits and the mineral phase transformations in cardiovascular calcification both *in vivo* and *in vitro*, with the ultimate goal of understanding the underlying molecular mechanisms. This work produced several original contributions presented to the scientific community for the first time, as highlighted below.

- We studied the evolution of mineral nucleation and evolution in a mouse model of medial arterial calcification. In addition to confirming that mineral deposition predominantly happens on the ELN-rich elastic lamina, we showed that mineral composition and crystallinity evolve over time and space. We found that mineral deposition happens through a precise series of events: adsorption of Ca ions on the elastic lamina, formation of ACP and OCP, and transformation to HA and CHA, which are reproduced after each nucleation event throughout the life of the mice. This new knowledge is relevant to understand how minerals interact with ECM and mineralization inhibitors.
- Our results imply that medial calcification is a multistep process like bone formation, starting from amorphous precursors and leading to overall more crystalline apatite deposits. These findings have a substantial clinical implication. An effective strategy to prevent vascular calcification associated with ELN may involve preventing the transformation of metastable and more soluble precursor phases into crystalline apatite deposits.

- We showed that an interdisciplinary approach combining animal models and materials science can provide insights into the mechanism of cardiovascular calcification. We also demonstrated the importance of NEXAFS in mineral analysis and suggested that analyzing the mineral phases rather than just the overall amount of calcification may help diagnose and possibly prevent disease development.
- We developed an *in vitro* model of medial calcification based on ELP membranes incubated in SBF. We showed that mineral deposition first occurs on filament and fiber-like structures, thus showing that the fiber-like nature of ELN makes it prone to calcification. We found that Ca-P phases form and evolve over time in this model similarly to what we reported in MGP-deficient mice, showing that a model based on ELP membranes immersed in SBF captures this crucial *in vivo* finding.
- This *in vitro* model could serve as a simple tool to study hypotheses related to medial arterial calcification mechanisms and to test therapeutic agents designed to stop or reverse calcification.
- We showed that the formation of Ca-P phases on ELP membranes immersed in SBF can significantly be accelerated by increasing SBF ionic concentration.
- We showed that SBF ion concentration is a crucial modulator *in vitro* since it regulates both mineral phase evolution and the final composition and structure of minerals. As the SBF ionic concentration increases, final apatite phases become less crystalline and mostly Ca-deficient, and the mineral deposits

become more disordered and densely packed compared to those formed in lower SBF ion concentration.

- We proposed that SBF ionic concentration can be tuned in our *in vitro* model depending on the *in vivo* situation we want to emulate. While the use of low SBF ion concentration is more appropriate to study medial calcification associated with the loss of calcification inhibitors, higher SBF concentrations may be more relevant to study medial calcification in patients with life-threatening diseases, such as CKD.
- We analyzed mineral deposits formed *in vivo* in the ECM of aortic valve leaflets. We showed profound differences in mineral composition and morphology between sexes, which may be responsible of the lower AVC loads in women compared to men. Calcifications in women are less crystalline and contain larger amounts of ACP and DCDP than in men.
- We showed that the presence of compact material, calcified fibers, and spherical particles in AVC is sex-dependant. Only compact material is detected in men, while female aortic valves show the presence of fibers and spherical particles in addition to compact material,
- We proposed that the mineralization process occurs more slowly in women than in men, and that it follows a different mineralization pathway. These findings have an important clinical implication since they pave the way for new approaches specifically geared towards men or women on diagnosis and treatment of AVC.

Chapter 9. Conclusions and future perspectives

This current work has opened up new areas of research to further understand the molecular mechanisms governing cardiovascular calcification. Future works in this regard may have important clinical implications for the treatment and management of cardiovascular calcification and associated diseases. Specific challenges and future perspectives are highlighted below.

- Our work confirmed the critical role of ELN as the main mineral scaffolding protein in medial arterial calcification. However, despite the large literature on ELN structure, no studies have rigorously studied which domains in ELN are responsible for its calcification. The *in vitro* model that we developed in Chapter 5 could be used to identify the nucleation sites on ELN. By changing the ELP sequence and analyzing the interactions between different ELP membranes with Ca and P ions, the sequence(s) in ELN that are involved in mineral nucleation could be investigated.
- Literature on vascular calcification clearly shows that MGP is a potent calcification inhibitor that prevents mineral deposition on ELN in medial calcification. However, up to now, no one has analyzed the interactions of these two proteins at a molecular level. Also, the exact details of calcification inhibition by MGP are still unknown, and the exact functions of MGP domains are not understood. One could use our *in vitro* model developed in Chapter 5 to identify the functional domain(s) in MGP essential for its anti-mineralization function. By analyzing the extent of Ca and P deposition on ELP membranes incubated in SBF in the presence of different MGP-derived peptides, one could

identify which peptides are the most likely inhibitors of ELN calcification. These findings may be relevant not only to medial calcification, but also more generally to ectopic calcification, since MGP inhibits mineralization in several tissues (trachea, growth plate cartilage, etc.)

- Our *in vitro* model could be easily used to test therapeutic agents designed to prevent the initiation and progression of calcification associated with ELN.
- While our *in vitro* model based on ELP membranes can simulate mineral phase transformation happening in vivo, it does not fully recapitulate the complex biological, structure, physical, and mechanical properties of the arterial wall involved in the initiation and progression of vascular calcification. Thus, a more realistic *in vitro* model that includes both cellular and extracellular components could be built. This model is missing so far in the literature and could become a more reliable tool to test further hypothesis on the mechanism of vascular calcification. For examples, adding lipid plaques could allow extending its use to understand mineral formation in atherosclerotic patients.
- To further understand the pathophysiological differences between sexes in AVC, it will be crucial to investigate the mechanisms of nucleation and growth of spherical particles and fibers, and what stabilizes ACP and DCPD as precursors in women. The reasons behind these profound differences may be biological and intrinsic to tissues, or dependant on hormone levels. But they may be also due to physical chemistry, and relate to different levels of calcification or phase transformation inhibitors circulating in blood serum of female and male patients. Exploring mineral formation and transformation *in*

vitro in presence of several factors, such as hormones and calcification inhibitors, could shed light on these questions. Animal models would be also crucial to understand the causes behind these pathophysiological differences.

- We showed that a material science approach including NEXAFS can provide critical insights that have important applications for understanding medial arterial calcification and AVC. A similar approach could be used to analyze mineral deposits found in intimal arterial calcification and thus get a deep understanding of the underlying molecular mechanism.

References

1. Giachelli C. Ectopic calcification: gathering hard facts about soft tissue mineralization. Am J Pathol. 1999;154(3):671–5.
2. Demer LL, Tintut Y. Vascular calcification: pathobiology of a multifaceted disease. Circulation. 2008;117(22):2938–48.
3. Hutcheson JD, Aikawa E, Merryman WD. Potential drug targets for calcific aortic valve disease. Nat Rev Cardiol. 2014;11(4):218–31.
4. Kelly-Arnold A, Maldonado N, Laudier D, Aikawa E, Cardoso L, Weinbaum S. Revised microcalcification hypothesis for fibrous cap rupture in human coronary arteries. Proc Natl Acad Sci USA. 2013;110(26):10741–6.
5. Shanahan C, Crouthamel M, Kapustin A, Giachelli C. Arterial calcification in chronic kidney disease: key roles for calcium and phosphate. Circ Res. 2011;109(6):697-711.
6. Kramer C, Zinman B, Gross J, Canani L, Rodrigues T, Azevedo M, et al. Coronary artery calcium score prediction of all cause mortality and cardiovascular events in people with type 2 diabetes: systematic review and meta-analysis. BMJ. 2013;346:f1654.
7. Pohle K, Mäffert R, Ropers D, Moshage W, Stilianakis N, Daniel W, et al. Progression of aortic valve calcification: association with coronary atherosclerosis and cardiovascular risk factors. Circulation. 2001;104(16):1927-32.
8. Statistics Canada. Table 102-0561 - Leading causes of death, total population, by age group and sex, Canada, annual, CANSIM (database). [Internet]. Ottawa (ON): Statistics Canada; 2018 Feb 23 [cited 2018 Mar 13]. Available at: http://www5.statcan.gc.ca/cansim/a26?lang=eng&id=1020561. [Internet].
9. Valdivielso J. Vascular calcification: types and mechanisms. Nefrologia. 2011;31(2):142-7.
10. Khavandgar Z, Roman H, Li J, Lee S, Vali H, Brinckmann J, et al. Elastin haploinsufficiency impedes the progression of arterial calcification in MGP-deficient mice. J Bone Miner Res. 2014;29(2):327–37.
11. Schinke T, McKee MD, Karsenty G. Extracellular matrix calcification: where is the action? Nat Genet. 1999;21(2):150-1.
12. Proudfoot D, Shanahan CM, Weissberg PL. Vascular calcification: new insights into an old problem. J Pathol. 1998;185(1):1-3.
13. Lanzer P, Boehm M, Sorribas V, Thiriet M, Janzen J, Zeller T, et al. Medial vascular calcification revisited: review and perspectives. Eur Heart J. 2014;35(23):1515-25.
14. Amann K. Media calcification and intima calcification are distinct entities in chronic kidney disease. Clin J Am Soc Nephrol. 2008;3(6):1599-605.
15. Martin GR, Schiffmann E, Bladen HA, Nylen M. Chemical and morphological studies on the in vitro calcification of aorta. J Cell Biol. 1963;16(2):243-52.
16. Janzen J, Vuong P. Arterial calcifications: morphological aspects and their pathological implications. Z Kardiol. 2001;90(Suppl 3):6-11.
17. Maurice P, Blaise S, Gayral S, L. D, Laffargue M, Hornebeck W, et al. Elastin fragmentation and atherosclerosis progression: the elastokine concept. Trends Cardiovasc Med. 2013;23(6):211-21.

18. Aikawa E, Aikawa M, Libby P, Figueiredo J, Rusanescu G, Iwamoto Y, et al. Arterial and aortic valve calcification abolished by elastolytic cathepsin S deficiency in chronic renal disease. Circulation. 2009;119(13):1785-94.
19. Roberts W, Ko J. Frequency by decades of unicuspid, bicuspid, and tricuspid aortic valves in adults having isolated aortic valve replacement for aortic stenosis, with or without associated aortic regurgitation. Circulation. 2005;111:920-5.
20. Mathieu P, Boulanger M. Basic mechanisms of calcific aortic valve disease. Can J Cardiol. 2014;30:982–93.
21. Owens D, Otto C. Is it time for a new paradigm in calcific aortic valve disease? JACC. 2009;2(8):928-30.
22. Mohler E. Mechanisms of aortic valve calcification. Am J Cardiol. 2004;94:1396–402.
23. Simard L, Côté N, Dagenais F, Mathieu P, Couture C, Trahan S, et al. Sex-related discordance between aortic valve calcification and hemodynamic severity of aortic stenosis: is valvular fibrosis the explanation? Circ Res. 2017;120:681–91.
24. Thomassen H, Cioffi G, Gerdts E, Einarsen E, Midtbø HB, Mancusi C, et al. Echocardiographic aortic valve calcification and outcomes in women and men with aortic stenosis. Heart. 2017;103(20):1619-24.
25. Clavel M, Messika-Zeitoun D, Pibarot P, Aggarwal S, Malouf J, Araoz P, et al. The complex nature of discordant severe calcified aortic valve disease grading: new insights from combined Doppler echocardiographic and computed tomographic study. J Am Coll Cardiol. 2013;62:2329–38.
26. Thaden J, Nkomo V, Suri R, Maleszewski J, Soderberg D, Clavel M, et al. Sex-related differences in calcific aortic stenosis: correlating clinical and echocardiographic characteristics and computed tomography aortic valve calcium score to excised aortic valve weight. Eur Heart J. 2016;37(8):693-9.
27. Simard L, Dagenais F, Pibarot P, Mathieu P, Mahmut A, Couture C, et al. Impact of sex on aortic valve calcification and fibrosis in aortic stenosis. Can J Cardiol. 2015;31(10):S312–S3.
28. Demer L, Tintut Y. Inflammatory, metabolic, and genetic mechanisms of vascular calcification. Arterioscler Thromb Vasc Biol. 2014;34(4):715–23.
29. Vengrenyuk Y, Carlier S, Xanthos S, Cardoso L, Ganatos P, Virmani R, et al. A hypothesis for vulnerable plaque rupture due to stress-induced debonding around cellular microcalcifications in thin fibrous caps. Proc Natl Acad Sci U S A. 2006.;103(40):14678-83. .
30. Virmani R, Burke A, Farb A, Kolodgie F. Pathology of the vulnerable plaque. J Am Coll Cardiol. 2006;47(8 Suppl):C13-C8.
31. Marulanda J, Alqarni S, Murshed M. Mechanisms of vascular calcification and associated diseases. Curr Pharm Des. 2014;20(37):5801-10.
32. Doherty T, Fitzpatrick L, Inoue D, Qiao J, Fishbein M, Detrano R, et al. Molecular, Endocrine, and Genetic Mechanisms of Arterial Calcification. Endocr Rev. 2004;25(4):629-72.
33. Speer M, Giachelli C. Regulation of cardiovascular calcification. Cardiovascular pathology. Cardiovasc Pathol. 2004;13(2):63-70.
34. Bachra B, Fischer H. Recalcification of decalcified bone collagen in vitro as a model for biologic calcification. CalcifTiss Res. 1968:Suppl 7.
35. Reynolds J, Joannides A, Skepper J, McNair R, Schurgers L, Proudfoot D, et al. Human vascular smooth muscle cells undergo vesicle-mediated calcification in response to changes in

extracellular calcium and phosphate concentrations: a potential mechanism for accelerated vascular calcification in ESRD. J Am Soc Nephrol. 2004;15(11):2857-67.
36. Steitz S, Speer M, Curinga G, Yang H, Haynes P, Aebersold R, et al. Smooth muscle cell phenotypic transition associated with calcification: upregulation of Cbfa1 and downregulation of smooth muscle lineage markers. Circ Res. 2001 89(12):1147-54.
37. Chen N, O'Neill K, Duan D, Moe S. Phosphorus and uremic serum up-regulate osteopontin expression in vascular smooth muscle cells. Kidney Int. 2002;62:1724–31.
38. Moe S, Duan D, Doehle B, O'Neill K, NX. C. Uremia induces the osteoblast differentiation factor Cbfa1 in human blood vessels. Kidney Int. 2003;63:1003–11.
39. Moe S, O'Neill K, Duan D, Ahmed S, Chen N, Leapman S, et al. Medial artery calcification in ESRD patients is associated with deposition of bone matrix proteins. Kidney Int. 2002; 61:638–47.
40. Jono S, McKee M, Murry C, Shioi A, Nishizawa Y, Mori K, et al. Phosphate regulation of vascular smooth muscle cell calcification. Circ Res. 2000;87:E10–E7.
41. Yang H, Curinga G, Giachelli C. Elevated extracellular calcium levels induce smooth muscle cell matrix mineralization in vitro. Kidney Int. 2004;66(6):2293-9.
42. Block G, Hulbert-Shearon T, Levin N, Port F. Association of serum phosphorus and calcium x phosphate product with mortality risk in chronic hemodialysis patients: a national study. Am J Kidney Dis. 1998;31(4):607-17.
43. Murshed M, Harmey D, Millan J, McKee M, Karsenty G. Unique coexpression in osteoblasts of broadly expressed genes accounts for the spatial restriction of ECM mineralization to bone. Genes Dev. 2005;19(9):1093-104.
44. Eicher E, Southard J, Scriver C, Glorieux F. Hypophosphatemia: mouse model for human familial hypophosphatemic (vitamin D-resistant) rickets. Proc Natl Acad Sci USA. 1976;73(12):4667-71.
45. Shimada T, Mizutani S, Muto T, Yoneya T, Hino R, Takeda S, et al. Cloning and characterization of FGF23 as a causative factor of tumor-induced osteomalacia. Proc Natl Acad Sci U S A. 2001;98(11):6500-5.
46. Urakawa I, Yamazaki Y, Shimada T, Iijima K, Hasegawa H, Okawa K, et al. Klotho converts canonical FGF receptor into a specific receptor for FGF23. Nature. 2006;444(7120):770-4.
47. Arnold W, Fertala A. Skeletal diseases caused by mutations that affect collagen structure and function. Int J Biochem Cell Biol. 2013;45(8):1556-67.
48. Hosaka N, Mizobuchi M, Ogata H, Kumata C, Kondo F, Koiwa F, et al. Elastin degradation accelerates phosphate-induced mineralization of vascular smooth muscle cells. Calcif Tissue Int. 2009;85:523 – 9.
49. Bostrom M, Boskey A, Kaufman J, Einhorn T. Orthopaedic basic science: Formation and function of bone. Simon SR (eds) Rosemont: American Academy of Orthopaedic Surgeons. 2000.
50. Proudfoot D, Skepper J, Hegyi L, Bennett M, Shanahan C, Weissberg P. Apoptosis regulates human vascular calcification in vitro: evidence for initiation of vascular calcification by apoptotic bodies. Circ Res. 2000;87:1055–62.
51. Durham A, Speer M, Scatena M, Giachelli C, Shanahan C. Role of smooth muscle cells in vascular calcification: implications in atherosclerosis and arterial stiffness. Cardiovasc Res. 2018;114(4):590-600.

52. Vattikuti R, Towler D. Osteogenic regulation of vascular calcification: an early perspective. Am J Physiol Endocrinol Metabol. 2004;286(5):E686-96.
53. Shao J, Cheng S, Pingsterhaus J, Charlton-Kachigian N, Loewy A, Towler D. Msx2 promotes cardiovascular calcification by activating paracrine Wnt signals. J Clinical Investigat. 2005;115(5):1210-20.
54. El-Maadawy S, Kaartinen M, Schinke T, Murshed M, Karsenty G, McKee M. Cartilage formation and calcification in arteries of mice lacking matrix Gla protein. Conect Tissue Res. 2003;44(Suppl 1):272-8.
55. Bostrom K, Tsao D, Shen S, Wang Y, Demer L. Matrix GLA pro-tein modulates differentiation induced by bone morphogeneticprotein-2 in C3H10T1/2 cells. J Biol Chem. 2001;276:14 044–14 52.
56. Zebboudj A, Imura M, K. B. Matrix GLA protein, a regu-latory protein for bone morphogenetic protein-2. J Biol Chem. 2002;277:4388–94.
57. Speer M, Yang H, Brabb T, Leaf E, Look A, Lin W, et al. Smooth muscle cells give rise to osteochondrogenic precursors and chondrocytes in calcifying arteries. Circ Res. 2009 104(6):733-41.
58. Lomashvili K, Wang X, Wallin R, O'Neill W. Matrix Gla protein metabolism in vascular smooth muscle and role in uremic vascular calcification. J Biological Chem. 2011;286(33):28715-22.
59. Villa-Bellosta R, Sorribas V. Phosphonoformic acid prevents vascular smooth muscle cell calcification by inhibiting calcium-phosphate deposition. Arterioscler Thromb Vasc Biol 2009;29(5):761-6. .
60. Sage A, Lu J, Tintut Y, Demer L. Hyperphosphatemia-induced nanocrystals upregulate the expression of bone morphogenetic protein-2 and osteopontin genes in mouse smooth muscle cells in vitro. Kidney Int. 2011;79(4):414-22.
61. Ho C, Shanahan C. Medial Arterial Calcification: An Overlooked Player in Peripheral Arterial Disease. Arterioscler Thromb Vasc Biol. 2016;36(8):1475-82.
62. Hackeng TM. Total chemical synthesis of human matrix Gla protein. Protein Sci. 2001;10(4):864-70.
63. Price P, Faus S, Williamson M. Warfarin causes rapid calcification of the elastic lamellae in rat arteries and heart valves. Arterioscler Thromb Vasc Biol. 1998;18(9):1400-7.
64. Booth S. Skeletal functions of vitamin K-dependent proteins: not just for clotting anymore. Nutrition Rev. 1997;55(7):282-4.
65. Schurgers L, Spronk H, Skepper J, Hackeng T, Shanahan C, Vermeer C, et al. Post-translational modifications regulate matrix Gla protein function: importance for inhibition of vascular smooth muscle cell calcification. J Thromb Haemost. 2007;5(12):2503-11.
66. Munroe P, Olgunturk R, Fryns J, Van Maldergem L, Ziereisen F, Yuksel B, et al. Mutations in the gene encoding the human matrix Gla protein cause Keutel syndrome. Nat Genet. 1999;21(1):142-4.
67. Luo G, Ducy P, McKee M, Pinero G, Loyer E, Behringer R, et al. Spontaneous calcification of arteries and cartilage in mice lacking matrix GLA protein. Nature. 1997;386(6620):78-81.
68. Murshed M, Schinke T, McKee M, Karsenty G. Extracellular matrix mineralization is regulated locally; different roles of two gla-containing proteins. J Cell Biol. 2004;165(5):625-30.

69. O'Young J, Liao Y, Xiao Y, Jalkanen J, Lajoie G, Karttunen M, et al. Matrix Gla protein inhibits ectopic calcification by a direct interaction with hydroxyapatite crystals. J Am Chem Soc. 2011;133(45):18406-12.
70. Schurgers L, Teunissen K, Knapen M, Kwaijtaal M, van Diest R, Appels A, et al. Novel conformation-specific antibodies against matrix gamma-carboxyglutamicacid (Gla) protein: Undercarboxylated matrix Gla protein asmarker for vascular calcification. Arterioscler Thromb Vasc Biol. 2005;25(8):1629–33.
71. Jahnen-Dechent W, Heiss A, Schafer C, Ketteler M. Fetuin-A regulation of calcified matrix metabolism. Circ Res. 2011;108(12):1494-509.
72. Price P, Lim J. The inhibition of calcium phosphate precipitation by fetuin is accompanied by the formation of a fetuin- mineral complex. J Biol Chem. 2003;278(24):22144-52.
73. Mehrotra R. Emerging role for fetuin-A as contributor to morbidity and mortality in chronic kidney disease. Kidney Int. 2007;72(2):137-40.
74. Li Q, Jiang Q, Pfendner E, Varadi A, Uitto J. Pseudoxanthoma elasticum: clinical phenotypes, molecular genetics and putative pathomechanisms. Exp Dermatol. 2009;18(1):1-11.
75. Jiang Q, Dibra F, Lee M, Oldenburg R, Uitto J. Overexpression of fetuin-a counteracts ectopic mineralization in a mouse model of pseudoxanthoma elasticum (abcc6(-/-)). J Investigat Dermatol. 2010;130(5):1288-96.
76. Giachelli C, S. S. Osteopontin: a versatile regulator of inflam- mation and biomineralization. Matrix Biol. 2000;19(615-622.).
77. Ikeda T, Shirasawa T, Esaki Y, Yoshiki S, Hirokawa K. Osteopontin mRNA is expressed by smooth muscle-derived foam cells in human atherosclerotic lesions of the aorta. J Clin Invest. 1993;92(6):2814-20.
78. Fitzpatrick L, Severson A, Edwards W, Ingram R. Diffuse calcification in human coronary arteries. Association of osteopontin with atherosclerosis. J Clin Invest. 1994;94:1597-604.
79. Hirota S, Imakita M, Kohri K, Ito A, Morii E, Adachi S, et al. Expression of osteopontin messenger RNA by macrophages in atherosclerotic plaques. A possible association with calcification. Am J Pathol. 1993;143(4):1003-8.
80. Speer M, McKee M, Guldberg R, Liaw L, Yang H, Tung E, et al. Inactivation of the Osteopontin Gene Enhances Vascular Calcification of Matrix Gla Protein-deficient Mice: Evidence for Osteopontin as an Inducible Inhibitor of Vascular Calcification In Vivo. J Exp Med. 2002;196:1047–55.
81. Paloian N, Giachelli C. A current understanding of vas-cular calcification in CKD. Am J Physiol Renal Physiol. 2014;307(8):F891-F900.
82. Collin-Osdoby P. Regulation of vascular calcification by osteoclast regulatory factors RANKL and osteoprotegerin. Circ Res. 2004;95:1046-57.
83. Zhou S, Fang X, Xin H, Li W, Qiu H, Guan S. Osteoprotegerin inhibits calcification of vascular smooth muscle cell via down regulation of the Notch1-RBP-Jkappa/Msx2 signaling pathway. PLoS One. 2013;8:e68987.
84. Bucay N, Sarosi I, Dunstan C, Morony S, Tarpley J, Capparelli C, et al. Osteoprotegerin-deficient mice develop early onset osteoporosis and arterial calcification. Genes Dev. 1998;12:1260-8.

85. Kazama J, Shigematsu T, Yano K, Tsuda E, Miura M, Iwasaki Y, et al. Increased circulating levels of osteoclastogenesis inhibitory factor (osteoprotegerin) in patients with chronic renal failure. Am J Kidney Dis. 2002;39:525-32.
86. Albalate M, de la Piedra C, Fernández C, Lefort M, Santana H, Hernando P, et al. Association between phosphate removal and markers of bone turnover in haemodialysis patients. Nephrol Dial Transplant. 2006;21(6):1626-32.
87. Johnson K, Polewski M, van Etten D, Terkeltaub R. Chondrogenesis mediated by PPi depletion promotes spontaneous aortic calcification in NPP1-/- mice. Arterioscler Thromb Vasc Biol. 2005;25(4):686-91.
88. de Oliveira R, Okazaki H, Stinghen A, Drüeke T, Massy Z, Jorgetti V. Vascular calcification in chronic kidney disease: a review. J Bras, Nefrol. 2013;35(2):147-61.
89. Yeo G, Keeley F, Weiss A. Coacervation of tropoelastin. Adv Colloid Interface Sci. 2011 167(1-2):94-103.
90. Muiznieks L, Cirulis J, van der Horst A, Reinhardt D, Wuite G, Pomès R, et al. Modulated growth, stability and interactions of liquid-like coacervate assemblies of elastin. Matrix Biol. 2014;36:39-50.
91. Tu Y, Wise S, Weiss A. Stages in tropoelastin coalescence during synthetic elastin hydrogel formation. Micron. 2010;41(3):268-72.
92. Annabi N, Mithieux SM, Camci-Unal G, Dokmeci MR, Weiss AS, Khademhosseini A. Elastomeric Recombinant Proteinbased Biomaterials. Biochem Eng J. 2013;77:110−8.
93. Yeo G, Aghaei-Ghareh-Bolagh B, Brackenreg EP, Hiob M, Lee P, Weiss A. Fabricated Elastin. Adv Healthcare Mater. 2015;4:2530−56.
94. Rosenbloom J. Elastin: An Overview. Methods Enzymol. 1987;144:72−196.
95. Daamen WF, Hafmans T, Veerkamp J, Van Kuppevelt T. Comparison of five procedures for the purification of insoluble elastin. Biomaterials. 2001;22(14):1997−2005.
96. Soskel N, Sandburg L. A comparison of six methods of extracting elastin residue from hamster lungs. Exp Lung Res. 1983;4(2):109−19.
97. Cox B, Starcher B, Urry D. Communication: Coacervation of tropoelastin results in fiber formation. J Biol Chem. 1974;249(3):997−8.
98. Schiffmann E, Lavender D, Miller E, Corcoran B. Amino Acids at the nucleating site in mineralizing elastic tissue. Calcif Tissue Res. 1969;3(1):125-35.
99. Schiffmann E, Martin G, Corcoran B. The role of the matrix in aortic calcification. Arch Biochem Biophys. 1964;107(2):284-91.
100. Rucker R, Goettlich-Riemann W, Tom K. Properties of chick tropoelastin. Biochim Biophys Acta. 1973;317(1).
101. Sandberg L, Weissman N, Gray W. Structural features of tropoelastin related to the sites of cross-links in aortic elastin. Biochemistry. 1971;10(1):52-6.
102. Smith D, Brown D, Carnes W. Preparation and properties of salt-soluble elastin. J Biol Chem. 1972;247(8):2427-32.
103. Ross R, Bornstein P. The elastic fiber I. The Separation and Partial Characterization of its Macromolecular Components. J Cell Biol. 1969;40(2):366–81.
104. Molinari-Tosatti M, Gotte L. Some features of the binding of calcium ions to elastin. Calcif Tissue Res. 1971;6(1):329-34.

105. Sobel A, Leibowitz S, Eilberg R, Lamy F. Nucleation by elastin. Nature. 1966;211(5044):45-7.
106. Petruska J, Sandberg L. The amino acid composition of elastin in its soluble and insoluble state. Biochem Biophys Res Commun. 1968;33(2):222-8.
107. Starcher B, Urry D. Elastin coacervate as a matrix for calcification. Biochem Biophys Res Commun. 1973;53(1):210–6.
108. Urry D, Krivacic J, Haider J. Calcium ion effects a notable change in elastin conformation by interaction with neutral sites. Biochem Biophys Res Commun. 1971;43(1):6-11.
109. Rucker R, Ford D, Riemann W, Tom K. Additional evidence for the binding of calcium ions to elastin at neutral sites. Calcif Tissue Res. 1974;14(1):317-25.
110. Koutsopoulos S, Paschalakis PC, Dalas E. The calcification of Elastin in vitro. Langmuir. 1993;10:2423-8.
111. Miranda-Nieves D, Chaikof EL. Collagen and Elastin Biomaterials for the Fabrication of Engineered Living Tissues. ACS Biomater Sci Eng. 2017;3(5):694-711.
112. Mecham RP. Methods in elastic tissue biology: Elastin isolation and purification. Methods Mol Biol. 2008;45(1):32−41.
113. Urry D, Long M, Cox B, Ohnishi T, Mitchell L, Jacobs M. The Synthetic Polypentapeptide of Elastin Coacervates and Forms Filamentous Aggregates. Biochim Biophys Acta, Protein Struct. 1974;371(2):597-602.
114. Miao M, Bellingham C, Stahl R, Sitarz E, Lane C, Keeley. Sequence and structure determinants for the self-aggregation of recombinant polypeptides modeled after human elastin. J Biol Chem. 2003;278:48553–62.
115. Bellingham C, Woodhouse K, Robson P, Rothstein S, FW. K. Self aggregation characteristics of recombinantly expressed human elastin polypeptides. Biochim Biophys Acta, Protein Struct Mol Enzymol. 2001;1550:6–19.
116. Miao M, Cirulis J, Lee S, Keeley F. Structural determinants of cross-linking and hydrophobic domains for self-assembly of elastin-like polypeptides. Biochemistry. 2005;44(43):14367–75.
117. Keeley F, Bellingham C, Woodhouse K. Elastin as a self-organizing biomaterial: use of recombinantly expressed human elastin polypeptides as a model for investigations of structure and self-assembly of elastin. Philos Trans R Soc, B. 2002;357:185–9.
118. Bellingham C, Lillie M, Gosline J, Wright G, Starcher B, Bailey A, et al. Recombinant human elastin polypeptides self-assemble into biomaterials with elastin-like properties. Biopolymers. 2003;70(4):445–55.
119. Reichheld S, Muiznieks L, Stahl R, Simonetti K, Sharpe S, FW. K. Conformational transitions of the cross-linking domains of elastin during self-assembly. J Biol Chem. 2014;289(14):10057-68.
120. Reichheld S, Muiznieks L, Keeley F, Sharpe S. Direct observation of structure and dynamics during phase separation of an elastomeric protein. Proc Natl Acad Sci U S A. 2017;114(22):E4408-E15.
121. Martin S, Vrhovski B, Weiss A. Total synthesis and expression in Escherichia coli of a gene encoding human tropoelastin. Gene. 1995;154(2):159–66.
122. Clarke A, Arnspang E, Mithieux S, Korkmaz E, Braet F, Weiss A. Tropoelastin massively associates during coacervation to form quantized protein spheres. Biochemistry. 2006;45(33):9989-96.

123. Muiznieks L. Genipin Cross-Linking of Elastin and Elastin-Based Proteins. Methods Mol Biol. 2018;1798:213-21.
124. McHale M, Setton L, Chilkoti A. Synthesis and in vitro evaluation of enzymatically cross-linked elastin like polypeptide gels for cartilaginous tissue repair. Tissue Eng. 2005;11(11-12):1768-79.
125. Tejeda-Montes E, Klymov A, Nejadnik M, Alonso M, Rodriguez-Cabello J, Walboomers X, et al. Mineralization and bone regeneration using a bioactive elastin-like recombinamer membrane. Biomaterials. 2014;35(29):8339-47.
126. Tejeda-Montes E, Smith K, Rebollo E, Gómez R, Alonso M, Rodriguez-Cabello J, et al. Bioactive membranes for bone regeneration applications: effect of physical and biomolecular signals on mesenchymal stem cell behavior. Acta Biomater. 2014;10(1):134-41.
127. Elsharkawy S, Al-Jawad M, Pantano M, Tejeda-Montes E, Mehta K, Jamal H, et al. Protein disorder–order interplay to guide the growth of hierarchical mineralized structures. Nat Commun. 2018;9:2145.
128. Shuturminska K, Tarakina N, Azevedo H, Bushby A, Mata A, Anderson P, et al. Elastin-Like Protein, with Statherin Derived Peptide, Controls Fluorapatite Formation and Morphology. Front Physiol. 2017;8:368.
129. Li Y, Rodriguez-Cabello JC, Aparicio C. Intrafibrillar Mineralization of Self-Assembled Elastin-Like Recombinamer Fibrils. ACS Appl Mater Interfaces. 2017;9:5838-46.
130. Welsh ER, Tirrell DA. Engineering the extracellular matrix: a novel approach to polymeric biomaterials. I. Control of the physical properties of artificial protein matrices designed to support adhesion of vascular endothelial cells. Biomacromolecules. 2000;1:23–30.
131. Jordan SW, Haller CA, Sallach RE, Apkarian RP, Hanson SR, Chaikof EL. The effect of a recombinant elastin-mimetic coating of an ePTFE prosthesis on acute thrombogenicity in a baboon arteriovenous shunt. Biomaterials. 2007; 28:1191–7.
132. Betre H, Setton LA, Meyer DE, Chilkoti A. Characterization of a genetically engineered elastin-like polypeptide for cartilaginous tissue repair. Biomacromolecules. 2002;3(5):910–6.
133. Nettles DL, Kitaoka K, Hanson NA, Flahiff C, Mata BA, Hsu EW, et al. In situ crosslinking elastin-like polypeptide gels for articular cartilage regeneration in a goat osteochondral defect model. Tissue Eng. 2008;14(7):1333–40.
134. Prieto S, Shkilnyy A, Rumplasch C, Ribeiro A, Arias F, Rodríguez-Cabello J, et al. Biomimetic calcium phosphate mineralization with multifunctional elastin-like recombinamers. Biomacromolecules. 2011;12(5):1480-6.
135. Messika-Zeitoun D, Bielak L, Peyser P, Sheedy P, Turner S, Nkomo V, et al. Aortic valve calcification: determinants and progression in the population. Arterioscler Thromb Vasc Biol. 2007;27(3):642-8.
136. Roger V, Go A, Lloyd-Jones D, Adams R, Berry J, Brown T, et al. Heart disease and stroke statistics—2011 update. Circulation. 2011;123(4):e18–e209.
137. Baumgartner H, Falk V, Bax J, De Bonis M, Hamm C, Holm P, et al. ESC/EACTS Guidelines for the management of valvular heart disease: the Task Force for the Management of Valvular Heart Disease of the European Society of Cardiology (ESC) and the European Association for Cardio-Thoracic Surgery (EACTS). Eur Heart J. 2017;38:2739–91.

138. Lindroos M, Kupari M, Heikkila J, Tilvis R. Prevalence of aortic valve abnormalities in the elderly: an echocardiographic study of a random population sample. J Am Coll Cardiol. 1993;21:1220–5.
139. Freeman R, Otto C. Spectrum of calcific aortic valve disease: Pathogenesis, disease progression, and treatment strategies. Circulation. 2005;111:3316-26.
140. New S, Aikawa E. Molecular imaging insights into early inflammatory stages of arterial and aortic valve calcification. Circ Res. 2011;108:381–1391.
141. Stewart B, Siscovick D, Lind B, Gardin J, Gottdiener J, Smith V, et al. Clinical factors associated with calcific aortic valve disease. Cardiovascular Health Study. J Am Coll Cardiol. 1997;29(3):630–4.
142. Rajamannan N, Evans F, Aikawa E, Grande-Allen K, Demer L, Heistad D, et al. Calcific aortic valve disease: not simply a degenerative process: A review and agenda for research from the National Heart and Lung and Blood Institute Aortic Stenosis Working Group. Executive summary: Calcific aortic valve disease-2011 update. Circulation. 2011;124(16):1783-91.
143. Otto C, Kuusisto J, Reichenbach D, Gown A, O'Brien K. Characterization of the early lesion of 'degenerative' valvular aortic stenosis, Histological and immunohistochemical studies. Circulation. 1994;90(844-853).
144. Hutcheson J, Goettsch C, Bertazzo S, Maldonado N, Ruiz J, Goh W, et al. Genesis and growth of extracellular-vesicle-derived microcalcification in atherosclerotic plaques. Nat Mater. 2016;15(3):335-43.
145. Mohler Er, Gannon F, Reynolds C, Zimmerman R, Keane M, Kaplan F. Bone formation and inflammation in cardiac valves. Circulation. 2001;103(11):1522-8.
146. El Accaoui R, Gould S, Hajj G, Chu Y, Davis M, Kraft D, et al. Aortic valve sclerosis in mice deficient in endothelial nitric oxide synthase. Am J Physiol Heart Circ Physiol. 2014;306:H1302–H13.
147. Pawade T, Newby D, Dweck M. Calcification in aortic stenosis: the skeleton key. J Am Coll Cardiol. 2015;66:561–77.
148. Peeters F, Meex S, Dweck M, Aikawa E, Crijns H, Schurgers L, et al. Calcific aortic valve stenosis: hard disease in the heart: A biomolecular approach towards diagnosis and treatment. Eur Heart J. 2018;39(28):2618-24.
149. Garg V, Muth A, Ransom J, Schluterman M, Barnes R, King I, et al. Mutations in NOTCH1 cause aortic valve disease. Nature. 2005;437(7056):270-4.
150. Nigam V, Srivastava D. Notch1 represses osteogenic pathways in aortic valve cells. J Mol Cell Cardiol. 2009;47:828–34.
151. Bostrom K, Watson K, Stanford W, Demer L. Atherosclerotic calcification: relation to developmental osteogenesis. Am J Cardiol. 1995;75:88B–91B.
152. Yang X, Fullerton D, Su X, Ao L, Cleveland JJ, Meng X. Pro- osteogenic phenotype of human aortic valve interstitial cells is associated with higher levels of Toll-like receptors 2 and 4 and enhanced expres- sion of bone morphogenetic protein 2. J Am Coll Cardiol. 2009;53:491–500.
153. Yang X, Meng X, Su X, Mauchley D, Ao L, Cleveland JJ, et al. Bone morpho- genic protein 2 induces Runx2 and osteopontin expression in human aortic valve interstitial cells: role of Smad1 and extracellular signal-regulated kinase 1/2. J Thorac Cardiovasc Surg. 2009;138(4):1008–15.

154. Côté N, El Husseini D, Pépin A, Guauque-Olarte S, Ducharme V, Bouchard-Cannon P, et al. ATP acts as a survival signal and prevents the mineralization of aortic valve. J Mol Cell Cardiol. 2012;52:1191–202.
155. Owens D, Katz R, Takasu J, Kronmal R, Budoff M, O'Brien K. Incidence and progression of aortic valve calcium in the Multi-ethnic Study of Atherosclerosis (MESA). Am J Cardiol. 2010;105:701–8.
156. Mohler E, Sheridan M, Nichols R, Harvey W, Waller B. Development and progression of aortic valve stenosis: atherosclerosis risk factors– a causal relationship? A clinical morphologic study. Clin Cardiol. 1991;14:995–9.
157. Porras A, McCoy C, Masters K. Calcific Aortic Valve Disease: A Battle of the Sexes. Circ Res. 2017;120(4):604-6.
158. Aggarwal S, Clavel M, Messika-Zeitoun D, Cueff C, Malouf J, Araoz P, et al. Sex differences in aortic valve calcification measured by multidetector computed tomography in aortic stenosis. Circ Cardiovasc Imaging. 2013;6(1):40-7.
159. Sritharen Y, Enriquez-Sarano M, Schaff H, Casaclang-Verzosa G, Miller J. Pathophysiology of Aortic Valve Stenosis: Is It Both Fibrocalcific and Sex Specific?. Physiology (Bethesda). 2017;32(3):182-96.
160. Chambliss K, Wu Q, Oltmann S, Konaniah E, Umetani M, Korach K, et al. Non-nuclear estrogen receptor alpha signaling promotes cardiovascular protection but not uterine or breast cancer growth in mice. J Clin Invest. 2010;120:2319 –30.
161. Cho J, Cadet P, Salamon E, Mantione K, Stefano G. The nongenomic protective effects of estrogen on the male cardiovascular system: clinical and therapeutic implications in aging men. Med Sci Monit. 2003;9:RA63–RA8.
162. Osako M, Nakagami H, Koibuchi N, Shimizu H, Nakagami F, Koriyama H, et al. Estrogen inhibits vascular calcification via vascular RANKL system: common mechanism of osteoporosis and vascular calcification. Circ Res. 2010;107:466–75.
163. Kannel W, Dawber T, Kagan A, N. R, Stokes Jr. Factors of risk in the development of coronary heart disease–six year follow-up experience. The Framingham Study. Ann Intern Med. 1961;55:33–50.
164. Shaw L, Bairey Merz C, Pepine C, Reis S, Bittner V, Kelsey S, et al. Insights from the NHLBI-Sponsored Women's Ischemia Syndrome Evaluation (WISE) study: part I: gender differences in traditional and novel risk factors, symptom evaluation, and gender-optimized diagnostic strategies. J Am Coll Cardiol. 2006;47:S4–S20.
165. Vanderschueren D, Vandenput L, Boonen S, Lindberg M, Bouillon R, Ohlsson C. Androgens and bone. Endocr Rev. 2004;25:389–425.
166. Zhu D, Hadoke P, Wu J, Vesey A, Lerman D, Dweck M, et al. Ablation of the androgen receptor from vascular smooth muscle cells demonstrates a role for testosterone in vascular calcification. Sci Rep. 2016;6:24807.
167. Masjedi S, Lei Y, Patel J, Ferdous Z. Sex-related differences in matrix remodeling and early osteogenic markers in aortic valvular interstitial cells. Heart Vessels. 2016;32(2):217-28.
168. McCoy C, Nicholas D, Masters K. Sex- related differences in gene expression by porcine aortic valvular interstitial cells. PLoS One. 2012;7:e39980.
169. Tomazic B. Characterization of Mineral Phases in Cardiovascular Calcification. Hydroxyapatite and related compounds; San Francisco: CRC Press; 1994. p.

93-116.
170. Rajamannan N, Subramaniam M, Rickard D, Stock S, Donovan J, Springett M, et al. Human aortic valve calcification is associated with an osteoblast phenotype.
. Circulation. 2003;107(17):2181-4.
171. Danilchenko S, Kuznetsov V, Stanislavov A, Kalinkevich A, Starikov V, Moskalenko R, et al. The mineral component of human cardiovascular deposits: morphological, structural and crystal-chemical characterization. Cryst Res Technol. 2013;48(3):153-62.
172. Clarke R, Hanlon E, Brody H, Isner J. Detection of calcific deposits in atherosclerotic lesions by laser Raman spectroscopy. J Raman Spectrosc. 1988;19(3):183–8.
173. Szytula A, Rokita E. X-ray analysis of mineral substances of blood vessels. X-ray and Neutron Structure Analysis in Material Science. JHasek Planum Press New York. 1989:85-8.
174. Prieto R, Gomila I, Söhnel O, Costa-Bauza A, Bonnin O, Grases F. Study on the structure and composition of aortic valve calcific deposits: etiological aspects. J Biophys Chem. 2011;2(1):19–25.
175. Cottignoli V, Cavarretta E, Salvador L, Valfré C, Maras A. Morphological and Chemical Study of Pathological Deposits in Human Aortic and Mitral Valve Stenosis: A Biomineralogical Contribution. Pathol Res Int. 2015;2015:1-14.
176. Rey C, Combes C, Drouet C, Glimcher MJ. Bone mineral: update on chemical composition and structure. Osteoporosis Int. 2009;20(6):1013–21.
177. Elliott JC. Calcium phosphate biominerals. Rev Mineral Geochem. 2002;48:427-53.
178. Wopenka B, Pasteris JD. A mineralogical perspective on the apatite in bone. Mater Sci Eng C. 2005;25:131-43.
179. Cosmidis J, Benzerara K, Nassif N, Tyliszczak T, Bourdelle F. Characterization of Caphosphate biological materials by scanning transmission X-ray microscopy (STXM) at the Ca L2,3-, P L2,3- and C K-edges. Acta Biomaterialia. 2015;12:260–9.
180. Schmid K, McSharry W, Pameijer C, Binette J. Chemical and physicochemical studies on the mineral deposits of the human atherosclerotic aorta. Atherosclerosis. 1980;37(2):199-210.
181. Eanes E, Gillessen I, Posner A. Intermediate states in the precipitation of hydroxyapatite. Nature. 1965;208:365–7.
182. LeGeros R. Formation and transformation of calcium phosphates: relevance to vascular calcification. Z Kardiol. 2001;90(Suppl 3):III/116–III/24.
183. Termine J, Eanes E. Comparative chemistry of amorphous and apatitic calcium phosphate preparations. Calcif Tissue Res. 1972;10:171-97.
184. Meyer J, Eanes E. A thermodynamic analysis of the amorphous to crystalline calcium phosphate transformation. Calcif Tiss Res. 1978;28:59-68.
185. Termine J, Peckauskas R, Posner A. Calcium phosphate formation in vitro. II. Effects of environment on amorphous-crystalline transformation. Arch Biochem Biophys J. 1970;140:318-25.
186. Johnsson M, Nancollas G. The role of brushite and octacalcium phosphate in apatite formation. Crit Rev Oral Biol Med. 1992;3(1-2):61-82.
187. Dorozhkin S. Calcium orthophosphates.Occurrence, properties, biomineralization, pathological calcification and biomimetic applications. Biomatter. 2011 1(2):121–64.

188. Mahamid J, Aichmayer B, Shimoni E, Ziblat R, Li C, Siegel S, et al. Mapping amorphous calcium phosphate transformation into crystalline mineral from the cell to the bone in zebrafish fin rays. Proc Natl Acad Sci U S A. 2010;107(14): 6316-21.
189. Mahamid J, Sharir A, Addadi L, Weiner S. Amorphous calcium phosphate is a major component of the forming fin bones of zebrafish: Indications for an amorphous precursor phase. Proc Natl Acad Sci U S A. 2008;105(35):12748-53.
190. Rey C, Hina A, Tofighi A. Maturation of poorly crystalline apatites: chemical and structural aspects in vivo and in vitro. Cells Mater. 1995;5(4):345–56.
191. Rey C, Shimizu M, Collins B, Glimcher M. Resolution-enhanced Fourier transform infrared spectroscopy study of the environment of phosphate ion in the early deposits of a solid phase of calcium phosphate in bone and enamel and their evolution with age: 2. Investigations in the nu3PO4 domain. Calcif Tissue Int. 1991;49(6):383-8.
192. Kim K, Trump B. Amorphous calcium precipitations in human aortic valve. Calcif Tiss Res. 1975;18(2):155-60.
193. Verberckmoes S, Persy V, Behets G, Neven E, Hufkens A, Zebger-Gong H, et al. Uremia-related vascular calcification: more than apatite deposition. Kidney Int. 2007;71(4):298–303.
194. Dritsa V, Pissaridi K, Koutoulakis E, Mamarelis I, Kotoulas C, Anastassopoulou J. An infrared spectroscopic study of aortic valve. A possible mechanism of calcification and the role of magnesium salts. In Vivo. 2014;28:91-8.
195. Gilinskaya LG, Grigorieva TN, Okuneva GN, Vlasov YA. Investigation of phatogenic mineralization on human heart valves. I. Chemical and phase composition. J Struct Chem. 2003;44(4):622-31.
196. Wang L, Nancollas G. Calcium orthophosphates: crystallization and dissolution. Chem Rev. 2008;108:4628–69.
197. Brown W. Crystal growth of bone mineral. Clin, Orthop Relat Res. 1966;44:205-20.
198. Brown W, Eidelman N, Tomazic B. Octacalcium phosphate as a precursor in biomineral formation. Adv Dent Res. 1987;1(2):306–13.
199. Brown W, Smith J, Lehr J, Frazier A. Octacalcium phosphate and hydroxyapatite: crystallographic and chemical relations between octacalcium phosphate and hydroxyapatite. Nature. 1962;196:1050-5.
200. Lu X, Leng Y. Theoretical analysis of calcium phosphate precipitation in simulated body fluid. Biomaterials. 2005;26(10):1097-108.
201. Tung M, Brown W. An intermediate state in hydrolysis of amorphous calcium phosphate. Calcif Tissue Int. 1983;35(6):783-90.
202. Mikroulis D, Mavrilas D, Kapolos J, Koutsoukos P, C. L. Physicochemical and microscopical study of calcific deposits from natural and bioprosthetic heart valves. Comparison and implications for mineralization mechanism. J Mater Sci Mater Med. 2002;13(9):885-9.
203. Pilarczyk M, Czamara K, Baranska M, Natorska J, Kapusta P, Undas A, et al. Calcification of aortic human valves studied in situ by Raman microimaging: following mineralization from small grains to big deposits. J Raman Spectrosc. 2013;44:1222-9.
204. Schlieper G, Aretz A, Verberckmoes S, Krüger T, Behets G, Ghadimi R, et al. Ultrastructural analysis of vascular calcifications in uremia. J Am Soc Nephrol. 2010;21(4):689–96.

205. Weska R, Aimoli C, Nogueira G, Leirner A, Maizato M, Higa O, et al. Natural and Prosthetic Heart Valve Calcification: Morphology and Chemical Composition Characterization. Artif Organs. 2010;34(4):311-8.
206. Marra S, Daghlian C, MF. F, Kennedy F. Elemental composition, morphology and mechanical properties of calcified deposits obtained from abdominal aortic aneurysms. Acta Biomater. 2006;2(5):515-20.
207. Bertazzo S, Gentleman E, Cloyd K, Chester A, MH. Y, Stevens M. Nano-analytical electron microscopy reveals fundamental insights into human cardiovascular tissue calcification. Nat Mater. 2013;12(6):576-83.
208. Russell R. Bisphosphonates: the first 40 years. Bone. 2011;49(1):2-19.
209. Simon J. Are all bisphosphonates the same? Potential reasons for clinical differences: a perspective. J Women's Health. 2010;19(4):719-27.
210. Boskey A. Bone mineral crystal size. Osteoporos Int. 2003;14(Suppl 5):S16–S20. discussion S–11.
211. Persy V, De Broe M, Ketteler M. Bisphosphonates prevent experimental vascular calcification: Treat the bone to cure the vessels? Kidney Int. 2006;70:1537–8.
212. Nitta K, Akiba T, Suzuki K, Uchida K, Watanabe R, Majima K, et al. Effects of cyclic intermittent etidronate therapy on coronary artery calcification in patients receiving long-term hemodialysis. Am J Kidney Dis. 2004;44(680–688.).
213. Toussaint N, Lau K, Strauss B, Polkinghorne K, Kerr P. Effect of alendronate on vascular calcification in CKD stages 3 and 4: a pilot randomized controlled trial. Am J Kidney Dis. 2010;56:57–68.
214. Mathew S, Tustison K, Sugatani T, Chaudhary L, Rifas L, Hruska K. The mechanism of phosphorus as a cardiovascular risk factor in CKD. J Am Soc Nephrol. 2008;19(6):1092-105.
215. Qunibi W, Moustafa M, Muenz L, He D, Kessler P, Diaz-Buxo J, et al. A 1-year randomized trial of calcium acetate versus sevelamer on progression of coronary artery calcification in hemodialysis patients with comparable lipid control: the Calcium Acetate Renagel Evaluation-2 (CARE-2) study. Am J Kidney Dis. 2008;51:952–65.
216. Shao J, Cai J, Towler D. Molecular mechanisms of vascular calcification: lessons learned from the aorta. Arterioscler Thromb Vasc Biol. 2006;26(7):1423–30.
217. Sage A, Tintut Y, Demer L. Regulatory mechanisms in vascular calcification. Nat Rev Cardiol. 2010;7(9):528–36.
218. Abedin M, Tintut Y, Demer L. Vascular calcification: mechanisms and clinical ramifications. Arterioscler Thromb Vasc Biol. 2004;24:1161–70.
219. Duer M, Friscić T, Proudfoot D, Reid D, Schoppet M, Shanahan C, et al. Mineral surface in calcified plaque is like that of bone: further evidence for regulated mineralization. Arterioscler Thromb Vasc Biol. 2008;28(11):2030–4.
220. Barrère F, van Blitterswijk C, de Groot K. Bone regeneration: molecular and cellular interactions with calcium phosphate ceramics. Int J Nanomedicine. 2006;1:317–32.
221. Khosroshahi H, Sahin S, Akyuz Y, Ede H. Long term follow-up of four patients with Keutel syndrome. Am J Med Genet A. 2014;164A:2849– 56.
222. Shemesh A. Crystallinity and diagenesis of sedimentary apatites. Geochim Cosmochim Acta. 1990;54:2433–8.

223. Morris M, Mandair G. Raman assessment of bone quality. Clin Orthop Relat Res. 2011;469(2160–2169).
224. Koningsberger D, Mojet B, Van Dorssen G, Ramaker D. XAFS spectroscopy; fundamental principles and data analysis. Top Catal. 2000;10:143–55.
225. Asokan K, Jan J, Chiou J, Pong W, Tseng P, Lin I. X-ray absorption spectroscopy studies of Ba(1-x)Ca(x)TiO3. J Synchrotron Radiat. 2001;8:839–41.
226. Eichert D, Salomé M, Banu M, Susini J, C. R. Preliminary characterization of calcium chemical environment in apatitic and non-apatitic calcium phosphates of biological interest by X-ray absorption spectroscopy. Spectrochimica Acta Part B. 2005;60:850–8.
227. Ravel B, Newville M. ATHENA, ARTEMIS, HEPHAESTUS: data analysis for X-ray absorption spectroscopy using IFEFFIT. J Synchrotron Radiat. 2005;12:537–41.
228. Leroux-Berger M, Queguiner I, Maciel T, Ho A, Relaix F, Kempf H. Pathologic calcification of adult vascular smooth muscle cells dif- fers on their crest or mesodermal embryonic origin. J Bone Miner Res. 2011;26:1543–53.
229. Mangialardo S, Cottignoli V, Cavarretta E, Salvador L, Postorino P, Maras A. Pathological biominerals: Raman and infrared studies of bioapatite deposits in human heart valves. Appl Spectrosc. 2012;66:1121–7.
230. Goodyear S, Gisbon I, Skale J, Wells R, Aspden R. A comparison of cortical and trabecular bone from C57 Black 6 mice using Raman spectroscopy. Bone. 2009;44:899–907.
231. Kay M, Young R, Posner A. Crystal structure of hydroxyapatite. Nature. 1964;204:1050–2.
232. Bertazzo S, Gentleman E. Aortic valve calcification: a bone of contention. Eur Heart J. 2017;38(16):1189-93.
233. Otero E, Sathaiah S, Jr L, Pomerantzeff P, Pasqualucci C. Raman spectroscopy for diagnosis of calcification in human heart valves. Spectroscopy. 2004;18(1):75-84.
234. Pu J, Mintz G, Brilakis E, Banerjee S, Abdel-Karim A, Maini B, et al. In vivo characterization of coronary plaques: novel findings from comparing greyscale and virtual histology intravascular ultrasound and near-infrared spectroscopy. Eur Heart J. 2012;33:372–83.
235. Baraga J, Feld M, Rava R. In situ optical histochemistry of human artery using near infrared Fourier transform Raman spectroscopy. Proc Natl Acad Sci U S A. 1992;89:3473–7.
236. Termine J, Posner A. Infrared analysis of rat bone: Age dependency of amorphous and crystalline mineral fraction. Science. 1966;113(3743):1523-5.
237. Cameron G, Cairns D, Wess T. The variability in type I collagen helical pitch is reflected in the D periodic fibrillar structure. J Mol Biol. 2007;372(4):1097-107.
238. Reyes-Gasga J, Martínez-Piñeiro E, Rodríguez-Álvarez G, Tiznado-Orozco GE G-, García R, Brès E. XRD and FTIR crystallinity indices in sound human tooth enamel and synthetic hydroxyapatite. Mater Sci Eng, C. 2013;33(8):4568–74.
239. Iafisco M, Foltran I, Sabbatini S, Tosi G, Roveri N. Electrospun nanostructured fibers of collagen-biomimetic apatite on titanium alloy. Bioinorg Chem Appl. 2012;123953.
240. Koutsopoulos S. Synthesis and Characterization of hydroxyapatite crystals: a review study on the analytical methods. J Biomed Mater Res, Part A. 2002;62(4):600-12.
241. Kavukcuoglu N, Li Q, Pleshko N, Uitto J. Connective Tissure Mineralization in Abcc6-/- mice, a model for Pseudoxanthoma Elasticum. J Matrix Biol. 2012;31(4):246-52.

242. Salenius J, Brennan J, Miller A, Wang Y, Aretz T, Sacks B, et al. Biochemical composition of human peripheral arteries examined with Near-Infrared Raman Spectroscopy. J Vasc Surg. 1998;27(4):710-9.
243. Buschman H, Deinum G, Feld M. Raman microspectroscopy of human coronary atherosclerosis: biochemical assessment of cellular and extracellular morphologic structures in situ. Cardiovasc Pathol. 2001;10:69-82.
244. Nelson D, Williamson B. Raman spectra of Phosphate and Monofluorophosphate Ion in several Dentally-Relevant Materilas. Caries Res. 1984;19(2):113-21.
245. Sage A, Tintut Y, Demer L. Regulatory mechanisms in vascular calcification. Nat Rev Cardiol. 2010;7(9):528–36.
246. Giachelli C. Ectopic calcification: gathering hard facts about soft tissue mineralization. Am J Pathol. 1999;154(3):671–5.
247. Seligman M, Eilberg R, Fishman L. Mineralization of elastin extracted from human aortic tissues. Calcif Tissue Res. 1975;17(3):229-34.
248. Khavandgar Z, Roman H, Li J, Lee S, Vali H, Brinckmann J, et al. Elastin haploinsufficiency impedes the progression of arterial calcification in MGP-deficient mice. J Bone Miner Res. 2014;29:327–37.
249. Reid JD, Andersenb ME. Medial calcification (whitlockite) in the aorta. Atherosclerosis. 1993;101(2):213-24.
250. Gourgas O, Marulanda J, Zhang P, Murshed M, Cerruti M. Multidisciplinary Approach to Understand Medial Arterial Calcification. Arterioscler Thromb Vasc Biol. 2018;38:363-72.
251. Lotsari A, Rajasekharan AK, Halvarsson M, Andersson M. Transformation of amorphous calcium phosphate to bone-like apatite. Nat Commun. 2018;9:4170.
252. Wise S, Yeo G, Hiob M, Rnjak-Kovacina J, Kaplan D, Ng M, et al. Tropoelastin - a versatile, bioactive assembly module. Acta Biomater. 2014;10(4):1532–41.
253. Poursamara S, Lehnerb A, Azamic M, Ebrahimi-Baroughc S, Samadikuchaksaraei A, Antunes APM. The effects of crosslinkers on physical, mechanical, and cytotoxic properties of gelatin sponge prepared via in-situ gas foaming method as a tissue engineering scaffold. Mater Sci Eng, C. 2016;63(1):1-9.
254. Nassif N, Martineau F, Syzgantseva O, Gobeaux F, Willinger M, Coradin T, et al. In Vivo Inspired Conditions to Synthesize Biomimetic Hydroxyapatite. Chem Mater. 2010;22(2):3653-63.
255. LeGeros R. Preparation of octacalcium phosphate (OCP): a direct fast method. Calcif Tissue Int. 1985 37(2):194-7.
256. Kokubo T, Takadama H. How useful is SBF in predicting in vivo bone bioactivity? Biomaterials. 2006;27(15):2907-15.
257. Vieth S, Bellingham C, Keeley F, Hodge S, Rousseau D. Microstructural and tensile properties of elastin-based polypeptides crosslinked with genipin and pyrroloquinoline quinone. Biopolymers. 2007;85(3):199-206.
258. Starcher B. A Ninhydrin-Based Assay to Quantitate the Total Protein Content of Tissue Samples. Anal Biochem. 2001;292(1):125–9
259. Chung M, Miao M, Stahl R, Chan E, Parkinson J, Keeley F. Sequences and domain structures of mammalian, avian, amphibian and teleost tropoelastins: Clues to the evolutionary history of elastins. Matrix Biol. 2006;25(8):492–504.

260. Cirulis J, Bellingham C, Davis E, Hubmacher D, Reinhardt D, Mecham R, et al. Fibrillins, fibulins, and matrix-associated glycoprotein modulate the kinetics and morphology of in vitro self-assembly of a recombinant elastin-like polypeptide. Biochemistry. 2008;47(47):12601-13.
261. Kozel B, Ciliberto C, Mecham R. Deposition of tropoelastin into the extracellular matrix requires a competent elastic fiber scaffold but not live cells. Matrix Biol. 2004;23(1):23-34.
262. Kozel B, Rongish B, Czirok A, Zach J, Little C, Davis E, et al. Elastic fiber formation: a dynamic view of extracellular matrix assembly using timer reporters. J Cell Physiol. 2006;207(1):87-96.
263. Bressan G, Pasquali-Ronchetti I, Fornieri C, Mattioli F, Castellani I, Volpin D. Relevance of aggregation properties of tropoelastin to the assembly and structure of elastic fibers. J Ultrastruct Mol Struct Res. 1986;94(3):209-16.
264. Bressan G, Castellani I, Giro M, Volpin D, Fornieri C, Pasquali Ronchetti I. Banded fibers in tropoelastin coacervates at physiological temperatures. J Ultrastruct Res. 1983;82(3):335-40.
265. Moghanian A, Firoozi S, Tahriri M, Sedghi A. A comparative study on the in vitro formation of hydroxyapatite, cytotoxicity and antibacterial activity of 58S bioactive glass substituted by Li and Sr. Mater Sci Eng, C. 2018;1(91):349-60.
266. Tavafoghi Jahromi M, Yao G, M. C. The importance of amino acid interactions in the crystallization of hydroxyapatite. J R Soc, Interface. 2012;10(80):20120906.
267. Shin K, Jayasuriya A, Kohn D. Effect of ionic activity products on the structure and composition of mineral self assembled on three-dimensional poly(lactide-co-glycolide) scaffolds. J Biomed Mater Res, Part A. 2007;83(4):1076-86.
268. Mahjoubi H, Kinsella J, Murshed M, Cerruti M. Surface Modification of Poly(d,l-Lactic Acid) Scaffolds for Orthopedic Applications: A Biocompatible, Nondestructive Route via Diazonium Chemistry. ACS Appl Mater Interfaces. 2014;6(13):9975-87.
269. Zuo Q, Lu S, Du Z, Friis T, Yao J, Crawford R, et al. Characterization of nano-structural and nano-mechanical properties of osteoarthritic subchondral bone. BMC Musculoskeletal Disord. 2016;17(1):367.
270. Paschalis EP, Mendelsohn R, Boskey AL. Infrared Assessment of Bone Quality: A Review. Clin Orthop Relat Res. 2011;469(8):2170–8.
271. Gadaleta SJ, Paschalis EP, Betts F, Mendelsohn R, Boskey AL. Fourier Transform Infrared Spectroscopy of the Solution-Mediated Conversion of Amorphous Calcium Phosphate to Hydroxyapatite: New Correlations Between X-Ray Diffraction and Infrared Data. Calcif Tissue Int. 1996;58(1):9–16.
272. Farlay D, Panczer G, Rey C, Delmas P, Boivin G. Mineral maturity and crystallinity index are distinct characteristics of bone mineral. J Bone Miner Metab. 2010;28(4):433–45.
273. Huang N, Short M, Zhao J, Wang H, Lui H, Korbelik M, et al. Full range characterization of the Raman spectra of organs in a murine model. Opt Express. 2012;19(23):22892-909.
274. Debelle L, Alix A, Jacob M, Huvenne J, Berjot M, Sombret B, et al. Bovine elastin and k-elastin secondary structure determination by optical spectroscopies. J Biol Chem. 1995;270(44):26099-103.
275. Frushour B, Koenig J. Raman scattering of collagen, gelatin, and elastin. Biopolymers. 1975;14(2): 379-91.
276. Muiznieks L, Keeley F. Biomechanical Design of Elastic Protein Biomaterials: A Balance of Protein Structure and Conformational Disorder. ACS Biomater Sci Eng. 2017;3(5):661-79.

277. Miao M, Reichheld S, Muiznieks L, Sitarz E, Sharpe S, Keeley F. Single nucleotide polymorphisms and domain/splice variants modulate assembly and elastomeric properties of human elastin. Implications for tissue specificity and durability of elastic tissue. Biopolymers. 2017;107(5):1-20.
278. Miao M, Sitarz E, Bellingham C, Won E, Muiznieks L, Keeley F. Sequence and domain arrangements influence mechanical properties of elastin-like polymeric elastomers. Biopolymers. 2013;99(6):392-407.
279. Rey C, Renugopalakrishnan V, Shimizu M, Collins B, Glimcher MJ. A resolution-enhanced Fourier Transform Infrared spectroscopic study of the environment of the CO32− ion in the mineral phase of enamel during its formation and maturation. Calcif Tissue Int. 1991;49(4):259–68.
280. Gaur A, Shrivastava B, Joshi S. Copper K-edge XANES of Cu (I) and Cu (II) oxide mixtures. J Phys: Conf Ser. 2009;190:012084.
281. Popescu M, Vasile C, Craciunescu O. Structural analysis of some soluble elastins by means of FT-IR and 2D IR correlation spectroscopy. Biopolymers. 2010;93(12):1072-84.
282. Vyavahare N, Ogle M, Schoen F, Levy R. Elastin Calcification and its Prevention with Aluminum Chloride Pretreatment. Am J Pathol. 1999;155(3):973–82.
283. Serrano V, Liu W, Franzen S. An Infrared Spectroscopic Study of the Conformational Transition of Elastin-Like Polypeptides. Biophys J. 2007;93(7):2429–35. .
284. Belbachir K, Noreen R, Gouspillou G, Petibois C. Collagen types analysis and differentiation by FTIR spectroscopy. Anal Bioanal Chem. 2009;395(3):829-37.
285. Rey C, Shimizu M, Collins B, Glimcher MJ. Resolution-enhanced Fourier transform infrared spectroscopy study of the environment of phosphate ions in the early deposits of a solid phase of calcium-phosphate in bone and enamel, and their evolution with age. I: Investigations in the v4 PO4 domain. Calcif Tissue Int. 1990;46:384-94.
286. Gourgas O, Muiznieks L, Guadarrama Bello D, Nanci A, Sharpe S. Crosslinked Elastin-Like Polypeptide (ELP) Membranes as a Model for Medial Arterial Calcification. Manuscript submitted for publication. 2019.
287. Barrere F, van Blitterswijk CA, de Groot K, Layrolle P. Nucleation of biomimetic Ca-P coatings on ti6A14V from a SBF x 5 solution: influence of magnesium. Biomaterials. 2002;23(10):2211-20.
288. Barrere F, van Blitterswijk CA, de Groot K, Layrolle P. Influence of ionic strength and carbonate on the Ca-P coating formation from SBF×5 solution. Biomaterials. 2002;23:1921–30.
289. Kim H, Kishimoto K, Miyaji F, Kokubo T, Yao T, Suetsugu Y, et al. Composition and structure of the apatite formed on PET substrates in SBF modified with various ionic activity products. J Biomed Mater Res A. 1999;46(2):228-35.
290. Chesnutt B, Yuan Y, Brahmandam N, Yang Y, Ong J, Haggard W, et al. Characterization of biomimetic calcium phosphate on phosphorylated chitosan films. J Biomed Mater Res A. 2007;82(2):343-53.
291. Chen Y, Mak A, Li J, Wang M, Shum A. Formation of apatite on poly(alpha-hydroxy acid) in an accelerated biomimetic process. J Biomed Mater Res B Appl Biomater. 2005;73(1):68-76.
292. Al-Munajjed AA, Plunkett NA, Glesson JP, Weber T, Jungreuthmayer C, Levingstone T, et al. Development of a Biomimetic Collagen-hydroxyapatite Scaffold for Bone Tissue Engineering Using a SBF Immersion Technique. J Biomed Mater Res B Appl Biomater. 2009;90(2):584-91.

293. Chou Y, Chiou W, Xu Y, Dunn J, Wu B. The effect of pH on the structural evolution of accelerated biomimetic apatite. Biomaterials. 2004;25(22):5323-31.
294. Costa D, Allo B, Klassen R, Hutter J, Dixon S, Rizkalla A. Control of surface topography in biomimetic calcium phosphate coatings. Langmuir. 2012;28(8):3871-80.
295. Kokubo T, Abe Y. Apatite coating on ceramics, metals and polymers utilizing a biological process. J Mater Sci Mater Med. 1990;1(4):233–8.
296. Kokubo T, Kushitani H, Sakka S, Kitsugi T, Yamamuro T. Solutions able to reproduce in vivo surface-structure change in bioactive glass-ceramic A–W. J Biomed Mater Res A. 1990;24:721-34.
297. Kokubo T. Bioactive glass ceramics: properties and applications. Biomaterials. 1991;12:155-63.
298. Ohtsuki C, Kushitani H, Kokubo T, Kotani S, Yamamuro T. Apatite formation on the surface of Ceravital-type glass-ceramic in the body. J Biomed Mater Res A. 1991;25:1363-70.
299. Oyane A, Kim HM, Furuya T, Kokubo T, Miyazaki T, Nakamura T. Preparation and assessment of revised simulated body fluids. J Biomed Mater Res A. 2003;65A:188-95.
300. Takadama H, Hashimoto M, Mizuno M, Kokubo T. Round-robin test of SBF for in vitro measurement of apatite-forming ability of synthetic materials. Phos Res Bull. 2004;17:119-25.
301. Eanes E, Rattner S. The effect of magnesium on apatite formation in seeded supersaturated solutions at pH 7.4. J Dent Res. 1981;60(9):1719-23.
302. Kibalczyc W, Christoffersen J, Christoffersen MR, Zielenkiewicz A, Zielenkiewicz W. The effect of magnesium ions on the precipitation of calcium phosphates. J Cryst Growth. 1990.;106:355–66.
303. Barrere F, Layrolle P, van Blitterswijk C, de Groot K. Biomimetic calcium phosphate coatings on Ti6AI4V: a crystal growth study of octacalcium phosphate and inhibition by Mg2+ and HCO3-. Bone. 1999;25(2 Suppl):107S-11S.
304. Liou S, Chen S, Lee H, Bow J. Structural characterization of nano-sized calcium deficient apatite powders. Biomaterials. 2004;25(2):189-96.
305. Stenvinkel P, Wang K, Qureshi A, Axelsson J, Pecoits-Filho R, Gao P, et al. Low fetuin-A levels are associated with cardiovascular death: Impact of variations in the gene encoding fetuin. Kidney Int. 2005;67(6):2383-92.
306. Eraso L, Ginwala N, Qasim A, Mehta N, Dlugash R, Kapoor S, et al. Association of lower plasma fetuin-a levels with peripheral arterial disease in type 2 diabetes. Diabetes Care. 2009;33(2):408–10.
307. Rutsch F, Ruf N, Vaingankar S, Toliat M, Suk A, Hohne W, et al. Mutations in ENPP1 are associated with 'idiopathic' infantile arterial calcification. Nat Genet. 2003;34:379–81.
308. Rutsch F, Vaingankar S, Johnson K, Goldfine I, Maddux B, Schauerte P, et al. PC-1 nucleoside triphosphate pyrophosphohydrolase deficiency in idiopathic infantile arterial calcification. Am J Pathol. 2001;158:543–54.
309. Ohtsuki C, Kokubo T, Yamamuro T. Mechanism of apatite formation on CaO-SiO2-P2O5 glasses in a simulated body fluid. J Noncryst Solids. 1992;143:84–92.
310. Davies J. Ion association. London: Butterworth Press. 1962.
311. McDowell H, Gregory TM, Brown WE. Solubility of Ca5(PO4)3OH in the System Ca(OH)2–H3PO4–H2O at 5, 15, 25, and 37°C. J Res Natl Bur Stand. 1977;81A:273– 81.

312. Marquis-Gravel G, Redfors B, Leon MB, Généreux P. Medical Treatment of Aortic Stenosis. Circulation. 2016;134:1766–84.
313. Warren B, Yong J. Calcification of the aortic valve: Its progression and grading. Pathology. 1997;29:360-8.
314. Albanese I, Yu B, Al-Kindi H, Barratt B, Ott L, Al-Refai M, et al. Role of Noncanonical Wnts Signaling Pathway in Human Aortic Valve Calcification. Arter Thromb Vasc Biol. 2016;37(3):543-52.
315. Mahmut A, Boulanger M, Fournier D, Couture C, Trahan S, Page S, et al. Lipoprotein lipase in aortic valve stenosis is associated with lipid retention and remodelling. European journal of clinical investigation. 2013;43:570-8.
316. Tiao J, Semmens J, Masarei J, Lawrence-Brown M. The effect of age on serum creatinine levels in an aging population: relevance to vascular surgery. Cardiovasc Surg. 2002 10(5):445-51.
317. Penel G, Leroy G, Rey C, Bres E. MicroRaman Spectral Study of the PO4 and CO3 vibrational modes in synthetic and biological apatites. Calcif Tiss Int. 1998;63(6):475-81.
318. Karampas I, Kontoyannis C. Characterization of calcium phosphate mixtures. Vib Spectrosc. 2013;64:126-33.
319. Orzechowska S, Wróbel A, Goncerz G, Podolec P, E. R. Physicochemical and micro-tomographic characterization of inorganic deposits associated with aortic stenosis. J Heart Valve Dis. 2014;23:40-7.
320. Rygula A, Majzner K, Marzec KM, Kaczor A, Pilarczyk M, Baranska M. Raman spectroscopy of proteins: a review. Journal of Raman Spectroscopy. 2013;44:1061-76.
321. Czamara K, Natorska J, Kapusta P, Baranska M, Kaczor A. Raman microspectroscopy of human aortic valves: investigation of the local and global biochemical changes associated with calcification in aortic stenosis. Analyst. 2015;140(7):2164-70.
322. Gilinskaya LG, Rudina NA, Okuneva GN, Vlasov YA. Pathogenic Mineralization on Human Heart Valves. III. Electron Microscopy. J Struct Chem. 2003;44(6):1038–45.
323. Tomazic B. Physiochemical principles of cardiovascular calcification. Z Kardiol. 2001;90:68-80.
324. Delogne C, Lawford P, Habesch S, Carolan V. Characterization of the calcification of cardiac valve bioprostheses by environmental scanning electron microscopy and vibrational spectroscopy. J Microsc. 2007;228(Pt1):62-77.
325. Crane N, Popescu V, Morris M, Steenhuis P, Ignelzi MJ. Raman spectroscopic evidence for octacalcium phosphate and other transient mineral species deposited during intramembranous mineralization. Bone. 2006;39(3):434-42.
326. Tarnowski C, Ignelzi MJ, Morris M. Mineralization of developing mouse calvaria as revealed by Raman microspectroscopy. J Bone Miner Res. 2002;17(6):1118-26.
327. Bigi A, Compostella L, Fichera A, Foresti E, Gazzano M, Ripamonti A, et al. Structural and chemical characterization of inorganic deposits in calcified human mitral valve. J Inorg Biochem. 1988;34(2):75-82.
328. Robinson RA. An electron microscopy study of the crystalline inorganic components of bone and its relationship to the organic matrix. J Bone Joint Surg. 1952;34(2):389-434.
329. McNally E, Schwarcz H, Botton G, Arsenault A. A model for the ultrastructure of bone based on electron microscopy of ion-milled sections. PLoS ONE. 2012;7:e29258.

330. Eimar H, Siciliano R, Abdallah M-N, Nader S, Amin W, Martinez P, et al. Hydrogen peroxide whitens teeth by oxidizing the organic structure. J Dent. 2012;40(Suppl 2):e25-e33.
331. Timchenko EV, Timchenko PE, Volova LT, Pershutkina SV, Shalkovskaya PY. Using Raman spectroscopy for the evaluation of extracellular matrices based on heart valves. J Opt Technol. 2018;85(2):73-6.

Appendix: Other papers published

In addition to the publications described in this thesis, I have also collaborated and co-authored the following articles during my doctoral studies:

1. Guerra ED, Baakdah F, **Gourgas O**, Tam M, Stevenson MM, Georges E, Bohle DS**,** and Cerruti M. Inorganic ions on hemozoin surface provide a glimpse into *Plasmodium* biology. *Submitted*.
2. Marulanda J*, Parashar A*, **Gourgas O**, Bai X, Karaplis AC, Mecham RP, Cerruti M, Brinckmann J, Murshed M. Vascular Calcification in MGP-deficient Mice: A Phosphate and Elastin Story. *Submitted.*
3. Zhang P, **Gourgas O**, Lainé A, Murshed M, Mantovani D, Cerruti M. Three-Dimensional Elastin In Vitro Models for Understanding Vascular Calcification. *Submitted.*
4. Khan K, Albanese I, Hamid Q, Yu B, Shalal Y, Al-Kindi H, de Varennes B, Shum-Tim D, Alaws H, Tardif JC, Rheaume E, Alreshidan M, **Gourgas O**, Cerruti M, Schwertani A. Urotensin II, Urotensin-Related Peptide and their Receptor in Aortic Valve Stenosis. *Submitted.*
5. Mascarella MA, Alrasheed A, Fnais N, **Gourgas O**, Jalani G, Cerruti M, Tewfik MA. Raman Spectroscopy for Inverted Papilloma: A Proof-of-Concept Study. *Otolaryngol. Head. Neck. Surg.* 2018; 159(3):587-589.
6. Yu B, Hafiane A, Thanassoulis G, Ott L, Filwood N, Cerruti M, **Gourgas O**, Shum-Tum D, Al- Kindi H, de Varennes B, Alsheikh-Ali A, Genest J, Schwertani A. Lipoprotein(a) Induces Human Aortic Valve Interstitial Cell Calcification. *JACC. Basic Tansl. Sci.* 2017; 2(4): 358-371.

7. Albanese I, Yu B, Al-Kindi H, Barratt B, Ott L, Al-Refai M, de Varennes B, Shum-Tim D, Cerruti M, **Gourgas O**, Rhéaume E, Tardif JC, Schwertani A. Role of Noncanonical Wnt Signaling Pathway in Human Aortic Valve Calcification. *Arterioscler. Thromb. Vasc. Biol.* 2017; 37(3): 543-552.